CHAPTER 1

Data Acquisition and Recording

1.1 INTRODUCTION

Physical oceanography is an evolving science in which the instruments, types of observations and methods of analysis have undergone considerable change over the last few decades. With most advances in oceanographic theory, instrumentation, and software, there have been significant advances in marine science. The advent of digital computers has revolutionized data collection procedures and the way that data are reduced and analyzed. No longer is the individual scientist personally familiar with each data point and its contribution to his or her study. Instrumentation and data collection are moving out of direct application by the scientist and into the hands of skilled technicians who are becoming increasingly more specialized in the operation and maintenance of equipment. New electronic instruments operate at data rates not possible with earlier mechanical devices and produce volumes of information that can only be handled by high-speed computers. Most modern data collection systems transmit sensor data directly to computer-based data acquisition systems where they are stored in digital format on some type of electronic medium such as a tape, hard-drive, or optical disk. High-speed analog-to-digital (AD) converters and digital-signal-processors (DSPs) are now used to convert voltage or current signals from sensors to digital values.

With the many technological advances taking place, it is important for oceanographers to be aware of both the capabilities and limitations of their sampling equipment. This requires a basic understanding of the sensors, the recording systems and the data-processing tools. If these are known and the experiment carefully planned, many problems commonly encountered during the processing stage can be avoided. We cannot overemphasize the need for thoughtful experimental planning and proper calibration of all oceanographic sensors. If instruments are not in near-optimal locations or the researcher is unsure of the values coming out of the machines, then it will be difficult to believe the results gathered in the field. To be truly reliable, instruments should be calibrated on a regular basis at intervals determined by use and the susceptibility of the sensor to drift. More specifically, the output from some instruments such as the piezoelectric pressure sensors and fixed pathlength transmissometers drift with time and need to be calibrated before and after each field deployment. For example, the zero point for the Paroscientific Digiquartz (0–10,000 psi) pressure sensors used in the Hawaii Ocean Time-series (HOT) at station “Aloha” 100 km north of Honolulu drifts about 4 dbar in three years. As a consequence, the sensors are calibrated about every six months against a Paroscientific laboratory standard, which is recalibrated periodically at special calibration facilities in the United States (Lukas, 1994). Our experience also shows that over-the-side field calibrations during oceanic surveys can be highly valuable. As we discuss in the following chapters, there are a number of fundamental requirements to be considered when planning the collection of field records, including such basic considerations as the sampling interval, sampling duration and sampling location.

It is the purpose of this chapter to review many of the standard instruments and measurement techniques used in physical oceanography in order to provide the reader with a common understanding of both the utility and limitations of the resulting measurements. The discussion is not intended to serve as a detailed "user's manual" nor as an "observer's handbook". Rather, our purpose is to describe the fundamentals of the instruments in order to give some insight into the data they collect. An understanding of the basic observational concepts, and their limitations, is a prerequisite for the development of methods, techniques and procedures used to analyze and interpret the data that are collected.

Rather than treat each measurement tool individually, we have attempted to group them into generic classes and to limit our discussion to common features of the particular instruments and associated techniques. Specific references to particular company products and the quotation of manufacturer's engineering specifications have been avoided whenever possible. Instead, we refer to published material addressing the measurement systems or the data recorded by them. Those studies which compare measurements made by similar instruments are particularly valuable.

The emphasis of the instrument review section is to give the reader a background in the collection of data in physical oceanography. For those readers interested in more complete information regarding a specific instrument or measurement technique, we refer to the references at the end of the book where we list the sources of the material quoted. We realize that, in terms of specific measurement systems, and their review, this text will be quickly dated as new and better systems evolve. Still, we hope that the general outline we present for accuracy, precision and data coverage will serve as a useful guide to the employment of newer instruments and methods.

1.2 BASIC SAMPLING REQUIREMENTS

A primary concern in most observational work is the accuracy of the measurement device, a common performance statistic for the instrument. Absolute accuracy requires frequent instrument calibration to detect and correct for any shifts in behavior. The inconvenience of frequent calibration often causes the scientist to substitute instrument precision as the measurement capability of an instrument. Unlike absolute accuracy, precision is a relative term and simply represents the ability of the instrument to repeat the observation without deviation. Absolute accuracy further requires that the observation be consistent in magnitude with some absolute reference standard. In most cases, the user must be satisfied with having good precision and repeatability of the measurement rather than having absolute measurement accuracy. Any instrument that fails to maintain its precision, fails to provide data that can be handled in any meaningful statistical fashion. The best instruments are those that provide both high precision and defensible absolute accuracy.

Digital instrument resolution is measured in bits, where a resolution of N bits means that the full range of the sensor is partitioned into 2^N equal segments ($N = 1, 2, \ldots$). For example, eight-bit resolution means that the specified full-scale range of the sensor, say $V = 10$ volts, is divided into $2^8 = 256$ increments, with a bit-resolution of $V/256 = 0.039$ volts. Whether the instrument can actually measure to a resolution or accuracy of $V/2^N$ units is another matter. The sensor range can always be divided into an increasing number of smaller increments but eventually one reaches a point where the value of each bit is buried in the noise level of the sensor.

1.2.1 Sampling interval

Assuming the instrument selected can produce reliable and useful data, the next highest priority sampling requirement is that the measurements be collected often enough in space and time to resolve the phenomena of interest. For example, in the days when oceanographers were only interested in the mean stratification of the world ocean, water property profiles from discrete-level hydrographic (bottle) casts were adequate to resolve the general vertical density structure. On the other hand, these same discrete-level profiles failed to resolve the detailed structure associated with interleaving and mixing processes that now are resolved by the rapid vertical sampling of modern conductivity–temperature–depth (CTD) profilers. The need for higher resolution assumes that the oceanographer has some prior knowledge of the process of interest. Often this prior knowledge has been collected with instruments incapable of resolving the true variability and may only be suggested by highly aliased (distorted) data collected using earlier techniques. In addition, theoretical studies may provide information on the scales that must be resolved by the measurement system.

For discrete digital data $x(t_i)$ measured at times t_i, the choice of the sampling increment Δt (or Δx in the case of spatial measurements) is the quantity of importance. In essence, we want to sample often enough that we can pick out the highest frequency component of interest in the time-series but not oversample so that we fill up the data storage file, use up all the battery power, or become swamped with a lot of unnecessary data. We might also want to sample at irregular intervals to avoid built-in bias in our sampling scheme. If the sampling interval is too large to resolve higher frequency components, it becomes necessary to suppress these components during sampling using a sensor whose response is limited to frequencies equal to that of the sampling frequency. As we discuss in our section on processing satellite-tracked drifter data, these lessons are often learned too late—after the buoys have been cast adrift in the sea.

The important aspect to keep in mind is that, for a given sampling interval Δt, the highest frequency we can hope to resolve is the *Nyquist* (or *folding*) *frequency*, f_N, defined as

$$f_N = 1/(2\Delta t) \tag{1.2.1}$$

We cannot resolve any higher frequencies than this. For example, if we sample every 10 h, the highest frequency we can hope to see in the data is $f_N = 0.05$ cph (cycles per hour). Equation (1.2.1) states the obvious—that it takes at least two sampling intervals (or three data points) to resolve a sinusoidal-type oscillation with period $1/f_N$ (Figure

1.2.1). In practice, we need to contend with noise and sampling errors so that it takes something like three or more sampling increments (i.e. ≥four data points) to accurately determine the highest observable frequency. Thus, f_N is an upper limit. The highest frequency we can resolve for a sampling of $\Delta t = 10$ h in Figure 1.2.1 is closer to $1/3\Delta t \approx 0.033$ cph.

An important consequence of (1.2.1) is the problem of *aliasing*. In particular, if there is considerable energy at frequencies $f > f_N$—which we obviously cannot resolve because of the Δt we picked—this energy gets folded back into the range of frequencies, $f < f_N$, which we are attempting to resolve. This unresolved energy doesn't disappear but gets redistributed within the frequency range of interest. What is worse is that the folded-back energy is disguised (or aliased) within frequency components different from those of its origin. We cannot distinguish this folded-back energy from that which actually belongs to the lower frequencies. Thus, we end up with erroneous (aliased) estimates of the spectral energy variance over the resolvable range of frequencies. An example of highly aliased data would be 13-h sampling of currents in a region having strong semidiurnal tidal currents. More will be said on this topic in Chapter 5.

As a general rule, one should plan a measurement program based on the frequencies and wavenumbers (estimated from the corresponding periods and wavelengths) of the parameters of interest over the study domain. This requirement then dictates the selection of the measurement tool or technique. If the instrument cannot sample rapidly enough to resolve the frequencies of concern it should not be used. It should be emphasized that the Nyquist frequency concept applies to both time and space and the Nyquist wavenumber is a valid means of determining the fundamental wavelength that must be sampled.

1.2.2 Sampling duration

The next concern is that one samples long enough to establish a statistically significant picture of the process being studied. For time-series measurements, this amounts to a requirement that the data be collected over a period sufficiently long that

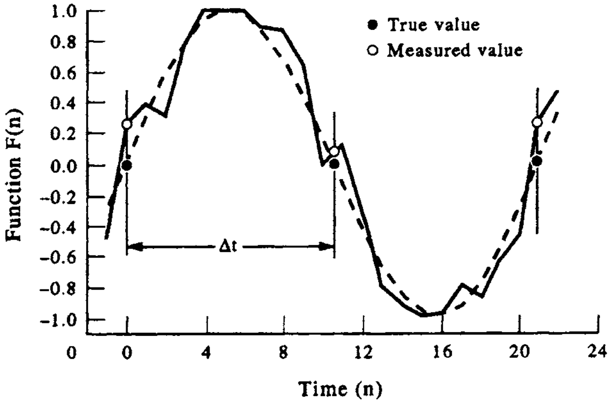

Figure 1.2.1. Plot of the function $F(n) = \sin(2\pi n/20 + \phi)$ *where time is given by the integer* $n = -1, 0, \ldots, 24$*. The period* $2\Delta t = 1/f_N$ *is 20 units and* ϕ *is a random phase with a small magnitude in the range* ± 0.1*. Open circles denote measured points and solid points the curve F(n). Noise makes it necessary to use more than three data values to accurately define the oscillation period.*

repeated cycles of the phenomenon are observed. This also applies to spatial sampling where statistical considerations require a large enough sample to define multiple cycles of the process being studied. Again, the requirement places basic limitations on the instrument selected for use. If the equipment cannot continuously collect the data needed for the length of time required to resolve repeated cycles of the process, it is not well suited to the measurement required.

Consider the duration of the sampling at time step Δt. The longer we make the record the better we are to resolve different frequency components in the data. In the case of spatially separated data, Δx, resolution increases with increased spatial coverage of the data. It is the total record length $T = N\Delta t$ obtained for N data samples that: (1) determines the lowest frequency (the *fundamental frequency*)

$$f_o = 1/(N\Delta t) = 1/T \tag{1.2.2}$$

that can be extracted from the time-series record; (2) determines the frequency resolution or minimum difference in frequency $\Delta f = |f_2 - f_1| = 1/N\Delta t$ that can be resolved between adjoining frequency components, f_1 and f_2 (Figure 1.2.2); and (3) determines the amount of band averaging (averaging of adjacent frequency bands) that can be applied to enhance the statistical significance of individual spectral estimates. In Figure 1.2.2, the two separate waveforms of equal amplitude but different frequency produce a single spectrum. The two frequencies are well resolved for $\Delta f = 2/N\Delta t$ and $3/2N\Delta t$, just resolved for $\Delta f = 1/N\Delta t$, and not resolved for $\Delta f = 1/2N\Delta t$.

In theory, we should be able to resolve all frequency components, f, in the frequency range $f_o \leq f \leq f_N$, where f_N and f_o are defined by (1.2.1) and (1.2.2), respectively. Herein lies a classic sampling problem. In order to resolve the frequencies of interest in a time-series, we need to sample for a long time (T large) so that f_o covers the low end of the frequency spectrum and Δf is small (frequency resolution is high). At the same time, we would like to sample sufficiently rapidly (Δt small) so that f_N extends beyond all frequency components with significant spectral energy. Unfortunately, the longer and more rapidly we want to sample the more data we need to collect and store, the more time, effort and money we need to put into the sampling and the better resolution we require from our sensors.

Our ability to resolve frequency components follows from Rayleigh's criterion for the resolution of adjacent spectral peaks in light shone onto a diffraction grating. It states that two adjacent frequency components are just resolved when the peaks of the spectra are separated by frequency difference $\Delta f = f_o = 1/N\Delta t$ (Figure 1.2.2). For example, to separate the spectral peak associated with the lunar–solar semidiurnal tidal component M_2 (frequency = 0.08051 cph) from that of the solar semidiurnal tidal component S_2 (0.08333 cph), for which $\Delta f = 0.00282$ cph, requires $N = 355$ data points at a sampling interval $\Delta t = 1$ h or $N = 71$ data points at $\Delta t = 5$ h. Similarly, a total of 328 data values at 1-h sampling are needed to separate the two main diurnal constituents K_1 and O_1 ($\Delta f = 0.00305$ cph). Note that if f_N is the highest frequency we can measure and f_o is the limit of frequency resolution, then

$$f_N/f_o = (1/2\Delta t)/(1/N\Delta t) = N/2 \tag{1.2.3}$$

is the maximum number of Fourier components we can hope to estimate in any analysis.

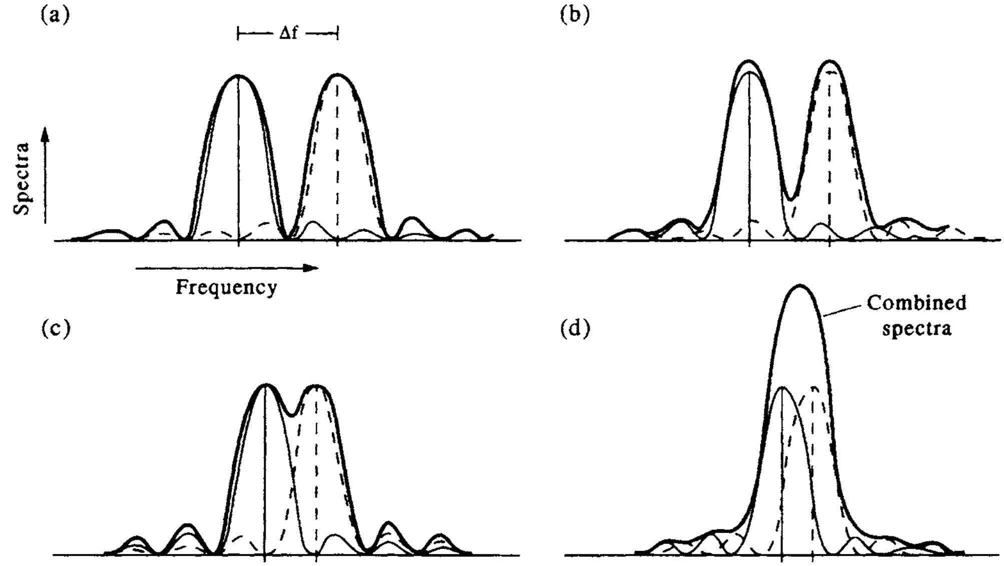

Figure 1.2.2. Spectral peaks of two separate waveforms of equal amplitude and frequencies f_1 and f_2 (dashed and thin line) together with the calculated spectrum (solid line). (a) and (b) are well-resolved spectra; (c) just resolved spectra; and (d) not resolved. Thick solid line is total spectrum for two underlying signals with slightly different peak frequencies.

1.2.3 Sampling accuracy

According to the two previous sections, we need to sample long and often if we hope to resolve the range of scales of interest in the variables we are measuring. It is intuitively obvious that we also need to sample as accurately as possible—with the degree of recording accuracy determined by the response characteristics of the sensors, the number of bits per data record (or parameter value) needed to raise measurement values above background noise, and the volume of data we can live with. There is no use attempting to sample the high or low ends of the spectrum if the instrument cannot respond rapidly or accurately enough to resolve changes in the parameter being measured. In addition, there are several approaches to this aspect of data sampling including the brute-force approach in which we measure as often as we can at the degree of accuracy available and then improve the statistical reliability of each data record through post-survey averaging, smoothing, and other manipulation.

1.2.4 Burst sampling versus continuous sampling

Regularly-spaced, digital time-series can be obtained in two different ways. The most common approach is to use a *continuous sampling mode*, in which the data are sampled at equally spaced intervals $t_k = t_o + k\Delta t$ from the start time t_o. Here, k is a positive integer. Regardless of whether the equally spaced data have undergone internal averaging or decimation using algorithms built into the machine, the output to the data storage file is a series of individual samples at times t_k. (Here, "decimation" is used in the loose sense of removing every nth data point, where n is any positive integer, and not in the sense of the ancient Roman technique of putting to death one in ten soldiers in a legion guilty of mutiny or other crime.) Alternatively, we can use a *burst sampling mode*, in which rapid sampling is undertaken over a relatively short time interval Δt_B or "burst" embedded within each regularly spaced time interval, Δt. That is, the data are sampled at high frequency for a short duration starting (or ending) at times t_k for which the burst duration $\Delta t_B \ll \Delta t$. The instrument "rests" between bursts.

There are advantages to the burst sampling scheme, especially in noisy (high frequency) environments where it may be necessary to average-out the noise to get at the frequencies of interest. Burst sampling works especially well when there is a "spectral gap" between fluctuations at the high and low ends of the spectrum. As an example, there is typically a spectral gap between surface gravity waves in the open ocean (periods of 1–20 s) and the 12-hourly motions that characterize semidiurnal tidal currents. Thus, if we wanted to measure surface tidal currents using the burst-mode option for our current meter, we could set the sampling to a 2-min burst every hour; this option would smooth out the high-frequency wave effects but provide sufficient numbers of velocity measurements to resolve the tidal motions. Burst sampling enables us to filter out the high-frequency noise and obtain an improved estimate of the variability hidden underneath the high-frequency fluctuations. In addition, we can examine the high-frequency variability by scrutinizing the burst sampled data. If we were to sample rapidly enough, we could estimate the surface gravity wave energy spectrum. Many oceanographic instruments use (or have provision for) a burst-sampling data collection mode. The "duty cycle" often used to collect positional data from satellite-tracked drifters is a cost-saving form of burst sampling in which all positional data within a 24-h period (about 10 satellite fixes) are collected only every third day. Tracking costs paid to Service Argos are reduced by a factor of three using the duty cycle. Problems arise when the length of each burst is too short to resolve energetic motions with periods comparable to the burst sample length. In the case of satellite-tracked drifters poleward of tropical latitudes, these problems are associated with highly energetic inertial motions whose periods $T = 1/(2\Omega \sin\theta)$ are comparable to the 24-h duration of the burst sample (here, $\Omega = 0.1161 \times 10^{-4}$ cycles per second is the earth's rate of rotation and $\theta \equiv$ latitude). Since 1992, it has been possible to improve resolution of high-frequency motions using a 1/3 duty cycle of 8 h "on" followed by 16 h "off". According to Bograd *et al.* (1999), even better resolution of high-frequency mid-latitude motions could be obtained using a duty cycle of 16 h "on" followed by 32 h "off".

1.2.5 Regularly versus irregularly sampled data

In certain respects, an irregular sampling in time or nonequidistant placement of instruments can be more effective than a more esthetically appealing uniform sampling. For example, unequal spacing permits a more statistically reliable resolution of oceanic spatial variability by increasing the number of quasi-independent estimates of the dominant wavelengths (wavenumbers). Since oceanographers are almost always faced with having fewer instruments than they require to resolve oceanic features, irregular spacing can also be used to increase the overall spatial coverage (fundamental wavenumber) while maintaining the small-scale instrument separation for Nyquist wavenumber estimates. The main concern is the lack of redundancy should certain key instruments fail, as often seems to happen. In this case, a quasi-regular spacing between locations is better. Prior knowledge of the scales of variability to expect is a definite plus in any experimental array design.

In a sense, the quasi-logarithmic vertical spacing adopted by oceanographers for bottle cast (hydrographic) sampling of 0, 10, 20, 30, 50, 75, 100, 125, 150 m, etc. represents a "spectral window" adaptation to the known physical–chemical structure of the ocean. Highest resolution is required near the surface where vertical changes are most rapid. Similarly, an uneven spatial arrangement of observations increases the number of quasi-independent estimates of the wavenumber spectrum. Digital data are most often sampled (or subsampled) at regularly-spaced time increments. Aside from the usual human propensity for order, the need for regularly-spaced data derives from the fact that most analysis methods have been developed for regular-spaced data. However, digital data do not necessarily need to be sampled at regularly-spaced time increments to give meaningful results, although some form of interpolation between values may eventually be required.

1.2.6 Independent realizations

As we review the different instruments and methods, the reader should keep in mind the three basic concerns of accuracy/precision, resolution (spatial and temporal), and statistical significance (statistical sampling theory). A fundamental consideration in ensuring the statistical significance of a set of measurements is the need for independent realizations. If repeat measurements of a process are strongly correlated, they provide no new information and do not contribute to the statistical significance of the measurements. Often a subjective decision must be made on the question of statistical independence. While this concept has a formal definition, in practice it is often difficult to judge. A simple guide suggested here is that any suite of measurements that is highly correlated (in time or space) cannot be independent. At the same time, a group of measurements that is totally uncorrelated, must be independent. In the case of no correlation, the number of "degrees of freedom" is defined by the total number of measurements; for the case of perfect correlation, the redundancy of the data values reduces the degrees of freedom to one for scalar quantity and to two for a vector quantity. The degree of correlation in the data set provides a way of roughly estimating the number of degrees of freedom within a given suite of observations. While more precise methods will be presented later in this text, a simple linear relation between degrees of freedom and correlation often gives the practitioner a way to proceed without developing complex mathematical constructs.

As will be discussed in detail later, all of these sampling recommendations have statistical foundations and the guiding rules of probability and estimation can be carefully applied to determine the sampling requirements and dictate the appropriate measurement system. At the same time, these same statistical methods can be applied to existing data in order to better evaluate their ability to measure phenomena of interest. These comments are made to assist the reader in evaluating the potential of a particular instrument (or method) for the measurement of some desired variable.

1.3 TEMPERATURE

The measurement of temperature in the ocean uses conventional techniques except for deep observations where hydrostatic pressures are high and there is a need to protect the sensing system from ambient depth/temperature changes higher in the water column as the sensor is returned to the ship. Temperature is the ocean property that is easiest to measure accurately. Some of the ways in which ocean temperature can be measured are:

(a) Expansion of a liquid or a metal.
(b) Differential expansion of two metals (bimetallic strip).
(c) Vapor pressure of a liquid.
(d) Thermocouples.
(e) Change in electrical resistance.
(f) Infrared radiation from the sea surface.

In most of these sensing techniques, the temperature effect is very small and some form of amplification is necessary to make the temperature measurement detectable. Usually, the response is nearly linear with temperature so that only the first-order term is needed when converting the sensor measurement to temperature. However, in order to achieve high precision over large temperature ranges, second, third and even fourth order terms must sometimes be used to convert the measured variable to temperature.

1.3.1 Mercury thermometers

Of the above methods, (a), (e), and (f) have been the most widely used in physical oceanography. The most common type of the liquid expansion sensor is the mercury-in-glass thermometer. In their earliest oceanographic application, simple mercury thermometers were lowered into the ocean with hopes of measuring the temperature at great depths in the ocean. Two effects were soon noticed. First, thermometer housings with insufficient strength succumbed to the greater pressure in the ocean and were crushed. Second, the process of bringing an active thermometer through the oceanic vertical temperature gradient sufficiently altered the deeper readings that it was not possible to accurately measure the deeper temperatures. An early solution to this problem was the development of min–max thermometers that were capable of retaining the minimum and maximum temperatures encountered over the descent and ascent of the thermometer. This type of thermometer was widely used on the Challenger expedition of 1873–1876.

The real breakthrough in thermometry was the development of reversing thermometers, first introduced in London by Negretti and Zambra in 1874 (Sverdrup *et al.*, 1942, p. 349). The reversing thermometer contains a mechanism such that, when the thermometer is inverted, the mercury in the thermometer stem separates from the bulb reservoir and captures the temperature at the time of inversion. Subsequent temperature changes experienced by the thermometer have limited effects on the amount of mercury in the thermometer stem and can be accounted for when the temperature is read on board the observing ship. This "break-off" mechanism is based on the fact that more energy is required to create a gas-mercury interface (i.e. to break the mercury) than is needed to expand an interface that already exists. Thus, within the "pigtail" section of the reversing thermometer is a narrow region called the "break-off point", located near appendix C in Figure 1.3.1, where the mercury will break when the thermometer is inverted.

The accuracy of the reversing thermometer depends on the precision with which this break occurs. In good reversing thermometers this precision is better than 0.01°C. In standard mercury-in-glass thermometers, as well as in reversing thermometers, there are concerns other than the break point which affect the precision of the temperature measurement. These are:

(a) Linearity in the expansion coefficient of the liquid.
(b) The constancy of the bulb volume.

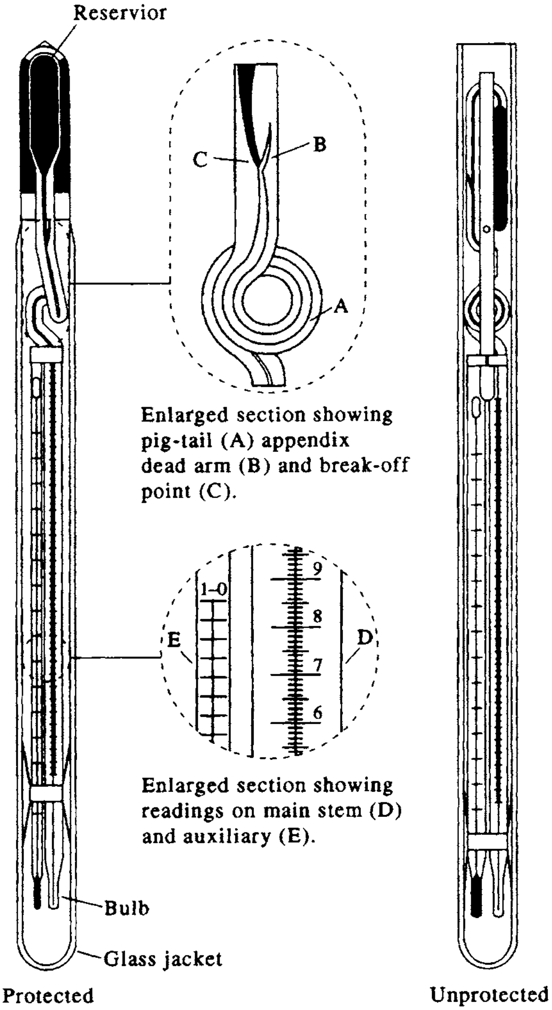

Figure 1.3.1. Details of a reversing mercury thermometer showing the"pigtail appendix".

(c) The uniformity of the capillary bore.
(d) The exposure of the thermometer stem to temperatures other than the bulb temperature.

Mercury expands in a near-linear manner with temperature. As a consequence, it has been the liquid used in most high precision, liquid–glass thermometers. Other liquids such as alcohol and toluene are used in precision thermometers only for very low temperature applications where the higher viscosity of mercury is a limitation. Expansion linearity is critical in the construction of the thermometer scale which would be difficult to engrave precisely if expansion were nonlinear.

In a mercury thermometer, the volume of the bulb is equivalent to about 6000 stem-degrees Celsius. This is known as the "degree volume" and usually is considered to comprise the bulb plus the portion of the stem below the mark. If the thermometer is to retain its calibration, this volume must remain constant with a precision not commonly realized by the casual user. For a thermometer precision within ±0.01°C, the bulb volume must remain constant within one part in 600,000. Glass does not have ideal mechanical properties and it is known to exhibit some plastic behavior and deform under sustained stress. Repeated exposure to high pressures may produce permanent deformation and a consequent shift in bulb volume. Therefore, precision can only be maintained by frequent laboratory calibration. Such shifts in bulb volume can be detected and corrected by the determination of the "ice point" (a slurry of water plus ice) which should be checked frequently if high accuracy is required. The procedure is more or less obvious but a few points should be considered. First the ice should be made from distilled water and the water–ice mixture should also be made from distilled water. The container should be insulated and at least 70% of the bath in contact with the thermometer should be chopped ice. The thermometer should be immersed for five or more minutes during which time the ice–water mixture should be stirred continuously. The control temperature of the bath can be taken by an accurate thermometer of known reliability. Comparison with the temperature of the reversing thermometer, after the known calibration characteristics have been accounted for, will give an estimate of any offsets inherent in the use of the reversing thermometer in question.

The uniformity of the capillary bore is critical to the accuracy of the mercury thermometer. In order to maintain the linearity of the temperature scale it is necessary to have a uniform capillary as well as a linear response liquid element. Small variations in the capillary can occur as a result of small differences in cooling during its construction or to inhomogeneities in the glass. Errors resulting from the variations in capillary bore can be corrected through calibration at known temperatures. The resulting corrections, including any effect of the change in bulb volume, are known as "index corrections". These remain constant relative to the ice point and, once determined, can be corrected for a shift in the ice point by addition or subtraction of a constant amount. With proper calibration and maintenance, most of the mechanical defects in the thermometer can be accounted for. Reversing thermometers are then capable of accuracies of ±0.01°C, as given earlier for the precision of the mercury break-point. This accuracy, of course, depends on the resolution of the temperature scale etched on the thermometer. For high accuracy in the typically weak vertical temperature gradients of the deep ocean, thermometers are etched with scale intervals between 0.1 and 0.2°C. Most reversing thermometers have scale intervals of 0.1°C.

The reliability and calibrated absolute accuracy of reversing thermometers continue to provide a standard temperature measurement against which all forms of electronic sensors are compared and evaluated. In this role as a calibration standard, reversing thermometers continue to be widely used. In addition, many oceanographers still believe that standard hydrographic stations made with sample bottles and reversing thermometers, provide the only reliable data. For these reasons, we briefly describe some of the fundamental problems that occur when using reversing thermometers. An understanding of these errors may also prove helpful in evaluating the accuracy of reversing thermometer data that are archived in the historical data file. The primary malfunction that occurs with a reversing thermometer is a failure of the mercury to break at the correct position. This failure is caused by the presence of gas (a bubble) somewhere within the mercury column. Normally all thermometers contain some gas within the mercury. As long as the gas bubble has sufficient mercury compressing it, the bubble volume is negligible, but if the bubble gets into the upper part of the capillary tube it expands and causes the mercury to break at the bubble rather than at the break-off point. The proper place for this resident gas is at the bulb end of the mercury; for this reason it is recommended that reversing thermometers always be stored and transported in the bulb-up (reservoir-down) position. Rough handling can be the cause of bubble formation higher up in the capillary tube. Bubbles lead to consistently offset temperatures and a record of the thermometer history can clearly indicate when such a malfunction has occurred. Again the practice of renewing, or at least checking, the thermometer calibration is essential to ensuring accurate temperature measurements. As with most oceanographic equipment, a thermometer with a detailed history is much more valuable than a new one without some prior use.

There are two basic types of reversing thermometers: (1) protected thermometers which are encased completely in a glass jacket and not exposed to the pressure of the water column; and (2) unprotected thermometers for which the glass jacket is open at one end so that the reservoir experiences the increase of pressure with ocean depth, leading to an apparent increase in the measured temperature. The increase in temperature with depth is due to the compression of the glass bulb, so that if the compressibility of the glass is known from the manufacturer, the pressure and hence the depth can be inferred from the temperature difference, $\Delta T = T_{\mathrm{Unprotected}} - T_{\mathrm{Protected}}$. The difference in thermometer readings, collected at the same depth, can be used to compute the depth to an accuracy of about 1% of the depth. This subject will be treated more completely in the section on depth/pressure measurement. We note here that the 1% accuracy for reversing thermometers exceeds the accuracy of 2–3% one normally expects from modern depth sounders.

Unless collected for a specific observational program or taken as calibrations for electronic measurement systems, reversing thermometer data are most commonly found in historical data archives. In such cases, the user is often unfamiliar with the precise history of the temperature data and thus cannot reconstruct the conditions under which the data were collected and edited. Under these conditions one generally assumes that the errors are of two types; either they are large offsets (such as errors in reading the thermometer) which are readily identifiable by comparison with other regional historical data, or they are small random errors due to a variety of sources and difficult to identify or separate from real physical oceanic variability. Parallax errors, which are one of the main causes of reading errors, are greatly reduced through use of an eye-piece magnifier. Identification and editing of these errors depends on the problem being studied and will be discussed in a later section on data processing.

1.3.2. The mechanical bathythermograph (MBT)

The MBT uses a liquid-in-metal thermometer to register temperature and a Bourdon tube sensor to measure pressure. The temperature sensing element is a fine copper tube nearly 17 m long filled with toluene (Figure 1.3.2). Temperature readings are recorded by a mechanical stylus which scratches a thin line on a coated glass slide. Although this instrument has largely been replaced by the expendable bathythermograph (XBT), the historical archives contain numerous temperature profiles collected using this device. It is, therefore, worthwhile to describe the instrument and the data it measures. Only the temperature measurement aspect of this device will be considered; the pressure/depth recording capability will be addressed in a latter section.

There are numerous limitations to the MBT. To begin with, it is restricted to depths less than 300 m. While the MBT was intended to be used with the ship underway, it is only really possible to use it successfully when the ship is traveling at no more than a

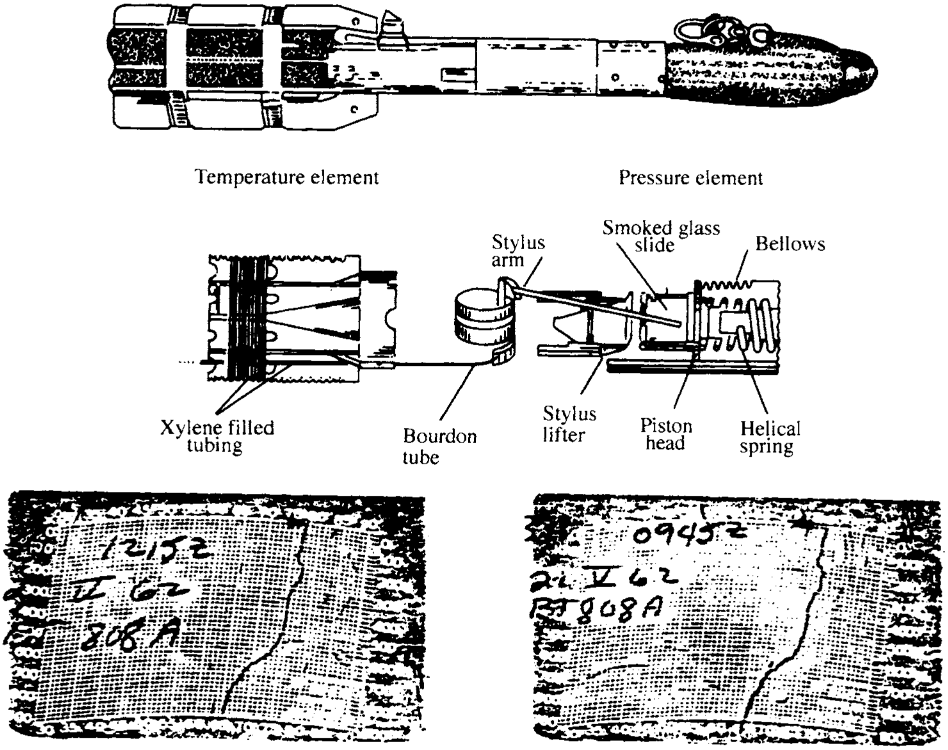

Figure 1.3.2. A bathythermograph showing its internal construction and sample BT slides.

few knots. At higher speeds, it becomes impossible to retrieve the MBT without the risk of hitting the instrument against the ship. Higher speeds also make it difficult to properly estimate the depth of the probe from the amount of wire out. The temperature accuracy of the MBT is restricted by the inherent lower accuracy of the liquid-in-metal thermometer. Metal thermometers are also subject to permanent deformation. Since metal is more subject to changes at high temperatures than is glass it is possible to alter the performance of the MBT by continued exposure to higher temperatures (i.e. by leaving the probe out in the sun). The metal return spring of the temperature stylus is also a source of potential problems in that it is subject to hysteresis and creep. Hysteresis, in which the up-trace does not coincide with the down-trace, is especially prevalent when the temperature differences are small. Creep occurs when the metal is subjected to a constant loading for long periods. Thus, an MBT continuously used in the heat of the tropics may be found later to have a slight positive temperature error.

Most of the above errors can be detected and corrected for by frequent calibration of the MBT. Even with regular calibration it is doubtful that the stated precision of 0.1°F (0.06°C) can be attained. Here, the value is given in °F since most of the MBTs were produced with these temperature scales. When considering MBT data from the historical data files, it should be realized that these data were entered into the files by hand. The usual method was to produce an enlarged black-and-white photograph of the temperature trace using the nonlinear calibration grid unique to each instrument. Temperature values were then read off of these photographs and entered into the data file at the corresponding depths. The usual procedure was to record temperatures for a fixed depth interval (i.e. 5 or 10 m) rather than to select out inflection points that best described the temperature profile. The primary weakness of this procedure is the ease with which incorrect values can enter the data file through misreading the temperature trace or incorrectly entering the measured value. Usually these types of errors result in large differences with the neighboring values and can be easily identified. Care should be taken, however, to remove such values before applying objective methods to search for smaller random errors. It is also possible that data entry errors can occur in the entry of date, time and position of the temperature profile and tests should be made to detect these errors.

1.3.3. Resistance thermometers (expendable bathythermograph: XBT)

Since the electrical resistance of metals, and other materials, changes with temperature, these materials can be used as temperature sensors. The resistance (R) of most metals depends on temperature (T) and can be expressed as a polynomial

$$R = R(1 + aT + bT^2 + cT^3 + \dots) \tag{1.2.4}$$

where a, b, and c are constants. In practice, it is usually assumed that the response is linear over some limited temperature range and the proportionality can be given by the value of the coefficient a (called the temperature resistance coefficient). The most commonly used metals are copper, platinum, and nickel which have temperature coefficients of 0.0043, 0.0039, and 0.0066 $(^\circ\mathrm{C})^{-1}$, respectively. Of these, copper has the most linear response but its resistance is low so that a thermal element would require many turns of fine wire and would consequently be expensive to produce. Nickel has a very high resistance but deviates sharply from linearity. Platinum has a relatively high resistance level, is very stable and has a relatively linear behavior. For these reasons, platinum resistance thermometers have become a standard by which the international scale of temperature is defined. Platinum thermometers are also widely used as laboratory calibration standards and have accuracies of ±0.001°C.

The semiconductors form another class of resistive materials used for temperature measurements. These are mixtures of oxides of metals such as nickel, cobalt, and manganese which are molded at high pressure followed by sintering (i.e. heating to incipient fusion). The types of semiconductors used for oceanographic measurements are commonly called thermistors. These thermistors have the advantages that: (1) the temperature resistance coefficient of $-0.05(^\circ\mathrm{C})^{-1}$ is about ten times as great as that for copper; and (2) the thermistors may be made with high resistance for a very small physical size.

The temperature coefficient of thermistors is negative which means that the resistance decreases as temperature increases. This temperature coefficient is not a constant except over very small temperature ranges; hence the change of resistance with temperature is not linear. Instead, the relationship between resistance and temperature is given by

$$R(T) = R_o \exp\left[\beta(T^{-1} - T_o^{-1})\right] \tag{1.2.5}$$

where $R_o = \beta/T^2$ is the conventional temperature coefficient of resistance, and T and T_o are two absolute temperatures (K) with the respective resistance values of $R(T)$ and

R_o. Thus, we have a relationship whereby temperature T can be computed from the measurement of resistance $R(T)$.

One of the most common uses of thermistors in oceanography is in expendable bathythermographs (XBTs). The XBT was developed to provide an upper ocean temperature profiling device that operated while the ship was underway. The crucial development was the concept of depth measurement using the elapsed time for the known fall rate of a "freely-falling" probe. To achieve "free-fall", independent of the ship's motion, the data transfer cable is constructed from fine copper wire with feed-spools in both the sensor probe and in the launching canister (Figure 1.3.3). The details of the depth measurement capability of the XBT will be discussed and evaluated in the section on depth/pressure measurements.

The XBT probes employ a thermistor placed in the nose of the probe as the temperature sensing element. According to the manufacturer (Sippican Corp.; Marion, Massachusetts, U.S.A.), the accuracy of this system is ±0.1°C. This figure is determined from the characteristics of a batch of semiconductor material which has known resistance–temperature (R–T) properties. To yield a given resistance at a standard temperature, the individual thermistors are precision-ground, with the XBT probe thermistors ground to yield 5000 Ω (Ω is the symbol for the unit of ohms) at 25°C (Georgi *et al.*, 1980). If the major source of XBT probe-to-probe variability can be attributed to imprecise grinding, then a single-point calibration should suffice to reduce this variability in the resultant temperatures. Such a calibration was carried out by Georgi *et al.* (1980) both at sea and in the laboratory.

To evaluate the effects of random errors on the calibration procedure, twelve probes were calibrated repeatedly. The mean differences between the measured and bath temperatures was ±0.045°C with a standard deviation of 0.01°C. For the overall calibration comparison, 18 cases of probes (12 probes per case) were examined. Six cases of T7s (good to 800 m and up to 30 knots) and two cases of T6s (good to 500 m and at less than 15 knots) were purchased new from Sippican while the remaining 10 cases of T4s (good to 500 m up to 30 knots) were acquired from a large pool of XBT probes manufactured in 1970 for the U.S. Navy. The overall average standard deviation for the probes was 0.023°C which then reduces to 0.021°C when consideration is made for the inherent variability of the calibration procedure.

A separate investigation was made of the R–T relationship by studying the response characteristics for nine probes. The conclusion was that the R–T differences ranged from +0.011°C to −0.014°C which then means that the measured relationships were within ±0.014°C of the published relationship and that the calculation of new coefficients, following Steinhart and Hart (1968), is not warranted. Moreover the final conclusions of Georgi *et al.* (1980) suggest an overall accuracy for XBT thermistors of ±0.06°C at the 95% confidence level and that the consistency between thermistors is sufficiently high that individual probe calibration is not needed for this accuracy level.

Another method of evaluating the performance of the XBT system is to compare XBT temperature profiles with those taken at the same time with an higher accuracy profiler such as a CTD system. Such comparisons are discussed by Heinmiller *et al.* (1983) for data collected in both the Atlantic and the Pacific using calibrated CTD systems. In these comparisons, it is always a problem to achieve true synopticity in the data collection since the XBT probe falls much faster than the recommended drop rate for a CTD probe. Most of the earlier comparisons between XBT and CTD profiles (Flierl and Robinson, 1977; Seaver and Kuleshov, 1982) were carried out using XBT temperature profiles collected between CTD stations separated by 30 km. For the

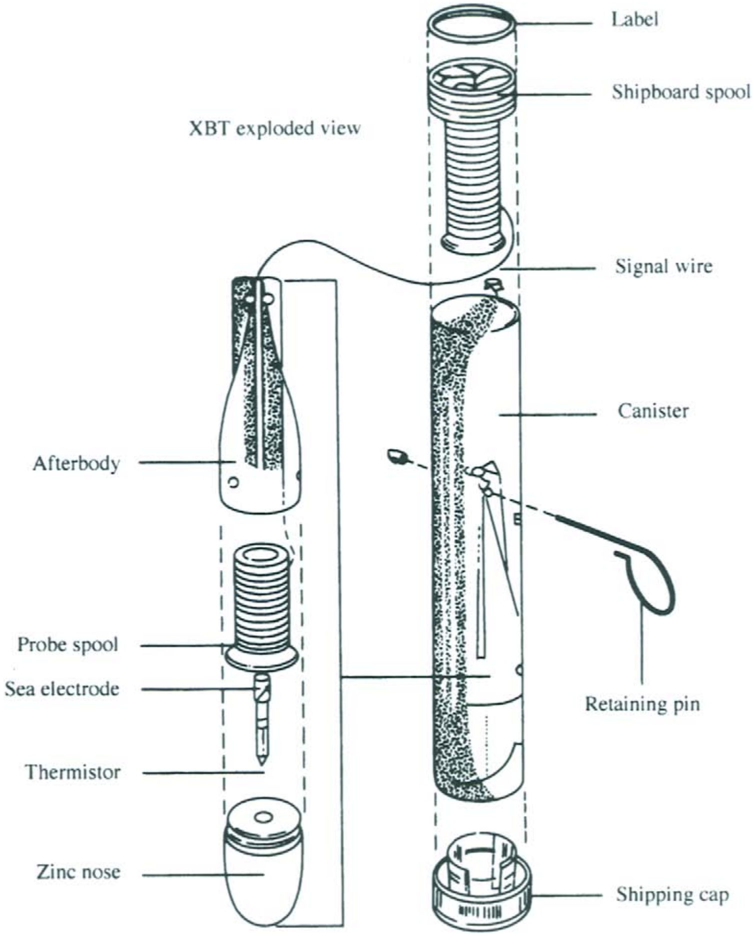

Figure 1.3.3. Exploded view of a Sippican Oceanographic Inc. XBT showing spool and canister.

purposes of intercomparison, it is better for the XBT and CTD profiles to be collected as simultaneously as possible.

The primary error discussed by Heinmiller *et al.* (1983) is that in the measurement of depth rather than temperature. There were, however, significant differences between temperatures measured at depths where the vertical temperature gradient was small and the depth error should make little or no contribution. Here, the XBT temperatures were found to be systematically higher than those recorded by the CTD. Sample comparisons were divided by probe type and experiment. The T4 probes (as defined above) yielded a mean XBT-CTD difference of about 0.19°C while the T7s (defined above) had a lower mean temperature difference of 0.13°C. Corresponding standard deviations of the temperature differences were 0.23°C, for the T4s, and 0.11°C for the T7s. Taken together, these statistics suggest an XBT accuracy less than the ±0.1°C given by the manufacturer and far less than the 0.06°C reported by Georgi *et al.* (1980) from their calibrations.

From these divergent results, it is difficult to decide where the true XBT temperature accuracy lies. Since the Heinmiller *et al.* (1983) comparisons were made *in situ* there are many sources of error that could contribute to the larger temperature differences. Even though most of the CTD casts were made with calibrated instruments, errors in operational procedures during collection and archival could add significant errors to the resultant data. Also, it is not easy to find segments of temperature profiles with no vertical temperature gradient and therefore it is difficult to ignore the effect of the depth measurement error on the temperature trace. It seems fair to conclude that the laboratory calibrations represent the ideal accuracy possible with the XBT system (i.e. better than ±0.1°C). In the field, however, one must expect other influences that will reduce the accuracy of the XBT measurements and an overall accuracy slightly more than ±0.1°C is perhaps realistic. Some of the sources of these errors can be easily detected, such as an insulation failure in the copper wire which results in single step offsets in the resulting temperature profile. Other possible temperature error sources are interference due to shipboard radio transmission (which shows up as high frequency noise in the vertical temperature profile) or problems with the recording system. Hopefully, these problems are detected before the data are archived in historical data files.

In closing this section we comment that, until recently, most XBT data were digitized by hand. The disadvantage of this procedure is that chart paper recording doesn't fully realize the potential digital accuracy of the sensing system and that the opportunities for operator recording errors are considerable. Again, some care should be exercised in editing out these large errors which usually result from the incorrect hand recording of temperature, date, time or position. It is becoming increasingly popular to use digital XBT recording systems which improve the accuracy of the recording and eliminate the possibility of incorrectly entering the temperature trace. Such systems are described, for example, in Stegen *et al.* (1975) and Emery *et al.* (1986). Today, essentially all research XBT data are collected with digital systems, while the analog systems are predominantly used by various international navies.

1.3.4 Salinity/conductivity–temperature–depth profilers

Resistance thermometers are widely used on continuous profilers designed to replace the earlier hydrographic profiles collected using a series of sampling bottles. The new *in situ* electronic instruments continuously sample the water temperature, providing much higher resolution information on the ocean's vertical and horizontal temperature structure. Since density also depends on salinity, electronic sensors were developed to measure salinity *in situ* and were incorporated into the profiling system. As discussed by Baker (1981), an early electronic profiling system for temperature and salinity was described by Jacobsen (1948). The system was limited to 400 m and used separate supporting and data transfer cables. Next, a system called the STD (salinity–temperature–depth) profiler was developed by Hamon and Brown in the mid-1950s (Hamon, 1955; Hamon and Brown, 1958). The evolution of the conductivity measurement, used to derive salinity, will be discussed in the section on salinity. This evolution led to the introduction of the conductivity–temperature–depth (CTD) profiling system (Brown, 1974). This name change identified improvements not only in the conductivity sensor but also in the temperature sensing system designed to overcome the mismatch in the response times of the temperature and conductivity sensors. This mismatch often resulted in erroneous salinity spikes in the earlier STD systems (Dantzler, 1974).

Most STD/CTD systems use a platinum resistance thermometer as one leg of an impedance bridge from which the temperature is determined. An important development was made by Hamon and Brown (1958) where the sensing elements were all connected to oscillators that converted the measured variables to audio frequencies which could then be sent to the surface via a single conducting element in the profiler support cable. The outer cable sheath acted as both mechanical support and the return conductor. This data transfer method has subsequently been used on most electronic profiling systems. The early STDs were designed to operate to 1000 m and had a temperature range of 0–30°C with an accuracy of ±0.15°C. Later STDs, such as the widely used Plessey Model 9040, had accuracies of ±0.05°C with temperature ranges of −2 to +18°C or +15 to +35°C (range was switched automatically during a cast). Modern CTDs, such as the Sea Bird Electronics SBE 25 and the General Oceanics MK3C (modified after the EG&G Mark V) (Figure 1.3.4) have accuracies of ±0.002°C over a range of −3 to +32°C and a stability of 0.001°C/month (Brown and Morrison, 1978; Hendry, 1993). To avoid the problem of sensor response mismatch the MK3C CTD combines the accuracy and stability of a platinum resistance thermometer with the speed of a thermistor. The response time of the platinum thermometer is typically 250 ms while the response time of the conductivity cell (for a fall rate of 1 m/s) is typically 25 ms. The miniature thermistor probe matches the faster response of the conductivity cell with a response time of 25 ms. These two temperature measurements are combined to yield a rapid and highly accurate temperature. The response of the combined system to a step input is shown in Figure 1.3.5 taken from Brown and Morrison (1978). Later modifications have sent the platinum resistance temperature up the cable along with the fast response thermistor temperature for later combination. It is also possible to separate the thermometer from the conductivity cell so that the spatial separation acts as a time delay as the unit falls through the water (Topham and Perkins, 1988).

1.3.5 Dynamic response of temperature sensors

Before considering more closely the problem of sensor response time for STD/CTD systems, it is worthwhile to review the general dynamic characteristics of temperature measuring systems. For example, no temperature sensor responds instantaneously to changes in the environment which it is measuring. If the environment temperature is changing, the sensor element lags in its response. A simple example is a reversing thermometer which, lowered through the water column, would at no time read the correct environment temperature until it had been stopped and allowed to equilibrate for some time. The time (*K*) that it takes the thermometer to respond to the temperature of a new environment is known as the response time or "time constant" of the sensor.

The time constant K is best defined by writing the heat transfer equation for our temperature sensor as

$$-\frac{\mathrm{d}T}{\mathrm{d}t} = \frac{1}{k}(T - T_w) \tag{1.3.5.1}$$

where T_w and T are the temperatures of the medium (water) and thermometer and t refers to the elapsed time. If we assume that the temperature change occurs rapidly as the sensor descends, the temperature response can be described by the integration of equation (1.3.5.1) from which:

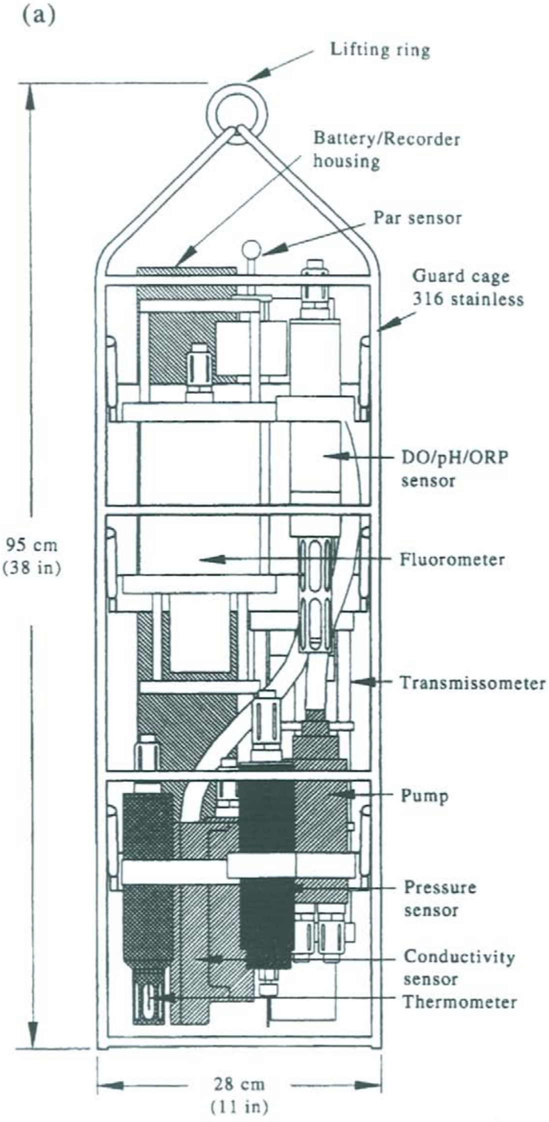

SHADED MODULES ARE INCLUDED IN BASIC SEALOGGER CTD

Figure 1.3.4. (a) Schematic of the Sea-Bird SBE 25 CTD and optional sensor modules (courtesy, Doug Bennett, Sea-Bird Electronics).

$$(T - T_w)/(T_o - T_w) = \Delta T/\Delta T_o = e^{-t/K} \tag{1.3.5.2}$$

In this solution, T_o refers to the temperature of the sensor before the temperature change and K is defined so that the ratio $\Delta T/\Delta T_o$ becomes e^{-1} (= 0.368) when 63% of the temperature change, ΔT, has taken place. The time for the temperature sensor to reach 90% of the final temperature value can be calculated using $e^{-t/k} = 0.1$. A more complex case is when the temperature of the environment is changing at a constant rate; i.e.

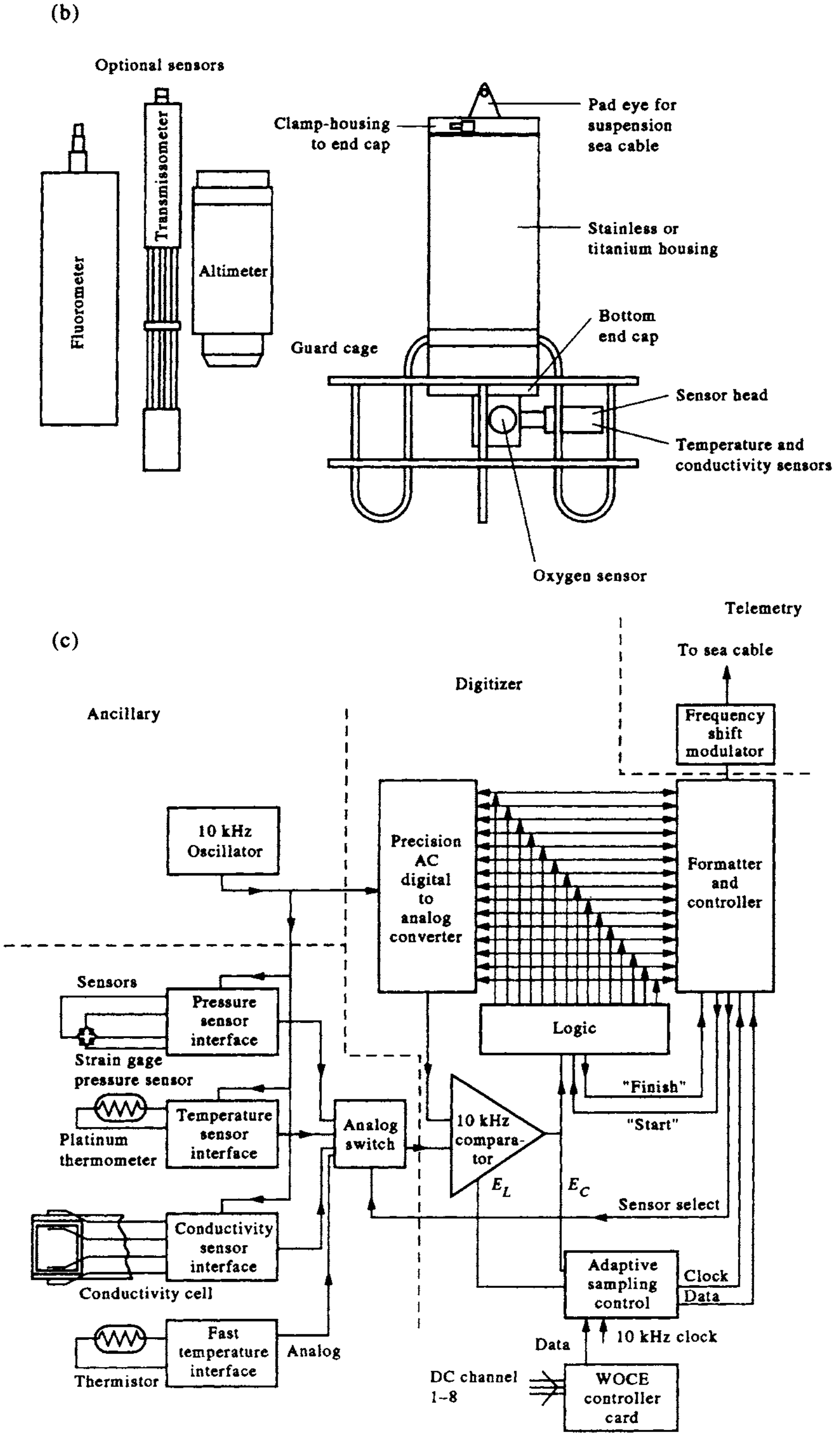

Figure 1.3.4. (b) schematic of General Oceanics MK3C/WOCE CTD and optional sensors; (c) schematic of electronics and sensors of General Oceanics MK3C/WOCE CTD (courtesy, Dan Schaas and Mabel Gracia, General Oceanics).

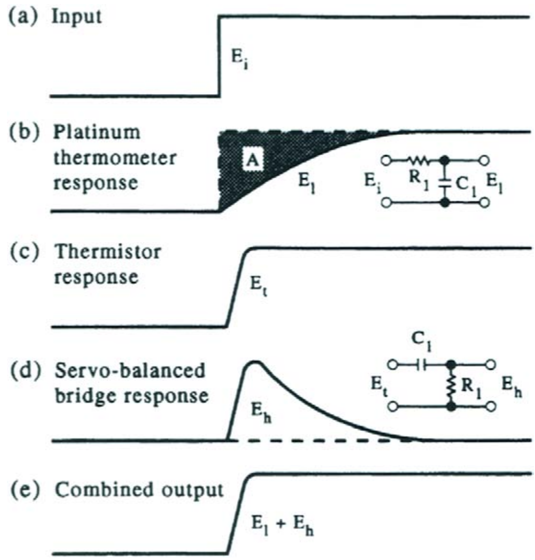

Figure 1.3.5. Combined output and response times of the resistance thermometer of a CTD.

$$T_w = T_1 + ct \tag{1.3.5.3}$$

where T_1 and c are constants. The temperature sensor then follows the same temperature change but lags behind so that

$$T - T_w = -cK \tag{1.3.5.4}$$

The response times, as defined above, are given in Table 1.3.1 for various temperature sensing systems. Values refer to the time in seconds for the sensor to reach the specified percentage of its final value.

The ability of the sensor to attain its response level depends strongly on the speed at which the sensor moves through the medium. An example of the application of these response times is an estimate for the period of time a reversing thermometer is allowed to "soak" to register the appropriate temperature. Suppose we desired an accuracy of $\pm 0.01\,^\circ$C and that our reversing thermometer is initially 10°C warmer than the water. From equation (1.3.5.2), $0.01/10.0 = \exp(-t/K)$, so that $t = 550$ s or 9.2 min. Thus, the usually recommended soak period of 5 min (for a hydrographic cast) is set by thermometer limitations rather than by the imperfect flushing of the water sample bottles. Another application is the estimation of the descent rate for a STD/CTD.

Table 1.3.1 Response times (in s) for various temperature sensors

Device	$K_{63\%}$	$K_{90\%}$	$K_{99\%}$
Mechanical bathythermograph	0.13	0.30	0.60
STD	0.30	0.60	1.20
Thermistor	0.04	0.08	0.16
Reversing thermometer	17.40	40.00	80.00

Assuming that the critical temperature change is in the thermocline where the temperature change is about 2°C/m then to sense this change, with an accuracy of 0.1°C, the STD/CTD response requires that $\exp(-t/0.6) = 0.1/2.0$ from which $t = 1.8$ s. Thus, we have the usual recommendation for a lowering rate of about 1 m/s. Today sensors, such as those used in the SBE 25 CTD (Figure 1.3.4a), General Oceanics MK3C CTD (Figure 1.3.4b, c) and the Guildline 8737 CTD have response times closer to 1.0 s.

1.3.6 Response times of CTD systems

As with any thermometer, the temperature sensor on the CTD profiler does not respond instantaneously to a change in temperature. Heat must first diffuse through the viscous boundary layer set up around the probe and through the protective coatings of the sensor (Lueck *et al.*, 1977). In addition, the actual temperature head must respond before the temperature is recorded. These effects lead to the finite response time of the profiler and introduce noise into the observed temperature data (Horne and Toole, 1980). A correction is needed to achieve accurate temperature, salinity and density data. Fofonoff *et al.* (1974) discuss how the single-pole filter model (1.3.5.2) may be used to correct the temperature data. In this lag-correction procedure, the true temperature at a point is estimated from (1.3.5.1) by calculating the time rate-of-change of temperature from the measured record using a least-square linear estimation over several neighboring points.

Horne and Toole (1980) argue that data corrected with this method may still be in error due to errors arising in the estimation of terms in the differential equation or the approximation of the equation to the actual response of the sensor. As an alternative, they suggest using the measured data to estimate a correction filter directly. This procedure assumes that the observed temperature data may be written as a convolution of the true temperature with the response function of the sensor such that

$$T(t) = H[T^*(t)] \tag{1.3.6.1}$$

where T is the observed temperature at time t, T^* is the true temperature and H is the transfer or response function of the sensor. The filter g is sought so that

$$g \cdot H = \delta(t) \tag{1.3.6.2}$$

where δ is the Dirac delta function. The filter g can be found by fitting, in a least-squares sense, its Fourier transform to the known Fourier transform of the function H. This method is fully described in the appendix to Horne and Toole (1980). The major advantage of this filter technique is only realized in the computation of salinity from conductivity and temperature.

In addition to the physical response time problem of the temperature sensor there is the problem of the nonuniform descent of the CTD probe due to the effects of a ship's roll or pitch (Trump, 1983). From a study of profiles collected with a Neil-Brown CTD, the effects of ship's roll were clearly evident at the 5-s period when the data were treated as a time-series and spectra were computed. High coherence between temperature and conductivity effects suggest that the mechanisms leading to these roll-induced features are not related to the sensors themselves but rather reflect an interaction between the environment and the sensor motion. Two likely candidates are: (a) the modification of the temperature by water carried along in the wake of the CTD probe from another depth; and (b) the effects of a turbulent wake overtaking the probe as it decelerates bringing with it a false temperature.

Trump (1983) concludes by saying that, while some editing procedure may yet be discovered to remove roll-related temperature variations, none is presently available. He, therefore, recommends that CTD data taken from a rolling ship not be used to compute statistics on vertical fine-structure and suggests that the best way to remove such contamination is to employ a roll-compensation support system for the CTD probe. Trump also recommends a series of editing procedures to remove roll effects from present CTD data and argues that of the 30,000 raw input data points in a 300 m cast that up to one-half will be removed by these procedures. A standard procedure is to remove any data for which there is a negative depth change between successive values on the way down and *vice versa* on the way up.

1.3.7 Temperature calibration of STD/CTD profilers

Although STD/CTD profilers were supposed to replace bottle casts, it was soon found that, due to problems with electronic drift and other subtle instrument changes, it was necessary to conduct *in situ* calibrations using one or more bottle samples. For this reason, and also to collect water samples for chemical analyses, most CTDs are used in conjunction with Rosette bottle samplers which can be commanded to sample at desired depths. A Rosette sampler consists of an aluminum cage at the end of the CTD conducting cable to which are fixed six, 12, or more water bottles that can be individually triggered electronically from the surface. Larger cages can accommodate larger volume bottles, typically up to 30 litres. While such *in situ* calibrations are more important for conductivity measurements, it is good practice to compare temperatures from the reversing thermometers with the CTD values. This comparison must be done in waters with near-uniform temperature and salinity profiles so that the errors between the CTD values and water sample are minimized. One must pick the time of the CTD values that coincide exactly with the tripping of the bottle. As reported by Scarlet (1975), *in situ* calibration usually confirms the manufacturer's laboratory calibration of the profiling instrument. Generally, this *in situ* calibration consists of comparisons between four and six temperature profiles, collected with reversing thermometers. Taken together with the laboratory calibration data these data are used to construct a "correction" curve for each temperature sensor as a function of pressure. Fofonoff *et al.* (1974) present a laboratory calibration curve obtained over an 18-month period for an early Neil-Brown CTD (the Niel-Brown CTD was the forerunner of the General Oceanics MK3C CTD). A comparison of 175 temperatures measured *in situ* with this profiler and those measured by reversing mercury thermometers is presented in Figure 1.3.6. In the work reported by Scarlet (1975), these calibration curves were used in tabular, rather than functional, form and intermediate values were derived using linear interpolation. This procedure was likely adequate for the study region (Scarlet, 1975) but may not be generally applicable. Other calibration procedures fit a polynomial to the reference temperature data to define a calibration curve.

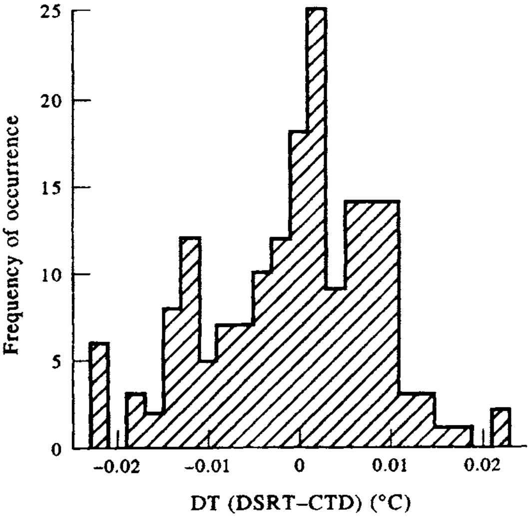

Figure 1.3.6. Histogram of temperature differences. Values used are the differences in temperature between deep-sea reversing mercury thermometers (DSRT) and the temperature recorded by an early Niel-Brown CTD. (From Fofonoff et al., 1974.)

1.3.8 Sea surface temperature

Sea surface temperature (SST) was one of the first oceanographic variables to be measured and continues to be one of the most widely made routine oceanographic measurements. Benjamin Franklin mapped the position of the Gulf Stream by suspending a simple mercury-in-glass thermometer from his ship while traveling between the U.S. and Europe.

1.3.8.1 Ship measurements

The introduction of routine SST measurements did away with the technique of suspending a thermometer from the ship. In its place, SST was measured in a sample of surface water collected in a bucket. When SST measurements were fairly approximate, this method was adequate. However, as the temperature sensors improved, problems with on-deck heating/cooling, conduction between bucket and thermometer, spillage, and other sources of error, led to modifications of the bucket system. New buckets were built that contained the thermometer and captured only a small volume of near-surface water. Due to its accessibility and location at the thermal boundary between the ocean and the atmosphere, the SST has become the most widely observed oceanic parameter. As in the past, the measurement of SST continues to be part of the routine marine weather observations made by ships at sea.

There are many possible sources of error with the bucket method including changes of the water sample temperature on the ship's deck, heat conduction through contact of the container with the thermometer, and the temperature change of the thermometer while it is being read (Tabata, 1978a). In order to avoid these difficulties, special sample buckets have been designed (Crawford, 1969) which shield both the container and the thermometer mounted in it from the heating/cooling effects of sun and wind. Comparisons between temperature samples collected with these special bucket samplers and reversing thermometers near the sea surface have yielded temperature differences of ±0.1°C (Tauber, 1969; Tabata, 1978a).

Seawater cooling for ship's engines makes it possible to measure SST from the temperature of the engine intake cooling system sensed by some type of thermometer imbedded in the cooling stream. Called "injection temperatures" these temperature values are reported by Saur (1963) to be on the average 0.7±0.9°C higher than corresponding bucket temperatures. For his study, Saur used SST data from 12 military ships transiting the North Pacific. Earlier similar studies by Roll (1951) and by Brooks (1926) found smaller temperature differences, with the intake-temperatures being only 0.1°C higher than the bucket values. Brooks found, however, that the engine-room crew usually recorded values that were 0.3°C too high. More recent studies by Walden (1966), James and Fox (1972) and Collins *et al.* (1975) have given temperature differences of 0.3, 0.3±1.3, and 0.3±0.7°C, respectively. Tabata (1978b) compared three-day average SSTs from the Canadian weather ships at Station "P" (which used a special bucket sampler) with ship injection temperatures from merchant ships passing close by. He found an average difference of 0.2±1.5°C (Figure 1.3.7). Again, the mean differences were all positive suggesting the heating effect of the engine room environment on the injection temperature.

The above comparisons between ship injection and ship bucket SSTs were made with carefully recorded values on ships that were collecting both types of measurements. Most routine ship-injection temperature reports are sent via radio by the ship's officers and have no corresponding bucket sample. As might be expected, the largest errors in these SST values are usually caused by errors in the radio transmission or in the incorrect reporting or receiving of ship's position and/or temperature value (Miyakoda and Rosati, 1982). The resulting large deviations in SST can normally be detected by using a comparison with monthly climatological means and applying some range of allowable variation such as 5°C.

This brings us to the problem of selecting the appropriate SST climatology—the characteristic SST temperature structure to be used for the global ocean. Until recently, there was little agreement as to which SST climatology was most appropriate. In an effort to establish a guide as to which climatology was the best, Reynolds (1983) compared the available SST climatologies with one he had produced (Reynolds, 1982). It was this work that led to the selection of Reynolds (1982) climatology for use in the Tropical Ocean Global Atmosphere (TOGA) research program.

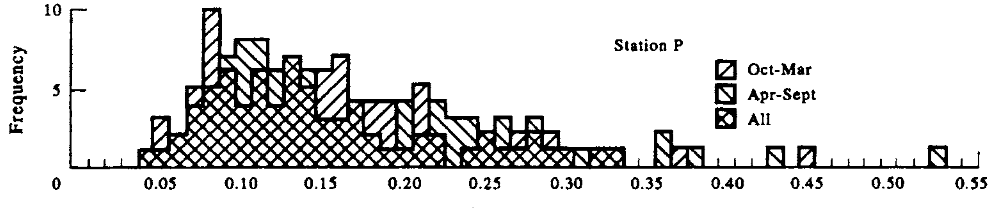

Figure 1.3.7. Frequency of occurrence of standard deviations associated with the 3.5-day mean sea surface temperature at Ocean Station"P"(50°N, 145°W). Difference between bucket temperature and ship intake surface temperature. (Modified after Tabata, 1978a.)

1.3.8.2 Satellite-sensed sea surface temperature (radiation temperature)

In contrast to ship and buoy measurements that sample localized areas on a quasi-synoptic basis, earth-orbiting satellites offer an opportunity to uniformly sample the surface of the globe on a nearly synoptic basis. Infrared sensors flown on satellites retrieve information that can be used to estimate SST, with certain limitations. Clouds are one of the major limitations in that they prevent long-wave, sea-surface radiation from reaching the satellite sensor. Fortunately, clouds are rarely stationary and all areas of the earth's surface are eventually observed by the satellite. In general, researchers wishing to produce "cloud-free" images of SST are required to construct composites over time using repeat satellite infrared data. These composites may require images spanning a couple of days to a whole week. Even with the need for composite images, satellites provide almost global coverage on a fairly short time scale compared with a collection of ship SST observations. The main problem with satellite SST estimates is that their level of accuracy is a function of satellite sensor calibration and specified corrections for the effects of the intervening atmosphere, even under apparently cloud-free conditions (Figure 1.3.8).

One of the first satellites capable of viewing the whole earth with an infrared sensor was ITOS 1 launched January 23, 1970. This satellite carried a scanning radiometer (SR) with an infrared channel in the 10.5–12.5 μm spectral band. The scanner viewed the earth in a swath with a nadir (sub-satellite) spatial resolution of 7.4 km as the satellite travelled in its near-polar orbit. A method that uses these data to map global SST is described in Rao *et al.* (1972). This program uses the histogram method of Smith *et al.* (1970) to determine the mean SST over a number of pixels (picture elements), including those with some cloud. A polar-stereographic grid of 2.5° of latitude by 2.5° of longitude, encompassing about 1024 pixels per grid point per day, was selected. In order to evaluate the calculated SST retrievals from the infrared measurements, the calibrated temperature values were compared with SST maps made from ship radio reports. The resulting root-mean-square (RMS) difference for the northern hemisphere was 2.6°C for three days in September 1970. When only the northern hemisphere ocean weather ship SST observations were used, this RMS value dropped to 1.98°C, a reflection of the improved ship SST observations. A comparison for all ships from the southern hemisphere, for the same three days, resulted in an RMS difference of 2.45°C. As has been discussed earlier in this chapter, one of the

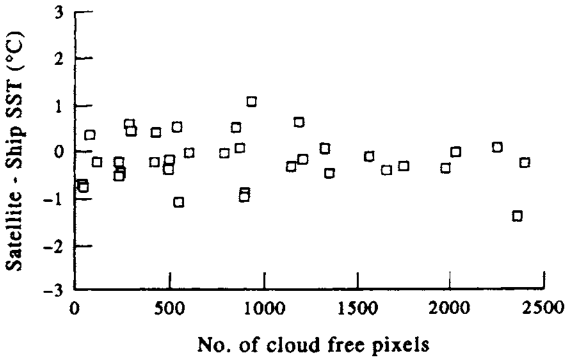

Figure 1.3.8. Sea surface temperature differences, satellite minus ship, plotted as a function of the number of cloud-free pixels in a 50 × 50 pixel array. (From Llewellyn-Jones et al., 1984.)

reasons for the magnitude of this difference is the uncertainty of the ship-sensed SST measurements.

The histogram method of Smith *et al.* (1970) was the basis for an operational SST product known as GOSSTCOMP (Brower *et al.*, 1976). Barnett *et al.* (1979) examined the usefulness of these data in the tropical Pacific and found that the satellite SST values were negatively biased by 1–4°C and so were, by themselves, not very useful. The authors concluded that the systematically cooler satellite temperatures were due to the effects of undetected cloud and atmospheric water vapor. As reported in Miyakoda and Rosati (1982), the satellite SST retrieval procedure was evolving at that time and retrieval techniques had improved (Strong and Pritchard, 1980). These changes included new methods to detect clouds and remove the effects of atmospheric water vapor contamination.

More recently, a new satellite sensor system, the Advanced Very High Resolution Radiometer (AVHRR) has become the standard for infrared SST retrievals. In terms of SST the main benefits of the new sensor system are: (a) improved spatial resolution of about 1 km at nadir; and (b) the addition of other spectral channels which improve the detection of water vapor by computing the differences between various channel radiometric properties. The AVHRR is a four- or five-channel radiometer with channels in the visible (0.6–0.7 μm), near-infrared (0.7–1.1 μm), and thermal infrared (3.5–3.9, 10.5–11.5, and 11.5–12.5 μm). The channel centered at 3.7 μm was intended as a nighttime cloud discriminator but is more useful when combined with the 11 and 12 μm channels to correct for the variable amounts of atmospheric water vapor (Bernstein, 1982). While there are many versions of this "two-channel" or "dual-channel" correction procedure (also called the "split-window" method), the most widely used was developed by McClain (1981).

The above channel correction methods have been developed in an empirical manner using some sets of *in situ* SST measurements as a reference to which the AVHRR radiance data are adjusted to yield SST. This requires selecting a set of satellite and *in situ* SST data collected over coincident intervals of time and space. Bernstein (1982) chose intervals of several tens of kilometers and several days (Figure 1.3.9) while McClain *et al.* (1983) used a period of one day and a spatial grid of 25 km. In a recent evaluation of both of these methods, Lynn and Svejkovsky (1984) found the Bernstein method yielded a mean bias of +0.5°C and the McClain equation a bias of –0.4°C, relative to *in situ* SST measurements. In each case, the difference from *in situ* values was smaller than the RMS errors suggested by the authors of the two methods. Bernstein (1982) compared mean maps made from 10 days of AVHRR retrievals with similar maps made from routine ship reports. He found the maps to agree to within ±0.8°C (one standard deviation) and concluded that this level of agreement was limited by the poor accuracy of the ship reports. He suggested that properly handled, the radiometer data can be used to study climate variations with an accuracy of 0.5–1.0°C. This is consistent with the results of Lynn and Svejkovsky (1984) for a similar type of data analysis.

Another possible source of satellite SST estimates is the Visible Infrared Spin Scan Radiometer (VISSR) carried by the Geostationary Orbiting Earth Satellite (GOES). Unfortunately, the VISSR has a spatial resolution of about 8 km at the sub-satellite point for the infrared channel. Another disadvantage of the VISSR is the lack of onboard infrared calibration similar to that available from the AVHRR (Maul and Bravo, 1983). While the VISSR does provide a hemispherical scan every half hour its shortcomings have discouraged its application to the general estimation of SST. In

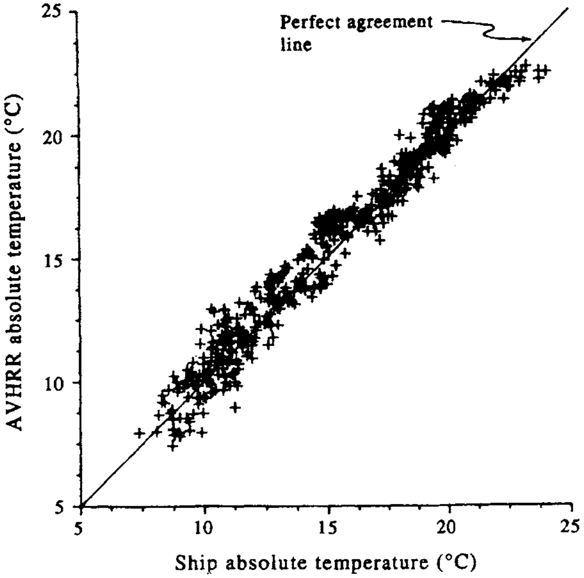

Figure 1.3.9. Grid point by grid point cross plot of the mapped values of sea surface temperature from ship-based and AVHRR-based maps. (Bernstein, 1982.)

some cases, VISSR data have been examined where there is a lack of suitable AVHRR data. In one such study, Maul and Bravo (1983) found that a regression between VISSR infrared and *in situ* SST data, using the radiative transfer equations, yielded satellite SST estimates that were no better than ±0.9°C. The conclusion was that, in general, GOES VISSR SST estimates are accurate to within ±1.3°C only. The primary problem with improving this accuracy is the presence of sub-pixel size clouds which contaminate the SST regression.

Efforts are underway to improve the accuracy of retrievals from AVHRR through a better understanding of the on-board satellite calibration of the radiometer and by the development of regional and seasonal "dual-channel" atmospheric correction procedures. Evaluation of these correction procedures, compared with collections of atmospheric radiosonde measurements, has demonstrated the robust character of the "dual-channel" correction and improvements only require a better estimate of the local versus global effects in deriving the appropriate algorithm (Llewellyn-Jones *et al.*, 1984). Thus, it appears safe to suggest that AVHRR SST estimates can be made with accuracies of about 0.5°C, assuming that appropriate atmospheric corrections are performed.

Three workshops were held at the Jet Propulsion Laboratory (JPL) to compare the many different techniques of SST retrievals from existing satellite systems. The first workshop (January 27–28, 1983) examined only the microwave data from the scanning multichannel microwave radiometer (SMMR) while the second workshop (June 22–24, 1983) considered SMMR, HIRS (high resolution infrared sounder) and AVHRR for two time periods, November 1979 and December, 1981. The third workshop (February 22–24, 1984) examined SST products derived from SMMR, HIRS, AVHRR, and VAS (atmospheric sounder on the GOES satellites) for an additional two months (March and July, 1982). A series of workshop reports is available from JPL and the results are summarized in journal articles in the November 1985 issue of the *Journal of Geophysical Research*.

In their review of workshop-3 results, Hilland *et al.* (1985) reported that the overall RMS satellite SST errors range from 0.5 to 1.0°C. In a discussion of the same workshop results, Bernstein and Chelton (1985) were more specific, reporting RMS differences between satellite and SST anomalies ranging from 0.58 to 1.37°C. Mean differences for this same comparison ranged from −0.48 to 0.72°C and varied substantially from month to month and season to season. They also reported that the SMMR SSTs had the largest RMS differences and time-dependent biases. Differences for the AVHRR and HIRS computed SSTs were smaller. When the monthly ship SST data were smoothed spatially to represent 600 km averages, the standard deviations of the monthly ship averages from climatology varied from 0.35 to 0.63°C. Using these smoothed ship SST anomalies as a reference, the signal-to-noise variance ratios were 0.25 for SMMR and 1.0 for both the AVHRR and HIRS.

The workshop review by McClain *et al.* (1985) of the AVHRR based multichannel SST (MCSST) retrieval method found biases of 0.3–0.4°C (with MCSST lower than ship), standard deviations of 0.5–0.6°C, and correlations of +0.3 to +0.7 (see also Bates and Diaz, 1991). They also discussed a refined MCSST technique being used with more recent NOAA-9 AVHRR data which yielded consistent biases of −0.1°C and RMS differences (from ship SSTs) of 0.5°C. In an application of AVHRR data to the study of warm Gulf Stream rings, Brown *et al.* (1985) discuss a calibration procedure which provides SST estimates accurate to ±0.2°C. This new calibration method is the result of thermal vacuum tests which revealed instrument specific changes in the relative emittance between internal (to the satellite) and external (deep space) calibration targets. By reviewing satellite prelaunch calibration data they found that there was an instrument-specific, nonlinear departure from a two-point linear calibration for higher temperatures. In addition, it was found that the calibration relationship between the reference PRT (platinum resistance thermocouples) and the sensor systems changed in the thermal vacuum tests; hence a limited instrument retest, as part of the calibration cycle, is recommended as a way to improve AVHRR SST accuracy. Such higher accuracy absolute SST values are of importance for future climate studies where small, long-term temperature changes are significant.

The workshop results for the geostationary sounder unit (VAS) (Bates and Smith, 1985) revealed a warm bias of 0.5°C with an RMS scatter of 0.8–1.0°C. The positive bias was attributed to a diurnal sampling bias and a bias in the original set of empirical VAS/buoy matchups. Use of a second set of VAS/buoy matches reduced this warm bias making VAS SSTs more attractive due to the increased temporal coverage (every half hour) over that of the AVHRR (one to four images per day).

All of these satellite SST intercomparisons were evaluated against either ship or buoy measurements of the near surface bulk temperature. As is often acknowledged in these evaluations, the bulk temperature is not generally equal to the sea surface skin temperature measured by the satellite. Studies directed at a comparison between skin and bulk temperatures by Grassl (1976), as well as Paulson and Simpson (1981), demonstrate marked (about 0.5°C) differences between the surface skin and subsurface temperatures. In an effort to better evaluate the atmospheric attenuation of infrared radiance, Schluessel *et al.* (1987) compare precision radiometric measurements made from a ship with SST calculated using a variety of techniques from coincident NOAA-7 AVHRR imagery. In addition, subsurface temperatures were continuously monitored with thermistors in the upper 10 m for comparison with the ship and satellite radiometric SST estimates.

As part of this study, Schluessel *et al.* (1987) examined the effects of radiometer scan angle on the AVHRR attenuation and concluded that differences in scan angle, resulting in different atmospheric paths, resulted in significant changes in the computed SST. To correct for atmospheric water vapor attenuation, HIRS radiances were used to correct the multichannel computation of SST from the AVHRR. The correspondence between the HIRS radiances and atmospheric water vapor content was found by numerical simulation of 182 different atmospheres. With the HIRS correction, AVHRR-derived SST was found to have a bias of +0.03°C and an RMS error of 0.42°C when compared with the ship radiometer measurements. Comparison between ship radiometric and *in situ* temperatures yielded a mean offset of 0.2°C and a range of −0.5 to +0.9°C about this value (Figure 1.3.10). According to Weinreb *et al.* (1990), even if the nonlinearity corrections for the sensor remained valid after satellite launch, the error in AVHRR data is still 0.55°C of which 0.35°C is traceable to calibration of the laboratory blackbody.

From all these various studies, it appears that the infrared satellite SST, when computed using a multichannel algorithm corrected by HIRS, is capable of yielding reliable estimates of SST in the absence of visible cloud. Microwave satellite SST sensing shows promise for future all weather sensing but present systems have a poor a signal-to-noise ratio and a consequent low spatial resolution. Future microwave systems will be designed to specifically measure atmospheric water vapor (in a separate channel) thus making the correction of the infrared SST estimates more straightforward. The frequent global coverage of satellite systems makes them attractive for the global, long-term studies required for an understanding of the world's climate.

1.3.9 The modern digital thermometer

In many oceanographic institutions, the mercury thermometer has been replaced by a digital deep-sea reversing thermometer built by Sensoren-Instrutmente-System (SIS) of Kiel that uses a highly stable platinum thermistor to measure temperature. The SIS RTM 4002 digital reversing thermometer has the outer dimensions of mercury instruments so that it fits into existing thermometer racks. Instead of the lighted magnifying glass needed to read most mercury thermometers, the user simply touches a small permanent magnet to the sensor "trigger" spot on the glass face of the thermometer to obtain a bright digital readout of the temperature to three decimal places. Since the instrument displays the actual temperature at the sample depth, there is no need to read an auxillary thermometer to correct the main reading, as is the case for reversing mercury thermometers. This makes life much more pleasant on a rolling ship in the middle of the night. Because the response time of the platinum thermometer is rapid compared with the "soaking" time of several minutes required for mercury thermometers, less ship time is wasted at oceanographic stations.

The RTM 4002 has a range of −2 to 40°C and a stability of 0.00025°C per month. According to the manufacturer, the instrument has a resolution of 0.001°C and an accuracy of 0.005°C over the temperature range −2 to 20°C. Both resolution and accuracy are considerably lower for temperatures in the range 20–40°C. A magnet is used to reset the instrument and to activate the light-emitting diode (LED). Sampling can be performed in the three sequential modes. The "Hold" mode displays the last

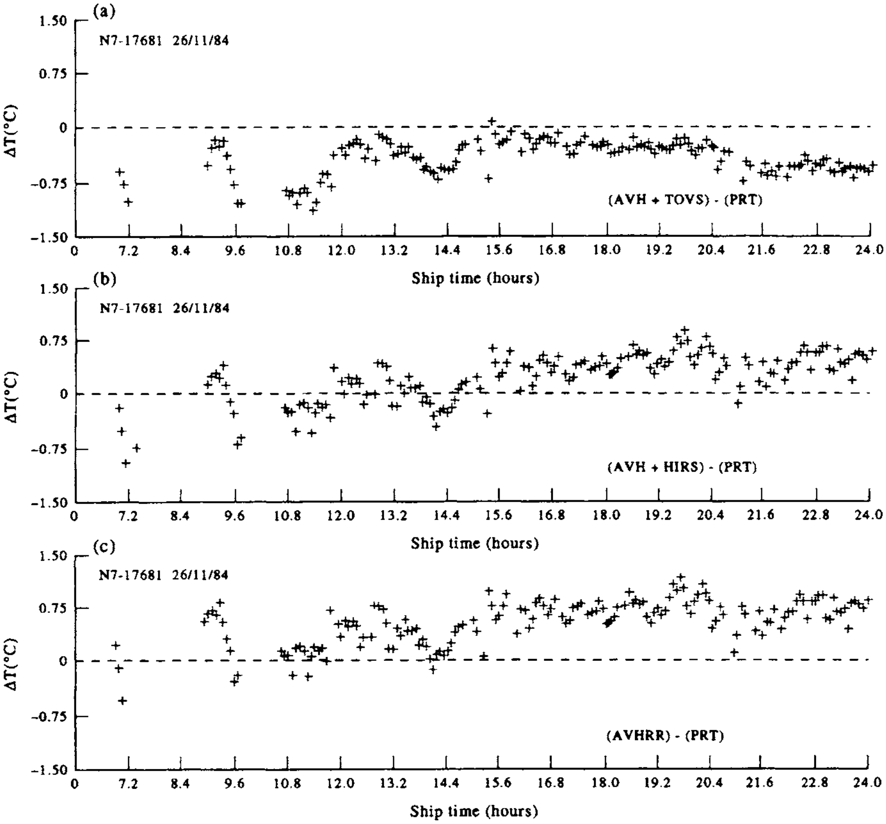

Figure 1.3.10. Difference between uncorrected (a) and corrected (b, c) satellite-sensed sea surface temperatures and ship radiometric in situ temperatures. HIRS = high-resolution infrared sounder; PRT = platinum resistance thermocouples.

temperature stored in memory; the "Cont" mode allows for continuous sampling for use in the laboratory while the "Samp" mode is used for reversing thermometer applications. The instrument allows for a minimum of 2700 samples on two small lithium batteries.

1.3.10 Potential temperature and density

The deeper one goes into the ocean, the greater the heating of the water caused by the compressive effect of hydrostatic pressure. The ambient temperature for a parcel of water at depth is significantly higher than it would be in the absence of pressure effects. Potential temperature is the *in situ* temperature corrected for this internal heating caused by adiabatic compression as the parcel is transported to depth in the ocean. To a high degree of approximation, the potential temperature defined as $\theta(p)$, or T_θ, is given in terms of the measured *in situ* temperature $T(p)$ as $\theta(p) = T(p) - F(R)$, where $F(R) \approx 0.1°\text{C km}^{-1}$ is a function of the adiabatic temperature gradient R. The results can have important consequences for oceanographers studying water mass characteristics in the deep ocean. The difference between the ambient temperature and θ increases slowly from zero at the ocean surface to about 0.5°C at 5000 m depth. At a depth of approximately 100 m and temperatures less than 5°C, the difference between the two forms of temperature reaches the absolute resolution (±0.01°C) of most thermistors (Figure 1.3.11). Such differences are significant in studies of deep ocean heating from hydrothermal venting or other heat sources where temperature anomalies of ten millidegrees (0.010°C) are considered large. In fact, if the observed temperatures are not converted to potential temperature, it is impossible to calculate the anomalies correctly.

We remark here that the use of potential temperature in the calculation of density leads to the definition of potential density, $\rho_\theta = \rho(S, \theta, 0)$ in kg m^{-3}, as the value of ρ for a given salinity and potential temperature at surface pressure, p = 0. The corresponding counterpart to $\sigma_t (= 10^3[\rho(S, T, 0) - 1000])$, is then called "sigma–theta" where $\sigma_\theta = 10^3[\rho(S, \theta, 0) - 1000]$. Since density surfaces (as well as isotherms) can be displaced vertically hundreds of meters by internal oscillations in the deep ocean, it is crucial that we compare temperatures correctly by taking into consideration the thermal compression effect. Readers familiar with the oceanographic literature will also note the use of σ_2, σ_4, and similar sigma expressions for density surfaces in the deep ocean. These expressions are used as reference levels for the calculation of density at depths where the effect of hydrostatic compression on density becomes important. For example, $\sigma_4 = 10^3[\rho(S, \theta, 4) - 1000]$ refers to density at the observed salinity and potential temperature referred to a pressure of 4000 dbar (40,000 kPa) or about 4000 m depth. Use of σ_θ in the deep Atlantic suggests a vertically unstable water mass below 4000 m whereas the profiles of σ_4 correctly increase toward the bottom (Pickard and Emery, 1992). As indicated by Table 1.3.2, the different sigma values differ significantly.

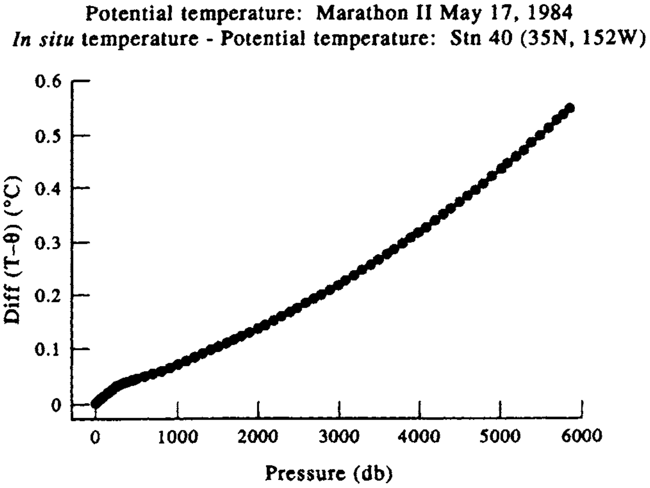

Figure 1.3.11. Difference between in situ temperature (T) recorded by a CTD versus the calculated potential temperature (θ) for a deep station in the North Pacific Ocean (35°N, 152°W). Below about 500 m, this curve is applicable to any region of the world ocean. (Data from Martin et al., 1987.)

Table 1.3.2 Comparison of different forms of sigma for the western Pacific Ocean near Japan (39°41'N, 147°56'E). (From Talley et al., 1988.) Columns 2 and 3 give the in situ and potential temperatures, respectively. Sigma units are kg m^{-3}

Depth (m)	*In situ* T (°C)	Pot. T (θ) (°C)	Salinity (psu)	σ_θ	σ_2	σ_4
0	18.909	18.909	32.574	23.192	31.706	39.852
100	1.160	1.156	33.158	26.555	35.830	44.689
500	3.338	3.305	34.108	27.145	36.286	45.020
1000	2.697	2.632	34.410	27.447	36.619	45.382
2000	1.868	1.734	34.600	27.672	36.890	45.696
3000	1.528	1.311	34.661	27.752	36.993	45.820
4000	1.456	1.138	34.679	27.778	37.029	45.865
5000	1.503	1.069	34.686	27.788	37.043	45.883
5460	1.547	1.054	34.688	27.791	37.046	45.886

1.4 SALINITY

It is the salt in the ocean that separates physical oceanography from other branches of fluid dynamics. Most oceanographers are familiar with the term "salinity" but many are not aware of its precise definition. Physical oceanographers often forget that salinity is a nonobservable quantity and was traditionally defined by its relationship to another measured parameter, "chlorinity". For the first half of this century, chlorinity was measured by the chemical titration of a seawater sample. In 1899 the International Council for the Exploration of the Sea (ICES) established a commission, presided over by Professor M. Knudsen, to study the problems of determining salinity and density from seawater samples. In its report (Forch *et al.*, 1902), the commission recommended that salinity be defined as follows: "The total amount of solid material in grams contained in one kilogram of seawater when all the carbonate has been converted to oxide, all the bromine and iodine replaced by chlorine and all the organic material oxidized."

Using this definition, and available measurements of salinity, chlorinity and density for a relatively small number of samples (a few hundred), the commission produced the empirical relationship

$$S\,(‰) = 1.805\mathrm{Cl}\,(‰) + 0.03 \tag{1.4.1}$$

known as Knudsen's equation and a set of tables referred to as Knudsen's tables. The symbol ‰ indicates "parts per thousand" (ppt) in analogy to percent (%) which is parts per hundred. In the more modern Practical Salinity Scale, salinity is a unitless quantity written as "psu" for *practical salinity units.* It is interesting to note that Knudsen himself considered using electrical conductivity (Knudsen, 1901) to measure salinity. However, due to the inadequacy of the apparatus available, or similar problems at the time, he decided that the chemical method was superior.

There are many different titration methods used to determine salinity but that most widely applied is the colorimetric titration of halides with silver nitrate ($AgNO_3$) using the visual end-point provided by potassium chromate (K_2CrO_4), as described in Strickland and Parsons (1972). With a trained operator, this method is capable of an accuracy of 0.02‰ in salinity using the empirical Knudsen relationship. For precise laboratory work Cox (1963) reported on more sensitive techniques for determining the titration end-point which yield a precision of 0.002‰ in chlorinity. Cox also describes an even more complex technique, used by the Standard Sea-water Service, which is capable of a precision of about 0.0005‰ in chlorinity. It is fairly safe to say that these levels of precision are not typically obtained by the traditional titration method and that preconductivity salinities are generally no better than ±0.02‰.

1.4.1 Salinity and electrical conductivity

In the early 1950s, technical improvements in the measurement of the electrical conductivity of seawater turned attention to using conductivity as a measure of salinity rather than the titration of chlorinity. Seawater conductivity depends on the ion content of the water and is therefore directly proportional to the salt content. The primary reason for getting away from titration methods was the development of reliable methods of making routine, accurate measurements of conductivity. As noted earlier, the potential for using seawater conductivity as a measurement of salinity was first recognized by Knudsen (1901). Later papers explored further the relationship between conductivity, chlorinity and salinity. A paper by Wenner *et al.* (1930) suggested that electrical conductivity was a more accurate measure of total salt content than of chlorinity alone. The authors' conclusion was based on data from the first conductivity salinometer developed for the International Ice Patrol. This instrument used a set of six conductivity cells, controlled the sample temperature thermostatically and was capable of measurements with a precision of better than 0.01‰. With an experienced operator the precision may be as high as 0.003‰ (Cox, 1963). The latter is a typical value for most modern conductive and inductive laboratory salinometers and is an order of magnitude improvement in the precision of salinity measurements over the older titration methods.

It is worth noting that the conductivity measured by either inductive or conductive laboratory salinometers, such as the widely-used Guildline 8410 Portable Salinometer, are relative measurements which are standardized by comparison with "standard seawater". As an outgrowth of the ICES commission on salinity, the reference or standard seawater was referred to as "Copenhagen Water" due to its earliest production by a group in Denmark. This standard water is produced by diluting a large sample of seawater until it has a precise salinity of 35‰ (Cox, 1963). Standard UNESCO seawater is now being produced by the "Standard Seawater Service" in Wormley, England as well as at other locations in the U.S.A. (i.e. Woods Hole Oceanographic Institution).

Standard seawater is used as a comparison standard for each "run" of a set of salinity samples. To conserve standard water, it is customary to prepare a "secondary standard" with a constant salinity measured in reference to the standard seawater. A common procedure is to check the salinometer every 10–20 samples with the secondary standard and to use the primary standard every 50 or 100 samples. In all of these operations, it is essential to use proper procedures in "drawing the salinity sample" from the hydrographic water bottle into the sample bottle. Assuming that the hydrographic bottle remains well sealed on the upcast, two effects must be avoided: first, contamination by previous salinity samples (that have since evaporated leaving a salt residue that will increase salinity in the sample bottle); and second, the possibility of evaporation of the present sample. The first problem is avoided by "rinsing" the salinity bottle and its cap two to three times with the sample water. Evaporation is avoided by using a screw cap with a gasket seal. A leaky bottle will give sample values that are distorted by upper ocean values. For example, if salinity increases and dissolved oxygen decreases with depth, deep samples drawn from a leaky bottle will have anomalously low salinities and high oxygens.

Salinity samples are usually allowed to come to room temperature before being run on a laboratory bench salinometer. In running the salinity samples one must be careful to avoid air bubbles and insure the proper flushing of the salinity sample through the conductivity cell. Some bench salinometers correct for the marked influence of ambient temperature on the conductivity of the sample by controlling the sample temperature while other salinometers merely measure the sample temperature in order to be able to compute the salinity from the conductivity and coincident temperature.

Another reason for the shift to conductivity measurements was the potential for *in situ* profiling of salinity. The development history of the salinity/conductivity–temperature–depth (STD/CTD) profilers has been sketched out in Section 1.3.4 in terms of the development of continuous temperature profilers. The salinity sensing aspects of the instrument played an important role in the evolution of these profilers. The first STD (Hamon, 1955) used an electrode-type conductivity cell in which the resistance or conductivity of the seawater sample is measured and compared with that of a sample of standard seawater in the same cell. Fouling of the electrodes can be a problem with this type of sensor. Later designs (Hamon and Brown, 1958) used an inductive cell to sense conductivity. The inductive cell salinometer consists of two coaxial torodoial coils immersed in the seawater sample in a cell of fixed dimensions. An alternating current is passed through the primary coil which then induces an EMF (electromagnetic force) and hence a current within the secondary coil. The EMF and current in the secondary coil are proportional to the conductivity (salinity) of the seawater sample. Again, the instrument is calibrated by measuring the conductivity of standard seawater in the same cell. The advantage of this type of cell is that there are no electrodes to become fouled. A widely used inductive type STD was the Plessey model 9040 which claimed an accuracy of ±0.03‰. Precision was somewhat better being between 0.01 and 0.02‰ depending on the resolution selected. Modern electrode-type cells measure the difference in voltage between conductivity elements at each end of the seawater passageway. With the conducting elements potted into the same material this type of salinity sensor is less prone to contamination by biological fouling. At the same time, the response time of the conductive cell is much greater than that of an inductive sensor leading to the problem of salinity spiking due to a mismatch with temperature response.

The mismatch between the response times of the temperature and conductivity sensors is the primary problem with STD profilers. Spiking in the salinity record occurs because the salinity is computed from a temperature measured at a slightly different time than the conductivity measurement. Modern CTD systems record conductivity directly, rather than the salinity computed by the system's hardware, and have faster response thermal sensors. In addition, most modern CTD systems use electrodes rather than inductive salinity sensors. As shown in Figure 1.4.1, this sensor has a set of four parallel conductive elements that constitute a bridge circuit for the measurement of the current passed by the connecting seawater in the glass tube containing the conductivity elements. The voltage difference is measured between the conducting elements in the bridge circuit of the conductivity cell. The primary advantage of the conductive sensor is its greater accuracy and faster time response. In their discussion of the predecessor of the modern CTD, Fofonoff *et al.* (1974) give an

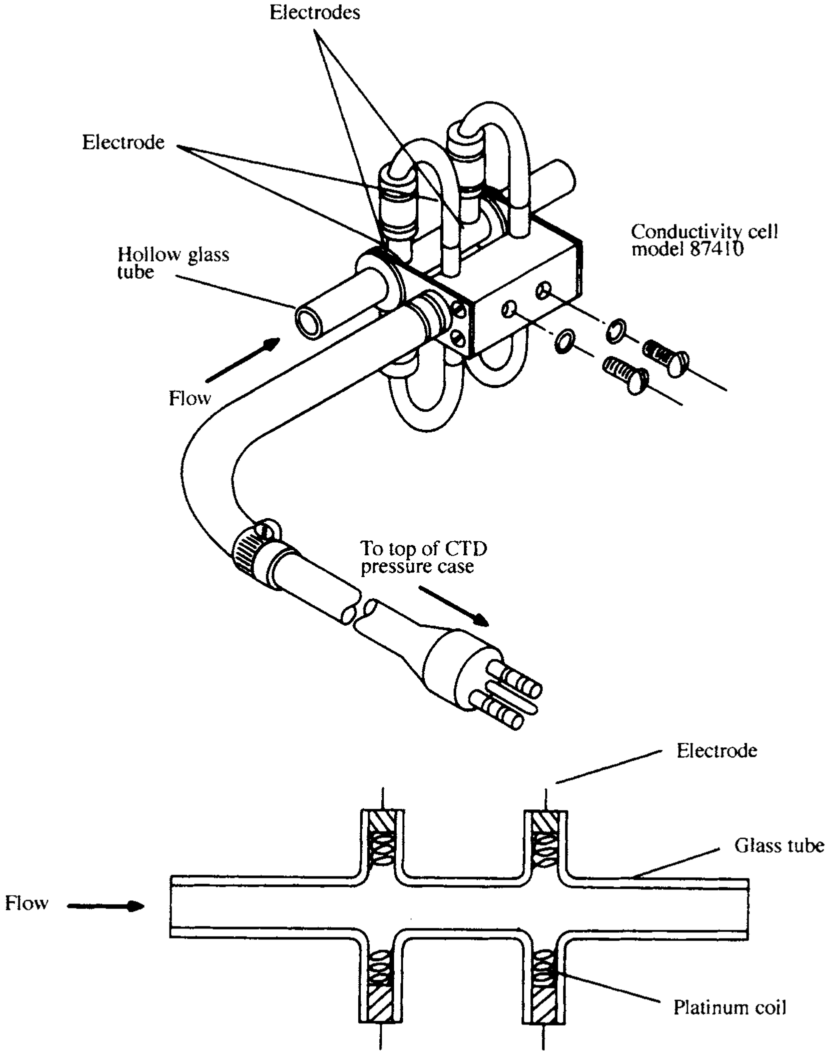

Figure 1.4.1. Guildline conductivity (salinity) sensor showing the location of four parallel conductive elements inserted into the hollow glass tube. Conductivity is measured as the water flows through the glass tube. Cable plugs into the top of the CTD end plate on the pressure case.

overall salinity accuracy for this instrument of ±0.003‰. This accuracy estimate was based on comparisons with *in situ* reference samples whose salinities were determined with a laboratory salinometer also accurate to this level (Figure 1.4.2). This accuracy value is the same as the standard deviation of duplicate salinity samples run in the lab, demonstrating the high level of accuracy of CTD profilers.

1.4.1.1 A comparison of two modern CTDs

In recent sea trials in the North Atlantic, scientists at the Bedford Institute of Oceanography (Bedford, Nova Scotia) examined *in situ* temperature and salinity records from a EG&G Mark V CTD and a Sea-Bird Electronics SBE 9 CTD (Hendry,

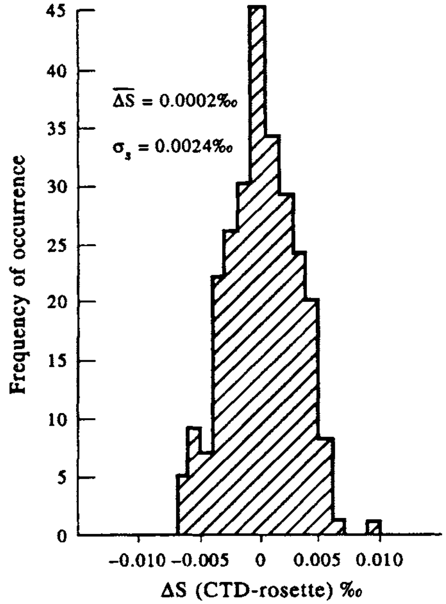

Figure 1.4.2. Histogram of salinity differences (in parts per thousand, ‰). Values used are the differences in salinity between salinity recorded by an early Niel-Brown CTD and deep-sea bottle samples taken from a Rosette sampler. $\overline{\Delta S}$ *is the mean salinity difference and* σ_S *is the standard deviation. (Modified after Fofonoff et al., 1974.)*

1993). The standards used for the comparisons were temperatures measured by Sensoren Instrumente Systeme (SIS) digital-reading reversing thermometers and salinity samples drawn from 10-litre bottles on a Rosette sampler and analyzed using a Guildline Instruments Ltd Autosal 8400A salinometer standardized with IAPSO Standard Water.

The Mark V samples at 15.625 Hz and used two thermometers and a standard inductive salinity cell. The fast response (250 ms time-constant) platinum thermometer is used to record the water temperature while the slower resistance thermometer, whose response time is more closely tuned to that of the conductivity cell, is used in the conversion of conductivity to salinity. Plots of the differences in temperature and salinity between the bottle samples and the CTD are presented in Figure 1.4.3. Using only the manufacturer's calibrations for all instruments, the Mark V CTD temperatures were lower than the reversing thermometer values by 0.0034±0.0023°C with no obvious dependence on depth (Figure 1.4.3a). In contrast, the Mark V salinity differences (Figure 1.4.3c) showed a significant trend with pressure, which may be related to the instrument used or a peculiarity of the cell. With pressure in dbar, regression of the data yields

$$\text{Salinity Diff (bottle} - \text{CTD)} = 0.00483 + 6.25910^{-4}\,\text{Pressure (CTD)} \qquad (1.4.2.1)$$

with a correlation coefficient $r^2 = 0.84$. Removal of the trend gives salinity values accurate to about ±0.003 psu. Pressure errors of several dbars (several meters in depth) were noted.

The SBE 9 and SBE 25 sample at 24 Hz and use a high-capacity pumping system and TC-duct to flush the conductivity cell at a known rate (e.g. 2.5 m/s pumping

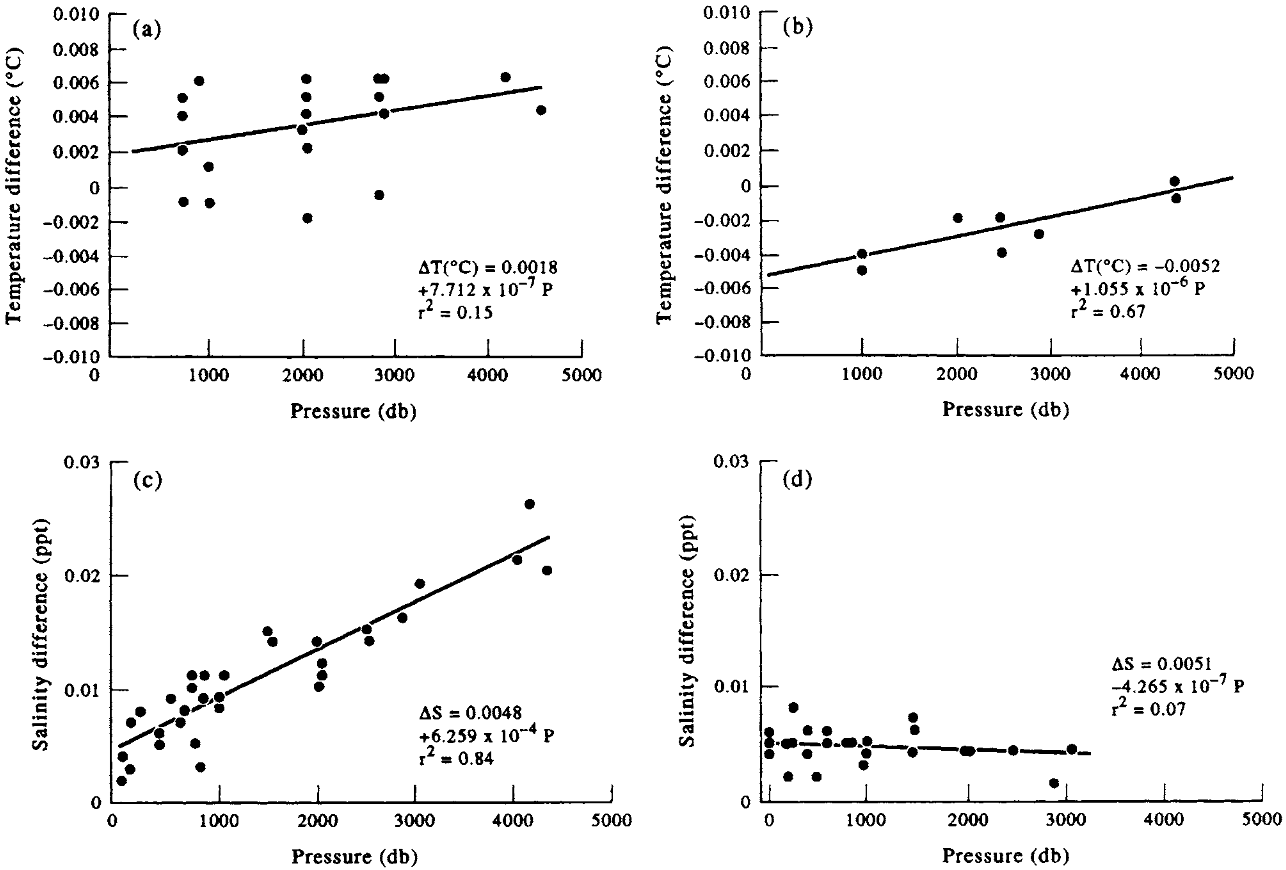

Figure 1.4.3. CTD correction data for temperature (bottle–CTD) and salinity (bottle–CTD) based on comparison of CTD data with in situ data from bottles attached to a Rosette sampler. (a) Temperature difference for the EG (b) same as (a) but for the Sea-Bird SBE 9 CTD; (c) salinity difference for the EG (d) same as (c) but for the SBE 9 CTD. Regression curves are given for each calibration in terms of the pressure, P, in dbar. r^2 *is the squared correlation coefficient. (Adapted from Hendry, 1993.)*

speed for a rate of 0.6–1.2 l/s). When on deck, the conductivity cell must be kept filled with distilled water. To allow for the proper alignment of the temperature and conductivity records (so that the computed salinity is related to the same parcel of water as the temperature), the instrument allows for a time shift of the conductivity channel relative to the temperature channel in the deck unit or in the system software SEASOFT (module AlignCTD). In the study, the conductivity was shifted by 0.072 s earlier to align with temperature. (The deck unit was programed to shift conductivity by one integral scan of 0.042 s and the software the remaining 0.030 s.) Using the manufacturer's calibrations for all instruments, the SBE 9 CTD temperatures for the nine samples were higher than the reversing thermometer values by 0.0002±0.0024°C with only a moderate dependence on depth (Figure 1.4.3b). Salinity data from 30 samples collected over a 3000 db depth range (Figure 1.4.3d) gave CTD salinities that were lower (fresher) than Autosal salinities by 0.005±0.002 psu, with no depth dependence. By comparison, the precision of a single bottle salinity measurement is 0.0007 psu. Pressure errors were less than 1 dbar. Due to geometry changes and the slow degradation of the platinum black on the electrode surfaces, the thermometer calibration is expected to drift by 2 m°C/year and the electronic circuitry by 3 m°C/year.

Based on the Bedford report, modern CTDs are accurate to approximately 0.002°C in temperature, 0.005 psu in salinity and <0.5% of full-scale pressure in depth. The report provides some additional interesting reading on oceanic technology. To begin with, the investigators had considerable difficulty with erroneous triggering (misfiring) of bottles on the Rosette. Those of us who have endured this notorious "grounding" problem appreciate the difficulty of trying to decide if the bottle did or didn't misfire and if the misfire registered on the shipboard deck unit. If the operator triggers the unit again after a misfire, the question arises as whether the new pulse fired the correct bottle or the next bottle in the sequence. Several of these misfires can lead to confusing data, especially in well-mixed regions of the ocean. It is good policy to keep track of the misfires for sorting out the data later.

Another interesting observation was that variations in lowering speed had a noticeable influence on the temperature and conductivity measurements. Since most modern CTDs dissipate 5–10 watts, the CTD slightly heats the water through which it passes. At a 1 m/s nominal fall rate, surface swell can cause the actual fall rate to oscillate over an approximate range of ±1 m/s with periodic reversals in fall direction at the swell period. (Heave compensation is needed to prevent the CTD from being pulled up and down.) As a result, the CTD sensors are momentarily yanked up through an approximately 1 m °C thermal wake which is shed from boundary layers of the package as it decelerates. Hendry (1993) claims that conditional editing based on package speed and acceleration is reasonably successful in removing these artifacts. Since turbulent drag varies with speed squared, mechanical turbulence was found to cause package vibration that affected the electrical connection from the platinum thermometer to the Mark V CTD. Mixing, entrainment and thermal contamination caused differences in down versus up casts in both instruments. The correction for thermal inertia of the conductivity cell in the SBE CTD resulted in salinity changes of 0.005 psu with negative downcast corrections when the cell was cooling and positive upcast corrections when the cell was warming (Lueck, 1990).

1.4.2 The practical salinity scale

In using either chlorinity titration or the measurement of conductivity to compute salinity, one employs an empirical definition relating the observed variable to salinity. In light of the increased use of conductivity to measure salinity, and its more direct relationship to total salt content, a new definition of salinity has been developed. As a first step in establishing the relationship between conductivity and salinity Cox *et al.* (1967) examined this relationship in a variety of water samples from various geographical regions. These results were used in formulating new salinity tables (UNESCO, 1966) from which Wooster *et al.* (1969) derived a polynomial fit giving a new formula for salinity in terms of the conductivity ratio (R) at 15°C. The RMS deviation of this fit from the tabulated values was 0.002‰ in chlorinity for values greater than 15‰ and 0.005‰ for smaller values. It is worth noting that Cox *et al.* (1967) found that deep samples (>2000 m depth) had a mean salinity, computed from chlorinity, that was 0.003‰ lower than that for conductivity. This was not true for the surface samples.

As noted earlier, a new salinity definition has been adopted called the "practical salinity scale" or PSS 78 (Lewis, 1980). This scale has been accepted by major oceanographic organizations and has been recommended as the scale in which to report future salinity data (Lewis and Perkin, 1981). The primary objections to the earlier salinity definition of Wooster *et al.* (1969) were:

(a) With salinity defined in terms of chlorinity it was independent of the different ionic ratios of seawater.
(b) The mixtures of reference seawaters used to derive the relationship between chlorinity and conductivity ratio were nonreproducible.
(c) The corresponding International Tables do not go below 10°C which makes them unsuitable for many *in situ* salinity measurements.

In the practical salinity scale, it is suggested that standard seawater should be a conductivity standard corresponding to, and having the same ionic content as, Copenhagen Water. The salinity of all other waters will be defined in terms of the conductivity ratio (R_{15} or C_{15} in the nomenclature of Lewis and Perkins) derived from a study of dilutions of standard seawater. This becomes then a practical salinity scale as distinct from an absolute salinity defined in terms of the total mass of salts per kilogram of solution.

A major problem in applying this new salinity scale is its application to archived hydrographic data. As discussed by Lewis and Perkins (1981), the correction procedure for such data depends not only on the reduction formula used but also on the calibration procedure used previously for the salinity instrument. Essentially, the correction procedure amounts to performing this calibration a second time using the differences, provided by Lewis and Perkins (1981) between the older salinity scale and PSS 78. Another alternative would be to return to the original raw data, if they have been saved, and to recompute the salinity according to PSS 78. From the discussion of Lewis and Perkins it is clear, however, that for salinities in the range of 33–37‰ differences of about ±0.01‰ can be anticipated between archived salinities and the corresponding values computed using PSS 78. This is about the same overall accuracy of modern CTD profilers.

It is interesting that the primary motivation for the development of PSS 78 came from people working in low salinity polar waters where the UNESCO tables did not apply. In areas such as estuarine environments which have very low salinities, and mid-ocean ridge regions with strong hydrothermal fluid venting, even PSS 78 is not adequate and there are still serious limitations to computing accurate salinities from conductivity measurements. There are several reasons for these limitations. First of all, the approach of relating specific conductance to salinity of total dissolved solids requires that the proportions of all the major ions in the natural electrolyte remain constant in time and space, and second, that the salinity expression represents all the dissolved solids in the fluid. Another factor to keep in mind is that the density calculated from the conductivity values is based on conducting ions in the fluid. If there are chemical components that contribute to the density of the fluid but not to the conductivity (i.e. nonconductive ions) then the density will be wrong. This is exactly the problem faced by McMannus *et al.* (1992) for deep CTD data from Crater Lake in Oregon. Here, silicic acid from hydrothermal venting in the south basin of the lake below 450 m depth did not contribute to the conductance but did alter the density. Without accounting for silicic acid the water column was weakly stratified; after accounting for it, the bottom waters became stratified. The different combinations of ions in hydrothermal fluids from mid-ocean ridges can seriously alter the salinity structure observed at the source during a normal deep CTD measurement. However, because of rapid entrainment of ambient bottom water, the ion mix becomes similar to that of normal seawater a few meters above the vent orifice. Typical ratios of ambient to hydrothermal fluid volumes are 7000:1. Vertical structure such as that in Figure 1.4.4 taken a few meters above venting fields on Juan de Fuca Ridge in the northeast Pacific, presumably results from unstable conditions arising from turbulent mixing in the rising plume, not from sensor response problems.

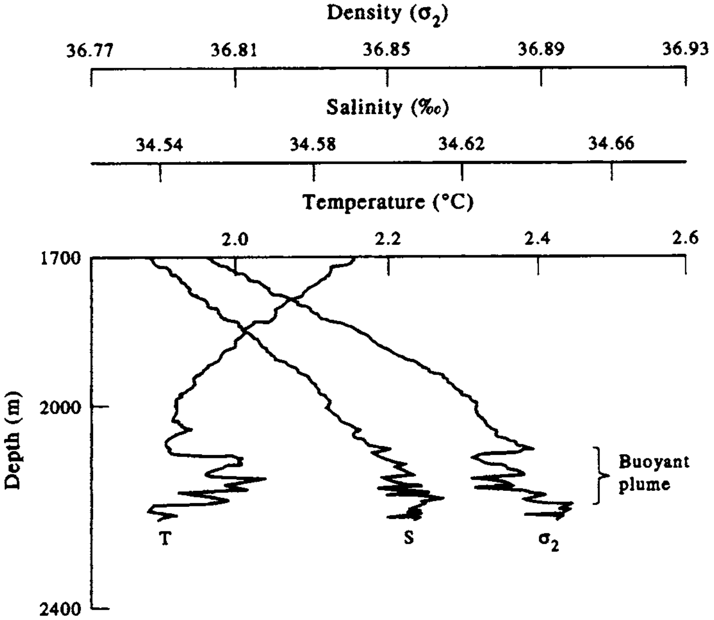

Figure 1.4.4. Vertical profiles of temperature, salinity (‰) and potential density collected from a CTD mounted on the submersible Alvin. Data collected during ascent away from the main hydrothemal vent field at Endeavour Ridge in the northeast Pacific (48°N, 129°W). Density is unstable over the depth range of the buoyant portion of the plume. (From Lupton et al., 1985.)

1.4.3 Nonconductive methods

Efforts have been made to infer salinity directly from measurements of refractive index and density. Since the refractive index (n) varies with the temperature (T) and salinity (S) of a water sample (and with the wavelength of the illumination), measurements of n and T can be used to obtain *in situ* estimate of salinity. In order to achieve a salinity accuracy of 0.01 psu, it is necessary to measure n to within 20×10^{-7} and to control temperature to within 0.005°C. Some refractometers are capable of measuring n to 100×10^{-7}, leading to a salinity precision of 0.06 psu. Handheld refractometers are simple and easy to use but yield salinity measurements no better than ±0.2 psu. For higher sensitivity, interference methods can be used giving a precision in n of 5×10^{-7} corresponding to a salinity precision of 0.003 psu. This is a comparative interference technique and requires a reference seawater sample. Since it is a comparative method, knowledge of the exact temperature is not critical as long as both samples are observed at the same temperature. Direct measurements of seawater density can yield a precision of ±0.008 in sigma-t (Kremling, 1972) which can be used to calculate salinities to within 0.02 psu. Since the measurement of density is much more complicated than those of temperature and electrical conductivity, these latter quantities are usually observed and used to compute the *in situ* density.

1.5. DEPTH OR PRESSURE

1.5.1 Hydrostatic pressure

The depths of profiling instruments are mainly derived from measured hydrostatic pressure, p. This is possible because of the almost linear relationship between hydrostatic pressure, $p = p(z)$, and geometric depth, z. The relationship is such that the "pressure expressed in decibars is nearly the same as the numerical value of the depth expressed in meters" (Sverdrup *et al.*, 1942). The validity of this approximation can be seen in Table 1.5.1 in which we have compared values of hydrostatic pressure

Table 1.5.1 Comparison of pressure (dbar) and depth (m) at standard oceanographic depths using the UNESCO algorithms. Percent difference = (pressure − depth)/pressure × 100%

Pressure (dbar)	Depth (m)	Difference (%)
0	0	0
100	99	1
200	198	1
300	297	1
500	495	1
1000	990	1
1500	1483	1.1
2000	1975	1.3
3000	2956	1.5
4000	3932	1.7
5000	4904	1.9
6000	5872	2.1

and geometric depth for a standard ocean. At depths shallower than 4000 m, the difference is within 2%. For most applications, this error is sufficiently small that it can be neglected and hydrostatic pressure values can be converted directly into geometric depth. The cause for the slight difference between pressure in decibars and depth in meters is found in the familiar hydrostatic relation,

$$p(z) = -g \int_{z}^{0} \rho(z)\,\mathrm{d}z$$

where $g = 9.81\ \mathrm{m\ s^{-2}}$ is the acceleration due to gravity and $\rho \approx 1.025 \times 10^3\ \mathrm{kg/m^3}$ is the mean water density. Units of p are $[\mathrm{kg/m^3}][\mathrm{m/s^2}][\mathrm{m}] = [\mathrm{kg/m}][1/\mathrm{s^2}]$. Also, p = force/area has units $[\mathrm{N/m^2}] = [\mathrm{Pa}] = [10^{-5}\ \mathrm{bar}]$. A newton (N) = kg m/s^2, so that $p \approx 1.025 \times 10^3(9.81)z = 1.005525z$ (m). A different value of density gives a slightly different p versus z relation.

Certain techniques allow for continuous measurement of hydrostatic pressure while others can be carried out at discrete depths only. An example of the latter is the computation of "thermometric depth" using a combination of protected and unprotected reversing thermometers to sense the effects of pressure on the temperature reading. This is still considered one of the most accurate methods of determining hydrostatic pressure and is often used as an *in situ* calibration procedure for CTD profilers. Specifically, the pressure, p (in decibars), obtained from a CTD is related to the temperature difference, ΔT, between the protected and unprotected thermometers by $p \approx g\Delta T/k$, where $k \approx 0.1°\mathrm{C}/(\mathrm{kg\,cm^2})$. The details of this procedure are well described in Sverdrup *et al.* (1942, p. 350) but with a significant printing error (a missing plus sign in the second bracket) which is not corrected in Defant (1961, Vol. 1, p. 35). When correctly applied (see LaFond, 1951; Keyte, 1965), the thermometer technique is capable of yielding pressure measurements accurate to ±0.5% (Sverdrup, 1947). Most modern CTD systems claim a similar accuracy using strain-gauge sensors to directly measure pressure. The accuracy of early CTD pressure sensors was a function of the depth (pressure) itself and varied from 1.5 db in the upper 1500 db to over 3.5 db below 3500 db (Brown and Morrison, 1978). A recent test of a Sea Bird SBE 9 CTD (Hendry, 1993) found pre- and postcruise pressure calibration offsets of less than 1 dbar. Nonlinearity and hysteresis were less than 0.5 dbar over the full range of the sensor.

The mechanical bathythermograph introduced earlier in this chapter measures pressure with a Bourdon tube sensor. The problem with this sensor is that the response of the tube to volume change is nonlinear and any alteration in tube shape or diameter will lead to abrupt changes in the pressure response. As a result of the nonlinear scaling of the MBT pressure readout and special optical reader needed to read the scales, this reading error, added to the inaccuracies of the Bourdon tube, results in limited accuracy of the MBT.

1.5.2 Free-fall velocity

Unlike the MBT, the more commonly used XBT, does not measure depth directly but rather infers it from the elapsed time of a "freely-falling" probe. While this is a key element that makes such an expendable system feasible it is also a possible source of error. In their study, Heinmiller *et al.* (1983) first corrected XBT profiles for systematic temperature errors and then compared the XBT profiles with corresponding CTD temperature profiles. In all cases, the XBT isotherm depths were less than the corresponding CTD isotherm depths for observations deeper than an intermediate depth (150 m for T4s and 400 m for T7s) with the largest differences at the bottom of each trace. Near the bottom of the XBT temperature profile, the difference errors exceeded the accepted limit of 2% error, with the deviation being far greater for the shallower T4 probes (Figure 1.5.1a). Added to this systematic error is an RMS depth error of approximately 10 m regardless of probe type (Figure 1.5.1b). Based on the data they analyzed, Heinmiller *et al.* (1983) provide a formula to correct for the systematic depth error. There are two primary sources of this depth error: first, the falling probe loses weight as the wire runs out of the probe supply spool, thus changing the fall rate and second, frictional forces increase as the probe enters more dense waters.

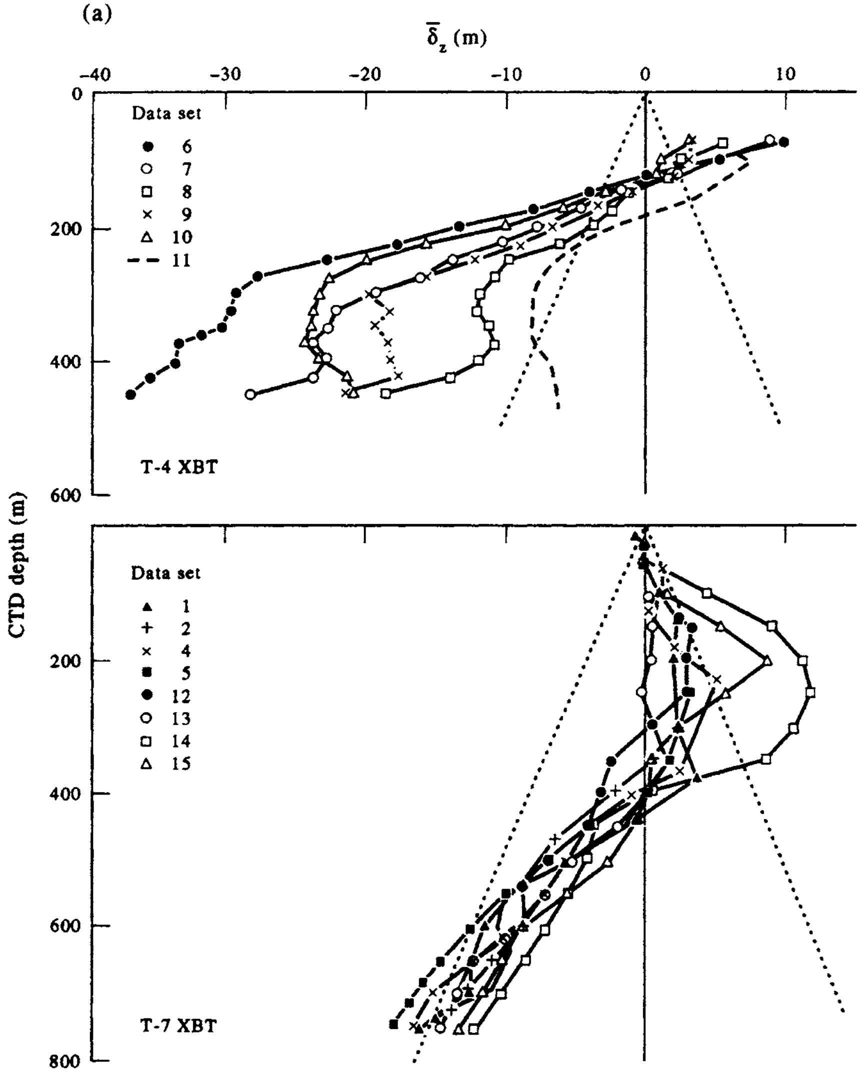

Figure 1.5.1. Vertical profiles of XBT-CTD depth differences for T-4 and T-7 XBTs for different data sets. (a) Mean values, $\overline{\delta_z}$ (m).

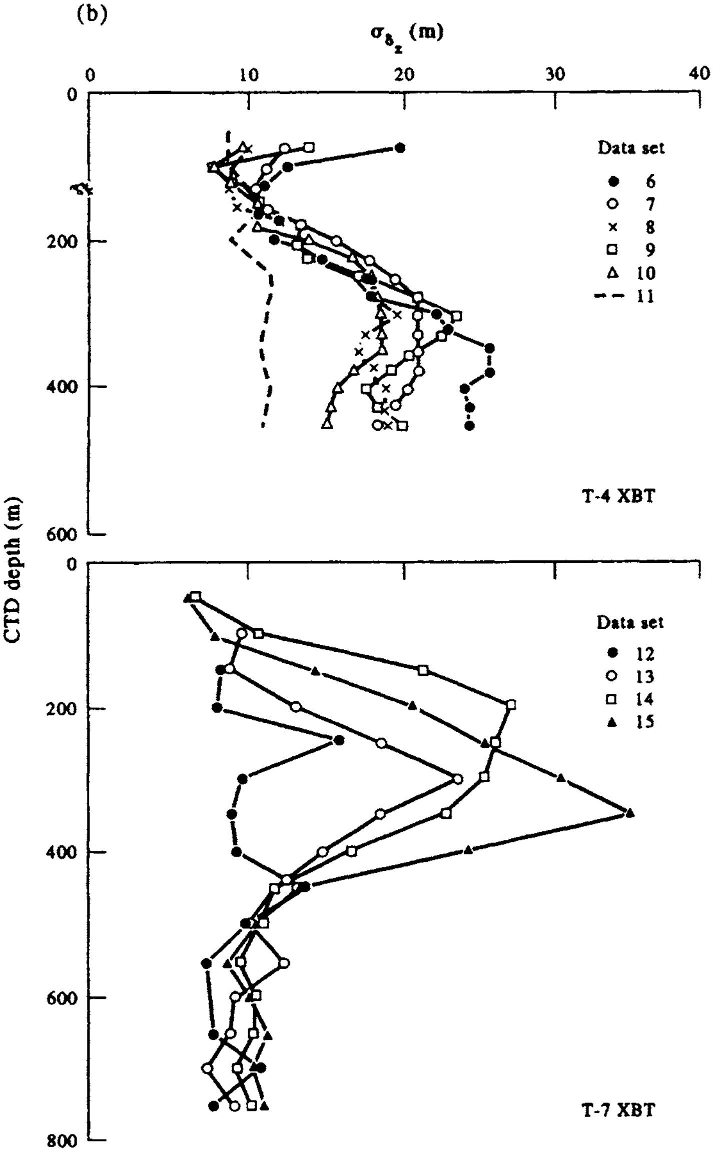

Figure 1.5.1. Vertical profiles of XBT-CTD depth differences for T-4 and T-7 XBTs for different data sets. (b) Standard deviations $\overline{\sigma_{\delta_z}}$ (m).

The issue of XBT depth error, first reported by Flierl and Robinson (1977) has been extensively investigated by many groups (Georgi *et al.*, 1980; Seaver and Kuleshov, 1982; Heinmiller *et al.*, 1983; Green, 1984; Hanawa and Yoritaka, 1987; Roemmich and Cornuelle, 1987; Hanawa and Yoshikawa, 1991; Hanawa and Yasuda, 1991; Rual, 1991) with varying results There is general agreement that the XBT probes fall faster than specified by the manufacturers and that some corrections are needed. Most of these assessments have been performed as a comparison with nearly coincident CTD profiles. The concentration assessments in the western Pacific shows the interest in this problem in Japan, Australia and Nouméa, New Caledonia.

A sample comparison between XBT and CTD temperature profiles (Figure 1.5.2a) shows the differences between the XBT and CTD temperature profiles as a function of depth. These profiles have not been corrected using the standard depth equation. The sample in Figure 1.5.2(b) has been depth corrected using the formulation given by Hanawa and Yoritaka (1987). Note the substantial changes in the shape of the difference profile and how the depth correction eliminates apparent minima in the differences. The overall magnitude of the differences has also been sharply reduced, demonstrating that many of the apparent temperature errors are, in reality, depth errors.

These XBT depth errors are known to be functions of depth since they depend on an incorrect fall-rate equation. This is clearly demonstrated in Figure 1.5.3 which gives the mean depth difference of a collection of 126 simultaneous temperature profiles, along with the standard deviation (shown as bars that represent the standard deviation on either side of the mean line) at the various depths. Also shown are the ±2% or ±5 m limits which are given as depth error bounds by the manufacturer. From this figure it is clear that there is a bias with the XBT falling faster than specified by the fall-rate equation, resulting in negative differences with the CTD profiles. The mean depth error of 26 m at 750 m depth translates into 3.5%, which obviously exceeds the manufacturer's specification.

When various investigators reduced these comparisons to new fall rate equations, where the depth (z) is given by

$$z = at - bt^2 \tag{1.5.1}$$

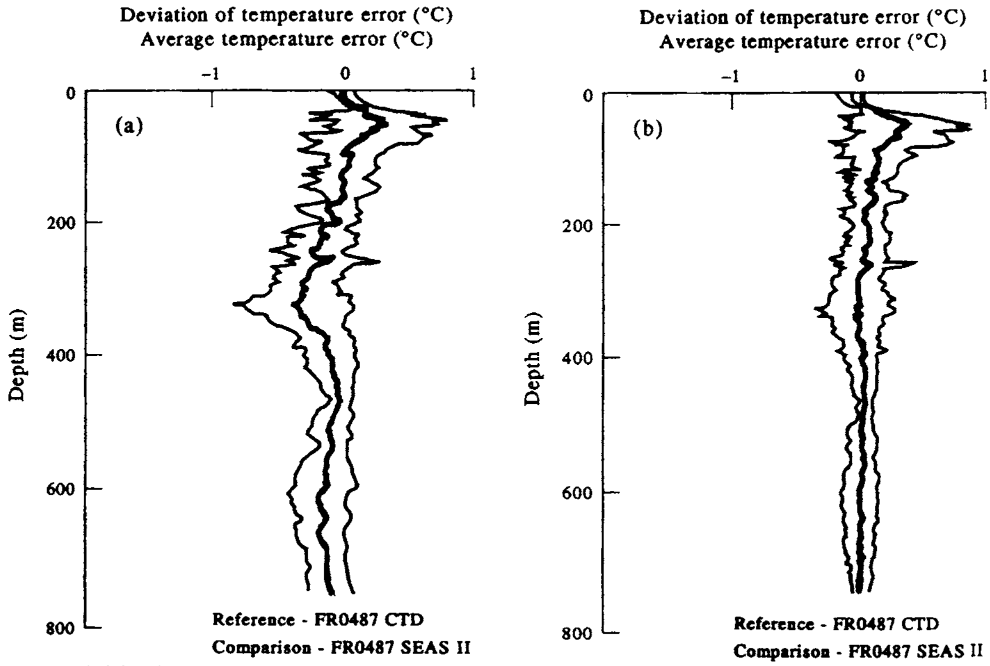

Figure 1.5.2. Average temperature error profiles (TXBT-TCTD) for XBT/CTD comparisons on FR0487 using the SEAS II XBT system; center line gives the mean value. (a) Depth uncorrected; (b) depth corrected using the formulation given by Hanawa and Yoritaka (1987). (From IOC-888, Annex IV, p. 6.)

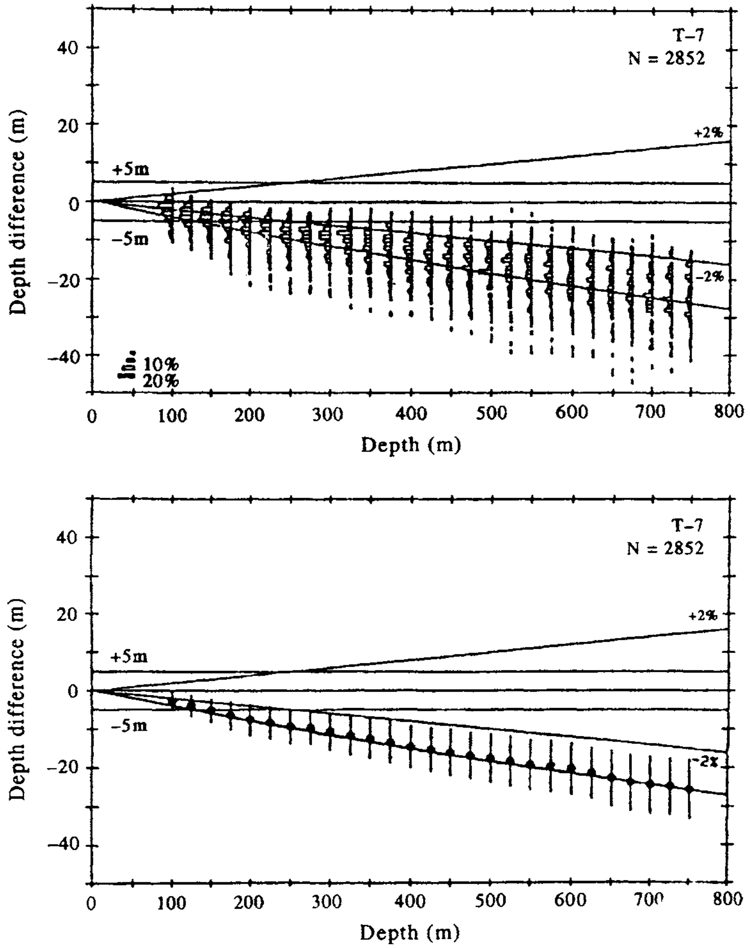

Figure 1.5.3. The mean depth difference of a collection of 126 simultaneous temperature profiles, along with the standard deviation (shown as bars that represent the standard deviation on either side of the mean line) at the various depths. (From IOC/INF-888, p. 13).

the coefficients were not very different (Figure 1.5.4). Along with the coefficients, this figure also shows contours of maximum deviations in depth relative to the revised equation of Hanawa and Yoshikawa (1991) for these different combinations of constants a and b in the fall rate equation (1.5.1). Most of the errors lie within the 110 m envelope of depth deviations, suggesting that it might be possible to develop a new fall-rate equation (i.e. new coefficients) that represents a universal solution to the fall-rate problem for XBT probes. An effort was made to develop this universal equation be reanalyzing existing XBT–CTD comparison profiles. This revised equation is

$$z = 6.733t - 0.00254t^2 \tag{1.5.2}$$

This revised fall-rate equation only applies to the T7 (roughly 700 m depth) XBT

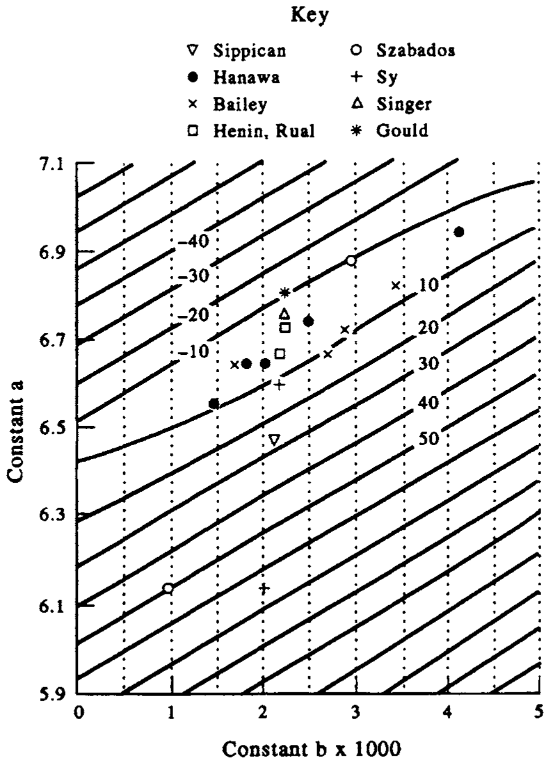

Figure 1.5.4. Fall-rate equation coefficients for different XBT studies listed in the key. (From IOC/INF-888.)

probes that were used in the comparisons. It was concluded that similar comparisons must be carried out for the other types of XBT probes.

1.5.3 Echo sounding

Acoustic depth sounders are now standard equipment on all classes and sizes of vessels. Marketed under a variety of names including echo sounder, fish finder, or depth indicator, the instruments all work on the same basic principle: The time it takes for an acoustic signal to make the round-trip from a source to an acoustic reflector such as the seafloor is directly proportional to the distance traveled. Water supports the propagation of acoustic pressure waves because it is an elastic medium. The acoustic waves radiate spherically and travel with a speed $c(E, \rho)$ which depends on the elasticity (E) and density $[\rho = \rho(S, T, P)]$ of the water. If the speed of the sound is known at each time t along the sound path, then the distance d from the sound source to the seafloor is given in terms of the two-way travel time by

$$d = \frac{1}{2}\int_{t_t}^{t_r} c(t)\,\mathrm{d}t \qquad (1.5.3.1)$$

where

$$\Delta t = t_r - t_t = 2 \int_{t_t}^{t_r} [1/c(S,T,P;t)]\, dz(t) \tag{1.5.3.2}$$

is the time between transmission time (t_t) of the sound pulse and reception time (t_r) of the reflected pulse or echo. In practice, the values of c along the sound paths are not known and equation (1.5.3.1) must be approximated by

$$d = \frac{1}{2}\langle c\rangle \Delta t \tag{1.5.3.3}$$

where $\langle c\rangle$ is a mean sound speed over the path length, a value normally entered into the echo sounder during its calibration. The depth determined using the time delay is called a "sounding". In hydrography, a "reduced" sounding is one that is referenced to a particular datum. As noted by Watts and Rossby (1977), equation (1.5.3.2) is similar in form to the equation for dynamic height (geopotential anomaly), suggesting that travel time measurements from an inverted echo sounder can be used to measure geostrophic currents (cf. Section 1.6.3).

Since the bulk properties of the medium depend on temperature, salinity and pressure, sound speed also depends on these parameters through the relation

$$c = c_{0,35,0} + \Delta c_T + \Delta c_S + \Delta c_P + \Delta c_{S,T,P} \tag{1.5.3.4}$$

in which $c_{0,35,0}$ = 1449.22 m/s (= the speed of sound at 0°C, 35 psu, and pressure p = 0, at depth z = 0). The remaining terms are the first-order Taylor expansion corrections for temperature (T), salinity (S), and hydrostatic pressure (P); the final term, $\Delta c_{S,T,P}$, is a nonlinear corrective term for simultaneous variation of all three properties. A well known set of values for this equation, having stated experimental standard deviation of 0.29 m/s, is attributed to W. Wilson (Hill, 1962; p. 478). To a good approximation (Calder, 1975; MacPhee, 1976)

$$\begin{aligned} c\,(\text{m/s}) &= 1449.2 + 4.6T - 0.055T^2 + 0.00029T^3 \\ &\quad + (1.34 - 0.010T)(S - 35) + 0.016z \end{aligned} \tag{1.5.3.5}$$

or (Mackenzie, 1981)

$$\begin{aligned} c\,(\text{m/s}) &= 1448.96 + 4.591T - 5.304 \times 10^{-2}T^2 + 2.374 \times 10^{-4}T^3 \\ &\quad + 1.340(S - 35) + 1.630 \times 10^{-2}z + 1.675 \times 10^{-7}z^2 \\ &\quad - 1.025 \times 10^{-2}T(S - 35) - 7.139 \times 10^{-13}Tz^3 \end{aligned} \tag{1.5.3.6}$$

where T is the temperature (°C) and S is the salinity (psu) measured at depth z (m). Accurate profiles of sound speed clearly require accurate measurement of temperature which may not be available in advance. A commonly used oceanic approximation is the mean calibration speed $\langle c\rangle$ = 1490 m/s that is generally applied to ship's sounders. Note that the speed of sound increases with increasing temperature, salinity and pressure, with temperature having by far the greatest effect (Figure 1.5.5). For exam-

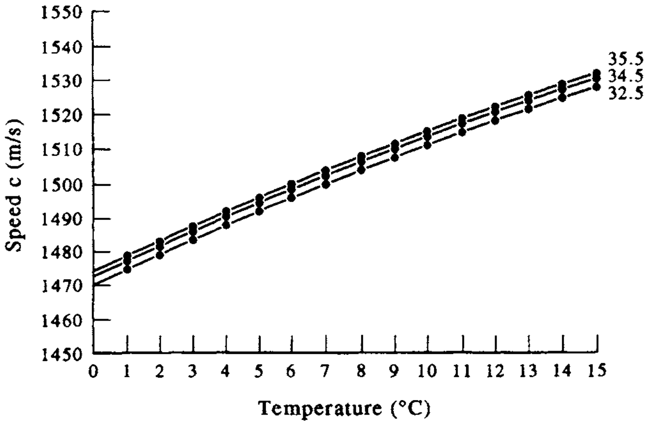

Figure 1.5.5. Speed of sound as a function of temperature for different mean salinities (32.5, 34.5, and 35.5 psu) and fixed depth, z = 1500 m.

ple, c increases by 1.3 m/s per 1 psu in salinity (range 34–35 psu); increases by 4.5 m/s per 1.0°C for temperature (range 0–10°C); and increases by 1.6 m/s per 100 m depth.

The depth capability of any sounder is limited by the power output of the transducer transmitting the sound pulses, by the sensitivity of the receiver listening for the echo returns and by the capability of the instrument electronics and software to resolve signal from noise. In modern sounders, pulse lengths typically range from 0.1 to 50 ms and a single transducer with a transmit/receive (T/R) switching arrangement is used to both generate and receive the acoustic signals. The depth capability of an echo sounder is limited also by a number of important environmental factors. Sound waves are attenuated rapidly in water according to the relation

$$\text{propagation loss (dB)} = 20 \log z + \alpha z/1000$$

where the propagation loss is measured in decibels (dB), z is the depth range in meters and α (Figure 1.5.6) is the attenuation coefficient (dB/km) in seawater as a function of frequency, temperature and salinity (Urick, 1967). The first term in the equation accounts for geometrical spreading of the transmitted and received signal while the second encompasses scattering and absorption. Diffraction and refraction arising from density gradients have a minor effect on the attenuation compared with these other factors. The higher the frequency of the source the greater the attenuation due to absorption and the more limited the depth range (Figure 1.5.7). It is for this reason that most deep-sea sounders operate in the 1.0–50 kHz range. Even though high-frequency sounders can provide more precise depth resolution through shorter wavelengths and narrower beam widths, they cannot penetrate deeply enough to be of use for general soundings. They do have other important applications in bioacoustical studies of zooplankton and fish.

The output transducer converts electrical energy to sound energy and the receiving transducer converts sound vibrations to electrical energy. Loss of the acoustic signal through geometrical spreading is independent of frequency and results from the spherical spreading of wave fronts, while frequency-dependent absorption leads to the conversion of sound into heat through viscosity, thermal conductivity, and

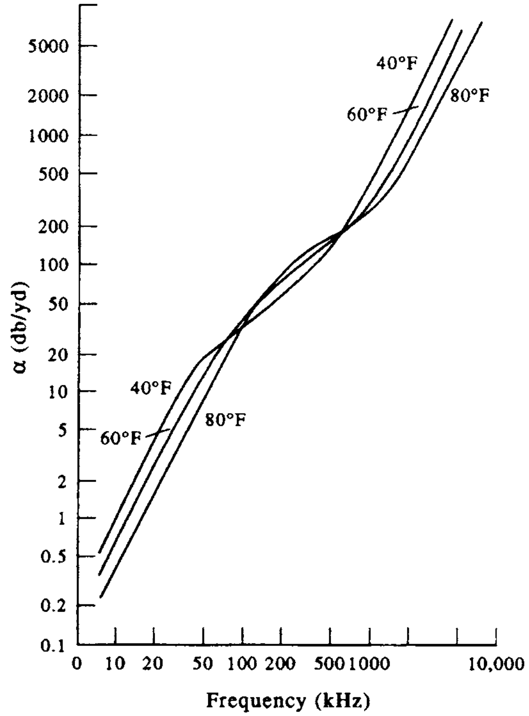

Figure 1.5.6. Absorption coefficient in seawater at salinity 35 psu as a function of frequency for three temperatures (40°F = 3.6°C; 60°F = 12.4°C; 80°F = 21.3°C). Conversion factor: 1 db/km = 1.0936 db/kyard; 1 kHz = 1000 cps. db ≡ dB(After Urick, 1967.)

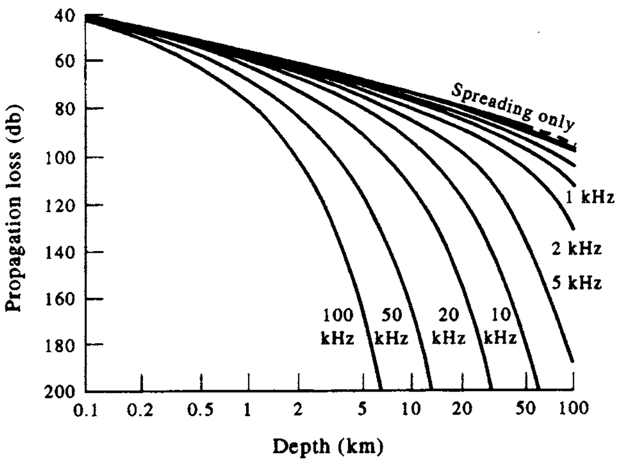

Figure 1.5.7. One-way sound attenuation (propagation loss, PL) in water as a function of sounder frequency (1 kHz = 1000 cps). Curves are derived using $PL = 20 \log R + \alpha R/1000$, *where R is in km and* α *is taken from Figure 1.5.6 using the conversion to db/km.*

inframolecular processes. Scattering is caused by suspended particles and living organisms. In the upper 25 m of the water column, air bubbles from breaking waves and gas exchange processes are major acoustic scatterers. If I_o is the intensity (e.g. power in watts) of the transducer and I_a is some reference intensity (nominally the output intensity in watts measured at 1-m distance from the transducer head) then the measured backscatter I_r is given by

$$I_r/I_a = b\exp(-\gamma z)/z^2 + A_n \tag{1.5.3.8}$$

where $b = I_o/I_a$ is the gain of the transducer, γ is the inverse scale length for absorption of sound in water, $1/z^2$ gives the effect of geometric spreading over the distance z from which the sound is being returned, and A_n is a noise level. A return signal intensity reduction by a factor of 2 corresponds to a loss of −3 dB [=10 log (1/2)] while a reduction by a factor of 100 corresponds to a loss of −20 dB [= 10 log (1/100)]. Echo sounders are generally limited to depths of 10 km. The low (1–15 kHz) frequencies needed for these depths result in poor resolutions of only tens of meters. Since it takes roughly 13 s for a transducer "ping" to travel to 10 km and back, the recorded depth in deep water is not always an accurate measure of the depth beneath the ship. Better resolution is provided for depths less than 5 km using frequencies of 20–50 kHz. High resolution sounders operate in a few hundred meters of water using frequencies of 30–300 kHz. Transducer beam width, side-lobe contamination and side echos ultimately reduce the resolution of any sounder.

1.5.3.1 Height above the bottom

In many oceanographic applications, the investigator is interested in real-time, highly accurate measurements of the altitude of his or her instrument package above the bottom. A real-time reporting echo sounder on the package will serve as an altimeter. Alternatively, the investigator can choose a cheaper route and attach a high-power omnidirectional "pinger" to the package. Rather than trying to measure the total depth of water, one uses the pinger on the package together with ship's transducer (or hydrophone lowered over the side of the ship) to obtain the difference in depth (i.e. difference in time) between the signal which has taken a direct route from the pinger and one which has been reflected from the bottom at an angle θ, where θ is roughly the angle the tow line makes with the bottom (Figure 1.5.8). The direct path PC takes a time t_d while the path reflected from the bottom (PBC) takes a total time t_r. The height, d, of the package above the bottom is

$$d = \frac{1}{2}(c\Delta t)\sin\theta = \frac{1}{2}c(t_r - t_d)\sin\theta \tag{1.5.3.9}$$

where Δt is the time delay between the direct and reflected pings and c is the speed of sound in water. As the instrument package approaches the bottom, the two strongest analog traces on the depth recorder can be seen converging toward a "crossover" point. When the time taken to cover the direct and reflected paths are equal ($\Delta t = 0$), the package has hit the bottom. The novice operator will be confused by the number of "false" bottom crossovers or wrap-around points when working in water that is deeper than integer multiples of the chosen sounder range. To avoid high levels of stress as each crossover is approached, the operator must know in advance how many false

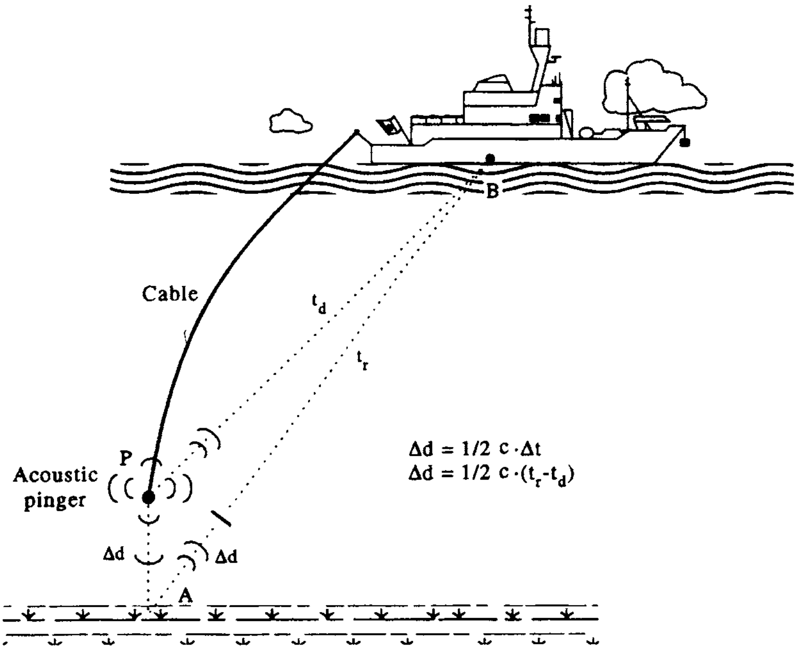

Figure 1.5.8. Schematic of how acoustic pinger and ship's sounder in the receive mode can be used to accurately determine proximity of a probe to the bottom. c is the speed of sound and t is time.

crossovers or wrap-arounds to expect before the instrument is truly in proximity to the bottom. For example, in water of depth 3230 m, a recorder chart set for a full-scale depth range of 0–750 m will register false bottoms when the pinger reaches water depths of 230, 980, and 1730 m (i.e. $3230 - n \times 750$ m, where $n = 4, 3, 2$). To the depth recorder, $3230 - 4 \times 750$ m is the same as 230 m.

Analog devices such as the PDR are the only real choice for this application since the analog trace provides a continuous visual record of how many crossovers have passed and how rapidly the final crossover is being approached. (The depth is first obtained from the ship's sounder which can then turned to "receive mode" only.) The two traces give a history of what has been happening so that it is easier to project in one's mind what to expect as the instrument nears the bottom. Problems arise if the package gets too far behind the vessel and the return echos become lost in the ambient noise or if the bottom topography is very rugged and numerous spurious side echos and shadows begin to appear. We recommend omnidirectional rather than strongly directional pingers so that if the package streams away from the ship or twists with the current and cable there is still some acoustic energy making its way to the ships hull. To help avoid hitting the bottom, it is best to have the ship's sounder output turned off so that only receive mode is working and the background noise is reduced; the operator can check on the total depth every once in a while by reconnecting the "transmit pulse". The ships echo sounder correctly measures the height above bottom since it is programmed to divide any measured time delay by a factor of 2 to account for two-way travel times. The depth accuracy of the method improves as the package approaches the bottom because both the direct and reflected paths experience the same sound speed *c*. A value of *c* more closely tuned to deep water is applicable here since all that really counts is c near the seafloor in the region of study. With a little experience and a good clean signal, one can get accuracies of several meters above the bottom using 8–12 kHz sounders in several kilometers of water.

Note that the depth errors using this method are negligible while the actual sounding depths from a depth sounder can be quite large. For example, if spatial differences in sound speed vary from 1470 to 1520 m/s over the sounding depth, then the percentage depth errors are $\Delta c/c = 50/1500 = 0.033 = 3.3\%$. In 4000 m of water, this amounts to an error of $0.033 \times 4000\text{ m} \approx 133$ m.

1.5.4 Other depth sounding methods

For sake of completeness, several lesser-known, remote-sensing, depth-sounding methods are introduced in the following sections.

1.5.4.1 Laser induced detection and ranging (LIDAR)

Lidar is an active electro-optical (LASER) remote-sounding method using a pulsed laser system as a radiation source flown from an aircraft. An airborne sensor measures the distance to the surface of the ocean and to the seafloor along the appropriate light path by measuring the time interval between emission of the pulse and the reception of its reflection from the surface and the bottom. A typical LIDAR unit consists of a pulsed laser transmitter, a receiver, and a signal analyzer-recorder. The technique is good to depths of a few tens of meters in coastal waters where extinction coefficients are typically around 0.4–1.6 m^{-1}. The rapid spatial sampling capability of this technique makes it highly useful to hydrographers wanting to map shoals, rocks and other navigational hazards.

1.5.4.2 Synthetic aperture radar (SAR)

One of the surprising aspects of SAR is its ability to "see" shallow banks, ridges and shoals in the coastal ocean. In this case, SAR does not measure the bottom topography directly but, instead, detects the distortion of the wave ripplet field over the feature caused by deflection and/or acceleration of the ocean currents. For a discussion of this effect, the reader is referred to Robinson (1985).

1.5.4.3 Satellite altimetry

The suggestion that there is a close connection between oceanic gravity anomalies and water depth was postulated as early as 1859 (Pratt, 1859, 1871). The idea of using measured gravity anomalies to estimate water depth began with Siemens (1876) who designed a gravity meter that obviated the need to spend hours for a single sounding (Vogt and Jung, 1991). It was not until the launching of the Seasat radar altimeter in 1978 that this concept could be used as alternative to large-scale sounding line measurements. Indeed, the first Seasat-derived gravity map of the world oceans (Haxby, 1985) closely resembles a bathymetric map with a resolution of about 50 km (Vogt and Jung, 1991). The idea of using satellite radar altimetry as a "bathymeter" is based on the good correlation observed between gravity anomalies and bathymetry in the 25–150 km wavelength radar band. Satellite bathymetry is especially valuable for sparsely sounded regions of the world ocean such as the South Pacific, and in regions where depths are based on older soundings in which navigation errors are 10 km or more. As pointed out by Vogt and Jung, however, one-dimensional predictions cannot be accurately ground-truthed with a single ship survey track since the geoid measured along the track is partly a function of the off-track density distribution. (Geoid refers to a constant geopotential reference surface, such as long-term mean sea-level, which is everywhere normal to the earth's graviational field.) A broad swath of shipborne data is needed to overlap the satellite track swath.

Satellites presently carrying radar altimeters to map sea-surface topography include GEOS-3, SEASAT, GEOSAT, ERS-1, and TOPEX/POSEIDON. Of these, only data from the U.S. Navy's GEOSAT have been processed to the accuracy and density of coverage needed to clearly resolve tectonic features in the marine gravity field on a global basis (Marks *et al.*, 1993; EOS). This mission was designed to map the marine geoid to a spatial resolution of 15 km. Detailed maps of the seafloor topography south of 30°S from the GEOSAT Geodetic Mission were declassified in 1992. These maps have a vertical RMS resolution of about 10–20 cm and, together with Seasat data, have been used to delineate fracture zones, active and extinct mid-ocean ridges, and propagating rifts. Satellite altimetry from ERS-1 has been used to map the marine gravity field over the permanently ice-covered Arctic Ocean (Laxon and McAdoo, 1994). Future declassification of military satellite data will lead to further analysis of the seafloor structure over the remaining portions of the world ocean.

As we discuss later in more detail, satellite altimetry shows much promise for interpreting large-scale circulation previously deduced from dynamic height data. Satellite altimetry is particularly well suited to examination of temporal variability of meso-scale features in the ocean, such as the propagation of Rossby waves.

1.6 SEA-LEVEL MEASUREMENT

The measurement of sea-level is one of the oldest forms of oceanic observation. Pytheus of Marseilles, who is reported to have circumnavigated Britain around 320BC, was one of the first to actually record the existence of tides and to note the close relationship between the time of high water and the transit of the moon. Nineteenth-century sea-level studies were related to vertical movements of the coastal boundaries in the belief that, averaged over time, the height of the mean sea-level was related to movements of the land. More recent applications of sea-level measurements include the resolution of tidal constituents for coastal tide height predictions and assisting in the prediction of El Niño/La Niña events in the Pacific. Tide gauge data are essential to studies of wind-generated storm surges which can lead to devastating flooding of highly populated low-lying areas such as Bangladesh. Tide gauges located along the perimeter of the Pacific Ocean and on Pacific islands form an important component of the tsunami warning system that alerts coastal residents to possible seismically-generated waves associated with major underwater earthquakes and crustal displacements.

In addition to measuring the vertical movement of the coastal land mass, long-term sea-level observations reflect variations in large-scale ocean circulation, surface wind stress, and oceanic volume. Because they provide a global-scale integrated measure of oceanic variability, long-term (>50 years) sea-level records from the global tide-gauge network provide some of the best information available on global climate change. Long-term trends in mean sea-level are called *secular* changes while changes in mean sea-level that occur throughout the world ocean are known as *eustatic* changes. As described later in this section, eustasy is associated with land-based glaciation, the accumulation of oceanic sediments, and tectonic activity, such as the change in ocean volume and the shape of the ocean basins. Since coastal stations really measure the movement of the ocean relative to the land, land-based sea-level measurements are referred to as relative sea-level (RSL) measurements. Mean sea-level is the long-term average sea-level taken over a periods of months or years. Datum levels used in hydrographic charts can be defined in many ways and generally differ from country to country (Thomson, 1981; Woodworth, 1991). For geodetic purposes, mean sea-level needs to be measured over several years.

Specifics of sea-level variability

As the previous discussion indicates, observed sea-level variations about some mean equilibrium "datum" level can arise from four principal components: (1) *short-term* temporal fluctuations in the height of the sea surface include those associated with wind waves and oceanic tides forced by the changing alignment of the sun, moon, and earth. In addition, there are changes due to atmospheric pressure (the inverse barometer effect), to wind-induced current set-up/set-down along the coast, to changes in river runoff, and to changes in the large-scale ocean circulation caused by fluctuations in the oceanic wind field. (2) *Long-term* temporal changes result from changes in the mass of the ocean due to melting or accumulation of land-based ice in the major ice sheets in Antarctica and Greenland, and in the smaller ice sheets and mountain glaciers. *Steric sea-level* changes arising from changes in ocean volume—without a change in mass—involve the heating (expansion) and cooling (contraction) of the ocean. Addition or removal of salt has the same steric effect as do cooling and heating. (3) *Coastal subsidence* involves the lowering of the land brought about by reduction in the thickness of unconsolidated coastal sediments, erosion, sediment deposition and with the withdrawal of fluids (water, oil, etc.) from the sediments. (4) Large-scale crustal movements produce sea-level change through *tectonic processes* (mountain building) and *glacio-isostatic rebound* (continued viscoelastic response of the earth to melting of glaciers during the last ice age).

The principal semidiurnal (M_2) and diurnal (K_1) tidal constituents with respective periods of 12.42 and 23.93 h can be accurately resolved using a 15.3-day tidal record of hourly values. Further resolution of the important spring-neap cycle of the tides (the 15-day fortnightly cycle) requires a record length of 29 days (0.98 lunar months; 1 lunar day = 25 h). For most practical purposes, this is the minimum length of record that is acceptable for construction of local tide tables. In fact, many countries maintain primary tide-gauge stations as reference locations for secondary (short-term) tide-gauge stations. Differences in the tide heights and times of high/low water are tabulated relative to the primary location. Accurate resolution of all 56 principal tidal constituents requires a record length of 365 days while an accurate measure of all components for long-term tidal applications requires a record of 18.6 years. The 18.6-year "Metonic" cycle or nuation is linked to the 5° tilt of the plane of the moon's orbit with respect to the plane of the earth's orbit and is the time it takes the line of intersection of these two planes to make one complete revolution (Thomson, 1981). Other tidal constituents include: The centimeter-scale Pole Tide (Chandler Effect) with a period of 14.3 months that arises from the Chandler Wobble in the instantaneous axis of the earth's rotation; an 8.8-year cycle associated with alterations in the eccentricity of the moon's orbit about the earth; and a 20,940-year cycle due to a wobble in the earth's orbit about the sun (precession of the equinox). Meteorological tides are caused by local atmospheric forcing and include large ($\sim$1 m) sea-level changes associated with storm surges that often flood low-lying areas (Murty, 1984). Their periodicities are related to changes in wind and atmospheric pressure.

In addition to the relatively small changes in sea-level associated with the Metonic cycle and other orbital factors, there are a variety of major variations due to geological processes. Geological techniques such as coring of Greenland glaciers show a relatively rapid rise of sea-level from 18,000 years ago, when sea-levels were roughly 130 m lower than today. The rate of sea-level rise, which averaged 10 mm/year during the glacial–interglacial transition period, slowed dramatically about 8000 years ago when the levels were 15 m below those of today. Present levels were reached roughly 4000 years ago. Since that time, mean sea-level changes have consisted of oscillations of small amplitude (Barnett, 1983). However, there is now concern that global sea-levels are rising at about 1–2 mm/year due to global warming through build up of CO_2 in the atmosphere. Many long-term stations show definite long-term trends (Figure 1.6.1) that may be related to global climate change. There is a general increase of about 0.1–0.15 m per century for gauges located in geologically "stable" regions of the world. One possible source of long-term variability is melting from global warming of water locked into the polar ice caps and northern hemisphere glaciers. Changes in the land-based ice cover alter both the ocean volume and the geodetic loading. However, it should be noted that the rate of rise varies considerably from station to station and is strongly dependent on regional tectonic activity and the lingering effects of the continuing glacio-isostatic response (Peltier, 1990; Tushingham and Peltier, 1992). Investigators attempting to extract a possible climate change component from global sea-level records spend considerable effort generating spatially-smoothed data sets consisting of a relatively small subset of the total tide gauge data available from the world archives.

Mean sea-levels are usually computed from long series of hourly observations. Generally, a simple arithmetic average of hourly values is computed, but other methods, including the application of low-pass numerical filters to eliminate tides and surges, may be used before the means are computed. The average of all high and low water levels is called the mean tide height; it is close to, but not identical with, mean sea-level. Monthly and annual mean sea-level series for a global network of stations are collected and published by the Permanent Service for Mean Sea-level (PSMSL) in England, together with details of gauge location and the definitions of the datums to which the measurements are referred. Data are held for 1446 "Metric" file stations of which 889 have had their data adjusted to a tide gauge benchmark datum to form the Revised Local Reference (RLR) data set. This datum is approximately 7.000 meters below mean sea-level, with the arbitrary choice made to avoid negative numbers in the resulting RLR monthly and annual mean values. Of these stations, 112 have data from before 1900. Most of these stations are in the northern hemisphere so that careful analysis is necessary to avoid geographic bias in their interpretation. Only one year of monthly data are needed for the Metric data to be converted to the common datum (Woodworth, 1991). Amsterdam has the longest tide-gauge record in world but the oldest data which satisfy the selection criteria of the PSMSl are from Brest, starting in 1807.

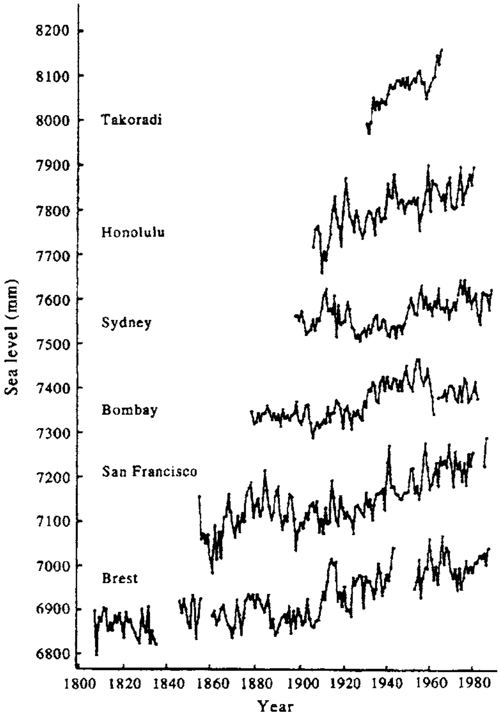

Figure 1.6.1. Annual mean sea-level values for the longest records for each continent. Data are Revised Local Reference (RLR) records from the Permanent Service for Mean Sea-level at the Bidston Observatory in Merseyside. Each record has been given an arbitrary offset for presentation purposes. The Takoradi record was truncated in 1965 when major problems with the gauge were reported. (From Woodworth, 1991.)

1.6.1 Tide and pressure gauges

Although pressure and acoustic gauges are becoming increasingly more popular around the world, most sea-level measurements are still made using a float gauge, in which the float rises and falls with the water level (Figure 1.6.2a). Modern recording systems replace the analog pen with a digital recording system that records on punched paper, magnetic tape, or hard-drive. Many of the digital recording systems have been equipped with telemetering systems that send sea-level heights and time via satellite, direct radio link or meteor-burst communication. The most important aspect of this type of sea-level measurement is the installation of the float stilling well. The nature of this installation will determine the frequency response of the float system and will help damp out unwanted high-frequency oscillations due to surface gravity waves. Stilling wells can have their inlet at the bottom of the well or use a pipe inlet connected to the lower part of the well. Both designs damp out the high-frequency sea-level changes. Maintenance of the sea-level gauge insures that the water inlet orifice is kept clear of obstructions from silt, sand, or marine organisms. Also, in areas of strong stratification such as rivers or estuaries, the water in the stilling well can be of a different density than the water surrounding it. When installing such a measurement

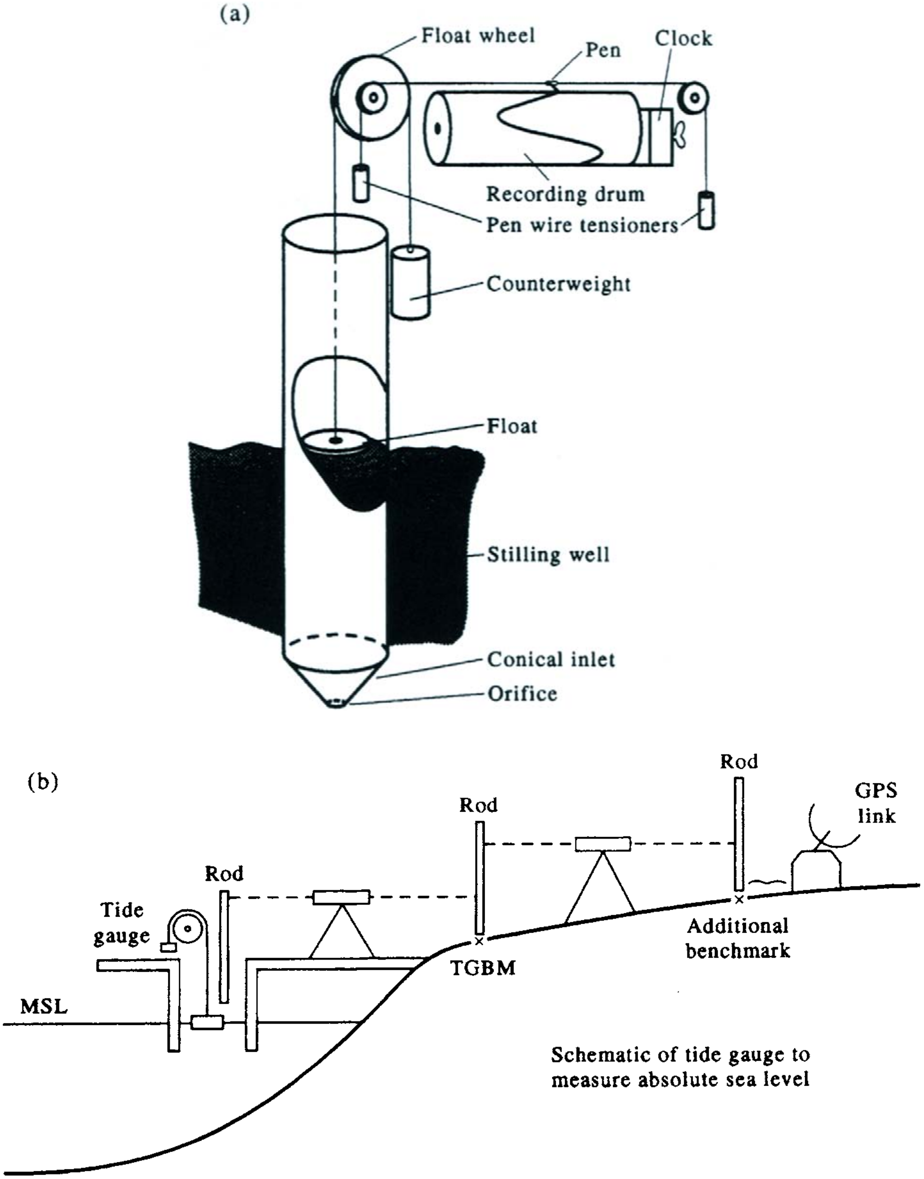

Figure 1.6.2. (a) A basic float stilling-well gauge used to measure water levels on the coast; (b) Schematic of tide-gauge station with the gauge, network of benchmarks and advanced geodetic link. TGBM = tide gauge bench mark. (After Woodworth, 1991.)

system, it is important to provide adequate protection from contamination of the stilling well and from damage to the recorder. A potential hazard in all harbor gauge installations is damage from ship traffic or contamination of the float response from ship wakes.

Proper installation of coastal sea-level gauges requires that they be surveyed into a legal bench mark so that measured changes will be known relative to a known land elevation (Figure 1.6.2b). When properly tied to a bench mark height, changes in gauge height relative to land can be taken into account when computing the mean sea-level. This tie-in with the local benchmark datum is done by running the level back to the nearest available geodetic datum. Modern three-dimensional satellite-based global positioning systems (GPS) and long-baseline telemetry systems will soon make it possible to accurately determine the vertical movement of a tide gauge relative to the geoid. Future accurate satellite altimeter measurements may also provide global measurements of the relative sea surface which can then be compared with the conventional sea-level measurements.

The usual test of a sea-level instrument (called the Van de Casteele test) involves operating the instrument over a full tidal cycle and comparing the results against simultaneous measurements made with a manual procedure. This procedure only shows if the recording device is operating properly so that a separate test of the stilling well is needed to accurately measure the response of the float. Other than mechanical problems, timing errors are one of the major sources of error in sea-level records. Sea-level gauges have either mechanical or electronic clocks which must be periodically checked to insure that there is no significant drift in the timing of the mechanism. When possible these checks should be made weekly. Depending on the specific instrument, well-maintained sea-level recorders are capable of measurements accurate to within a several millimeters.

Another type of sea-level measuring device is the pneumatic or bubbler gauge (Figure 1.6.3). This system links changes in the hydrostatic pressure at the outlet

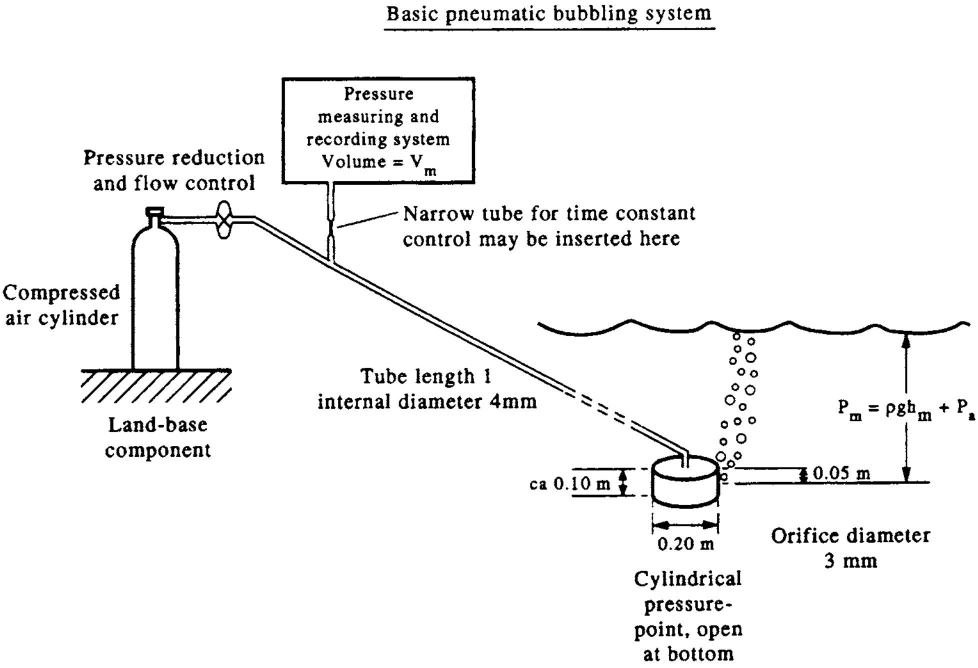

Figure 1.6.3. The pneumatic or bubbler gauge. This system links changes in the hydrostatic pressure, P_m, at the outlet point of the bubbles to variations in sea-level, h_m, water density and atmospheric pressure, P_a.

point of the bubbles to variations in sea-level. Like other pressure sensing gauges, this gauge measures the combined sea-level height and atmospheric pressure. As a consequence, most bubbler gauges operate in the differential mode whereby the recorded value is the difference between the measured pressure and the atmospheric pressure. While these instruments are somewhat less accurate than float gauges, they are useful in installations where a float gauge would be subject to either damage from ship traffic or strongly influenced by wave motion. In a study in Tasmania in the 1970s, the plastic pressure tubes leading from the electronics package to the ocean were constantly being destroyed by curious wombats.

Sea-level heights are recorded in a variety of formats. Graphical records must be digitized and care taken to record only values properly resolved by the instrument. Differences in recording scale will lead to variations in the resolution of the gauge thereby limiting the accuracy of the digitized data. Modern gauges eliminate this possible problem by recording digital data. During digitization of the data, it is important to edit out any of the obvious errors due to pen-ink problems or mechanical failures in the advance mechanism. Also, when long-term sea-level variations are of interest, one must be careful to filter out high-frequency fluctuations due to waves and seiches. The choice of time reference is important in creating a sea-level time series. The usual convention is to use the local time at the location of the tide gauge which can then be referenced to Greenwich Mean Time (GMT, now called Universal Temps Coordinée, UTC). The sea-level record should also contain some information about the reference height datum on which the sea-level heights are based. Digital recording systems are subject to clock errors and care should be taken to correct for these errors when the digital records are examined.

In recent years, sensitive and accurate pressure sensors have been developed for measurement of deep sea tides where fluctuations of the order of 1 mm need to be detected in depths of thousands of meters. At first, these sensors were largely based on the "Vibraton" built by United Control Corporation which measured pressure by changes in the frequency of oscillation of a wire under tension. This frequency change was measured to an accuracy of 6×10^{-4} Hz and led to a sea-level accuracy of 0.8 mm (Snodgrass, 1968). To maintain this high level of accuracy, it was necessary to correct for temperature effects to a resolution of 0.001°C. When Vibraton sensors ceased to be commercially available they were replaced by resonating quartz crystal transducers (Wimbush, 1977), which are the standard for measurement in both deep sea and coastal pressure gauge recorders. Produced by Parosscientific (Paros, 1976), these sensors have a sensitivity of 1×10^{-4} dbars for shallow applications (<500 m depth) and a sensitivity of 1×10^{-3} dbars for deep sea measurements. Most modern pressure gauges used in coastal and deep sea tidal measurements make use of these sensors. (Pressure gauges used in coastal waters are often known as water level gauges.) Temperature correction is required to maintain accurate depth measurements. Wearn and Baker (1980) report measurements made by such quartz sensors from year-long moorings in the Southern Ocean. Unfortunately, instabilities in the quartz sensors lead to sensor drifts which limit the use of the sensors in long-term, deep pressure measurements. The use of dual pressure sensors helps to correct for drift since each pressure sensor will have somewhat different drift characteristics but will produce similar responses to higher frequency oceanic variability.

1.6.2 Satellite altimetry

Conventional sea-level measurement systems are limited by the need for a fixed platform installation. As a result, they are only possible from coastal or island stations where they can be referenced to the land boundary. Unfortunately, there are large segments of the world's ocean without islands, so that the only hope for long-term sea-level measurements lies with satellite-borne radar altimetry. Early studies (Huang *et al.*, 1978) using GEOS-3 altimeter data with its fairly low precision of 20–30 cm, demonstrated the value of such data for estimating the variability of the sea surface from repeated passes of the satellite radar. In this case, the difference between repeated collinear satellite passes eliminates the unknown contribution of the earth's geoid to the radar altimeter measurement. This same technique was employed by Cheney *et al.* (1983) using 1000 orbits of high-quality SEASAT radar altimeter data.

With a known precision of 5–8 cm, the early radar data provided some of the first large-scale maps of mesoscale variability in the world's ocean. Satellite altimetry is one of the future monitoring capabilities now being actively pursued by physical oceanographers interested in ocean circulation problems. While the experience with GEOS-3 and SEASAT altimeter data demonstrated the great potential of these systems, it is not yet entirely clear if planned altimetry satellites will provide sufficient accuracy to allow the specification of the mean ocean circulation related to the ocean surface topography. The primary concern is for the contribution of the earth's geoid to the satellite altimeter measurements. The geoid is known to have variations with space scales similar to the scales of sea-level fluctuations associated with the mean and mesoscale ocean circulation. In addition, satellite altimetry data must be corrected for atmospheric effects which requires knowledge of the intervening atmospheric temperature and water vapor profiles. It is hoped that present research efforts will better specify these constituents of the altimeter signal so that future satellite altimeter measurements can be used to monitor both the mean and time variable (using crossovers or colinear satellite tracks) ocean circulation.

Considerable headway has been made recently in the area of satellite altimetry due to the successful deployment of a number of space-borne altimeters. The first to generate a lot of new data was the GEOSAT satellite first launched in 1985 by the U.S. Navy in an effort to more precisely map the influences of the geoid on missile tracks. After an 18-month "geodetic mission" the Navy was convinced by Dr Jim Mitchell and others to put the satellite into an "exact repeat orbit" in November, 1986, using the same orbit as the previous SEASAT satellite (Tapley *et al.*, 1982). The altimeter data from this orbit had already been made public data and thus the classified altimeter data from the geodetic mapping mission were already compromised for this orbit. By having the satellite operate in this orbit, scientists would be able to collect and analyze data on the ocean's height variability. Fortunately, the GEOSAT altimeter continued to function into 1989 providing almost three full years of repeat altimetry measurements. In addition, the navy has released the "crossover" data from the geodetic mission. In this mission, the track did not repeat but the crossovers between ascending and descending tracks provided valuable information on ocean height variability. Thus, it is possible to combine data from the earlier cross overs and repeat orbits from the "exact repeat mission" (ERM) to form a nearly five-year time-series of sea surface height variations. It should be stressed that without a detailed knowledge of the earth's geoid it is not possible to compute absolute currents and the main area of investigation provided by the GEOSAT data was in studying the ocean's height variability.

Considerable experience was gained in computing the various corrections that are needed to correct satellite altimeter data (Chelton, 1988). These include the ionospheric correction, the dry tropospheric correction, the wet tropospheric correction. Added to these are the errors due to EM (electromagnetic) bias, antenna mispointing, antenna gain calibration, the inverse barometer effect, ocean/earth tides and precise orbit determination. Since the GEOSAT satellite did not carry a radiometer to compute tropospheric water vapor other operational satellite sensors were used to compute the atmospheric moisture to correct the altimeter path length (Emery *et al.*, 1989a). Many experiments were conducted to better understand the EM-bias correction (Born *et al.*, 1982; Hayne and Hancock, 1982). Other corrections can be routinely computed from available sources, including the dry troposphere correction which requires knowledge of the atmospheric pressure (Chelton, 1988).

GEOSAT data have been used to map both the large-scale and smaller scale regional circulations of the ocean. Miller and Cheney (1990) used GEOSAT data to monitor the meridional transport of warm surface water in the tropical Pacific during an El Niño event. Combining crossover and colinear data, the authors constructed a continuous time-series of sea-level changes on a 2° × 1° grid in the Pacific between 20°N and 20°S for the four-year period from 1985 to 1989. They concluded that the 1986–1987 El Niño was a low-frequency modulation of the normal seasonal sea-level cycle and that a build-up of sea-level in the western Pacific was not required as a precursor to an El Niño event. A similar analysis of colinear GEOSAT data for the tropical Atlantic (Arnault *et al.*, 1990) showed good agreement between the satellite sensed sea-level changes and those measured *in situ* using dynamic height methods. Using GEOSAT sea-level residuals computed from a two-year mean Vazquez *et al.* (1990) examined the behavior of the Gulf Stream downstream of Cape Hatteras. Comparisons with NOAA infrared satellite imagery show a fair agreement in Gulf Stream path with some sea-level deviation maps not showing a clear location of the main stream. In the same geographic region Born *et al.* (1987) used a combination of GEOSAT altimetry and airborne expendable bathythermograph data, to map geoid profiles as the difference between the altimetric sea-level and the baroclinic dynamic height. Many other oceanographers have used GEOSAT data to study a great variety of oceanographic circulation systems (e.g. Figure 1.6.4).

In the summer of 1992, the long awaited TOPEX-POSEIDON altimetric satellite was launched. Carrying two altimeters (one French and one U.S.) with a single antenna, TOPEX/POSEIDON marked a significant step forward in altimetric remote sensing. The NASA altimeter is a dual-frequency altimeter which will be able to compensate for the influence of ionospheric changes. The French altimeter is the first solid-state instrument to be deployed in space. In addition, there is a boresight microwave radiometer (TOPEX Microwave Radiometer, TMR) to provide real time atmospheric water vapor measurements for the computation of wet troposphere corrections for the onboard altimeters. The resulting combination of data provides altimeter heights accurate to ±10 cm. A truly joint project, the satellite was built in the U.S. and launched by the French *Ariane* launch vehicle. A large group of French and U.S. science teams have been working to prepare for this mission and will continue to work on the analysis of these important data.

1.6.3 Inverted echo sounder (IES)

As noted in Section 1.5, accurate depth measurements using acoustic sounders requires corrections on the order of ±1% for variations in sound speed introduced by

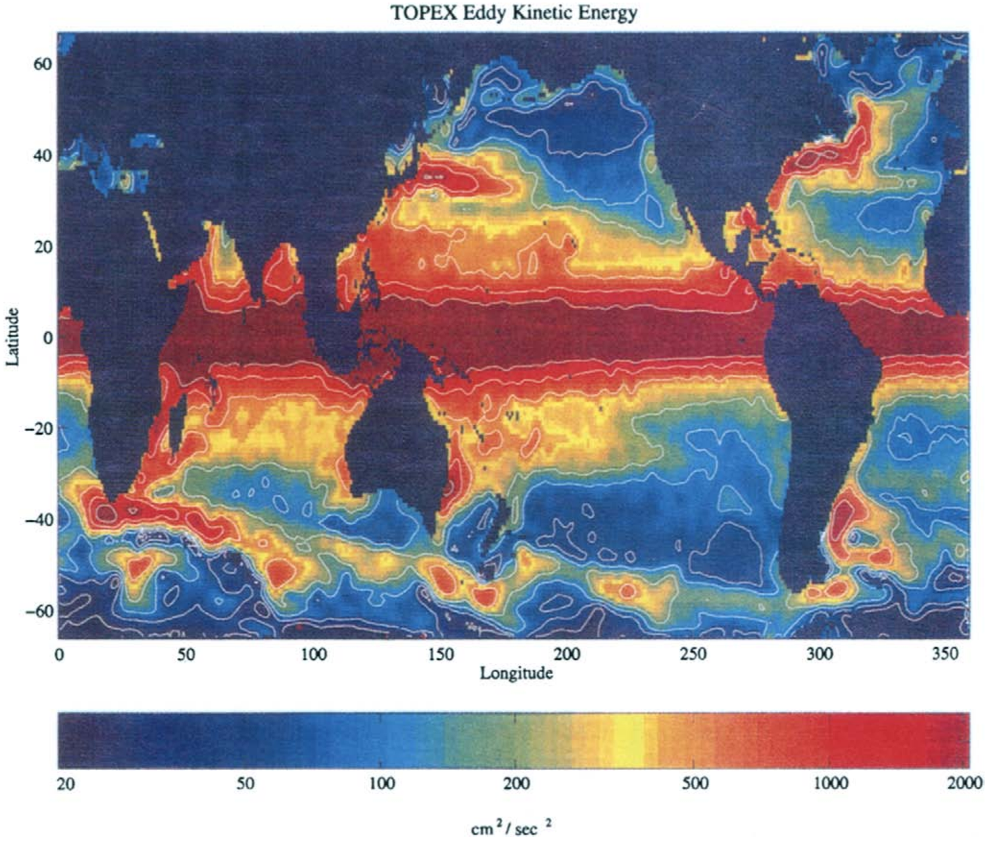

Figure 1.6.4. Average eddy kinetic energy maps from two years of Geosat altimeter data (November 1986 to November 1988) for ascending and descending passes (after Shum et al., 1990).

changes in oceanic density. Rossby (1969) suggested that this effect could be used to advantage since it provided a way to measure variations in travel times of acoustic pulses from the sea floor due to changes in the depth of the thermocline. Moreover, the fact that travel times are integrated measurements means that they effectively filter out all but the fundamental mode of any vertical oscillations. This idea led to the development of the inverted echo sounder (IES) in which the round-trip travel time of regularly-spaced 10 kHz acoustic pulses from the seafloor are now used to determine temporal variability in the integrated density structure of the ocean. The IES has been widely used in studies of the Gulf Stream where its records are interpreted in terms of thermocline depth, heat content and dynamic height (Rossby, 1969; Watts and Rossby, 1977). It has also been used in the equatorial Pacific and Atlantic although interpretation of the data is more uncertain because of a lack of repeated deep CTD casts to determine density variability (Chiswell *et al.*, 1988).

Tidal period variability and large changes caused by El Niño–Southern Oscillation (ENSO) events are potentially serious problems in the interpretation of echo sounding data. In particular, the CTD data are needed to convert time-series of acoustic travel-time Δt between two depth levels (z_1, z_2) to a time-series of dynamic height ΔD

integrated over the pressure range p_1 to p_2 with an accuracy of 0.01–0.04 dynamic meters. The obvious similarity between these two parameters (Watts and Rossby, 1977) can be seen from the relations

$$\Delta t_{z1/z2} = 2 \int_{z_1}^{z_2} [1/c(S, T, p)]\, dz \tag{1.6.3.1}$$

and

$$\begin{aligned} \Delta D_{p2/p1} &= \int_{p_1}^{p_2} [1/\rho(S,T,p) - 1/\rho(35,0,p)]\, dp \\ &= 10^3 \int_{p_1}^{p_2} \delta\, dp \end{aligned} \tag{1.6.3.2}$$

where c is the speed of sound (at specified salinity S, temperature T, and pressure p), z = depth (positive downward), and ρ is density. Finally, δ, defined as

$$\delta = \alpha(S, T, p) - \alpha(35, 0, p) = 1/\rho(S, T, p) - 1/\rho(35, 0, p) \tag{1.6.3.3}$$

is the specific volume anomaly. In these expressions, we use SI units with depth in meters, density in kg/m^3, pressure in decibars, and dynamic height in dynamic meters (1 dyn m = 10 m^2 s^{-2}).

Chiswell *et al.* (1988) compare time-series of dynamic height from an inverted echo sounder with sea-level height ($z_1 = -\eta$) from a pressure sensor located 70 km away on Palmyra Island in the central equatorial Pacific. The spectra for the dynamic height variations determined from the ISE closely resembled those from the pressure gauge. Significant coherences were found between the two signals at the 99.9% level of significance. Although, in principle, varying mixtures of vertical internal modes could produce a frequency dependence in the conversion of ISE to dynamic height, the effect was not significant over the year-long data series. Wimbush *et al.* (1990) discussed moorings in 4325 m of water 72 km west of the subsurface pressure gauge in the Palmyra Lagoon (5°53′N, 162°05′W). The IES was set to 1/2-hour sampling, each sample consisting of 20 pulses 10 s apart. Outliers are eliminated and the median value taken as representative of the acoustic travel time. According to Wimbush *et al.*, a conventional IES without a pressure sensor adequately records synoptic-scale dynamic height oscillations with 20–100-day periods. Chiswell (1992) discussed 14-month records from five inverted echo sounders deployed in February 1991 in a 50-km array in 4780 m of water near 23°N, 158′W north of Hawaii. The CTD and ADCP (acoustic Doppler current profiler) data collected during monthly surveys at the array site provided sufficient density data to calibrate the IES data in terms of dynamic height and geostrophic currents.

Wimbush *et al.* (1990) used the response method of Munk and Cartwright (1966) to get the daily and semidiurnal tides and filtered with a 40-h Gaussian low-pass filter while Chiswell has attempted to resolve the tidal motions through 36-h burst sampling of the density structure from three-hourly CTD profiles. IES deployments show that there is a linear relationship between dynamic height and travel time (Figure 1.6.5), with the calibration slope dependent on the particular *T–S* properties of the region. In this case, we can link variations in ΔD (for depths shallower than the reference level p_{ref} used in the dynamic height calculation) to the acoustic travel time Δt_{ref}

$$\Delta D = m\Delta t_{ref} \tag{1.6.3.4}$$

where total acoustic travel time to the bottom is

$$\Delta t = \Delta t_{ref} + \gamma H_2 \tag{1.6.3.5}$$

in which $\gamma = 2/c_b$ and c_b is the average sound speed (assumed constant) between p_{ref} and the bottom. The depth H_2 is the depth range between the seafloor (pressure $= p_b$) and the reference pressure level, p_{ref}. Solving yields,

$$\Delta D = m[\Delta t - (\gamma/\rho_b' g')p_b] \tag{1.6.3.6}$$

where gravity and bottom density are scaled as $g' = 0.1g$ and $\rho_b' = 10^{-3}\rho_b$, respectively. For oscillations in density having periods longer than about 20 days, the second term on the right-hand side of equation (1.6.3.6) may be dropped, whereby

$$\Delta D = m\Delta t \tag{1.6.3.7}$$

Wimbush *et al.* find $m = -70$ dyn m s^{-1} to convert Δt to ΔD, while Chiswell (1992) finds $m = -57.8$ dyn m s^{-1} for Δt defined for z = 0–4500 m and ΔD at 100 m referenced to 1000 m. The high correlation coefficient, r^2 = 0.93, is based on 186 shallow (1000 m) and 17 deep (4500 m) CTD casts. The error in the slope using the deep casts is 4 dyn m s^{-1} with an RMS deviation of 0.017 dyn m; for the shallow casts the mean is 0.1 dyn m s^{-1} with a deviation of 0.029 dyn m. The travel times for the subtropical Pacific moorings of Chiswell correlate better with dynamic height

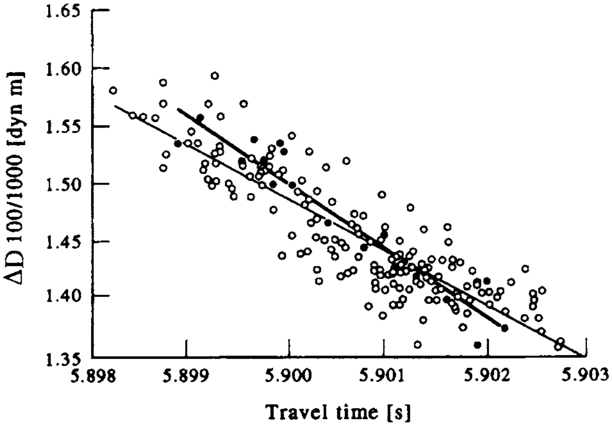

Figure 1.6.5. Dynamic height at 100 m relative to 1000 m ($\Delta D_{100/1000}$) from 186 shallow CTD casts plotted against corresponding travel time measured by IESs (open circles). Thin line is the least squares fit. Thick line and solid circles give $\Delta D_{100/1000}$ calculated from 17 deep casts plotted against the corresponding travel time from 4500 m to the surface, $T_{0/4500}$ (r^2 = 0.93 and slope = −57.8 dyn m/s). (From Chiswell, 1992.)

measured below 100 m than with surface dynamic heights. This is because large variations in the temperature and salinity relation in the upper 100 m affect dynamic height more than they affect acoustic travel time (Chiswell *et al.*, 1988). The tidal range of 8 dyn cm is relatively large compared with the seasonal range of 25 dyn cm and illustrates the need for detailed CTD sampling. Geostrophic currents have been derived from the array using the time-series of dynamic height created from the multiple IES moorings. Aliasing of the records by high frequency motions and a lack of CTD data to the depth of the IES remain problems for this method.

1.6.4. Wave height and direction

Any discussion of sea-level would be incomplete without some mention of surface gravity wave measurement. Methods include: a capacitance staff which measures the change in capacitance of a conductor as the air–water interface moves up and down with passage of the waves; an upward-looking, high-frequency acoustic sounder or acoustic Doppler current profiler with a vertical-pointing transducer which can be used to examine both the surface elevation and the associated orbital currents; a fixed graduated-staff attached to a drill platform, stuck in the sand or otherwise attached to the seafloor; satellite altimetry; a bottom-mounted pressure gauge with rapid sampling time; a shipborne Tucker wave-recorder system; and the waverider and directional waverider buoys. For brevity, we limit our presentation to the directional waverider since it represents reliable off-the-shelf technology.

Built by the Datawell company of The Netherlands, the directional waverider is a spherical, 0.9-m diameter buoy for measuring wave height and wave direction. The buoy contains a heave–pitch–roll sensor, a three-axis fluxgate compass and two fixed "x" and "y" accelerometers. The directional (x, y, z) displacements in the buoy frame of reference are based on digitial integration of the horizontal (x, y) and vertical (z) accelerations. Horizontal motions rather than wave slope are measured by this system. Vertical motions are measured by an accelerometer placed on a gravity-stabilized platform. The platform consists of a disk which is suspended in a fluid within a plastic sphere placed at the bottom of the buoy. Accelerations are derived from the electrical coupling between a fixed coil on the sphere and a coil on the platform. A fluxgate compass is used to convert displacements from the buoy frame of reference to true earth coordinates.

Displacement records are internally filtered at a high-frequency cut-off of 0.6 Hz. Onboard data reduction computes energy density, the prevailing wave direction, and the directional spread of the waves. Frequency resolution is around 0.01 Hz for waves in the range 0.025–0.59 Hz. Transmission of data is to Argos satellite or through standard 27–40 MHz radio-link to shore. The buoy will measure heave in the range ±20 m with 1 cm resolution for wave periods of 1.6–20 s in the moored configuration. The direction range is 0–360° with a resolution of 1.5°.

A crucial aspect of collecting reliable, long-term wave data is the mooring configuration. If not designed and moored correctly, there is little chance the mooring will survive the constant stresses of the wave motions. As illustrated in Figure 1.6.6, the recommended configuration consists of a single-point vertical mooring with two standard rubber shock cords and heavy bottom chain. This arrangement ensures sufficient symmetrical horizontal buoy response for small motions at low frequencies while the low stiffness of the rubber cords allows the waverider to follow waves up to

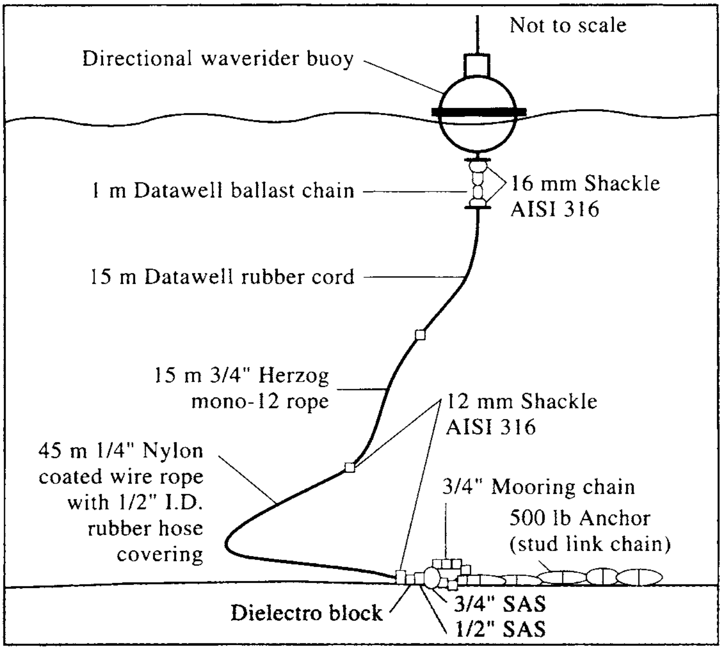

Tofino directional waverider mooring for rogue wave study

Water depth: 35–40 metres

Notes:

Herzog Mono–12 is Polypropylene 12 strand single braid rope.

SAS is safety anchor shackle crosby G–2130

AISI 316 are stainleess steel shackles

Figure 1.6.6. Mooring configuration for a Datawell Directional Waverider buoy on a shallow continental shelf. (Modified after Datawell bv, 1992; Courtesy T. Juhász and R. Kashino.)

40 m high. Current velocities can be up to 2.5 m/s, depending on water depth (Datawell bv, 1992).

1.7 EULERIAN CURRENTS

The development of reliable, self-recording current meters is one of the major technological advances of modern oceanography. These sturdy, comparatively lightweight instruments are, in part, a byproduct of the rapid improvement in electronic recording systems which make it possible to record large volumes of digital data at high sampling rates (Baker, 1981). Although they can be used in either moored or profiling modes, most current meters are used in time-series measurement of current speed and direction at fixed locations. [Such fixed-location measurements are called Eulerian measurements after the Swiss mathematician Leonhard Euler (1707–1783) who first formulated the equations for fluid motion in a fixed frame of reference.] The development of reliable mooring technology and procedures also has played a major role in advancing the use of moored current meters and associated instrumentation. Acoustic release technology, which has proven so critical to oceanic research, will be discussed at the end of this section.

Most commercially available current meters have sufficient internal power and data storage to be moored for several months to a year. The instrument's duration depends on the selected sampling rate, the data storage capacity, the battery life and the ambient water temperature. Greater power can be obtained from lithium batteries than from more conventional batteries but the user sometimes faces numerous transportation regulations and operational concerns with lithium batteries. Operating time for all types of batteries decreases with water temperature. Despite their sophistication, most current meters are made to withstand a fair amount of abuse during deployment and recovery operations. Typical "off-the-shelf" current meters (and releases) can be deployed to depths of 1000–2000 m, and many manufacturers fabricate deep versions of their products with heavy-duty pressure cases and connectors for deployments to depths of 6000 m. Most modern current meters also allow for the addition of ancillary sensors for concurrent measurement of temperature, conductivity (salinity), water clarity (light attenuation and turbidity), pressure, and other scalars.

Current meters differ in their type of speed and direction sensors, and in the way they internally process and record data. Although most oceanographers would prefer to work with the scalar components u, v of the horizontal current velocity vector, $\mathbf{u} = (u, v)$, it is a fact of life that current meters can directly measure only the speed ($|\mathbf{u}|$) and direction (θ) of the horizontal flow. (For now, we ignore the vertical velocity component, w.) It is because of this constraint that most current meter editing and analysis programs historically work with speed and direction. From a practical point of view, both the (u, v) and the $(|\mathbf{u}|, \theta)$ representations have their advantages, despite the difficulties with the discontinuity in direction at the ends of the interval of 0–360°.

Speed sensors can be of two types: *mechanical sensors* which measure the current-induced spin of a rotor or paddle wheel; and *nonmechanical sensors* which measure the current-induced change in a known electromagnetic field or the differences in acoustic transmission times along an acoustic path. Despite these fundamental differences, all current meters have certain basic components that include speed sensors, a compass to determine orientation relative to the earth, built-in data averaging algorithms, and a digital storage device. Possible speed sensors include:

(a) Propellers (with or without ducts).
(b) Savonious rotors.
(c) Acoustic detectors (sound propagation or Doppler shift).
(d) Electromagnetic sensors (induced magnetic field).
(e) Platinum resistors (flow-induced cooling).

Flow direction relative to the axes of the current meter is usually sensed using a separate vane or by configuring the speed sensors along two or three orthogonal axes. In all current meters, the absolute orientation of the instrument relative to the earth's magnetic field is determined by an internal compass. At polar latitudes where the horizontal component of the earth's magnetic field is weak, measurement of absolute current requires that the meter be positioned rigidly in a known orientation. Direction resolution depends on the type of compass used in the measurement; e.g. clamped potentiometer for Aanderaa RCMs, optical disk for Marsh–McBirney electromagnetic current meters, and flux gate (Hall effect) compass for the EG&G Vector Measuring Current Meter, InterOcean S4 current meter and SimTronix Ultrasonic Current Meter UCM 40. For each deployment, compass direction must be corrected for the local deviation of the earth's magnetic field before the velocity data are converted to north–south and east–west components. The accuracy, precision, and reliability of a particular current meter are functions of the specific sensor configuration and the kind of processing applied to the data. Rather than comment on all the many possible variations, we will discuss a few of the more generic and successful configurations.

The problems and procedures associated with the use of these instruments, and the analysis of the resultant data, are sufficiently similar that the discussion should be instructive in the use of instruments not specifically mentioned.

1.7.1 Early current meter technology

One of the earliest forms of current measurement was the tilt of a weighted line lowered from a ship. The time it took an object to travel the length of the ship also provided a measure of the surface flow. [The term "knot" is from the use by Dutch sailors of a knotted line to measure the speed of their sailing vessel.] Although we like to think of the current meter as a recent innovation, the Ekman current meter was in use as early as the 1930s (Ekman, 1932). Although many different mechanical current meters built in those days (see Sverdrup *et al.*, 1942), few worked and most scientists went back to the Ekman meter. To measure the current, the instrument was lowered over the side of the ship to a specific depth, started by a messenger, and then allowed several minutes before being stopped by a second messenger. The current speed for each time increment was determined by reading a dial that recorded the number of revolutions of an impeller turned by the current. A table was used to convert impeller revolutions to current speed. Current direction was determined from the distribution of copper balls that fell into a compass box below the meter. A profile from 10 to 100 m typically took about 30 min. Obvious problems with this instrument included low accuracy in speed and direction, limited endurance, and the need to work from a ship or other stationary platform. One of the first commercial current meters was the self-contained Geodyne 850 current meter built in the United States in the 1960s. The Geodyne was a large and bulky, vertically-standing unit with a small direction vane and four-cup Savonious rotor. Burst sampling was permissible in the range of 60–660 s. The Nerpic CMDR current meter built in France in the 1960s was a torpedo-like device that oriented itself with the current flow and used an impellor-type rotor to measure current speed. In the original versions, data were recorded on punched paper tape. The Kaijo Denki current meter built in Japan in the 1970s was one of the earliest types of acoustic current meter.

Although some oceanographers might disagree, the age of the modern current meter appears to have started with the Aanderaa Recording Current Meter (RCM) developed by Ivar Aanderaa in Norway in the early 1960s under sponsorship of the North Atlantic Treaty Organizaton (NATO). The fact that many thousands of these internally recording current meters remain in operation attests to the instrument's durability. Many oceanographers still consider the Aanderaa RCM4 (Figure 1.7.1) and its deep (>2000 m) counterpart, the RCM5, the "workhorses" of physical oceanography. It certainly is the most common and reliable current meter used to measure ocean currents. For this reason, there have been more studies, intercomparisons and soul-searching with this instrument than with any other type of meter.

1.7.2 Rotor-type current meters

The RCM series of current meters

The Geodyne and RCM4 current meters were the first current meters to use a Savonious rotor to measure current speed. This rotor consists of six axisymmetric, curved blades enclosed in a vertical housing which is oriented normally to the direction of flow (Figure 1.7.1). Data in the RCM4 are recorded on a small 1/4 inch reel-to-reel magnetic tape. Allowable sampling rate settings are 3.75×2^N min (e.g. 3.75, 7.5, 15, 30, 60 min) where N (= 0, 1, 2, ...) is an integer. Although shorter sampling periods are possible, they are not practical given the mechanical limitations of the rotor. Speed is obtained from the number of rotor revolutions for the entire sample interval while direction is the single direction recorded at the end of the sample period. Thus, speed is based on the average value for the recording interval while direction involves a single measurement. In the past, the number of revolutions per recorded data "count" was varied by changing the entire rotor counter module. More recent RCMs allow the investigator to set the number of revolutions per count (e.g. 2^M revolutions per count, where $M = 1, 2, 3, ...$) so that the speed range of the instrument can be adjusted for the flow conditions. For example, in the coastal tidal passes of British Columbia and Alaska, the common upper range of 3 m/s for standard rotor settings is not always sufficient to measure peak tidal speeds; the peak speed of 7.5 m/s that occurs in Nakwakto Rapids in coastal British Columbia is beyond the design of most modern current meters. The direction vane of the RCM4 is rigidly affixed to the pressure case containing the data logger. The unit is then inserted in the mooring line and the entire current meter allowed to orient in the direction of the current. Although the RCM does not average internally, vector-averaged currents can be obtained through post-processing of the data (Thomson *et al.*, 1985). A meteorological package for surface applications also is available with the same data logging system (Pillsbury *et al.*, 1974).

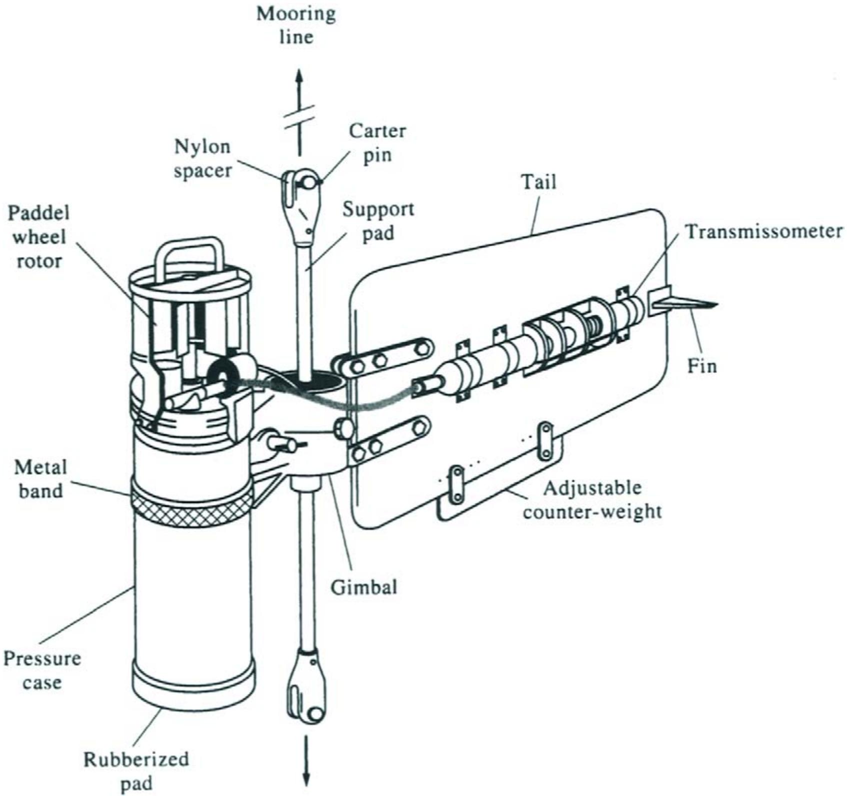

Figure 1.7.1. Caption overleaf.

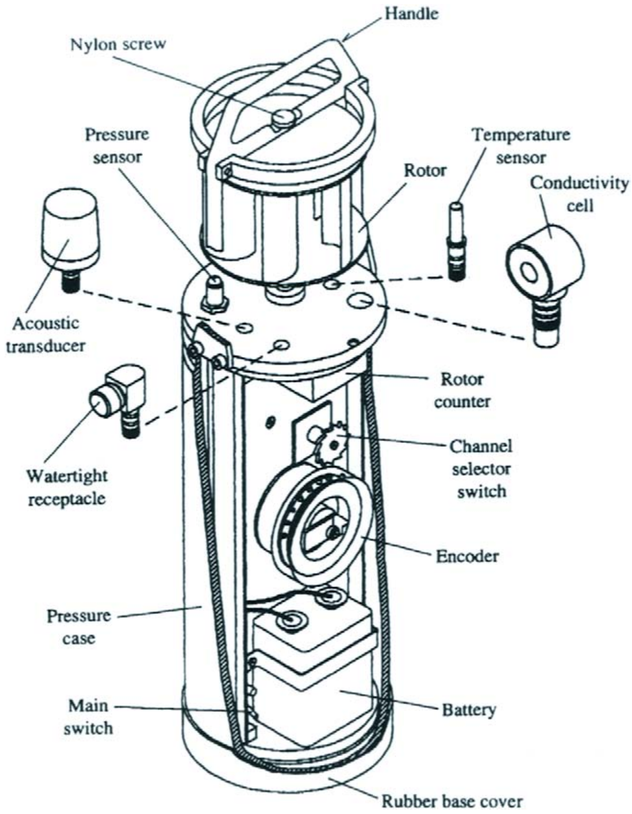

Figure 1.7.1. Exploded view of the encoder side of the Aanderaa RCM4 current meter. The reverse side contains a reel-to-reel 1/4-in tape system for recording the data from the different channels. The recorder unit is attached to a directional vane. (Courtesy G. Gabel, G. S. Gabel Corp.)

Part of the reason for the popularity of the RCM series of current meters has been their reliability, comparatively low cost, and relatively simple operation. Both calibration and maintenance of the instruments can be performed by individuals with fairly limited electronics expertise. In more recent years, many of the other types of current meters, such as electromagnetic current meter (ECM) and the acoustic current meter (ACM), have advanced to the point that they require electronics expertise due to the advanced computer diagnostics available from the manufacturers of these instruments. Another attractive feature of the RCM is the easy addition of sensors for measuring temperature, conductivity and pressure (depth) on the same data logger. The Aanderaa RCM7 introduced in the late 1980s can be purchased with standard temperature (−2 to +35°C), expanded temperature (i.e. over a narrower range such as 0–10°C), conductivity (for salinity), and total pressure. The 0–5 volt output from a Sea Tech transmissometer for measuring water clarity can be readily incorporated in the instrument package. Thus, there is the potential to collect a wide range of parameters other than just currents alone.

The profiling Cyclesonde (van Leer *et al.*, 1974; Baker, 1981) consists of a RCM4 current meter affixed to a buoyancy-driven platform which makes repeated automatic round trips between the surface and some specified depth (<500 m) along a taut-wire mooring. The vertical cycling of the instrument is controlled by changing the density of the instrument package by a few percent using an inflatable bladder. Depending on the prescribed sampling interval and the duration of each round-trip (or depth of water sampled), the instrument can provide time-series of currents, temperature and salinity over periods of weeks to months at depths of every 10 m or so through the water column.

Processing of RCM4 data includes four major steps: (1) tape transcription (quarter-inch tape to computer format); (2) calibration, or conversion to physical units; (3) error detection, spike removal and interpolation; and (4) data analysis. The last point will be discussed in detail in later chapters of this book. The first three steps provide an example of the procedure required in producing useful data from moored current meters. The data in an RCM4 are recorded as 10-bit binary words (numbers from 0 to 1023) on 1/4-inch magnetic tape. For each cycle, six binary words are written on the tape. For the temperature channnel, a near-linear calibration curve is applied to the measured value to convert it to temperature. Current speed for earlier versions is handled somewhat differently since speeds must be calculated as the difference between consecutive integers recorded on the appropriate data channel. The relationship between speed in physical units (e.g. cm/s) and rotor count (X) is nearly linear so that speed also can be calculated from a linear calibration.

Tape translation is carried out by connecting a 1/4-inch tape recorder to a digital computer. With this set-up, the digital data are transferred from the 1/4-inch tape to computer compatible format for further editing and analysis. To these raw character data must be added "header" information such as the start and stop times of the particular mooring. As a check one calculates the number of instrument cycles that should have occurred during the mooring period and this should equal the number of records in the raw data file. If this is not the case, then the data have timing errors which must be corrected before processing can continue. Timing errors will be more closely addressed in a later section.

To convert the dated raw data to physical units (i.e. speed, direction) calibration constants are needed for the individual sensors. For most parameters the calibration values are found for each meter separately as quadratic fits to the calibration data. As has been mentioned above, this is not the case for the speed parameter for which a general curve can be used for all rotors if currents are typically greater than 10 cm/s. Directions also are handled somewhat differently in that no formula is derived from the calibration data but rather a simple look-up table is developed for the calibration data from which the compass readings can be converted directly into degrees from true or magnetic north.

1.7.2.1 The vector averaging current meter (VACM)

As discussed by Baker (1981), one of the important data reduction techniques in oceanography was the introduction of the "burst sampling" scheme of Richardson *et al.* (1963) whereby short samples of densely packed data are interspersed with longer periods of no data. In continuous mode, the average current speed and instantaneous direction are recorded once per sampling interval. In burst mode, a rapid series of speed and direction measurements are averaged over a short segment of the sampling interval. In vector-average mode, the instrument uses speed and direction to calculate the horizontal and vertical components of the absolute velocity during the burst. It then separately averages each component internally to provide a single value of velocity vector for each burst. If enough is known about the spectra of the flow variability, the burst samples can be used to adequately estimate the total energy in the various frequency bands. This procedure greatly reduces the amount of recording space needed to sample the currents. The vector-averaging current meter (VACM) introduced in the 1970s uses both burst sampling and internal processing to compute the vector-average components of the current for each sampling period. Current speed is obtained using a Savonious rotor similar to that on the RCMs but direction is from a small vane that is free to rotate relative to the chassis of the current meter. Vectors are computed for every eight revolutions of the rotor and averaged over periods of from 4 to 15 min, depending on the selected sampling interval.

Problems with the Savonious rotor

Because of its widespread use in oceanography, the Savonious rotor sensor needs to be covered in some detail. We begin by noting that a principal shortcoming of the RCM4/5 is its inability to record currents accurately in regions affected by surface wave motions. The problem with the Savonius rotor response is that it is omnidirectional and therefore responds excessively to oscillatory wave action. An intercomparison experiment using a mooring array shown schematically in Figure 1.7.2(a) demonstrated the differences between Savonius rotor measurements and those made with an EM current meter (Woodward *et al.*, 1990). Even under moderate wave conditions, the near-surface moored RCM4 can have its speeds increased by a factor of two through wave pumping (Figure 1.7.2b). The effect of wave pumping on the Savonius rotor

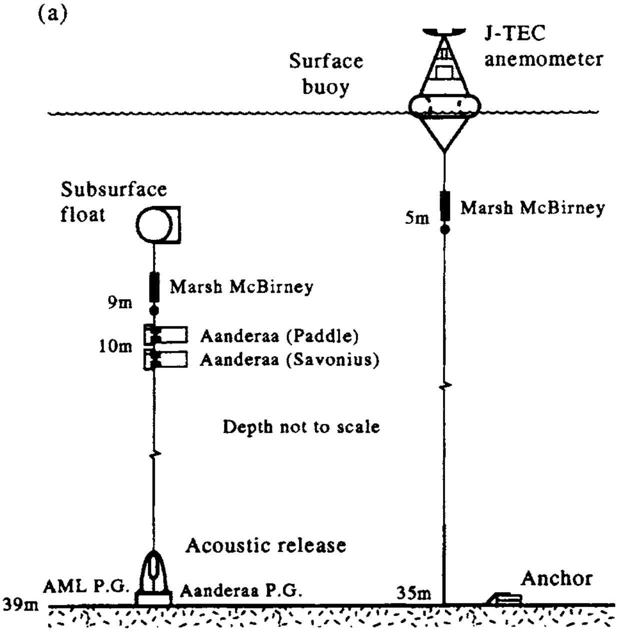

Figure 1.7.2. (a) Mooring arrangement for comparison of current speed and direction from Aanderaa RCM4 (Savonious rotor) and RCM7 (paddle wheel) current meters and Marsh-McBirney (Electromagnetic) current meters moored at 10 m depth during September 1983 in an oceanic wave zone (Hecate Strait, British Columbia).

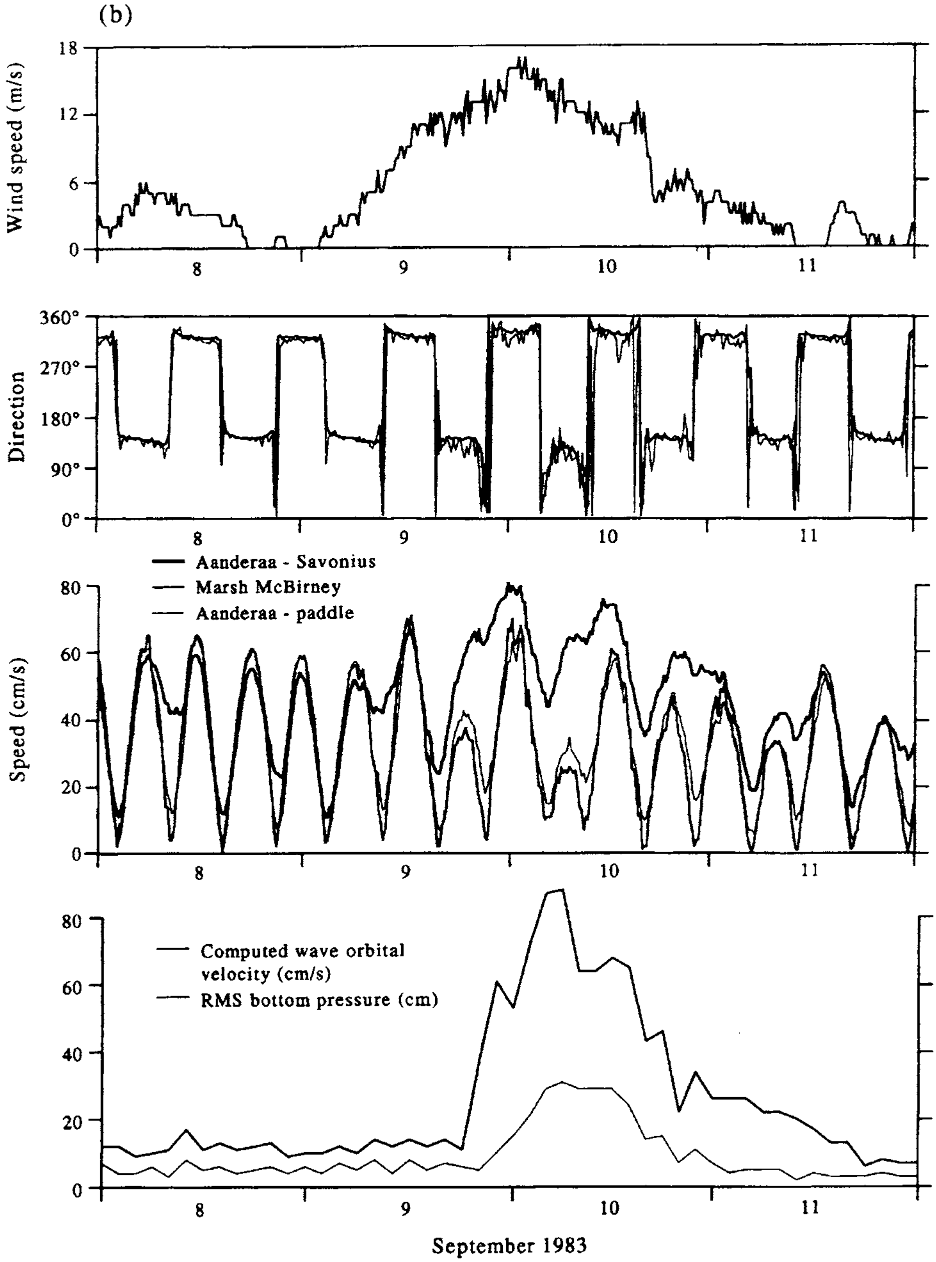

Figure 1.7.2. (b) Mooring configuration, including bottom-mounted Aanderaa and Applied Microsystems pressure gauges. Winds were measured using a J-Tec vortex-shedding anemometer. In moderate wind-wave conditions, a surface or near-surface moored RCM4 with Savonius rotor can have its speeds increased by a factor of 2 through wave pumping. The paddle wheel RCM7 behaves somewhat better.

significantly increases the spectral energy at both low and high frequencies (Figure 1.7.2c). Hence, the instrument is best suited to moorings supported with subsurface floats but is not suitable for mooring beneath surface buoys or in the upper ocean wave regime. Unlike the earlier Aanderaa current meters, VACMs provide accurate measurements when deployed in near-surface wave fields and from surface-following

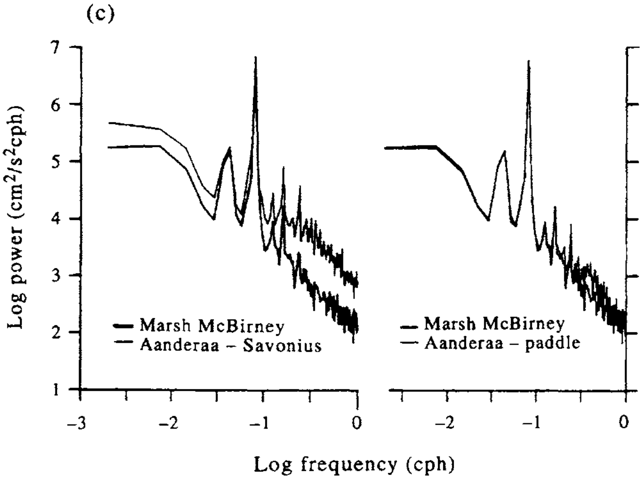

Figure 1.7.2. (c) Power spectra for current measurements in (a). (Adapted from Woodward et al., 1990.)

moorings (Halpern, 1978). In a comparison between Aanderaa and VACM measurements, Saunders (1976) concluded that "the Aanderaa instrument, excellent though it is on subsurface moorings, is not designed, nor should it be used, where wave frequency fluctuations are a significant fraction of the signal." In this, and a later paper, Saunders (1980) pointed out that the contamination of the Aanderaa measurements in near-surface applications is due also to a lag in the response of the direction vane to oscillatory flow.

Since 1991, Aanderaa has gone to a vector-averaging RCM7 current meter with a paddle-wheel rotor (Fig. 1.7.1a) and internal solid state, E-prom modular memory. In earlier versions of the RCM7, the paddle-wheel rotor was partially shielded by a semicircle baffle which was intended to reduce wave induced "pumping". This has now been abandoned since the baffle sheds small-scale eddies which interfere with the response of the paddle-wheel in other operations. Field tests indicate that the vector-averaging RCM7 has only slightly better wave-region performance than the earlier RCMs (Figure 1.7.2c) and the overall improvements are marginal for most applications. During the selected recording interval, the number of rotor revolutions and compass direction are sampled 50 times per recording interval; e.g. every 12 s for a 10-min sampling interval. As with other vector-averaging current meters, the speed and direction are then resolved internally into east–west and north–south components and successive components are added and temporarily stored. When the selected recording interval has elapsed, the resulting average vector and its angle are calculated and stored. A problem with the electronic memory is that data are lost if the instrument floods, as it often does when the instrument is hit by fishnet or tug lines. This was not the case for the 1/4-inch magnetic tapes used in the RCM4. Thomson (1977) reports finding an old RCM that had lain on the bottom of Johnstone Strait for over three years. Although the metal components and circuit boards had turned to mush, the salt-encrusted tape contained a full record of error-free data.

Another problem common to all Savonius rotor current meters is that bearing friction results in fairly high threshold of the rotor and an improper response of the rotor to low current speeds. For the Aanderaa RCM4/5, this threshold level is about

2 cm/s and current measurements taken in quiescent portions of the ocean will have many missing values where the currents were too slow to turn the rotors during the sampling interval. According to manufacturer specifications, the response is linear for current speeds between 2.5 and 250 cm/s so that once the rotor is turning it has acceptable response characteristics. In this range, accuracy is given as ±1 cm/s or 2% of the speed, whichever is greater. Accuracies for the other associated sensors are 1% for pressure, ±0.3°C for temperature and ±0.05 psu for salinity. All of these accuracies are really "relative" values and regular calibration is required to insure reliable measurements. Such a calibration procedure is discussed in detail in Pillsbury *et al.* (1974) for RCM4s. We will only highlight some of the more important aspects of this calibration in order to suggest problem areas where data from Aanderra current meters may be subject to error.

As described by Pillsbury *et al.* (1974), calibration of the RCM4 compass is important because more compass failures occurred for a set of instruments than all other sensor failures combined. Careful calibration will reveal the several different kinds of compass failure. The compass calibration is performed for selected compass bearings by rotating the instrument through 360° on a pivoted stand. This operation is repeated 10 times. A reliable compass is one which repeats its calibration curve within 3°. From calibration work reported by Gould (1973), it is clear that there is a significant departure from linearity in most RCM4 compasses. The magnitude of the nonlinearity errors (approximately 1% of the scalar mean speed per degree of compass nonlinearity) means that many of the residual velocity values observed in the ocean could be introduced by a nonlinearity of 1° or 2° in the direction sensor. If such residual values are to be trusted, care must be taken to "calibrate out" instrument nonlinearities in the data analysis procedure. Such precautions are particularly important if the current meter records are to be used to deduce shears from pairs of instruments or circulation patterns from horizontal current meter arrays.

Turning to the rotor, it was found that for speeds several centimeters per second above the threshold, the calibration of all rotors of a given type can be considered as equal. For calibration, this threshold was found to be roughly 10 cm/s, below which each rotor should be calibrated with its corresponding current meter. For mean speeds greater than 10 cm/s, a general calibration curve can be used for all instruments (Figure 1.7.3). This calibration curve is fitted by a line and used for all calibrations. Deviations from this line varied from 19% at 2 cm/s to less than 1% at 30 cm/s, with a mean value of 4%.

1.7.2.2 Vector measuring current meter (VMCM)

To circumvent the nonlinear response problems of the RCM4, Weller and Davis (1980) developed the vector measuring current meter (VMCM) which uses two orthogonal propeller current sensors with an accurate cosine response. This instrument produces negligible rectification and therefore should accurately measure mean flow in the presence of unsteady oscillating flow. In laboratory tests, the VMCM performed well in the presence of combined mean plus oscillatory flow as compared with poorer performances by Savonius rotor/vane systems and by electromagnetic and acoustic sensors. The open fan-type rotors of the VMCM are highly susceptable to fouling by small filaments of weed and other debris.

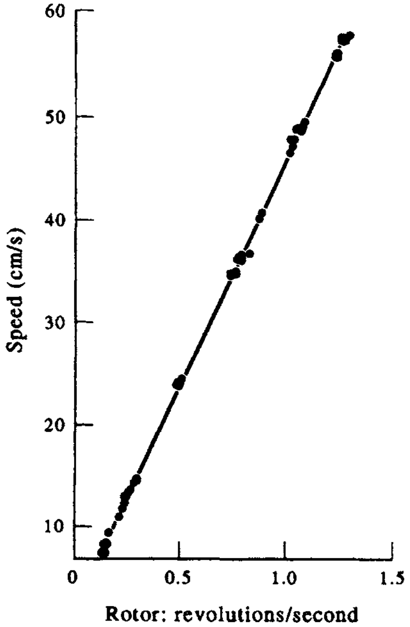

Figure 1.7.3. A general calibration curve of current speed (cm/s) versus rotor counts in revolutions/second for mean speeds greater than 10 cm/s. This particular calibration curve has a linear relation for all calibrations.

1.7.3 Nonmechanical current meters

1.7.3.1 Acoustic current meters (ACM)

Nonmechanical current meters determine current speed and direction by measuring speed along two or three orthogonal sensor axes. Once the flow direction relative to the current meter is determined, absolute direction is found using a built in magnetic compass. Acoustic current meters (ACMs) measure the difference in the time delay of short, high frequency (megahertz) sound pulses transmitted between an acoustic source and receiver separated by a fixed distance, L. In all cases, the transducer and receiver are combined into one source–receiver unit. The greater the speed of the current component in the direction of sound propagation, the shorter the pulse travel time and vice versa. For instance, suppose that the speed of sound in the absence of any current has a value c. The times for sound to travel simultaneously in opposite directions from two combined transducer-receiver pairs in the presence of an along-axis current of speed v is: $t_1 = L/(c + v)$ for transducer–receiver pair No. 1 and $t_2 = L/(c - v)$ for transducer–receiver pair No. 2. The velocity component along the transducer axis is therefore

$$v = L(t_2 - t_1)/(2t_1t_2) \tag{1.7.1}$$

A three-axis current meter determines the three-dimensional velocity by simultaneously measuring time differences along three orthogonal axes.

Examples of commercial acoustic current meters include the SimTronix UCM 40 and the Niel Brown ACM current meters. Because of the rapid (≈1500 m/s) propagation of sound in water, these current meters are capable of high frequency sampling and processing, with typical data rates of 10–20 Hz. The instruments also can provide estimates of the sound velocity along the two paths of length L between the sensors. More specifically, $c = 2L/t$, where $t = t_1t_2/(t_1 + t_2)$ is the effective time of propagation. Manufacturer specifications vary but may be characterized as follows:

- *Speed accuracy*: on the order ±1 cm/s at flow speeds of 10 cm/s.
- *Speed resolution*: approximately ±1 mm/s
- *Threshold speed*: 1 mm/s.
- *Speed range*: 0–5 m/s
- *Compass direction*: accuracy ±2°; resolution 0.1% of the range.
- *Sampling rate*: 20 Hz.
- *Acoustic frequency*: 4 mHz.
- *Allowable tilt*: a true cosine tilt response up to ±20°.
- *Sound speed*: range of 1350–1600 m/s and accuracy of ±5 m/s.

Because of their sophisticated technology, acoustic current meters are often difficult to operate and maintain without dedicated technical support. For example, biofouling of the transducers can be a problem on any long-term mooring in the euphotic (near-surface light influenced) zone. The instruments also must undergo frequent recalibration due to problems with sensor misalignment and changes in the physical dimensions of the transducer-receiver pairs. As discussed by Weller and Davis (1980), this is a particular weakness of the ACM which has proved difficult to calibrate due to drifts in the zero level and in the amplifier gain. In one comparison, they found that the background electrical noise of the ACM had the same level as the signal. As they point out, these problems are with the system electronics and should be solvable. Similar problems were encountered by Kuhn *et al.* (1980) in their intercomparison test but they were quick to point out that their ACM was an early prototype model and many of the problems that they encountered have since been solved by the manufacturer (Gytre, Norway).

1.7.3.2 Electromagnetic current meters (ECM)

Electromagnetic current meters such as the Marsh-McBirney 512 and the Inter-Ocean S4 use the fact that an oceanic current behaves as a moving electrical conductor. As a result, when an ocean current moves through a magnetic field generated within the instrument, an electromotive force is induced which is directly proportional to the speed of the ocean current and at right angles to both the magnetic field and the direction of the current (Faraday's law of electromagnetic induction). In general, the magnetic field may be that of the earth or the one generated by an electric current flowing through appropriately shaped coils (Figure 1.7.4). Faraday tried to measure the flow of the Thames River using electrodes on either side but was unsuccessful because his galvanometers were not sensitive enough. Following the Second World War, the principle was used successfully to estimate the flow along the English Channel by measuring the potential difference between electrodes on either side using a telegraph cable for the distant electrode and the vertical component of the earth's magnetic field.

A two-axis electromagnetic current meter with an internal compass is used to produce horizontal components referenced to earth coordinates. The induced elect-

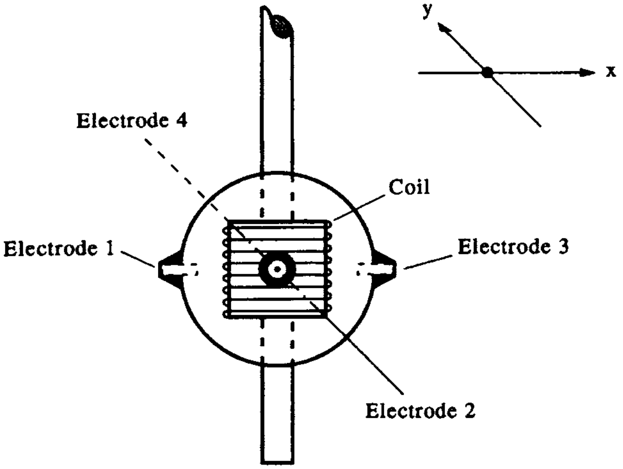

Figure 1.7.4. Principle of the electromagnetic current meter. Instrument measures the electromotive force (EMF) on an electric charge (the oceanic flow) moving through the magnetic field generated by the coil. This produces a voltage potential at right angles to both the magnetic induction field and the direction of flow.

rical current gives the oceanic flow components relative to the instrument axes while the internal compass determines the orientation of the axes relative to the horizontal component of the earth's magnetic field. Electromagnetic current meters such as the S4 measure the electrical potential generated across two pairs of exposed metal (titanium) electrodes located on opposite sides of the equatorial plane on the surface of a plastic sphere (Figure 1.7.5). The electrodes form orthogonal (x,y) axes that detect changes in the induced electrical potential associated with the ocean current. The induced voltage potential (or electromagnetic force, EMF) **E** is found by Faraday's Law through the cross-product

$$\mathbf{E} = \int_0^\infty \mathbf{v} \times \mathbf{B}\, \mathrm{d}L \tag{1.7.2}$$

where **v** is the velocity of the flow past the electrodes, **B** is the strength of the applied magnetic field supplied by a battery-driven coil oriented along the vertical axis of the instrument, and L is the distance from the center of the coil. The magnetic field is directed vertically past the electrodes so that current flow parallel to the x-axis generates a voltage along the y-axis that is directly proportional to the strength of the current. The electric current induced by the voltage potential can be measured directly and converted to components of the flow velocity using laboratory calibration factors. Alternatively, a gain-controlled amplifier can be used to maintain a constant DC voltage at the logical output. The feedback current needed to maintain that electric current is directly proportional to the flow speed. As with the acoustic current meters, manufacturer's specifications vary but may be characterized as follows:

- *Speed accuracy*: roughly ±2% of reading (with a minimum of 1 cm/s).
- *Speed resolution*: about ±1–2 mm/s for a standard velocity range of 0–3.5 m/s (higher accuracies for narrower ranges).

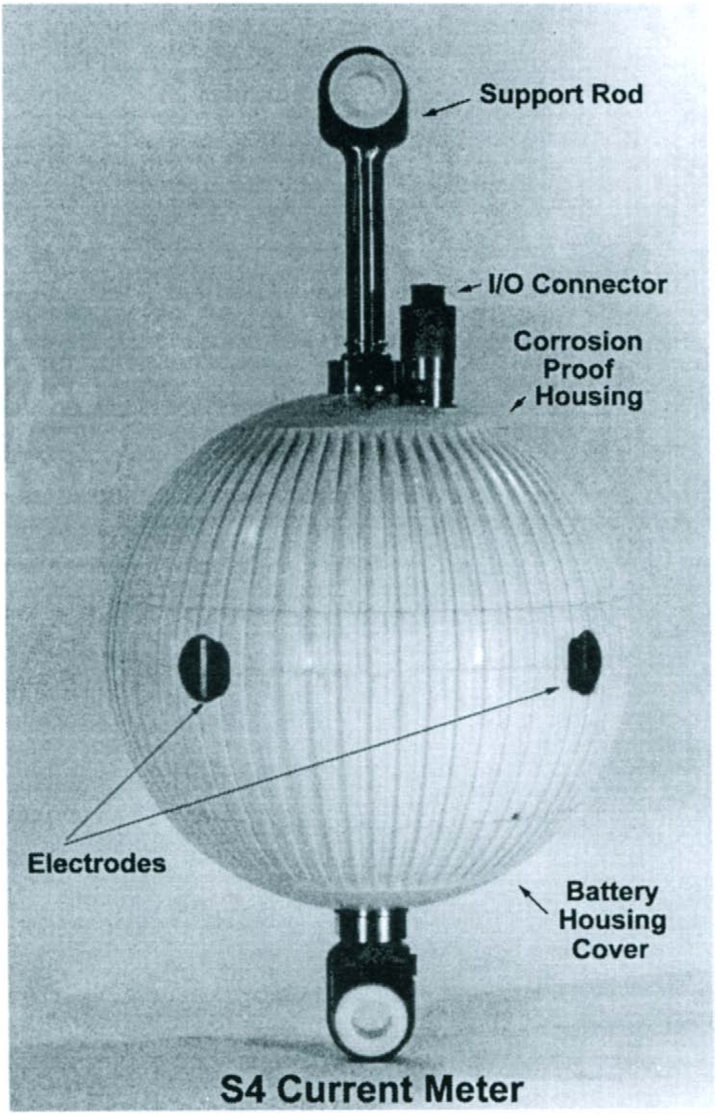

Figure 1.7.5. Inter-Ocean S4 electromagnetic current meter. (a) View of the instrument showing electrodes. (Courtesy, Mark Geneau, Inter-Ocean.)

- *Threshold speed*: 1 mm/s; limited by noise.
- *Speed range*: 0–3.5 m/s, but can expanded to 0–5 m/s or reduced for higher resolution.
- *Compass direction*: accuracy of ±2° and resolution of 0.5°.
- *Allowable tilt*: cosine tilt response to up to ±25°.

Most electromagnetic current meters allow for measurement of temperature, conductivity and pressure. Data can be averaged over regular intervals of a few seconds to tens of minutes, or set to burst sampling with a specified number of samples per burst at a given sampling interval. For example, one can set the number

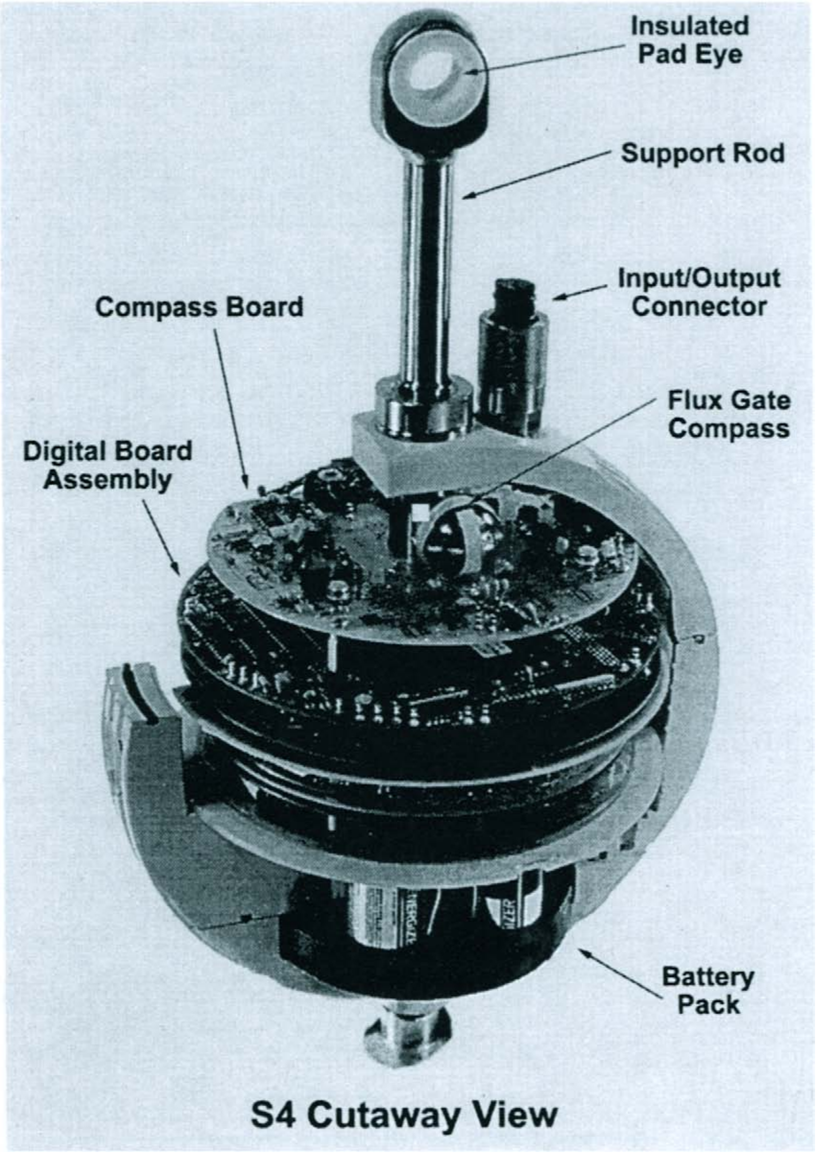

Figure 1.7.5. Inter-Ocean S4 electromagnetic current meter. (b) Cut-away view of the electronics. The spherical hull has a diameter of 25 cm and the instrument weighs 1.5 kg in water. (Courtesy, Mark Geneau, Inter-Ocean.)

of samples per burst (say continuous sampling for 2 min every hour) and set the number of times velocity is sampled compared with conductivity and temperature. The limitations are the storage capacity of the instrument (thousands of kilobytes) and the amount of power consumption. In the case of the S4, the surface of the housing is grooved to maintain a turbulent boundary layer and prevent flow separation at higher speeds.

1.7.4 Profiling acoustic Doppler current meters (ADCM)

Acoustic Doppler current meters (ADCMs) measure current speed and direction by transmitting high frequency sound waves and then determining the Doppler frequency shift of the return signal scattered from assemblages of "drifters" in the water column. In a sense, the instrument "whistles" at a known frequency and listens for changes in the frequency of the echo. The technique relies on the fact that: (1) sound is reflected and/or scattered when it encounters marked changes in density; and (2) the frequency of the reflected sound is increased (decreased) in direct proportion to the rate at which the reflectors are approaching (or receding from) the instrument. Principle (2) is used by astronomers to measure the rate at which stars and galaxies are moving relative to the earth. The commonly observed "red shift" of starlight suggests that most distant objects in the universe are receding from the earth. Reflectors ensonified by ADCMs include "clouds" of planktonic organisms such as euphausiids, copepods and gellies, fish (with and without swim bladders), suspended particles, and discontinuities in water density. Buoyant wastewater plumes from coastal sewage outfalls and hydrothermal plumes from seafloor spreading regions are two common examples of density discontinuities that can be detected acoustically.

Unlike the current meters discussed in the previous sections, which measure current time-series at a fixed depth, ADCMs provide time-series profiles of the flow averaged over a suite of depth bins. The ADCM is like having a stack of current meters. Commercial acoustic Doppler current meters are built by Amatak-Straza, Aanderaa Instruments and RD Instruments. Of the instruments available, the recently-commercialized Aanderaa Doppler current meter (DCM 12) and the better-known RD Instruments acoustic Doppler current profiler (ADCP) are specifically designed for oceanographic research. The ADCP, in particular, has been the focus of numerous comparisons and analyses (e.g. Pettigrew and Irish, 1983; Pettigrew *et al.*, 1986; Flagg and Smith, 1989; Schott and Leaman, 1991). RD Instruments makes a self-contained (SC) internally-recording unit (Figure 1.7.6), a direct reading (DR) unit, and a vessel-mounted (VM) unit. The standard instruments are available at frequencies of 75, 150, 300, 600, and 1200 kHz; the more newly developed Broadband^{TM} ADCP also includes a 2400 kHz unit. The choice of frequency is dependent on the particular application. Because the ADCP is geared to oceanographic applications, we will consider this instrument in some detail. The standard ADCP measures current by first estimating the relative frequency change, Δf, of backscattered echos from a single transmit pulse (Gordon, 1996). The newer Broadband ADCP measures the current by determining the phase shifts ("time dilation") $\Delta\phi$ of backscattered echos from a series of multiple transmitted pulses. The Aanderaa DCM, which was in development at the time this book was being written, operates at 607 kHz, has fewer vertical bins than the ADCP and considerably greater speed uncertainty (>3 cm s^{-1}). A report on an intercomparison between a 614 kHz Broadband ADCP and two 607 kHz DCMs moored in 11.5 m of water in Øresund, Denmark has been prepared by the Danish Hydraulic Institute (Rørbaek, 1994).

Aside from some custom-built units, the standard narrow-band ADCPs employ four separate transducers oriented in a Janus configuration with beams pointing at an angle of 30° to the plane of the transducers (Janus was the Roman god who looked both forward and backward at the same time). In the newer broadband unit, the angle has been reduced to 20°. We assume that the small drifters reflecting the transmitted sound pulse are being carried passively by the current and that their drift velocity has

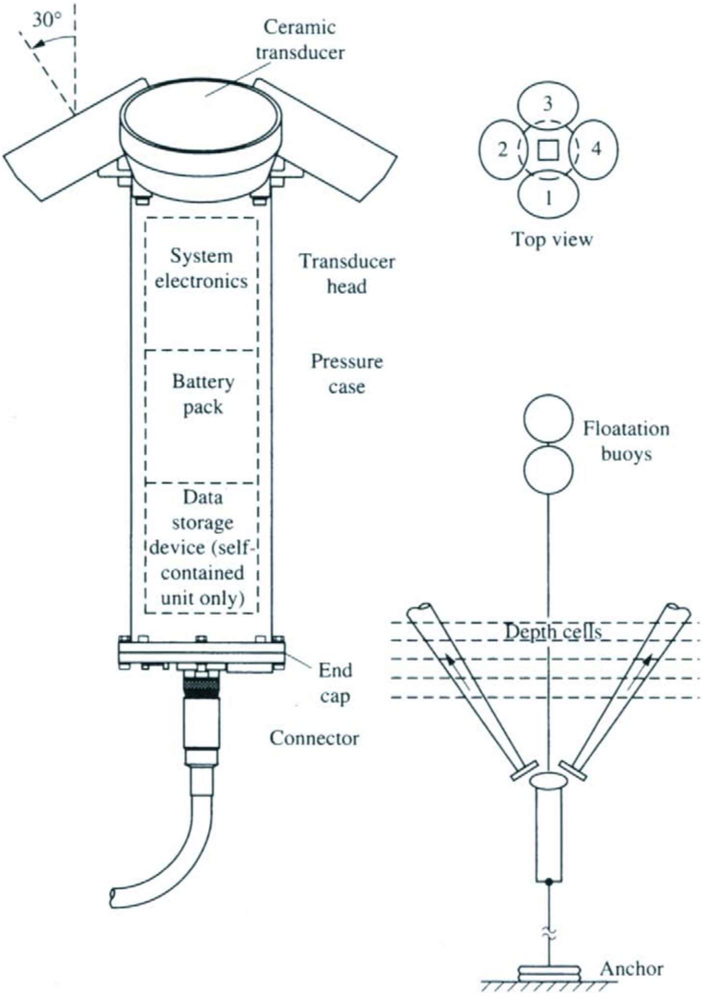

Figure 1.7.6. A direct reading 150 kHz acoustic Doppler current meter with external RS-232 link manufactured by RD Instruments. Side view shows three of the four ceramic transducers. Each transducer is oriented at 30° to the axis of the instrument. The pressure case holds the system electronics and echo sounder power boards.

a near-uniform distribution over the horizontal area ensonified by the ADCP. For a narrow-band ADCP with a transmit pulse having a fixed length of a few milliseconds, the frequency shift, Δf, of the backscattered signal is proportional to the component of relative velocity, $v \cos \theta$, along the axis of the acoustic beam between the backscatterers and the transducer head (Figure 1.7.7a). For a given source frequency, f, and bin k (depth range = D_k) we find

$$v_k = \frac{\frac{1}{2}(\Delta f_k / f)c}{\cos \theta_k} \tag{1.7.3}$$

where v_k is the relative current velocity for *bin* k at depth D_k, θ_k is the angle between the relative velocity vector and the line between the scatters and the ADCP beam, c is

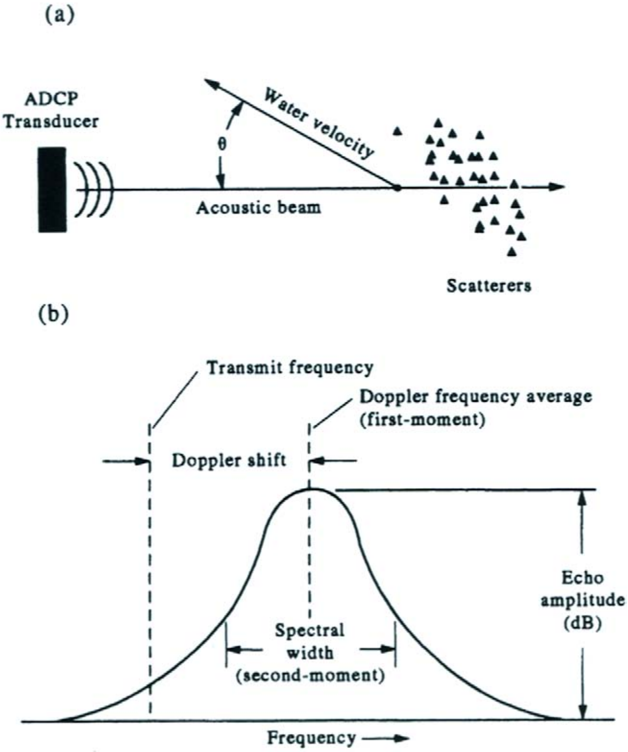

Figure 1.7.7. Principles of ADCP measurement. (a) Relative velocity, $v \cdot \cos\theta$, along the axis of the acoustic beam between the backscatterers and the transducer head; (b) auto-spectrum of returned acoustic signal showing the Doppler frequency shift for a given bin. (RD Instruments, 1989.)

the speed of sound at the transducer and Δf is the frequency shift measured by the instrument. The ADCP first determines current velocity relative to the instrument by combining the observed values of frequency change along the axes of each of the acoustic beams (the instrument can only "see" along the axis of a given transducer, not across it). Absolute velocity components in east-west and north–south coordinates, called "earth" coordinates, are obtained using measurements from an internal magnetic compass.

The relative frequency shift, $\Delta f_k/f$ for bin D_k is derived from the observed frequency of the returning echo (Figure 1.7.7b). To calculate the Doppler frequency shift, the ADCP first estimates the autocovariance function, $C(\tau)$, of the echo using an internal hardware processing module. The slope of $C(\tau)$ as a function of time lag, τ, is then related to the frequency change due to the movement of the scatterer during the time that it was ensonified by the transmit pulse. Because of inherent noise in the instrumentation and the environment, as well as distortion of the backscattered signal due to differences in acoustic responses of the possible targets, the returned signal will have a finite spectral shape centered about the mean Doppler shifted frequency (Figure 1.7.7b). The spectral width SW of this signal has the form SW $= 500/D$, where D is the bin thickness in meters, and is a direct measure of the uncertainty of the velocity estimate due to the finite pulse length, turbulence and nonuniformity in scattering velocity. In the case of the standard RD Instruments ADCP, depth cell lengths, D, can range from 1 to 32 m but are usually set at 4–8 m. For the Broadband ADCP, depth cell size ranges from 0.12 m for the higher frequencies to 32 m for the lower frequencies. Each acoustic beam of the ADCP has a width of 2–4° (at the −3 dB or half-power point of the transducer beam pattern) so that the "footprint" over which the acoustic averaging is performed is fairly small. At a distance of 300 m, the footprint has a radius of 5–10 m. However, the horizontal separation between beams is roughly equal to the distance to the depth-cell so that the assumption of horizontal uniformity of the current velocity is not always valid, especially for those cells furthest from the transducers.

Sidelobes of the transducer acoustic pattern can limit the reliability of the data. For the standard 30° ADCP, measurements taken over the last 15% $[\approx (1 - \cos 30°)]$ of the full-scale depth range are not valid if the ocean surface (or seafloor) are within the range of an upward (or downward) looking instrument. In general, the range $R_{\max}$ of acceptable data for a vertically-oriented ADCP within proximity to a "hard" reflecting surface such as the sea surface or sea floor is given by $R_{\max} \approx H\cos\varphi$, where H is the distance from the ADCP to the reflecting surface and φ is the angle the transducers make with the instrument axis (for a 20° instrument, only 6% of the range is lost near the sea surface or seafloor). For vessel-mounted systems working in areas of rough or rapidly sloping bottom topography, a more practical estimate is $R_{\max} \approx H(\cos\varphi - \alpha)$, where $\alpha \approx 0.05$ is a correction factor that accounts for differences in water depth during short (<10 min) ensemble averaging periods.

The higher the frequency, the shorter the distance an acoustic sounder can penetrate the water, but the greater the instruments ability to resolve velocity structure (Table 1.7.1). The 75 and 150 kHz units are mainly used for surveys over depth ranges of 0–500 m while higher frequencies such as the 600 and 1200 kHz units are favored for examining flow velocity in shallow water of 25–50 m depth. As noted above, ADCPs employ four separate transducers each pointing at an angle of 20° or 30° to the plane of the transducers. Since only the current speeds along each of the beam axes can be estimated, trigonometric functions must be applied to the velocities to transform them into horizontal and vertical velocity components. The instrument provides one estimate of the horizontal velocity and two independent estimates of the

Table 1.7.1. RD Instruments acoustic wavelengths (λ) and depth ranges (m) for different transducer frequencies for the low power and high power settings (low power is for self-contained units while high power is for either self-contained or externally powered units). Standard deviation for velocity of given frequency are for ensemble averages of N pings per ensemble, a depth cell size (bin length and length of transmit pulse) of 8 m and 30° beam angle orientation. For 20° angle multiply values by 1.5; for other depth cell sizes D (m) multiply values by 8/D. The values e_1 and e_2 are different published estimates of

vertical velocity. The ADCP senses the Doppler frequency shift in each 1-s acoustic "ping" by looking at the time-delayed gated signal returning from distinct "bins" (depth or distance ranges) from the transducer along each of the four-beam axes. The resultant speed estimates are then converted within the instrument to common bin positions centered at $p2^N$ meters ($N = 1, 2, ..., 8$ to a maximum of 128 bins) along the central axes normal to the plane of the transducers. Since the different time delays t_k of each pulse correspond to different distances D_k from the transducers, the instrument provides estimates of the horizontal (u, v) and vertical (w) components of velocity averaged over adjoining depth ranges (or depth bins). As illustrated by Figure 1.7.8, the averaging consists of a linear weighting over twice the bin length, $D = z_{k+1} - z_k = c(t_{k+1} - t_k)$, where c is the sound speed. For the 4-m bin length selected in Figure 1.7.8, the triangular weighted average is over 8 m. The depth range of a particular bin covers the distance:

from: blank depth + (bin number) × (bin length) − (bin length)/2

to: blank depth + (bin number) × (bin length) + (bin length)/2

A 4-m blanking is applied to the beginning of the beam to eliminate nonlinear effects near the transducer. The minimum length of the blank is frequency dependent but a larger value can be selected by the user. For the particular setup shown, there are 15 1-s pings for each 20-s ensemble; bottom-tracking is turned on every four pings. This option, together with machine processing "overhead" and time for transmission up the tow cable, uses up a segment of the total time available for each ensemble averaging period.

The maximum range of the standard (single transmit pulse) ADCP depends on the depth at which the strength of the return signal drops to the noise level. Depending on the rate of energy loss and heat dissipation, the instrument is generally capable of measuring current velocity to a range $R(\mathrm{m}) = 250(300/f)$, where f is the frequency in kilohertz. The velocities (and backscatter intensity which we discuss later in the section) from a series of pings are averaged to form an "ensemble" record. This saves on storage space in memory, reduces the amount of processing and improves the error estimate for the velocity record. Each acoustic ping lasts about 1–10 ms and 10 or more separate pings, together with an equal number of compass readings, are typically used to calculate an ensemble-averaged velocity estimate for each recorded increment of time in the time-series. The random error of the horizontal velocity for each ensemble is given as

$$\sigma(\mathrm{m/s}) = (1.6 \times 10^2)/(fDN^{1/2})$$

where N is the number of individual 1-s pings per ensemble and D is the bin length ($=2^m$, $m = 1, 2, ...$) in meters. For example, a 30-s ensemble averaging period chosen during the instrument set-up procedure, generally allows for about 20 pings plus 10 s of processing time. This overhead time is inherent to the system and must be taken into account when determining the error estimates. As indicated in Table 1.7.2, the standard deviation of the vertical and horizontal velocity estimates for this case is about 3 cm/s for $D = 8$ m and a 150 kHz transducer. The greater the number of pings used in a given ensemble, the greater the accuracy of the velocity estimate, with $\sigma \approx N^{-1/2}$. Tilt sensors are used to calculate changes in the orientation of the transducer axis and to ensure that data are binned into correct depth ranges. These sensors

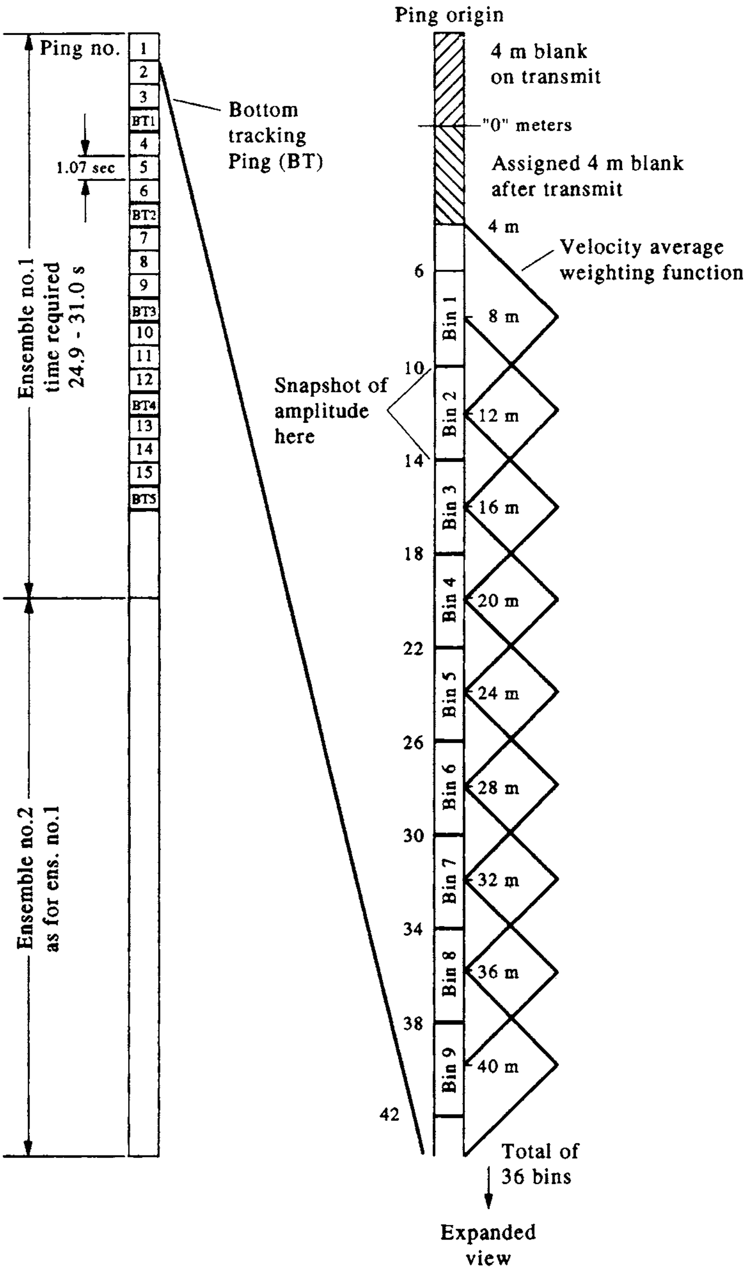

Figure 1.7.8. Allocation of depth bins and machine overhead for a narrow band (standard) 150 kH ADCP having a bin length of 4 m, a blanking range of 4 m and a depth range of 36 bins. The instrumen obtained 15 1-s pings for each 20-s ensemble and used the remaining time for internal processing and dat transmission up an electrical cable. The information on the right is an expansion of the bin allocation fo the first ping. A triangular weighting is used to determine the velocity for each bin. Similar results appl to the remaining pings for each of ensemble. A 4-m blanking is applied to the beginning of the beam t eliminate nonlinear effects near the transducer. (Courtesy, George Chase.)

Table 1.7.2. Comparison of hourly time-series of longshore currents over 90 day period from 308 kHz ADCP and conventional current meters off northern California (adapted from Pettigrew and Irish, 1986). Results are found using the two-beam solution for the ADCP

Depth (m)	Moored current meter	Correlation coefficient, r	Speed difference (cm/s) Mean	RMS
10	VACM	0.94	−3.7	8.1
20	VMCM	0.97	0.8	4.6
35	VMCM	0.98	0.2	2.7
55	VMCM	0.98	0.0	2.4
70	VMCM	0.98	0.3	2.2
90	VMCM	0.98	1.0	2.2
110	VMCM	0.98	0.5	1.9
120	VACM	0.97	−0.1	2.0

are limited to ±20° so that for greater tilts, the velocity components can not be determined accurately. Only three of the beams are needed for each three-dimensional velocity calculation. The built-in redundancy provides for an "error velocity" estimate for each ensemble velocity which involves subtracting the two independent estimates of the vertical velocity component for each ping. When the two vertical velocity estimates agree closely, the horizontal velocity components are most likely correct. In addition to the reliability check, the fourth beam serves as a backup should one of the transducers fails. Another measure provided by the ADCP is the "percent good" which is the percentage of pings that exceed the signal-to-noise threshold. Normally, the percent good rapidly falls below 50% at some depth and stays below that level. In practical terms, there usually is little difference in the data for assigned values of 25, 50, or 75 percent-good.

Since Doppler current meters were originally designed for measuring currents from a moving platform, the ADCP records instrument heading, pitch, roll and yaw. These data are then used to correct the measured velocities. In order to determine the true current velocity in "earth coordinates" from a moving vessel, the ADCP is capable of measuring the velocity of the instrument over the seafloor, providing the bottom is within range of the transducer and the bottom reflection exceeds the background noise level. A separate bin is used for this bottom-tracking. The bottom tracking mode is usually turned on for a fraction of the total sampling time, uses a longer pulse length and provides a more accurate estimate of relative velocity than other bins. Unfortunately, modern shipboard GPS systems in the standard (nondifferential) mode are only accurate to about ±100 m. This means that estimates of the ship speed taken at time increments of seconds to minutes will have errors of the order of 10–100 cm s^{-1} which usually are comparable to the kinds of current speeds we are trying to measure. Differential GPS, which relies on error corrections transmitted from a land-based reference station for which satellite positioning and timing errors have been calculated, is accurate to better than 10 m. Shipboard systems working in this mode can be used to determine absolute currents by subtracting the accurately determined ship's velocity over-the-ground from relative currents measured by the ADCP (see note at the end of this section).

There are several factors that limit the accuracy of the ADCP: (1) The accuracy of the frequency shift measurement used to obtain the relative velocity. This estimate is conducted by software within the instrument and strongly depends on the signal/noise ratio and the velocity distribution among the scatters; (2) the size of the foot-print and the homogeneity of the flow field. At a distance of 300 m from the transducer, the spatial separation between sampling volumes for opposite beams is 300 m so that they are seeing different parts of the water column, which may have different velocities; (3) The actual passiveness of the drifters (i.e. how representative are they of the *in situ* current?). In the shipboard system, the ADCP can track the bottom and obtain absolute velocity, provided the acoustic beam ranges to the bottom. Once out of range of the bottom, only the velocity relative to the ship or some level-of-no-motion can be measured. As noted above, standard GPS positioning without the highly accurate (±10 m) differential mode cannot be used to obtain ship velocity since the accuracy of the standard mode (±100 m) yields ship speed accuracies that are, at best, comparable to the current we are trying to measure. Erroneous velocity and backscatter data are commonly obtained from shipboard ADCP measurements due to vessel motions in moderate to heavy seas. In addition to exposure of the transducer head, the acoustic signal is strongly attenuated by air bubbles under the ship's hull or through the upper portion of the water column. Much better data are collected from a ship "running" with the seas than one lying in the trough or hove-to in heavy seas. Our experience is that data collected in moderate to heavy seas is often unreliable and needs to be carefully scrutinized. In deep water, zooplankton aggregations can lead to the formation of "false bottoms" in which the instrument mistakes the high reflectivity from the scattering layer as the seafloor.

The only way to improve velocity measurement accuracy with the standard single-pulse narrow-band ADCP is to lengthen the transmit pulse. A longer transmit pulse extends the length of the autocorrelation function and increases the number of lag values that can be used in the calculation of velocity. Since bin length is proportional to pulse length, this results in improved uncertainty in the velocity estimates. The tradeoff is reduced depth resolution. By transmitting a series of short pulses, the newer Broadband$^{\mathrm{TM}}$ ADCP circumvents these problems. Because of the multiple transmit pulses, the Broadband ADCP is capable of much better velocity resolution and higher vertical resolution. The time between pulses sets the correlation lags available for velocity computation while pulse length governs the size of the depth cells, as in the standard unit. Moreover, velocity is determined from differences in the arrival times of successive pulses. By increasing the effective bandwidth of the received signal by two orders of magnitude, the Broadband ADCP can reduce the variance of the velocity measurement by as much as two orders of magnitude. Figure 1.7.9 is an example of alongshore currents obtained using a shipboard Broadband ADCP during a cross-shelf transect of the inner continental shelf east of Sydney, Australia. The new ADCP system offers "real-time" computer screen display for at-sea operations. The standard narrow-band ADCP uses a data acquisition system, that is no longer supported by RD Instruments, to display output of velocity components, beam-averaged backscatter intensity, percent good, and other ship related parameters such as heading and pitch and roll.

A further note on GPS measurements. There are currently a variety of chart datums that are used in the setup menu of a GPS and one must be sure to select that datum which matches the chart being used for navigation. The general default datum is WGS-84 (World Geodetic Survey 1984) which applies to any region of the world. A commonly used datum in the eastern North Pacific and western North Atlantic is NAD-27 (North American Datum 1927) which has recently been replaced by NAD-83

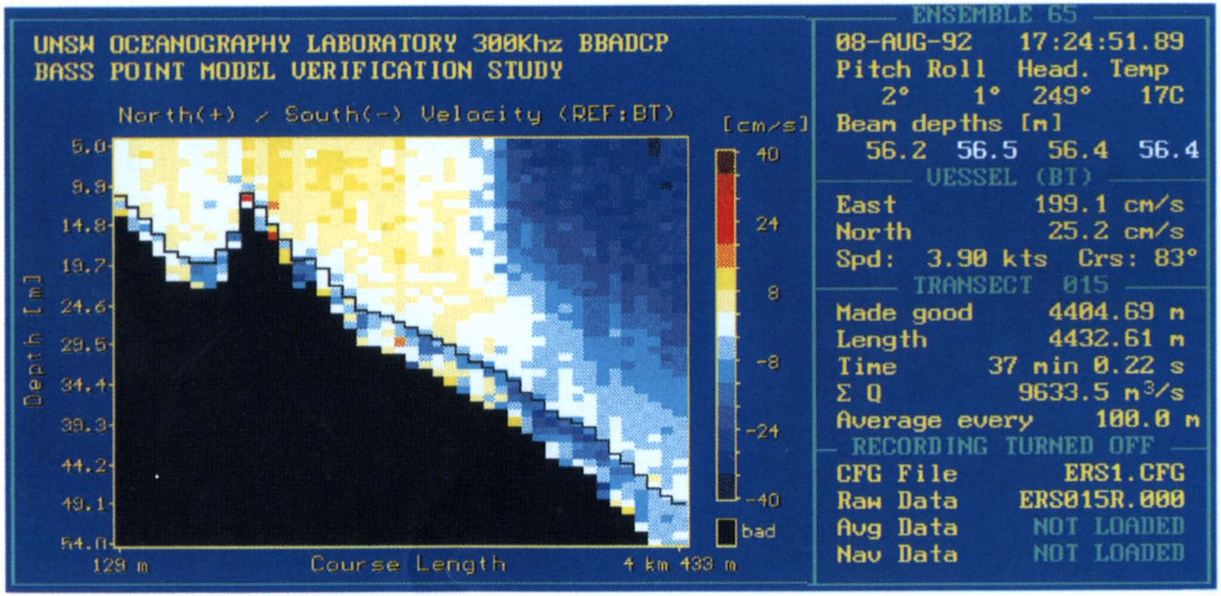

```
      ENSEMBLE 65
08-AUG-92      17:24:51.89
Pitch Roll  Head.  Temp
   2°    1°   249°   17C
Beam depths [m]
  56.2  56.5  56.4  56.4
      VESSEL (BT)
East            199.1 cm/s
North            25.2 cm/s
Spd:  3.90 kts  Crs: 83°
      TRANSECT 015
Made good      4404.69 m
Length         4432.61 m
Time        37 min 0.22 s
Σ Q           9633.5 m³/s
Average every    100.0 m
  RECORDING TURNED OFF
CFG File        ERS1.CFG
Raw Data     ERS015R.000
Avg Data      NOT LOADED
Nav Data      NOT LOADED
```

Figure 1.7.9. Alongshore currents measured by a Broadband RD Instruments Vessel-Mounted 300 kHz system along an eastward transect to the south of the Bass Point headland near Sydney, Australia (see Middleton et al., 1993). (a) Cross-section of the flow for all depth bins, with red corresponding to northward flow and blue to southward flow. (Courtesy, Jason Middleton and Greg Nippard.)

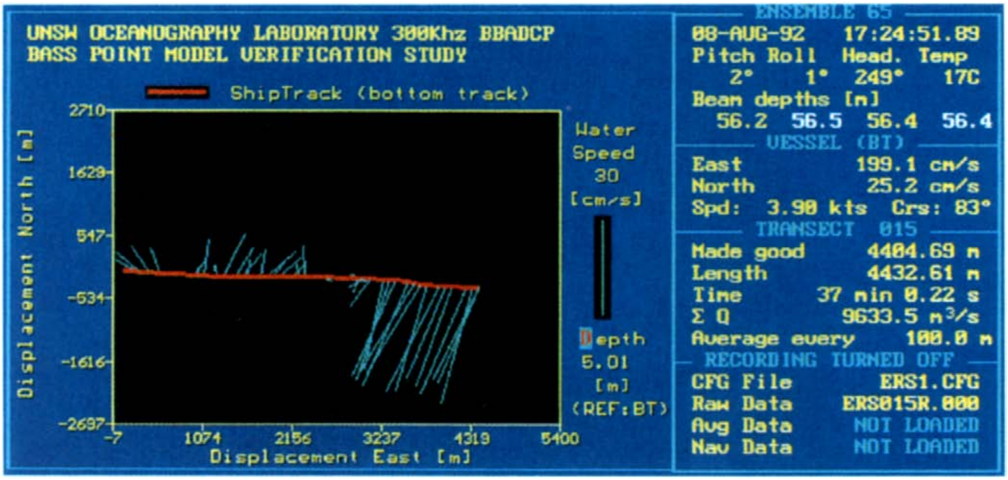

```
              ENSEMBLE 65
08-AUG-92       17:24:51.89
Pitch Roll   Head.  Temp
   2°     1°   249°    17C
Beam depths [m]
   56.2  56.5  56.4  56.4
             VESSEL (BT)
East              199.1 cm/s
North              25.2 cm/s
Spd:  3.90 kts  Crs: 83°
            TRANSECT 015
Made good         4404.69 m
Length            4432.61 m
Time          37 min 0.22 s
Σ Q             9633.5 m³/s
Average every      100.0 m
        RECORDING TURNED OFF
CFG File          ERS1.CFG
Raw Data       ERS015R.000
Avg Data        NOT LOADED
Nav Data        NOT LOADED
```

Figure 1.7.9. Alongshore currents measured by a Broadband RD Instruments Vessel-Mounted 300 kHz system along an eastward transect to the south of the Bass Point headland near Sydney, Australia (see Middleton et al., 1993). (b) Ensemble-average velocity at 5 m depth for the cross-section in (a). Flow was northward in the wake of the headland and southward seaward of the point. (Courtesy, Jason Middleton and Greg Nippard.)

(North American Datum 1983). Other datums are WGS-72, Australian, Tokyo, European and Alaska/Canada. *Selective Availability* is the name given by the United States Department of Defense for degradation of the GPS satellite constellation accuracy for civilian use. When disabled (as it was during the Gulf War with Iraq), GPS accuracy increases by about a factor of 10.

1.7.4.1 Acoustic backscatter

Although it was originally designed to measure currents, the ADCP has become a highly useful tool for investigating the distribution and abundance of zooplankton in the ocean. In particular, the intensity of backscattered sound waves for each depth bin—actually a "snapshot" of the intensity at a distance of two-thirds the way along the bin (Figure 1.7.8)—can be used to estimate the integrated mass of the backscatters over the "footprint" volume (width and thickness) of the original acoustic beams (Flagg and Smith, 1989). As with velocity, the instrument compensates for apparent changes in bin depth due to instrument tilt and roll. Calculation of the backscatter anomaly caused by plankton or other elements in the water column requires an understanding of the various factors causing dispersion and attenuation of the sound waves in water. Proper calibration of the acoustic signal as a function of acoustic range is essential for correct interpretation of the ADCP backscatter data. The measured backscatter intensity (also energy or amplitude squared) I_r is given by

$$I_r/I_a = b\exp(-2e_i z)/z^2 + A_n \tag{1.7.5}$$

where $b = I_o/I_a$ is the transducer gain, I_o is the intensity of the ADCP transducer output, I_a is a reference intensity, e_i is the absorption coefficient for water (cf. Table 1.7.1; $i = 1, 2$), $1/z^2$ is the effect of geometric beam spreading over the range z, and A_n is the relative noise level. The factor b arises because the ADCP does not record output intensity from the transducers, only relative intensity. The target strength TS of the ADCP is then given by the logarithm of (1.7.5) as

$$TS = 10\log(I_r/I_o) - 10\log(b) \tag{1.7.6}$$

where the first term is the absolute target strength of the ADCP and the second term is an unknown additive constant. Since the later term is unknown, a relative measure of the target strength TS_c to some standard calibration region can be determined as $TS' = TS - TS_c$ (Thomson *et al.*, 1991, 1992; Burd and Thomson, 1994). Thomson *et al.* (1992) use a vertically towed vehicle and are therefore able to calibrate their data relative to the near-uniform backscatter layer at intermediate depths (1000–1500 m) in the northeast Pacific.

The ADCP does not measure directly the input or output of the acoustic backscatter intensity but rather the voltage from the so-called Automatic Gain Control (AGC) which is an internal adjustment, positive feedback circuit in the output device which attempts to keep the transducer output power constant. The average compensation voltage in the AGC is recorded and can be used to estimate the relative backscatter intensity. By incorporating a user exit program, the ensemble average AGC for each of the four beams for each bin can also be recorded. As we will discuss later, this is proportional to the biomass (density × cross-section) of the scatterers. The instrument also measures temperature—which it needs to calculate response correctly—and percent-good, which is a measure of the number of reasonable pings per ensemble.

The speed of sound in water varies with temperature, salinity and depth but is generally around 1500 m/s. Therefore, sound oscillations of 153 kHz (a common frequency used on shipboard systems and moored systems) have a wavelength of about 1 cm. Using the standard rule of thumb that the acoustic wave detects objects of about one-quarter wavelength, objects greater than 2.5 mm will reflect sound while objects less than this scatter the sound. The proportion of the sound beam transmitted, reflected or scattered by the object is influenced by small contrasts in compressibility and density between the water and the features of the object. Organisms with a bony skeleton, scaly integument and air bladder reflect/scatter more sound than an organism made up mostly of protoplasm such as salps and jellyfish (Flagg and Smith, 1989). Similarly, organisms which are aggregated into patches or layers return more scattered sound energy per unit volume (i.e. have a greater effective scattering volume) than uniform distributions of the same organisms.

A major problem with using the ADCP for plankton studies is common to all bioacoustical measurements; namely, determining the species composition and size distribution of the animals contributing to the acoustic backscatter. Invariably, *in situ* sampling using net tows is needed to calibrate the acoustic signal. If the ADCP is incorporated in the net system, the package has the advantage that the volume flow through each net can be determined accurately using the ADCP-measured velocity

(Burd and Thomson, 1993). An attempt to calibrate the ADCP against net samples was conducted by Flagg and Smith (1989) who also pointed out problems with the response of the shipboard system to temperature fluctuations in the ADCP electronics.

1.7.5 Comparisons of current meters

As noted earlier, a major problem with the Savonius rotor is contamination of speed measurements by mooring motions (Gould and Sambuco, 1975). The contamination of the rotor speed is caused primarily by vertical motion or "rotor pumping" as the mooring moves up and down under wave action. In effect, the speed overestimates of the rotor result from its ability to accelerate about three times faster than it decelerates. Pettigrew *et al.* (1986) summarize studies on the ability of VMCMs and VACMs in laboratory tests to accurately measure horizontal flow in the presence of surface waves. For wave orbital velocities, W, of the same magnitude as the steady towing speed, U, of the current meter through the water (i.e. $W/U \approx 1$), the accuracy of the VACM depends on the ratio W/U. The percentage error increases as the ratio W/U increases and substantial over-estimation of the true speed occurs for $W/U > 0.5$. The results for the VMCM differ significantly from those of the VACM. In particular, the VMCM underestimates the true velocity by as much as 30% for $W/U \approx 1$, while for $W/U > 2$, speed errors do not appear to be strongly dependent on either W/U or on the relative orientation of the mean and wave current motions. For $W/U < 1/3$, the VMCM was within 2% of the actual speed. While vector averaging can reduce the effect of vertical motion on the recorded currents by smoothing out the short-term oscillatory flow, the basic sensor response is not well tuned to conditions in the wave zone or those for surface moorings. Intercomparisons of conventional current meters (Quadfasel and Schott, 1979; Halpern *et al.*, 1981; Beardsley *et al.*, 1981) have shown that VACM speeds are only slightly higher on surface moorings than on subsurface moorings and that contamination by mooring motion was only important for higher frequencies (>1 cph). At frequencies above 3-4 cph ocean current spectra computed from VACM current meters did not flatten (i.e. not decrease with frequency) as much as spectra from other rotor equipped current meters. Near the surface this is due to horizontal motion of the mooring (Zenk *et al.*, 1980) which is rectified by the Savonius rotor while at greater depths the surface float motion translates into vertical motion which aliases the rotor speed due to rotor pumping. Further details can be found in Weller and Davis (1980), Mero *et al.* (1983), and Beardsely (1987).

Another problem with the Savonius rotor is that it does not have a cosine response to variations in the angle of attack of the flow due to interference of the support posts. In a study of rotor contamination, Pearson *et al.* (1981) conclude that Savonius rotor measurements, made from a mooring with a float 18 m below the sea surface, were not seriously contaminated by surface wave-induced mooring motion. In sharp contrast, Woodward *et al.* (1984) compared a standard Savonius rotor with a paddle-wheel (PW) rotor designed for wave-field applications, and an electromagnetic (EM) current meter. The EM speed sensors appeared to perform well in the near-surface wave field while the standard Savonius rotor was severely contaminated by wave induced currents (Figure 1.7.2).

Field comparisons (Halpern *et al.*, 1981) demonstrated that above the thermocline (5–27 m depth) the VMCM, the VACM and acoustic current meters (ACMs) all produced similar results for frequencies below 0.3 cph, regardless of mooring type. Above 4 cph, it was recommended that the VACM be used with a spar buoy surface float while both the VMCM and the ACM could be used with surface following floats such as a donut buoy. In general, better quality measurements were made at depths from subsurface moorings than from surface moorings, indicating that even the VMCM data were contaminated somewhat by mooring motion.

The processing of current meter data is specific to the type of meter being used. It is interesting to read in current meter comparisons such as Beardsley *et al.* (1981) or Kuhn *et al.* (1980) the variety of processing procedures required to produce compatible data for the intercomparison of observations from different current meters. An important part of the data processing is the application of the instrument specific calibration values to render measurements in terms of engineering units. In this regard, it is also important to have both a pre- and post-experiment calibration of the instrument to detect any serious changes in the equipment that might have occurred during the measurement period.

One of the earliest comparisons between a bottom-mounted ADCP and conventional mechanical current meters was conducted in 133 m of water near the shelf-break off northern California in 1982 (Pettigrew and Irish, 1983; Pettigrew *et al.*, 1986). The 90-day time-series of horizontal currents from a prototype upward-looking 308 kHz ADCP with 4 m bin length was compared with currents from a nearby ($\approx$300 m) string of VACMs and VMCMs. Despite the fact that only two of the beams could be used and the instrument had a 10° list, results show striking agreement between the two sets of data (Table 1.7.2). Mean differences between corresponding acoustic and mechanical current meters were typically less than 0.5 cm/s while RMS differences were about 2 cm/s. Since acoustic currents were based on two beams tilted at 20° to the vertical, the relatively poor correlation at 10 m depth probably resulted from rotor-pumping and over-speeding of the VACM rather than side-lobe contamination of the ADCP which would occur in the upper 6% of the depth range. Similar results were obtained by Schott (1986).

1.7.6 Electromagnetic methods

The dynamo interaction of moving, conducting seawater with the earth's stationary magnetic field induces electric currents in the ocean. These "motional" electric fields, whose existence in the ocean was first postulated by Faraday in 1832, produce a spatially-smoothed measure of the water velocity at subinertial periods [periods longer than $1/f = 11.964$ h/sin(latitude)]. For a given point on the seafloor, the electric fields are proportional to the vertically-averaged, seawater-conductivity weighted water velocity averaged over a horizontal radius of a few water depths (Chave and Luther, 1990). Technologies that measure the horizontal electric field (HEF) yield direct observations of the barotropic transport in the overlying water column. Electric field measurements of transport are obtained from abandoned submarine communication cables or from self-contained bottom recorders. For a submarine cable, the motional HEF is integrated along the cable length.

According to theory (Sanford, 1971; Chave and Luther, 1990; Chave *et al.*, 1992), the horizontal velocity vector field $\mathbf{v}^*$ is related to the horizontal electric field $\mathbf{E}_h$, by

$$\mathbf{E}_h = F_z \mathbf{k} \times \mathbf{v}^* \qquad (1.7.7a)$$

(sensor in a reference frame fixed to the seafloor)

$$= -F_z \mathbf{k} \times (\mathbf{V} - \mathbf{v}^*) \qquad (1.7.7b$$

(sensor moving relative to seafloor), where F_z is the local vertical component of th geomagnetic field, **k** is a unit vector in the upward vertical direction, **V** is the vecto sum of the horizontal velocities of the ocean relative to the earth and the senso relative to the ocean, and

$$\mathbf{v}^* = C \int_{-H}^{0} \sigma(z')\mathbf{v}_h(z')\,dz' \Big/ \int_{-H}^{0} \sigma(z')\,dz' \qquad (1.7.8$$

is the scaled (by the constant C), horizontal water velocity. The water velocity i averaged vertically over the water column of thickness H and weighted by the seawate conductivity, $\sigma(z)$. Equation (1.7.8) reduces to the scaled barotropic velocity $C\mathbf{v}$ whe either the conductivity profile or the horizontal velocity is depth-independent. In th northern hemisphere, where **F** points into the earth, the north electric field i proportional to the west component of velocity while the east electric field i proportional to its north component. Neglecting the noise, we can solve (1.7.7a) t obtain

$$\mathbf{v}^* = -\mathbf{k} \times \mathbf{E}_h / F_z \qquad (1.7.9$$

Since **F** is known to one part in 10^4 for the entire globe, measurement of $\mathbf{E}_h$ yields th horizontal flow field.

Measurement of the HEF is entirely passive, being based on naturally occurrin fields, and hence has low power requirements and is nonintrusive. Motional EM ma be used in an Eulerian configuration (bottom recorders or submarine cables) or Lagrangian configuration (surface drifter, subsurface float, or towed fish). Equatio (1.7.7b) shows that a relative velocity estimate is possible by measuring the HEF fro a moving platform. On many instances, lack of a specific knowledge of $\mathbf{v}^*$ is not critical limitation since it is independent of depth by (1.7.8). The moving frame o reference equation (1.7.7b) is exploited by vertical profilers such as the electromagnetic velocity profiler (EMVP) and the expendable current profiler (XCP produced by Sippican. Horizontal profiles of the HEF can be obtained from a towe instrument and used with precise navigation to yield estimates of $\mathbf{v}^*$ and the surfac water velocity. The original form of such a towed instrument is the geomagneti electrokinetograph (GEK) of von Arx (1950).

1.7.7 Other methods of current measurement

There are numerous other ways to measure currents though not all have bee successfully commercialized. For example, prior to the ADCP, scientists in Japa used towed electrodes at the ocean surface (the GEK) to routinely monitor the currents off the east coast of Japan. Coastal Ocean Doppler Radar (CODAR) determine surface current velocity by using shore-based microwave radar with frequencies o around 12 MHz to sense the backscatter from wind-generated capillary waves. Thes waves ride on the ocean currents so that the Doppler shift of the radar signal can b used to estimate the current speed in the direction of the shore-based rada illumination. Two independent radar transmitters provide maps of the two-dimensional flow over the area covered by the radar signals. Goldstein *et al.* (1989) report on the use of synthetic aperture radar (SAR) to measure surface currents from the phase-delay maps of aircraft-borne radar. Other recent techniques, such as the correlation sonar and acoustic "scintillation" flow measurements use pattern recognition and cross-correlation methods, respectively, to determine the current over a volume of ensonified water (Farmer *et al.*, 1987; Lemon and Farmer, 1990). The acoustic scintillation method determines the flow in a turbulent medium by comparing the combined spatial and temporal variability of forward-scattered sound along two closely-spaced parallel acoustic paths separated by a distance, Δx. Assuming that the turbulent field does not change significantly during the time it takes the fluid to travel between the two paths, the pattern of amplitude and phase fluctuations at the downstream receiver will, for some time lag Δt, closely resemble that of the upstream receiver. Examination of the time delay in the peak of the covariance function for the two signals gives Δt which then determines the mean velocity $v = \Delta x/\Delta t$ normal to the two acoustic paths. The technique has been used successfully to measure the horizontal flow in tidal channels and rivers, as well as the vertical velocity of a buoyant-plume rising from a deep-sea hydrothermal vent in the northeast Pacific (Lemon *et al.*, 1996).

Numerous papers have discussed the computation of surface currents from the displacements of patterns of sea surface temperature (SST) in thermal AVHRR imagery. In the maximum cross-correlation (MCC) method, the cross-correlation between successive satellite images is used to map the displacements due to the advection of the SST pattern (Emery *et al.*, 1986). More recently, Wu (1991, 1993) has advanced a "relaxation labeling method" for computing sea surface velocity from sequential time-lapsed images. The method attempts to address two major deficiencies with the maximum cross-correlation method, namely: (1) the MCC approach is strictly statistical and does not exploit *a priori* knowledge of the physical problem; and (2) pattern deformation and rotation, as well as image noise, can introduce significant error into MCC vector estimates. The latter problem was addressed by Emery *et al.* (1992) who showed that rotation can be resolved using large search windows.

1.7.8 Mooring logistics

In terms of accuracy and reliability, current meter data from surface and subsurface moorings cannot be divorced from the mooring itself. While many common mooring procedures are available, there is no single accepted technique nor is there agreement on the subsequent behavior of the mooring while in the water. Surface moorings with their flotation on the wavy surface of the ocean will behave differently than subsurface moorings in which the buoyancy is distributed vertically along the mooring line. For the case of subsurface moorings, the addition of pressure sensors to most current meters has helped to characterize mooring motion and determine its effect on the measured currents. Variations in the depth of the sensor can be calculated from the pressure fluctuations and used to estimate the depth and position of the moored instruments as a function of time. Also, models of mooring behavior have been developed which enable the user to predetermine line tensions and mooring motions based on the cross-sectional areas of the mooring components and estimates of the horizontal current profile. For example, the program SSMOOR distributed by Cable Dynamics and Mooring Systems in Woods Hole (Berteaux, 1990), uses a finite element technique to integrate the differential equilibrium equations for cables subjected to steady state currents. Factors taken into consideration include: the mooring wire (or rope) diameter, weight in water, and modulus of elasticity; and the shapes, cross-sections, drag coefficients, weights, and centers of buoyancy of the recording instruments. Up to 10 current speeds can be specified for the current profile and as many as 20 instruments inserted in the anchoring line.

Mooring motions are largest when surface floats are used. For surface moorings in deep water, the length of the mooring line creates a relatively large "watch circle" that the surface float can occupy. This will add apparent horizontal motion to the attached current meters while, at depth, the surface wave and wind driven fluctuations translate into mainly vertical oscillations of the mooring elements. Some intercomparison experiments have tried to use a variety of mooring types to test the effects of moorings alone. Zenk *et al.* (1980) compare VACM measurements from a taut-line surface mooring with a single line spar buoy float and a more rigid two-line, H-shaped mooring. As expected, the H-shaped mooring was more stable and the other two exhibited much stronger oscillations. The current meters on the rigid H-mooring registered the greater current oscillations since the meters on the other, less restricted, moorings moved with the flow rather than measuring it.

In their current meter comparison, Halpern *et al.* (1981) discuss four different types of mooring buoyancy; three surface and one subsurface. The surface floats were: a toroid, a spar-buoy and a torpedo-shaped float. They found that rotor-pumping was much greater under the toroid than under the spar buoy and that the effect of rotor-pumping on the resulting current spectra was significant at frequencies above 4 cph. While this was true for near-surface current meters, they also found that for deeper instruments the spar buoy float transmitted larger variations to the deeper meters making it a poor candidate for flotation in deep water current measurements. They found that both the VMCM and the ACM are less affected by the surface motions of a toroidal buoy. In a different comparison, Beardsley *et al.* (1981) tested an Aanderaa current meter suspended from a surface spar buoy, and found a significant reduction in the contamination of the measured signal by wave effects due to both currents and orbital motion with the spar buoy. Even with this flotation system, however, the Aanderaa continued to register high current speeds compared with other sensors.

In an overall review of the recent history of current meter measurement, Boicourt (1982) makes the interesting observation that "results from current measurement studies are independent of the quality of the data". In making this claim, he remarks that often the required results are only qualitative, placing less rigorous demands on the accuracy of the measurements. He also points out that present knowledge of the high-frequency performance of most flow sensors is inadequate to allow definitive analysis of the current measuring system. In this regard, he states that acoustic and electromagnetic current meters, with their fast velocity response sensors, hold great promise for overcoming the fundamental problems with mechanical current sensing systems. Finally, he calls for added research in defining the high-frequency behavior of common current meters.

Field work by the Bedford Institute of Oceanography on Georges Bank in the western Atlantic has revealed another unwelcome problem with moored rotor-type current meters. Comparisons between currents measured by a sub-surface array of Aanderaa current meters on the bank and a ship-board acoustic Doppler current profiler indicated that current speeds from the moored array were 20–30% lower than concurrent speeds from the profiler. To test the notion that the under-speeding was due to high-frequency mooring vibration caused by vortex shedding from the spherical floatation elements, an accelerometer was built into one of the sub-surface moorings. Accelerations measured by this device confirmed that the current meters were being subjected to high-frequency side-to-side motions. Under certain flow conditions, the amplitudes of the horizontal excursions were as large as 0.5 m at periods of 3 s. Tests confirmed that the spherical buoyancy packages were the source of the motions. By enclosing the spherically-shaped buoyancy elements in more streamlined torpedo-shaped packages, the mooring line displacements were reduced to about 10% of what they were for the original configuration. Excellent agreement was found between the current meter and vessel-mounted ADCP current records.

In certain areas of the world (e.g. Georges Bank), the survivability of a mooring can have more to do with fishing activity than to environmental conditions. Also, in the early days of deep-sea moorings, the Scripps Institution of Oceanography lost equipment on surface moorings to theft and vandalism. Preventing mooring and data loss in such regions can be difficult and expensive. For fishery oceanography studies the dilemma is that, to be of use, the measurements must be obtained in areas where they are most vulnerable to fish-net fouling and fish-line entanglement. Damage to nets equates to lost fishing time and damaged or lost instrumentation. Aside from providing detailed information on the mooring locations in printed material handed out to commercial fishermen, fish processing companies and coastguard, the scientist may need to resort to closely-spaced "guard buoys" in an attempt to keep fishermen and shipping traffic from subsurface moorings. Our experience is that a limited array of only three or so coastguard-approved buoys more than 0.5 km from the mooring is inadequate, and that certain operators will even use the buoys to guide their operations, thereby increasing the chance of damage.

1.7.9 Acoustic releases

An acoustic release is a remotely-controlled motorized linkage device that connects the expendable bottom anchor (often a set of train wheels) to the recoverable elements of a mooring (Figure 1.7.10). Modern acoustic releases are critical for free-fall deployment of moorings from ships and for reliable recovery of equipment on acoustic demand (Heinmiller, 1968). Operation of the release requires a deck unit specially built for the particular type of release and a transducer for acoustic interrogation of the release. A ship's sounder can be used in place of the hand-held transducer provided it is of compatible frequency and has a wide beam. This is useful since it allows the technician to talk to the release from the ship's laboratory rather than by lowering a transducer over the side of the ship. However, for "acoustically noisy" ships, lowering a transducer over the side is often the only way to talk to the release. More advanced releases enable the user to measure the *slant range* from the ship to the release based on the two-way time delay. By taking into account the slant of the acoustic path, the user can determine the coordinates of the release. Long-life (three-year) acoustic "pingers" built into the releases also are used to locate the depth and position of moorings using triangulation procedures. This is particulary useful for those moorings that fail to surface on command and must be dredged from the ship using a long line and hook. In some acoustic releases, a rough estimate of the orientation of the release can be obtained remotely through changes in ping-rate. For example, in the case of the Inter-Ocean release, a doubled ping-rate means that it is lying on its side rather being upright in the water column.

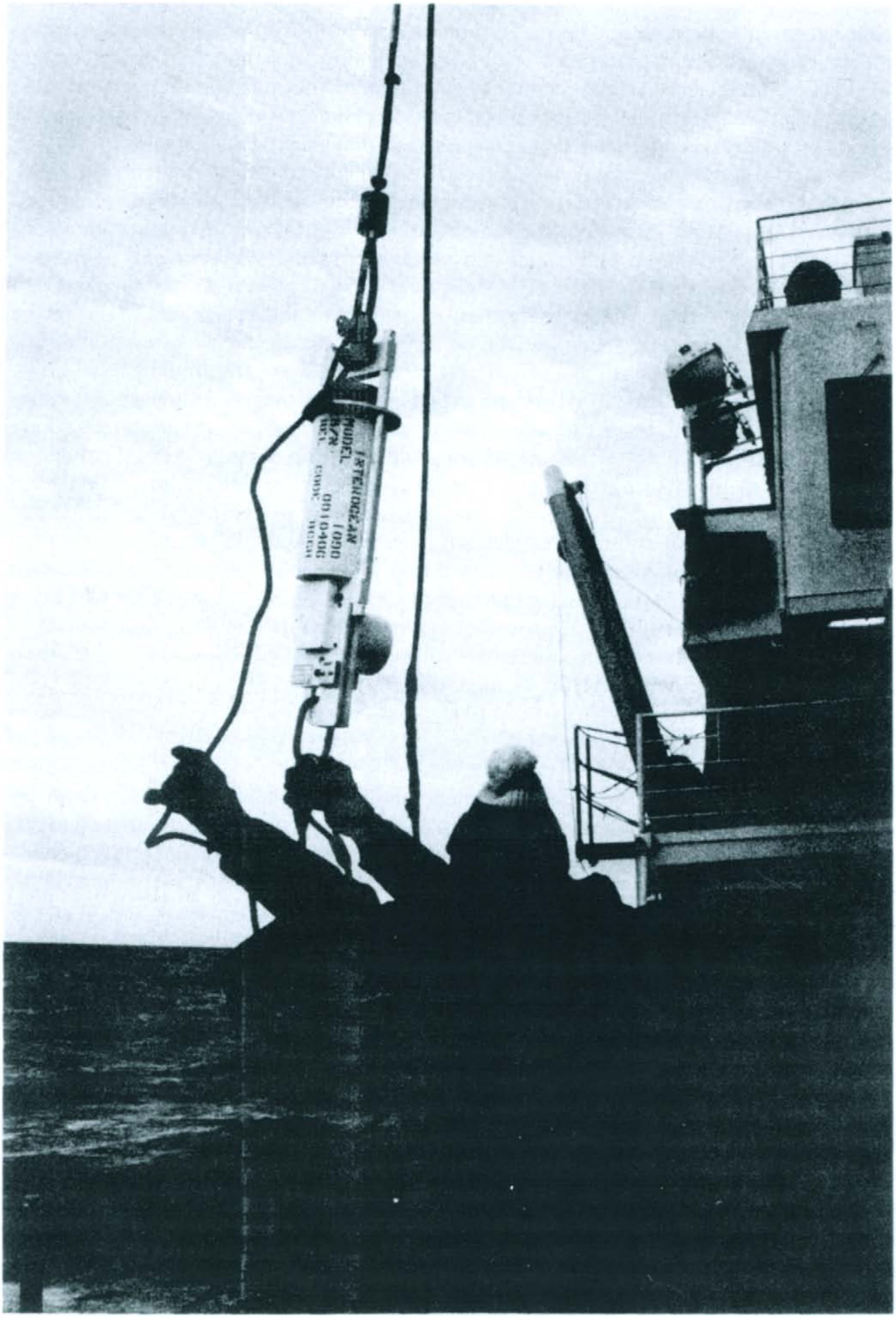

Figure 1.7.10. (a) Inter-Ocean acoustic release and attached anchor being lowered over the side of a ship. (Courtesy, Mark Geneau, Inter-Ocean.)

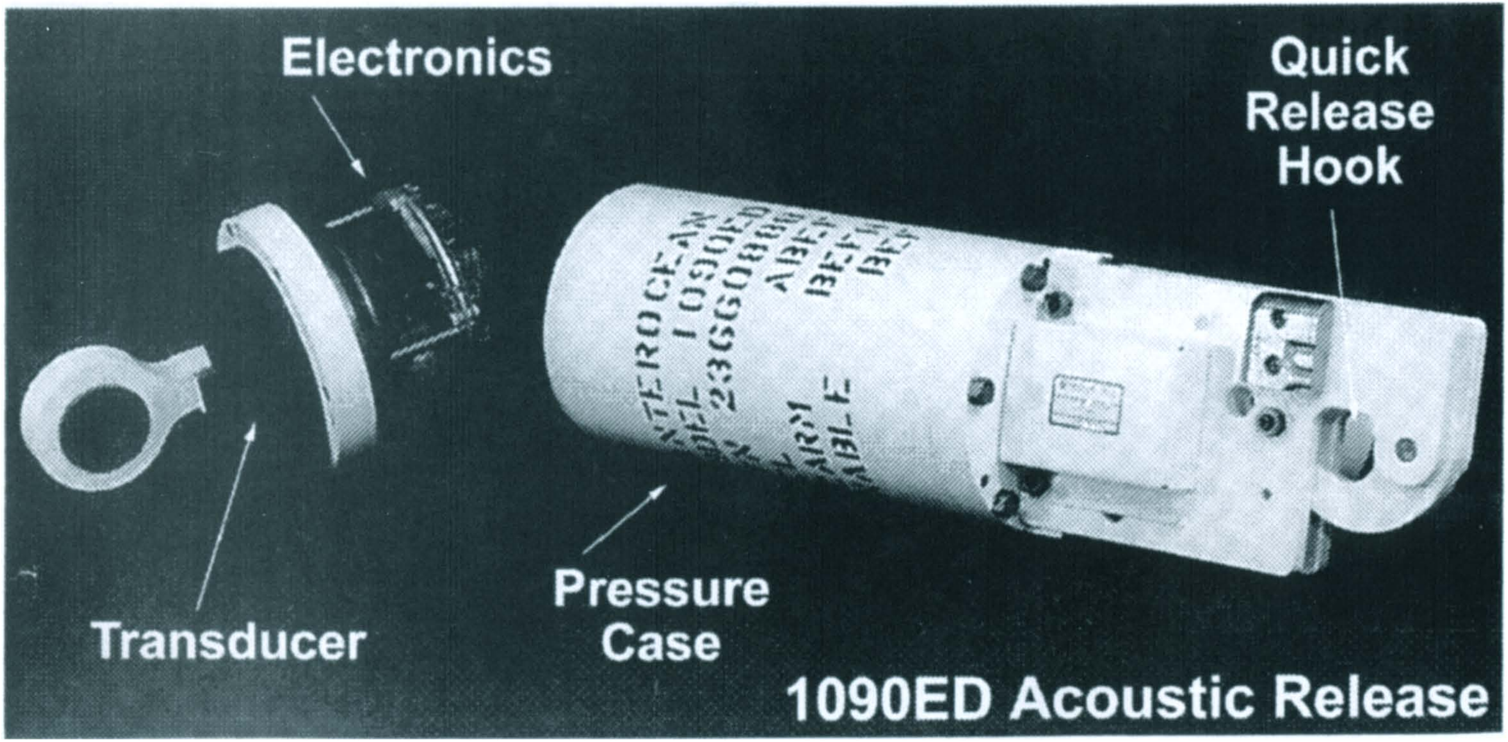

Figure 1.7.10. (b) Exploded view of the Inter-Ocean acoustic release. (Courtesy, Mark Geneau, Inter-Ocean.)

Most modern releases use separate "load" and "release" codes so that the release can be remotely opened and closed. Some releases also provide a release code that signals the oceanographer on the ship that the mooring has released and should be expected to surface in a time appropriate for the depth and net buoyancy of the mooring elements. This is always a tense time in mooring operations as it is sometimes difficult to predict precisely where the mooring will surface. Spotting the mooring from the ship can be a real challenge, especially in rough weather. Attachment of a pressure-rated radio beacon and flashing light to the top float of the mooring can aide considerably with the recovery operation. If the mooring fails to surface after an appropriate time, a search can initiated assuming that the mooring has surfaced and has not been spotted.

Past experience has demonstrated the wisdom of having a dual release system with two acoustic releases side-by-side in a parallel harness. A triangular bridle at the top connects the releases to a single point in the mooring line while a spreader bar connects the package to a single attachment point on the anchor chain. The extra cost can help avoid the need to dredge for the mooring if one of the releases should fail. Dredging is a last resort since in can be extremely harmful to the mooring hardware, leading to severe damage to the current meters and other instruments on the mooring line. In addition, there is a correct dredging procedure and oceanographers new to the field should talk to more experienced colleagues for guidance.

1.8 LAGRANGIAN CURRENT MEASUREMENTS

A fundamental goal of physical oceanography is to provide a first-order description of the global ocean circulation. The idea of following individual parcels of water (the Lagrangian perspective) is attractive since it permits investigation of a range of processes taking place within a tagged volume of water. Named after Joseph L. Lagrange (1736–1811), the French mathematician noted for his early work on fluid dynamics and tides, Lagrangian descriptions of flow can be used to investigate a range of processes from the dispersion of substances discharged into the ocean from a point source to the productivity of a semi-enclosed biological ecosystem as it drifts across the ocean. Early Lagrangian measurements consisted of tracking some form of tracer such as a surface float or dye patch. While giving vivid displays of water motions over short periods of time, these techniques demanded considerable onsite effort on the part of the investigator. Initial technical advances were made more rapidly in the development of moored current meters which yielded a strictly Eulerian picture of the current. However, improvements in tracking systems and buoy technology since the 1970s have made it possible to follow unattended surface and subsurface drifters for periods of many months to several years. Satellite-tracked surface buoys and acoustically-tracked, neutrally-buoyant SOFAR (SOund Fixing And Ranging or "Swallow") floats have been able to provide reliable, long-term, quasi-Lagrangian trajectories for many different parts of the world. (The trajectories are called quasi-Lagrangian since the drifters have a small "slip" of the order of 1–3 cm/s relative to the advective flow and because they do not move on true density surfaces. Surface drifters, for example, move on a two-dimensional plane rather than a three-dimensional density surface.)

Remotely-tracked drifters provide a convenient and relatively inexpensive tool for investigating ocean variability without continued direct involvement by the investigator. In the case of the satellite-tracked buoys, the scientist can now dial-up the position of drifters or collect data from ancillary sensors on the buoys. The number of possible satellite positional fixes varies with latitude (Table 1.8.1). Time delays between the time the data are collected by the spacecraft and the time they are available to the user is typically less than a few hours (Table 1.8.2). This feature makes the drifters useful for tracking floating objects or oil spills. Oceanic platforms and satellite data transmission systems have become so reliable that both moored and drifting platforms are now used for the collection of a variety of oceanic and meteorological data, including sea surface temperature, sea surface pressure, wind velocity and mixed layer temperature. A new era of oceanographic data collection is in progress with less direct dependence on ships and more emphasis on data collection from autonomous platforms.

Table 1.8.1. The mean number of satellite passes over a 24-h period for the Service Argos two-satellite system

Latitude (°)	Mean number of passes
0	7
15	8
30	9
45	11
55	16
65	22
75	28
90	28

Table 1.8.2. Data availability (global throughput times in hours) for June 1994. Percentage of the time that the delay between the satellite observation and the time that the data are processed and available from Service Argos. Service Argos Bulletin, July, 1994

Data availability	June (%)	December (%)
DA < 1 h	19.72	23.98
DA < 2 h	41.15	47.61
DA < 3 h	61.99	67.78
DA < 4 h	72.59	71.89
DA < 5 h	80.45	78.55
DA < 6 h	85.71	83.75
DA < 8 h	100.00	100.00

1.8.1 Drift cards and bottles

Until the advent of modern tracking techniques, estimates of Lagrangian currents were obtained by seeding the ocean surface with marked waterproof cards or sealed bottles and determining where these "drifters" came ashore. The card or bottle contained a note requesting that the finder notify the appropriate addressee of the time and location of recovery. To improve the chances of notification, a small token reward was usually offered (one Australian group gave out boomerangs). Although drift cards and bottles provide a relatively low-cost approach to Lagrangian measurements, they have major limitations. Because they float near the surface of the ocean, the movements of the cards and bottles are strongly affected by wind drag and wave-induced motions. In fact, much of what these type of drifters measure is wave-induced drift rather than underlying ocean currents. Moreover, even if the recovery rate was fairly high (1% is considered excellent for most drift card studies), the drifters provide, at best, an estimate of the lower bound of the mean current averaged over the time from deployment to recovery. Unless the card/bottle was recovered at sea, the scientist could never know if the drifter had recently washed ashore or had been laying on the beach for some time. In addition, the drifter provided no information on the current patterns between the deployment and recovery points.

1.8.2 Modern drifters

Quasi-Lagrangian drifters can be separated into two basic types: (1) Surface drifters having a surface buoy which is tethered to a subsurface drogue at some specified depth (typically less than 300 m); and (2) Subsurface, neutrally-buoyant floats which are designed to remain on fixed subsurface density surfaces. Modern surface drifters have a radio frequency transmitter (called a platform transmit terminal or PTT) for communication to a listening device while subsurface drifters may act either as a source or receiver of acoustic signals. Examples of the possible drogue configurations for modern satellite-tracked drifters are presented in Figure 1.8.1(a) along with the design for the standard holey sock WOCE/TOGA near-surface velocity drifter (Figure 1.8.1b). The purpose of the drogue is to reduce "slippage" between the drifter package

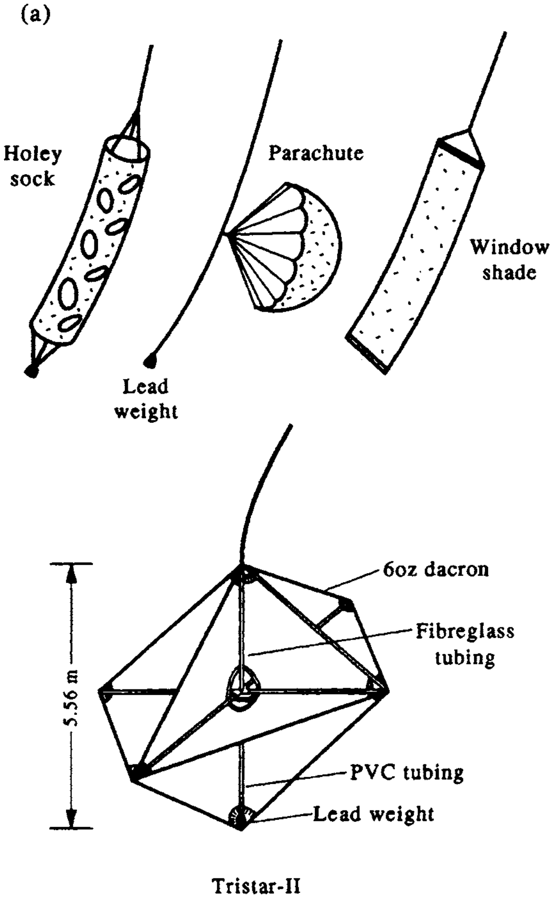

Figure 1.8.1. (a) Examples of the basic drogue designs for satellite-tracked drifters: holey-sock drogue; parachute drogue; window-shade drogue; and Tristar drogue (Niiler et al., 1987).

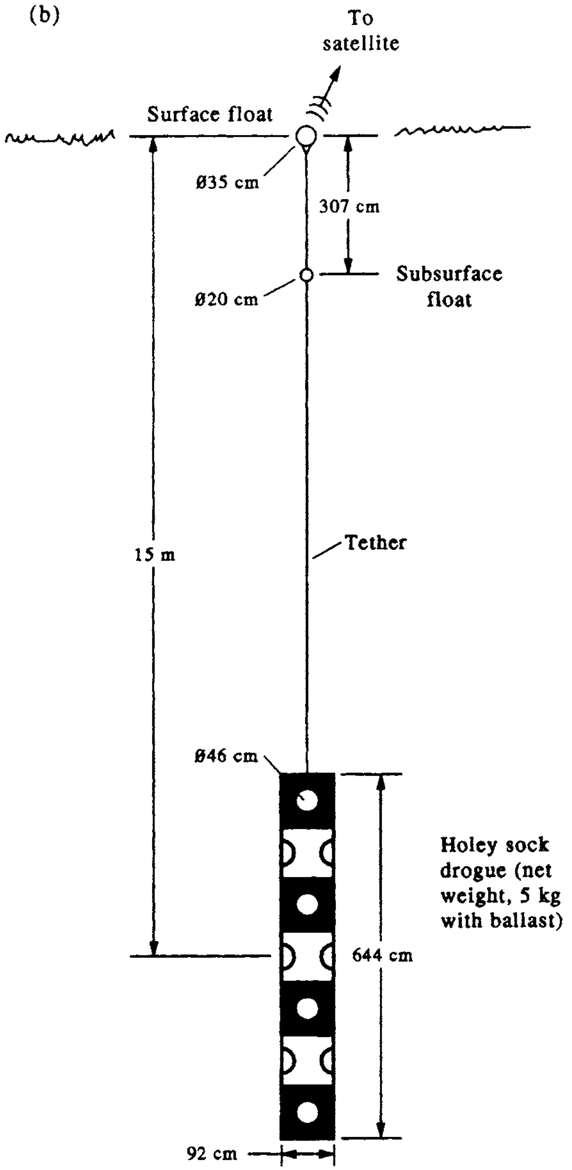

Figure 1.8.1. (b) Schematic of the standard WOCE/TOGA holey-sock surface-drifter showing pattern of holes in cloth panels. (From Sybrandy and Niiler, 1990.)

and the water. The surface float contains the PTT, temperature, and pressure sensors and other electronics (Figure 1.8.1c); the purpose of the subsurface buoy is reduce the "snap loading" on the drogue and cable by absorbing some of the shock from surface wave motion. In the case of the WOCE/TOGA holey sock drifter, the ratio of the drogue cross-sectional area to the cross-sectional area of the other drifter components (such as the wire tether and subsurface float) is about 45:1, a relatively high drag-area ratio for typical drogues.

Trajectories from an early type of drifter deployed in the NORPAX experiment are found in McNally *et al.* (1983). Similar tracks from more modern drifters are

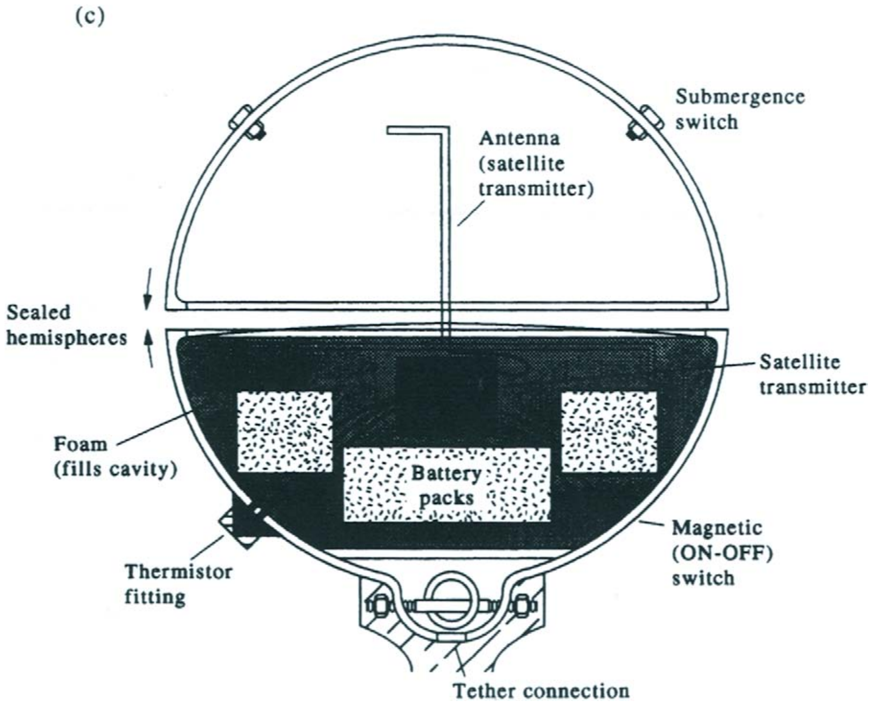

Figure 1.8.1. (c) Cut-away view of foam-filled Plexiglass shell and PTT (satellite transmitter) used for the surface buoy. When complete, the surface float has an excess buoyancy greater than 7 kg. (From Sybrandy and Niiler, 1990.)

presented in Figure 1.8.2. As examples, we have chosen trajectories from the North Atlantic near the Azores convergence zone (Figure 1.8.2a) and from the TOGA/WOCE equatorial Pacific (Figure 1.8.2b). Note that, despite the extensive buoy coverages in these two cases, there are still regions unvisited by the drifters. Our final example (Figure 1.8.2c) is a unique point-source deployment from the 106-mile site southeast of New York city. This site was the only ocean disposal site in the U.S.A. designated for dumping sewage sludge during the 1980s.

The essential technology for the above type of tracking was the development of a random access positioning system for polar orbiting satellites that could simultaneously fix the positions of many platforms using the Doppler-shift of the radio signals transmitted at regular intervals from the buoy. Early versions of the satellite tracking system were flown on the NIMBUS 6 (Kirwan *et al.*, 1975) and the French EOLE (Cresswell, 1976) satellites. Cresswell (1976) tested the accuracy of this system by examining the time-series from a moored buoy and from an antenna mounted on top of a laboratory. For both sites, the uncertainties were less than 1.0 km. Similar RMS position fix errors were reported for the NIMBUS 6 systems by Kirwan *et al.* (1975) and by Richardson *et al.* (1981).

The early satellite tracking systems have been replaced by the French ARGOS system (Collecte Localisation Satellite, CLS) carried onboard U.S. NOAA polar-orbiting weather satellites. As reported by Krauss and Käse (1984), this twin satellite system is capable of positional accuracies better than 0.2 km. Location quality depends on a number of factors such as the quality of the ephemeris data (orbital

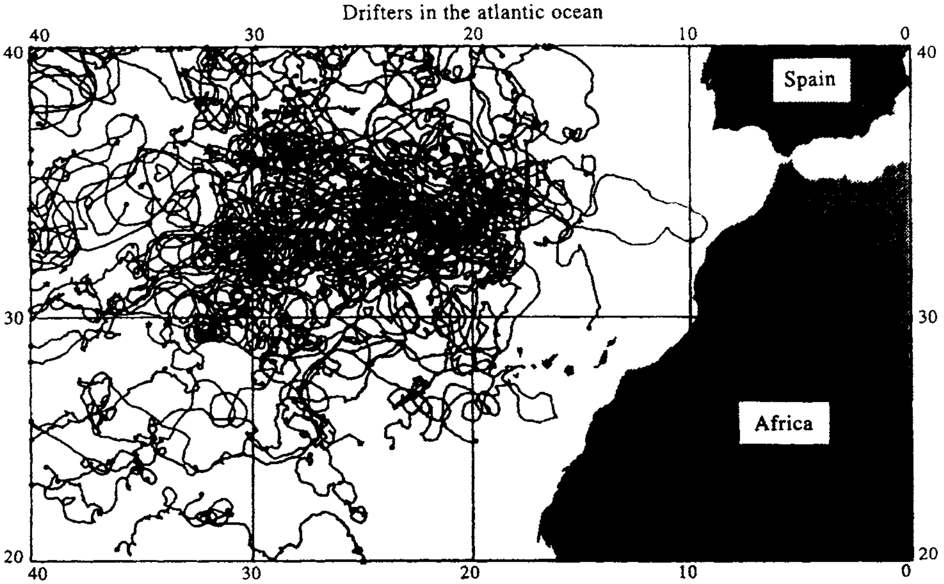

Figure 1.8.2. Trajectories from modern surface drifters with shallow (10–15 m) drogue depths. (a) Trajectories of 103 WOCE holey-sock drifters deployed near the Azores in the eastern North Atlantic from July 6, 1991 to October 25, 1993 (courtesy, Mayra Pazos, NOAA).

parameters), the stability of the receiver oscillator and temperature control, the duration of the satellite pass and the number of messages it receives from the drifter. Statistical information processed by Service ARGOS from thousands of fixed or slow-drifting platforms (Service ARGOS, 1992) indicates that quality locational fixes have 68% ($= \pm 1\sigma$) accuracies of 150 m while standard fixes have 68% accuracies of 350 m. As indicated by Table 1.8.1, the number of fixes per day is a function of latitude and higher accuracy is possible when the platform is fixed over periods longer than 7 min during two successive satellite passes. The drifters themselves cost a few thousand dollars and are considered expendable. Typical tracking costs are of the order of $5000 per year for full tracking (no positional fixes omitted) and one-third of this for the one-third duty cycle permitted by Service ARGOS (i.e. full-time tracking for 8 or 24 h followed by no tracking for 16 or 48 h, respectively).

1.8.3 Processing satellite-tracked drifter data

Position data obtained through satellite tracking need to be carefully examined for erroneous locations and loss of drogue. In fact, one of the main problems with surface drifters, aside from the need for accurate positioning, is knowing if and when the drogue has fallen off. Strain sensors are often installed to sense drogue attachment, but they have proven unreliable. The tether linkage between the surface buoy and the drogue is the major engineering problem in designing robust and long-life drifters. Because of this problem, drifters often have a subsurface float to help absorb the snap loading on the drogue caused by surface waves and also ensure that the surface element isn't constantly submerged in rough weather. An abrupt and sustained order-of-magnitude increase in the velocity variance derived from first differences of the

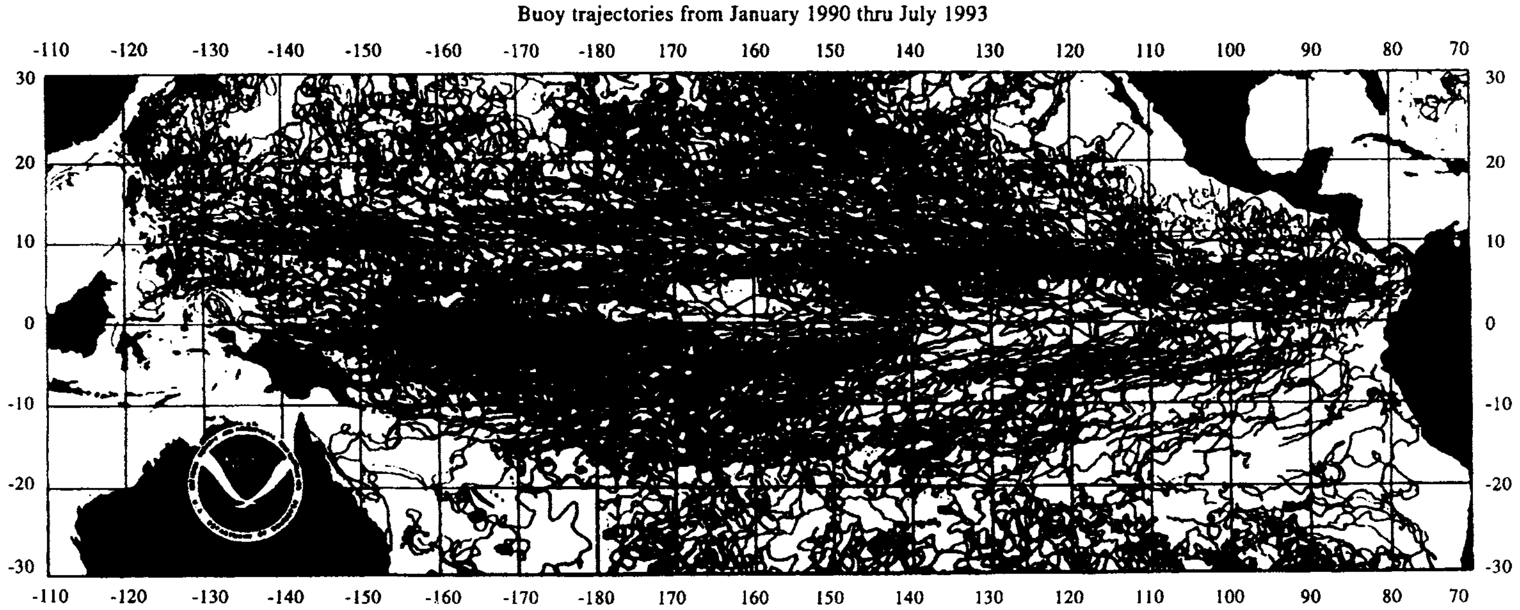

Figure 1.8.2. Trajectories from modern surface drifters with shallow (10–15 m) drogue depths. (b) Trajectories of TOGA/WOCE holey-sock drifters for the Equatorial Pacific from January 1990 to July 1993 (courtesy, Mayra Pazos, NOAA).

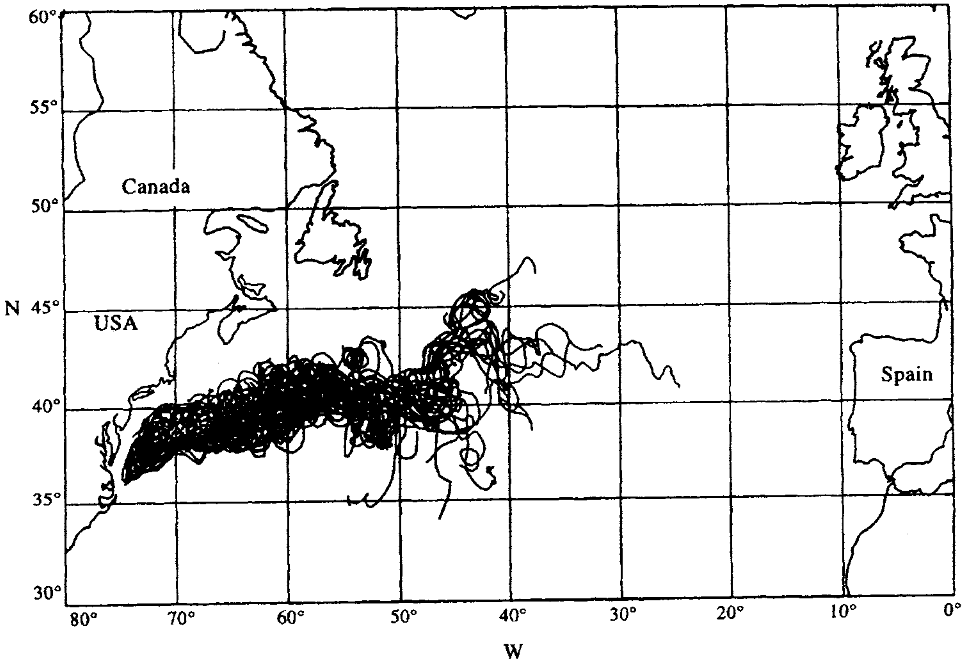

Trajectories of satellite-tracking drifting buoys released at the 106-mile site October 1989 to June 1991

Figure 1.8.2. Trajectories from modern surface drifters with shallow (10–15 m) drogue depths. (c) Tracks of 66 holey sock drifters centered at 10 m depth released from 106-mile site southeast of New York between October 1989 and June 1991 (courtesy Paul Dragos, Battelle Ocean Sciences; Service Argos Newsletter 46, May 1993).

edited positional data can be considered as evidence for drogue loss. The cubic spline routine in most software analysis packages works well for positional data provided the sampling interval is only a few hours. Although it is not recommended, the user can obtain the velocity components (u, v) directly from spline coefficients for the positional data.

1.8.4 Drifter response

As with all Lagrangian tracers, it is difficult to know how accurately a drifter is coupled to the water and what effects external forces on the drifter's hull might have on its performance. In most applications, the coupling between the buoy and the water is greatly improved by the drogue. For shallow drifters with drogue depth centers less than 30 m, typical drogue-to-tether drag ratios are around 40:1. For deeper drogues (>100 m) the ratio decreases due to the added length of the tether. A smaller diameter wire can help offset the increased drag but at the expense of durability. There are as many different drogue designs as there are buoy hull shapes and it is difficult to get a consensus on the efficiencies of these drifter system elements. In a theoretical and experimental study, Kirwan *et al.* (1975) examined the effects of wind and currents on various hull and drogue types. They found that parachute drogues were more efficient than the common window-shade drogues, in strong contrast to the finding by Vachon (1973) that a bottom-ballasted window blind drogue was the most effective.

Subsequent studies by Dahlen and Chhabra (1983) have determined that a holy-sock drogue is more efficient than either the window shade or the parachute. This shape is easy to deploy and was selected for the standard drifter used in the WOCE program (Sybrandy and Niiler, 1990). Another innovative drogue called the Tristar developed by Niiler *et al.* (1987) uses a cross-pattern of window-shades with an additional horizontal plane (Figure 1.8.1a). The idea behind this drogue design is to reduce "sailing" of the drogue as is often occurs with a single window shade. Although easy to deploy (it goes into the water in a soluble box), this type of drifter is difficult to recover. For compatibility reasons, the standard drifter used in the WOCE Surface Velocity Program (WOCE-SVP) uses a holey-sock drogue.

In addition to the disagreements about which type of drogue is best, the field studies of Kirwan *et al.* (1978) reported that the wind drag correction formula, given by Kirwan *et al.* (1975), is much too large for periods of high wind. The subsequent conclusion was that drifter velocities uncorrected for wind drag are better indicators of the true prevailing surface currents than are those corrected for the influence of wind drag on the buoy hull. In this context, it should be recognized that Lagrangian drifting buoys respond to the integrated drag forces including the forces on the drogue and the direct forcing on the hull. The driving forces in the water column consist of a superposition of geostrophic currents plus wind- and tide-generated currents. To evaluate the role of wind forcing on drifter trajectories, McNally (1981) compared monthly mean drifter trajectories with the flow lines for mean monthly winds computed from Fleet Numerical Weather Central's (now the Fleet Numerical Ocean Center, FNOC) synoptic wind analysis. He found that the large-scale, coherent surface flow followed isobars of sea-level pressure and was 20–30° to the right of the surface wind in the North Pacific (Figure 1.8.3). Overall buoy speeds were 1.5 of the geostrophic wind speed during periods of strong atmospheric forcing (fall, winter, and spring). In the summer, mesoscale ocean circulation features, unrelated to the local wind, tended to determine the buoy trajectories.

McNally (1981) also compared trajectories among buoys with drogues at 30 m depth, buoys with drogues at 120 m, and buoys without drogues. He found that drifters drogued below 100 m depth behaved very differently from ones drogued at 30 m, but that those drogued at 30 m and those without drogues behaved similarly. Using the record from a drogue tension sensor (drogue on–off sensor), McNally found that it was not possible to detect from the trajectory alone when a buoy had lost its drogue. This result suggests a lack of vertical current shear in the upper 30 m where the flow apparently responds more directly to wind-driven currents than to baroclinic geostrophic flow. The result was supported by the poor correlation between mean seasonal dynamic height maps and the tracks of near-surface drifters reported by McNally *et al.* (1983). McNally (1981) also described an annual increase by a factor of 5 of the wind speed in the North Pacific while the drifter speeds increased by a factor of 3.5, somewhat surprising considering that the wind stress that drives the currents is proportional to the square of the wind speed. During this same time the mean seasonal dynamic height amplitude changed only slightly.

Emery *et al.* (1985) confirmed the lack of agreement between drifter tracks and the synoptic geostrophic current estimates, as well as the high correlation between drifter displacements and the geostrophic wind speed and direction (Figure 1.8.4). In a rather complex analysis of the wind driven current derived from drifter trajectories, Kirwan *et al.* (1979) concluded that, while the drifter response is best described by a two-parameter linear system (consistent with the driving of the buoy by wave-driven

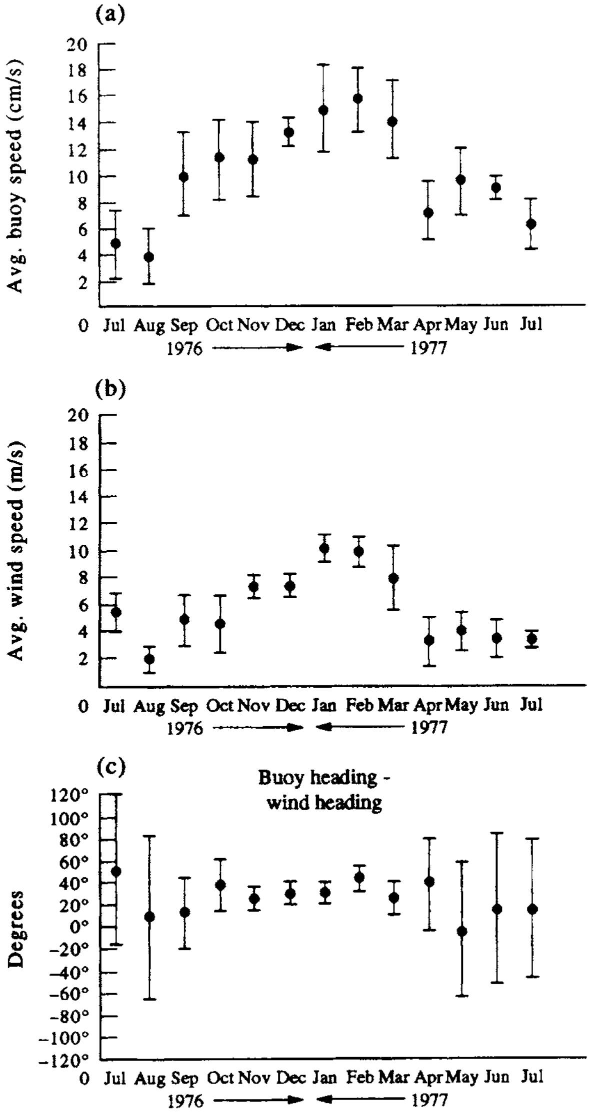

Figure 1.8.3. Monthly average wind and buoy speeds over the ADS North Pacific region from June 1976 through July 1977. (a) Monthly average drifter speeds; (b) monthly average wind speeds; (c) monthly average difference angle between wind direction and drifter direction. Vertical bars denote ±1 standard deviation.

Stokes drift), a combination of Ekman current plus Stokes drift also adequately described the resulting trajectories. Calculations by Emery *et al.* (1985), based on the nominal hull size, suggest that the Stokes drift component is relatively small and that the current in the surface Ekman layer is the primary driving mechanism for the mean drifter motion. That the angle this current makes to the wind is less than the 45° predicted by Ekman (1905), is expected since in the real ocean conditions never seem to meet the conditions for Ekman's derivation. McNally (1981) found an average angle

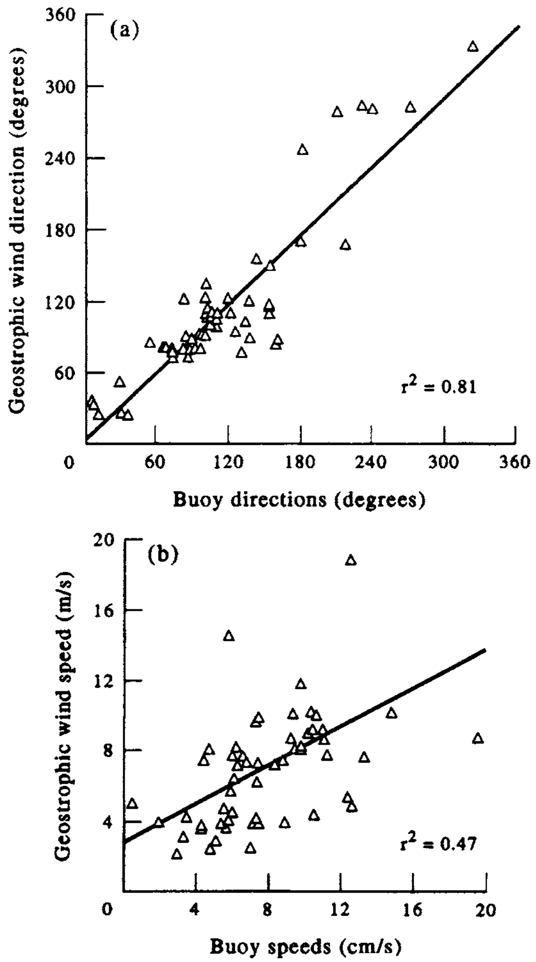

Figure 1.8.4. (a) Comparison between monthly mean buoy and geostrophic wind directions. (b) Comparison between monthly mean buoy and geostrophic wind speeds. (From Emery et al., 1985.)

of 30° while Kirwan *et al.* (1979) reported an angle of 15°, both to the right of the wind for the northern hemisphere.

A search for the elusive Ekman spiral was conducted from November 20, 1991 to February 29, 1992 by Krauss (1993) using ten satellite drifters drogued at five different levels within well-mixed homogeneous water of 80 m depth in the North Sea midway between England and Norway. The holey-sock drogues used in the study were 10 m long and centered at 5 m depth intervals from 7.5 to 27.5 m (Figure 1.8.5a). Results for the first four weeks of drift when the drifters were relatively close together revealed a clockwise turning and decay of the apparent wind stress with depth as required by Ekman-layer theory (Figure 1.8.5b). Here, the apparent wind stress is derived from the fluctuations in current velocity shear measured by the satellite-tracked drifters. Sea surface slopes needed to complete the calculations are from a numerical model. The observed amplitude decay of 0.90 and deflection of 10° near the surface are in close agreement with theory (apparent wind increases from 0° at the surface and is associated with an Ekman current that should be 45° to the right of the

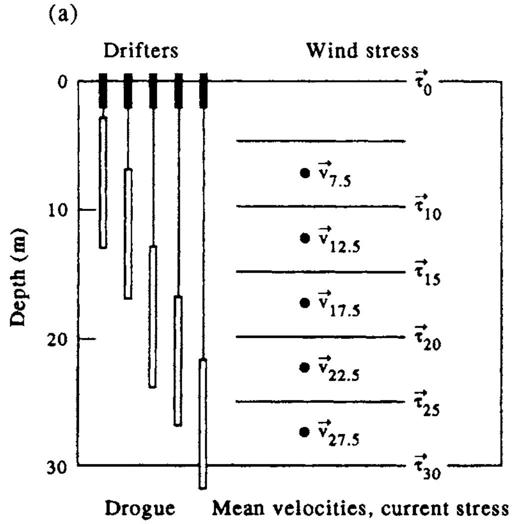

Figure 1.8.5. Test of Ekman's theory. The clockwise turning and decay of the apparent wind stress τ_D *at depth D (m) relative to the observed surface wind stress. The apparent wind stress is derived from the current velocity shear* dv_D/dz *measured by satellite-tracked drifters (a) drogued at different depths during homogeneous winter conditions. (Courtesy W. Krauss, 1994.)*

apparent wind). The angle increases to 41.6° in 25 m depth. The total current field is a superposition of barotropic currents due to sea-level variations and Ekman currents. The classical Ekman theory is unable to fully describe the observed deflection of the apparent wind (and Ekman current) to the right of the wind and its decay with depth. To be consistent with Ekman's theory, an eddy viscosity of 10^3 cgs units would be needed, which is well beyond the norm. However, as noted by Krauss, "... the deflections are a strong indication that some type of Ekman spiral dominates within the upper 30 m."

In an older study McNally and White (1985) examined wind-driven flow in the upper 90 m using a set of buoys drogued at different depths. They found a sharp change in buoy behavior when the drogue entered the deepening surface mixed layer. This response was characterized by a sudden increase in the amplitude of near-inertial motions with a downwind drifter velocity component three times that of the crosswind component. They also found that 80–90% of the observed crosswind component could be explained by an Ekman slab model. The large downwind response leads to surface currents, calculated from the buoy displacements, that are greater than 0° but less than 45° (about 30°) to the right of the wind. This behavior was true for all buoys with drogues above the upper mixed layer; once in the mixed layer all buoys behaved the same regardless of drogue depth.

In summary, it seems that the question of the relative coupling of drogued and undrogued drifting buoys to the water is still not completely resolved. Drifters measure currents, but which components of the flow dominate the buoy trajectories is still a topic of debate. Based on the recent literature, it appears that shallow drifters with drogue depths less than about 50 m are driven mainly by the wind-forced surface frictional Ekman layer whereas deep drifters with drogue depths exceeding 100 m are more related to geostrophic currents. The likely percentage of contribution by these

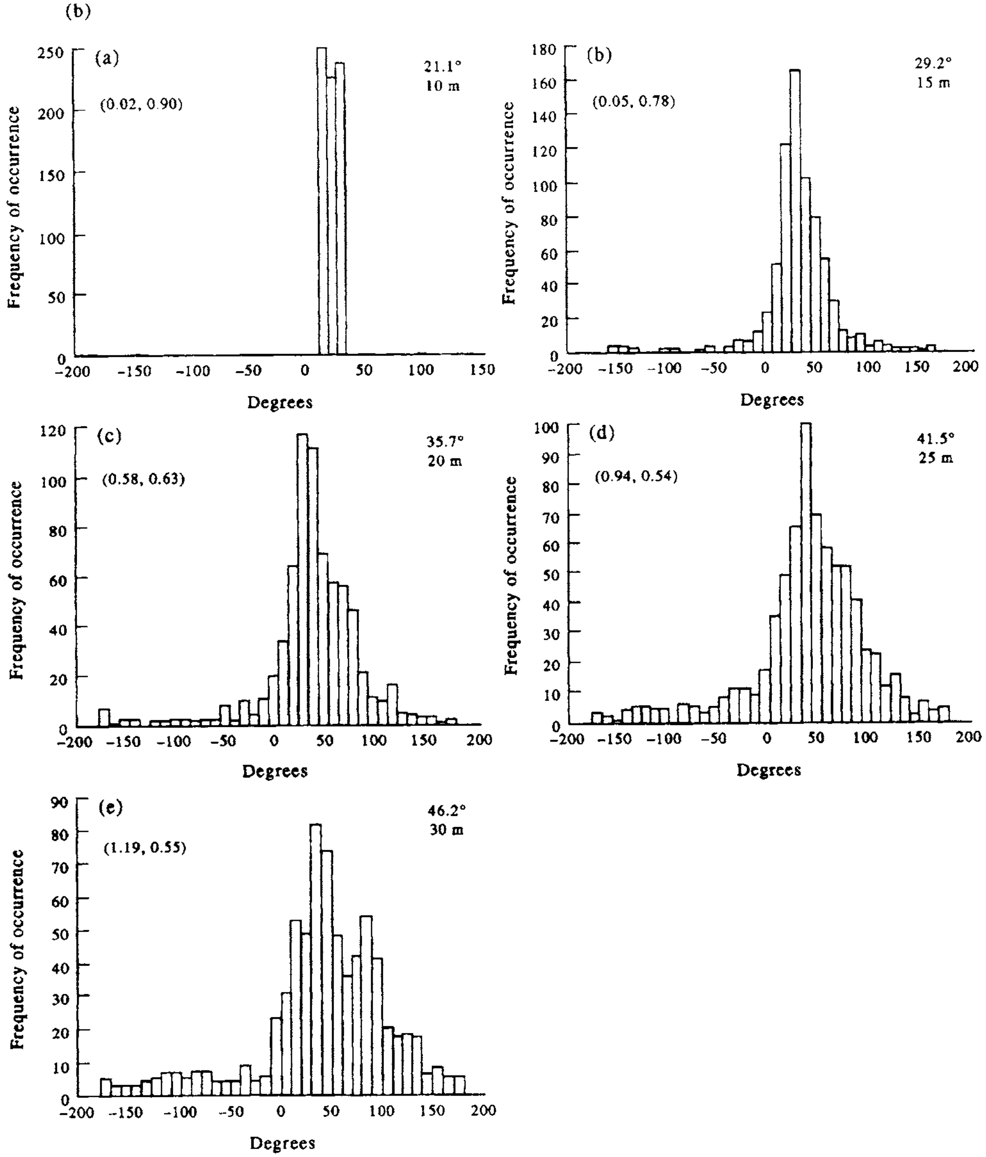

Figure 1.8.5. Test of Ekman's theory. The clockwise turning and decay of the apparent wind stress τ_D *at depth D (m) relative to the observed surface wind stress. The apparent wind stress is derived from the current velocity shear* dv_D/dz *measured by satellite-tracked drifters (b) Histogram of the relative angle (in degrees) between the surface wind-stress vector and the calculated apparent wind-stress as a function of depth (surface wind minus apparent wind). Linear regression values* (α, β) *give apparent wind-stress as a function of surface wind-stress. Offset results from the different time scales of the winds and the currents. Mean values given in upper right corner of figure. (Courtesy W. Krauss, 1994.)*

two current types depends on the type of drogue system that is used. A problem with trying to measure the deeper currents is that deeper drogue systems tend to fail sooner and it is difficult to access quantitatively the role of the drogue in the buoy trajectories. Drogue loss due to wave loading and mechanical decoupling of the surface buoy and the drogue is still the main technical problem to extending drifter life.

There are other problems with drifters worth noting. In addition to drogue loss and errors in positioning and data transmission, the transmitters submerge in heavy weather and loose contact with the passing satellite. Low drag ratios lead to poor flow response characteristics and, because of the time between satellite passes, there is generally inadequate sampling of tidal and near-inertial motions (especially at low latitudes or for the one day on–two days off duty cycles) leading to aliasing errors. Drifters also have an uncanny tendency to go aground and to concentrate in areas of surface convergence.

1.8.5 Other types of surface drifters

Before leaving this topic, it is appropriate to mention that while the satellite-tracked buoys are perhaps the most widely used type of surface follower for open waters, there are other buoy tracking methods being used in more confined coastal waters. A common method is to follow the surface buoy using ship's radar or radar from a nearby land-based station. More expensive buoys are instrumented with both radar reflectors and transponders to improve the tracking. The accuracies of such systems all depend on the ability of the radar to locate the platform and also on the navigational accuracy of the ship. Fixes at several near-simultaneous locations are needed to triangulate the position of the drifter accurately. Data recording techniques vary from hand plotting on the radar screen to photographing the screen continuously for subsequent digital analysis. These techniques are manpower intensive when compared with the satellite data transmission which provides direct digital data output.

In addition to radar, several other types of buoy tracking systems have been developed. Most rely on existing radio-wave navigation techniques such as LORAN or NAVSTAR (satellite navigation). For example, the subsurface drogued NAVocean and Candel Industries Sea Rover-3 Loran-C drifters have built-in Loran-C tracking systems that can both store and transmit the positional data to a nearby ship within a range of 25–50 km. Absolute positional accuracy in coastal regions is around 200 m but diminishes offshore with decreased Loran-C accuracy. However, relative positional errors are considerably smaller. Based on time-delay transmission data from three regional Loran-C transmitters, Woodward and Crawford (1992) estimated relative position errors of a few tens of meters and drift speed uncertainty of 2 cm s^{-1} for drifters deployed off the west coast of Canada. Once it is out of range of the ship, the Loran-C drifter can be lost unless it is also equipped with a satellite transmission system. Meteor-burst communication is a well-known technique that makes use of the high degree of ionization of the troposphere by the continuous meteor bombardment of the earth. A signal sent from a coastal master station skips from the ionosphere and is received and then retransmitted by the buoy up to several thousand kilometers from the source. Since the return signal is highly directional, it gives the distance and direction of the buoy from the master station. Buoys can also be positioned using VHF via direction and range. The introduction of small, low-cost GPS receivers makes it possible for buoy platforms to position themselves continuously to within 110 m. Provision for differential GPS (using a surveyed land-based shore station) has improved the accuracy to order of 10 m. Data are then relayed via satellite to provide a higher resolution buoy trajectory than is presently possible with ARGOS tracking buoys. Given the high positioning rate possible for GPS systems, it is the spatial accuracy of the fixes that limits the accuracy of the velocity measurements.

1.8.6 Subsurface floats

New technological advances in subsurface, neutrally-buoyant float design have improved interpretation and understanding of deep ocean circulation in the same way that surface drifters have improved research in the shallow ocean. In their earliest form (Swallow, 1955), subsurface quasi-Lagrangian drifters took advantage of the small absorption of low-frequency sound emitted in the sound channel (the sound velocity minimum layer) located at intermediate depths in the ocean. The sound-emitting drifters were tracked acoustically over a relatively short range from an attending ship. The development of the autonomous SOFAR (SOund Fixing And Ranging) float, which is tracked from listening stations moored in the sound channel (Rossby and Webb, 1970) has removed the burden of ship tracking and made the SOFAR float a practical tool for the tracking of subsurface water movements. Although positional accuracies of SOFAR floats depend on both the tracking and float–transponder systems, the location accuracy of 1 km given by Rossby and Webb (1970) is a representative value. In this case, neutrally-buoyant SOFAR floats have a positional accuracy that is comparable in magnitude to the satellite-tracked drifting buoys. Using high-power 250-Hz sound sources, the early SOFAR floats are credited with the discovery of mesoscale variability in the ocean and for pioneering our understanding of Lagrangian eddy statistics (Freeland *et al.*, 1975). The now familiar "spaghetti-diagram" (Figure 1.8.6) is characteristic of the type of eddy-like variability measured by SOFAR floats deployed in the upper ocean sound channel (Richardson, 1993).

SOFAR floats transmit low-frequency sound pulses which are tracked from shore listening positions or from specially moored "autonomous" listening stations. The need to generate low-frequency sound means that the floats are long (8 m) and heavy (430 kg), making them expensive to build and difficult to handle. Since greater expense is involved in sending sound signals than receiving them, a new type of float called the RAFOS (SOFAR spelled backwards) float has been developed in which the buoys listen for, rather than transmit, the sound pulses (Figure 1.8.7). In this configuration, the float acts as a drifting acoustic listening station that senses signals emanating from moored sound sources (Rossby *et al.*, 1986). The positions of RAFOS floats in a particular area are then determined through triangulation from the known positions of the moored source stations. A typical moored sound source, which broadcasts for 80 s every two days at a frequency of 260 Hz, has a range of 2000 km and an average lifetime of three years (*WOCE Notes*, June 3, 1991)

Since RAFOS floats are much less expensive to construct than SOFAR floats and more difficult to locate (since they are not a sound source), RAFOS floats are considered expendable. The data processed and stored by each RAFOS buoy as it drifts within the moored listening array must eventually be transmitted to shore via the ARGOS satellite link. To do this, the RAFOS float must come to the surface periodically to transmit its trajectory information. After "uplinking" its data, the buoy again descends to its programmed depth and continues to collect trajectory data. The cycle is repeated until the batteries run out.

The need for deep ocean drifters that are independent of acoustic tracking networks has led to the development of the "pop-up" float. The float is primarily a satellite PTT and a ballast device that periodically comes to the surface and transmits its location data and "health" status (an update on its battery voltage and other parameters) to the ARGOS system (Davis *et al.*, 1992). The only known points on the buoy trajectory are

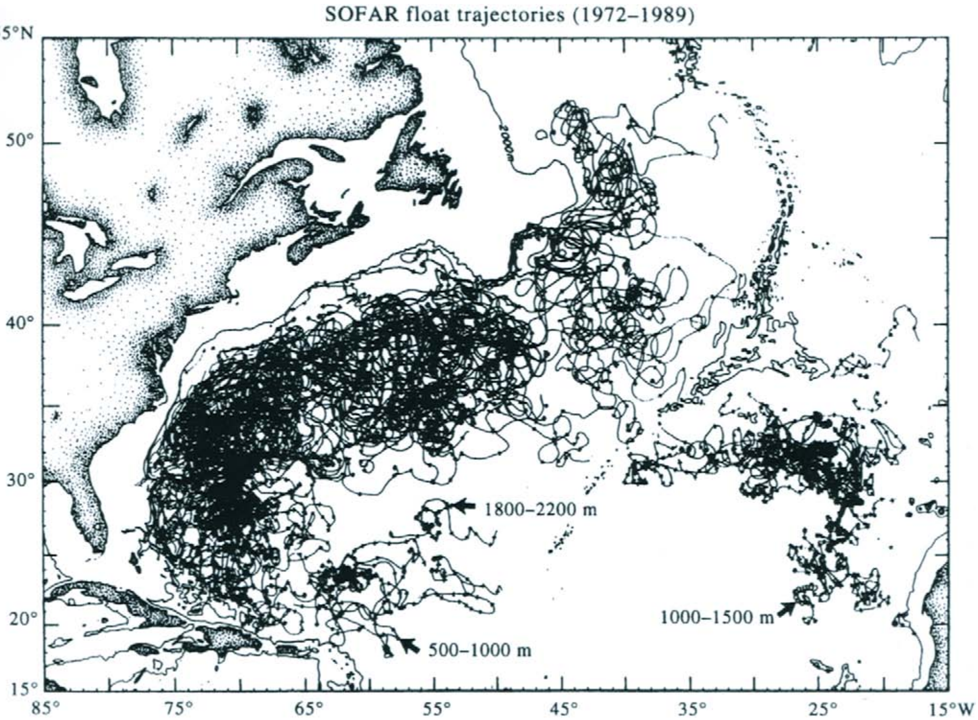

Figure 1.8.6. "Spaghetti-diagram" of all SOFAR float tracks from 1972 to 1989, excluding data from the POLYMODE Local Dynamics Experiment. Ticks on tracks denote daily fixes. Short gaps have been filled by linear interpretation. Plots are characteristic of the type of eddy-like variability measured by SOFAR floats deployed in the upper ocean sound channel. (Courtesy, Phillip Richardson, 1994.)

those obtained when the buoy is on the surface. As with the RAFOS buoys, the pop-up float sinks to its prescribed depth level after transmitting its data to the ARGOS system and continues its advection with the deep currents. The advantage of such a system is that it can be designed to survive for a considerable time using limited power consumption. Assuming that deep mean currents are relatively weak, the pop-up float is an effective tool for delineating the spatial pattern of the deep flow, which up to now has not been possible over large areas. The Autonomous Lagrangian Circulation Explorer (ALACE) described by Davis *et al.* (1992) drifts at a preset depth (typically less than 1000 m) for a set period of 25 days, then rises to the surface for about a day to transmit it position to the satellite. The drifter then returns to a prescribed depth which is maintained by pumping fluid to an external bladder which changes its volume and hence its buoyancy. Modern ALACE floats built by Webb Research Corp. are capable of making about 100 round-trips to depths of less than 1 km over a lifetime of about five years. Errors are introduced by surface currents when the device is on the surface. The floats also provide temperature and salinity profiles during ascent or descent.

As with the surface drifter data, the real problem in interpreting SOFAR float data is their fundamental "quasi-Lagrangian" nature (Riser, 1982). From a comparison of the theoretical displacements of true Lagrangian particles in simple periodic ocean current regimes with the displacements of real quasi-Lagrangian floats, Riser concludes that the planetary scale (Rossby wave) flows in his model contribute

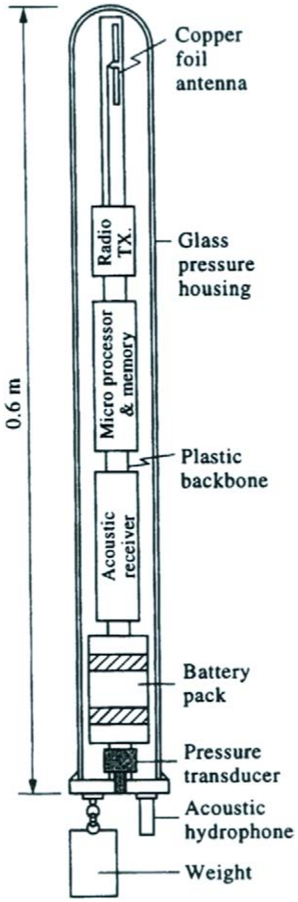

Figure 1.8.7. Schematic of a RAFOS float. (Courtesy, Thomas Rossby.)

more significantly to the dispersion of 700 m depth SOFAR floats than do motions associated with near-inertial oscillations or internal waves of tidal period. Based on these model speculations, he suggests that while a quasi-Lagrangian drifter will not always behave as a Lagrangian particle it nevertheless will provide a representative trajectory for periods of weeks to months. For his Rossby wave plus internal wave model, Riser derived a correlation time scale of about 100 days. He also suggests that the residence of some floats in the small scale (25 km) features, in which they were deployed, provides some justification for his conclusions.

For pop-up floats, problems in the interpretation of the positional data arise from: (1) interruptions in the deep trajectory every time the drifter surfaces; (2) uncertainty in the actual float position between satellite fixes; and (3) contamination of the deep velocity record by motions of the float on the surface or during ascent and descent. An essential requirement in the accurate determination of the subsurface drift is to find the exact latitude/longitude coordinates of the buoy when it first breaks the ocean surface and when first begins to re-sink. The ability to interpolate ARGOS fixes to these times is determined by the nature of the surface flow and the number satellite fixes. ALACE ascends more rapidly than it descends and spends little time at the surface. In a trial to 1 km, the drifter spent 0.3 h in the upper 150 m, and 4 h between 150 and 950 m depth. Thus, according to Davis *et al.* (1992), most of the error comes from vertical velocity shear at depths of 150 m and deeper, below the surface wind-driven layer (see Thomson and Freeland (1999) for further details).

1.8.7 Surface displacements in satellite imagery

As noted briefly at the end of Section 1.7.6, well-navigated (geographically-located) sequential satellite images can be used as "pseudo-drifters" to infer surface currents. The assumption is that the entire displacement of surface features seen in the imagery is caused by surface current advection. This displacement estimate method (called the maximum cross-correlation or MCC) was applied successfully to sea ice displacements by Ninnis *et al.* (1986). Later, the same approach was applied to infrared images of sea-surface temperature (SST) by Emery *et al.* (1986). The patterns and velocities of the SST-inferred currents were confirmed by the drifts of shallow (5 m drogue) drifters and by a CTD survey. Later studies (Tokamamkian *et al.*, 1990; Kelly and Strub, 1992) have confirmed the utility of this method in tracking the surface displacements in different current regimes. When applied to the Gulf Stream (Emery *et al.*, 1992), the MCC method reveals both the prevailing flow and meanders. A numerical model of the Gulf Stream, used to evaluate the reliability of the MCC currents found that, for images more than 24 h apart, noise in this strong flow regime begins to severely distort the surface advection pattern.

The MCC method can also be applied to other surface features such as chlorophyll and sediment patterns mapped by ocean color sensors. In the future, it may be possible to combine ocean color tracking with infrared image tracking. Infrared features are influenced by heating and cooling, in addition to surface advection, while surface chlorophyll patterns respond to *in situ* biological activity. Since these two features should reflect the same advective patterns (assuming similar advective characteristics for temperature and color), the differences in calculated surface vectors should reflect differences in surface responses. Thus, by combining both color and SST it should be possible to produce a unique surface flow pattern that corrects for heating/cooling and primary biological production.

1.9 WIND

Although it might be surprising to find a section on wind data in an oceanographic text, we can state with some confidence that most of the scientific assessment of wind data over the ocean has been done by oceanographers searching for the best way to define the meteorological forcing field for oceanic processes. This is especially true of observationalists working on upper ocean dynamics and numerical modelers who require climatological winds to drive their circulation models. It is not the intent of this book to discuss in detail the many types of available wind sensors and to evaluate their performance, as is done with the oceanographic sensors. Instead, we will briefly review the types of wind data available for ocean regions and make some general statements about the usefulness and reliability of these data.

Open-ocean wind data are of three types: (1) six-hourly geostrophic wind data computed from measured distributions of atmospheric sea surface pressure over the ocean; (2) directly measured wind data from ships and moored platforms (typically at hourly intervals); and (3) inferred six-hourly wind data derived from satellite sensors. Atmospheric pressure maps are prepared from combinations of data recorded by ships at sea, from moored or drifting platforms such as buoys, and from ocean island stations. Analysis procedures have changed over the years with early efforts depending on the subjective hand contouring of the available data. More recently, there has been a shift to computer-generated "objective analysis" of the atmospheric pressure data. Since they are derived from synoptic weather networks, the pressure data are originally computed at six-hourly intervals (00, 06, 12, and 18 UTC). While some work has been done to correct barometer readings from ships to compensate for installation position relative to sea-level, no systematic study has been undertaken to test or edit these data or analyses. However, in general, sea-level pressure patterns appear to be quite smooth, suggesting that the data are generally reliable. Objective analysis smooths the data and suppresses any noise that might be present.

It is not a simple process to conformally map a given atmospheric pressure distribution into a surface wind field. While the computation of the geostrophic wind velocity from the spatial gradients of atmospheric pressure is fairly straightforward, it is more difficult to extrapolate the geostrophic wind field through the sea-surface boundary layer. The primary problem is our imperfect knowledge of the oceanic boundary layer and the manner in which it transfers momentum from the wind to the ocean surface. While most scientists have agreed on the drag coefficient for low wind speeds (<5 m/s), there continues to be some disagreement on the appropriate coefficient for higher wind speeds. Added to this is a lack of understanding of boundary layer dynamics and how planetary vorticity affects this layer. This leads to a lack of agreement on the backing effect and the resulting angle one needs to apply between the geostrophic wind vector and the surface wind vector. Thus, wind stress computations have required the *a priori* selection of the wind stress formulae for the transformation of geostrophic winds into surface wind stresses. The application of these stress calculations will therefore always depend on the selected wind stress relation and any derived oceanographic inferences are always subject to this limitation.

Anemometers installed on ships, buoys or island stations provide another source of open-ocean wind data. The ship and buoy records are subject to problems arising from measuring the wind around structures and relative to a moving platform, which is itself being affected by the wind. These effects are difficult to estimate and even more difficult to detect once the data have been recorded or transmitted. Many of the earlier ship-wind data in climatological archives are based on wind estimates made by the ship's officers from their evaluation of the local sea state. (The Beaufort Scale was designed for the days of sailing vessels and uses the observed wave field to estimate the wind speed.) Analysis of the ship-reported winds from the Pacific (Wyrtki and Meyers, 1975a, b) has demonstrated that, with some editing and smoothing, these subjective data can yield useful estimates of the distribution of wind over the equatorial Pacific. Barnett (1983) has used objective analysis on these same data to produce an even more filtered set of wind observations for this region. Following a slightly different approach, Busalacchi and O'Brien (1981) reanalyzed the ship wind-data to fill in spatial gaps before applying the wind fields to oceanographic model studies.

Included in other widely used sets of wind data are the synoptic wind fields produced by the U.S. Fleet Numerical Ocean Center (FNOC) in Monterey, California. These analyses use not only ship, buoy and island reports but also winds inferred from the tracking of clouds in sequences of visible and infrared satellite imagery. In this technique, one uses the infrared image to estimate the temperature and, therefore, infer the elevation of the cloud mass being followed. By examining sequences of satellite images, specific cloud forms can be followed and the corresponding wind speed and direction computed for the altitude of the cloud temperature. Naturally, this procedure is dependent not only on the accuracies of the satellite sensors but also on the interpretive skills of the operator. As a consequence, no real quantitative levels of accuracy can be attached to these data. Comparison between the FNOC winds and coincident winds measured from an open-ocean buoy (Friehe and Pazan, 1978) showed excellent agreement in speed and direction over a period of 60 days. Although this single-point comparison is too limited to establish any uncertainty values for the FNOC wind fields, the comparison provides some confirmation of the validity of techniques used to derive the FNOC winds.

A wind product for the Pacific Ocean similar to the FNOC winds is generated by the National Marine Fisheries Service (NMFS) in Monterey, California (Holl and Mendenhall, 1972; Bakun, 1973). In this product, the geostrophic "gradient" winds are first computed at a 3° × 3° latitude–longitude grid spacing from spatial gradients in the six-hourly synoptic atmospheric pressure fields at the 500 or 800 mb surfaces. To obtain the surface-wind vectors in the frictional atmospheric boundary layer, the magnitudes of the calculated geostrophic wind vectors are reduced by a factor of 0.7 and the wind vectors rotated (backed) by 15°; here, "backed" refers to a counter-clockwise motion in the northern hemisphere and a clockwise rotation in the southern hemisphere. (Some of the original work on this method can be traced to Fofonoff, 1960.)

Thomson (1983) compared winds computed by the NMFS with winds measured from moored buoys off the coast of British Columbia during the summers of 1979 and 1980 (Figure 1.9.1). In this comparison, it was concluded that winds computed from atmospheric pressure provided an accurate representation of the oceanic winds for time scales longer than several days but failed to accurately resolve short-term wind reversals associated with transient weather systems. Computed winds also tended to underestimate percentages of low and high wind speed. Similar results were reported by Marsden (1987) for the northeast Pacific (including Ocean Weather Station P) and by Macklin *et al.* (1993) for the rugged coast of western Alaska. The poor correlation of observed and computed winds at short time scales is thought to be due to the large (3° × 3°) spacing, the coarse six-hour sampling of the pressure field and the strong influence of orographic effects in mountainous coastal regimes. In Thomson's study, peak computed winds were roughly 20° to the right of the observed peak inner-shelf winds, suggesting that the computed winds were representative of more offshore conditions or that the 15° correction for frictional effects was too small. Spectra of observed winds were found to be dominated by motions at much larger wavelengths than were found in the computed values. The NMFS winds were found to contain a significant 24-h sea-breeze component in the inner shelf observed winds but not in the records farther offshore. Based on spectral comparisons it was concluded that the NMFS winds closely represented the actual winds for periods longer than two days (frequencies less than 0.02 cph) and only marginally matched actual winds for periods shorter than two days.

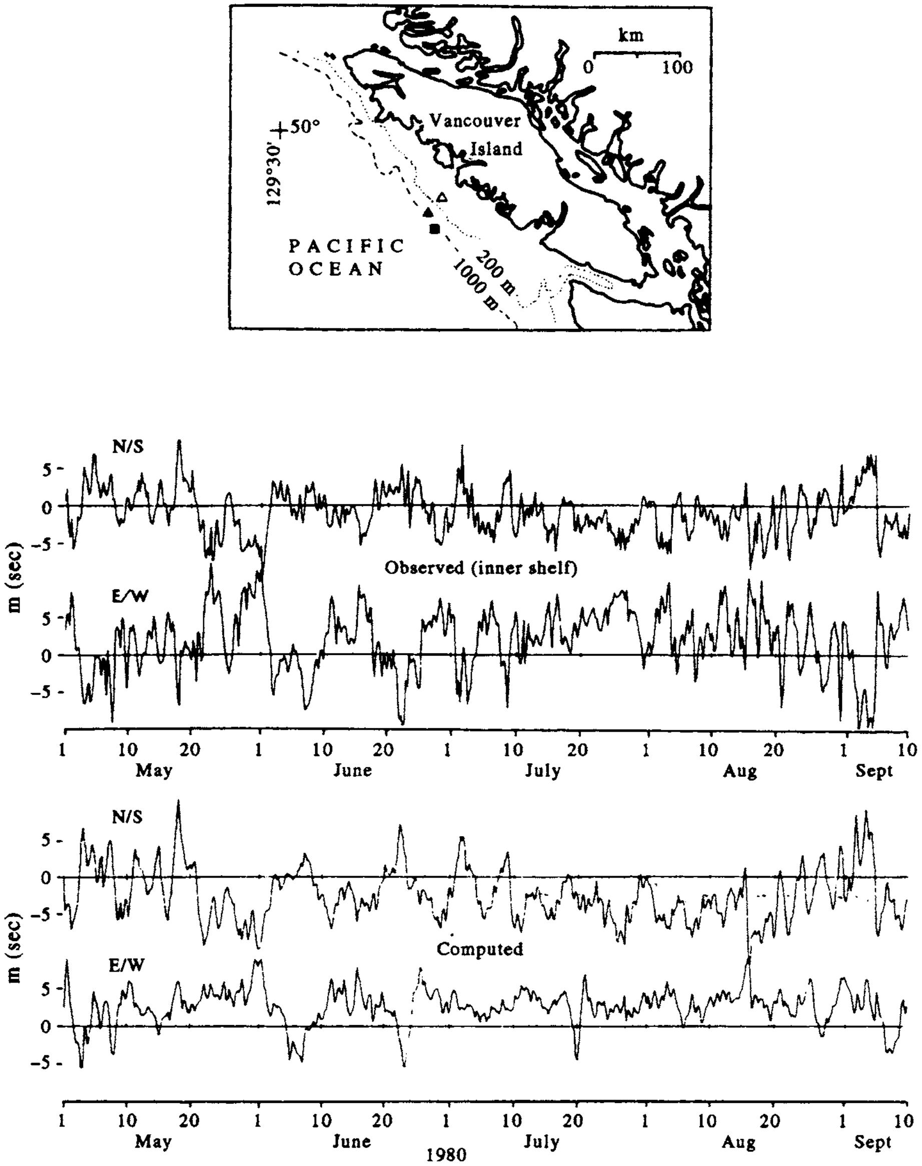

Figure 1.9.1. Comparison of observed and calculated oceanic winds for the period May to September 1980 on the west coast of Vancouver Island. Insert shows location of the moored bouys for 1979 and 1980 (triangles) and location of grid point (49°N, 127°W) for the geostrophic winds. Observed winds are from anemometers on moored buoys; calculated winds are the six-hourly geostrophic winds provided by the National Marine Fisheries Service (NMFS) in Monterey, California. (From Thomson, 1983.)

Oceanographers often use winds measured at coastal stations when studying problems of the nearshore marine environment. The primary caution with these data is that winds should be corrected for local orographic effects especially along mountainous coasts (Macklin *et al.*, 1993). If the wind data are to be considered representative of the coastal ocean region, the wind sensor must be unobstructed along the direction of the wind. If not ideally situated, the measured wind data can still be used if the directional data are weighted to account for the bias due to local wind-channeling by the topography. Marsden (1987) found good agreement between measured and calculated winds at the rugged but exposed anemometer site at Cape St. James on the British Columbia coast, but relatively poor agreement for these winds at the protected coastal station at Tofino Airport 300 km to the south of the Cape.

Finally some comments about future wind measurements are appropriate. As new *in situ* sensing methods evolve, emphasis is being placed on the ability to measure wind over the ocean. An attractive new method is to detect changes in the ambient acoustic noise level due to wind-driven surface effects. The exact mechanisms causing these acoustic noise variations are still being investigated but empirical data clearly suggest a linear relationship to wind-stress fluctuations. Even more attractive is the future possibility of monitoring the wind over the ocean from polar orbiting satellites using a microwave scatterometer. The usefulness of such data was clearly demonstrated during the SEASAT mission (Brown, 1983) which confirmed scatterometer accuracies of 1–2 m/s (speed) and 1–20° (direction). A study of SEASAT data (Thompson *et al.*, 1983) has shown that radar backscatter from the ocean depends on surface wind stress for a wide range of transmitted wavelengths. These authors found that SEASAT synthetic aperture radar (SAR) data, combined with simultaneous SEASAT scatterometer data, provided a good estimate of the coefficient of wind speed to wind stress. Hence, in the future, it may be possible to measure wind stress directly rather than infer it from wind or pressure measurements. In the past decade, a number of new systems have been deployed that are capable of measuring wind speed over the ocean. The GEOSAT altimeter discussed earlier is able to observe wind speed from the change in the shape of the altimeter waveform. While direction sensing is not possible, the altimeter is able to provide relatively accurate wind speeds along the satellite subtracks every few kilometers (Witter and Chelton, 1991). This capability has been used by the U.S. Navy to routinely map the global wind field over the ocean. Comparisons of these winds with moored buoys and operational numerical model analyses have demonstrated the relative accuracy of these satellite winds.

In addition, the passive microwave sensor on the Defense Meteorological Satellite Program (DMSP) satellites, called the Special Sensor Microwave Imager (SSM/I), is able to sense wind speed but not direction (Figure 1.9.2; color plate). The SSMI is a seven-channel four-frequency, linearly-polarized microwave radar operating in a sun-synchronous orbit at an altitude of 860 km. Three of the four channels (19.3, 37.0, and 85.5 GHz) are dual-polarized while the 22.2 GHz channel is only vertically polarized, for a total of seven channels. The nearly 1400 km swathe of the conically scanned SSM/I produces complete coverage between 87°36′S to 87°36′N every three days per satellite (Halpern *et al.*, 1993). There are now at least two SSM/I operating. While the spatial resolution is poor due to the sensing capabilities at the microwave frequencies, algorithms have been developed that appear to produce reliable estimates of wind speed over the open ocean (Wentz *et al.*, 1986; Gooberlet *et al.*, 1990; Halpern *et al.*, 1993). Wind speed accuracies are about ±2 m/s for the range of speeds between 3 and 25 m/s under rain-free conditions. Since the emissivity of land is very different from that of water, the SSM/I cannot be used to estimate wind speed within 100 km of land. Similarly, surface wind speed within 200 km of the ice edge cannot be computed from SSM/I data. However, wind speeds computed from the SSM/I compare reasonably well with open-ocean winds (Emery *et al.*, 1994). Waliser and Gautier (1993) find that in the central and eastern equatorial Pacific, SSM/I wind-speed comparisons were well

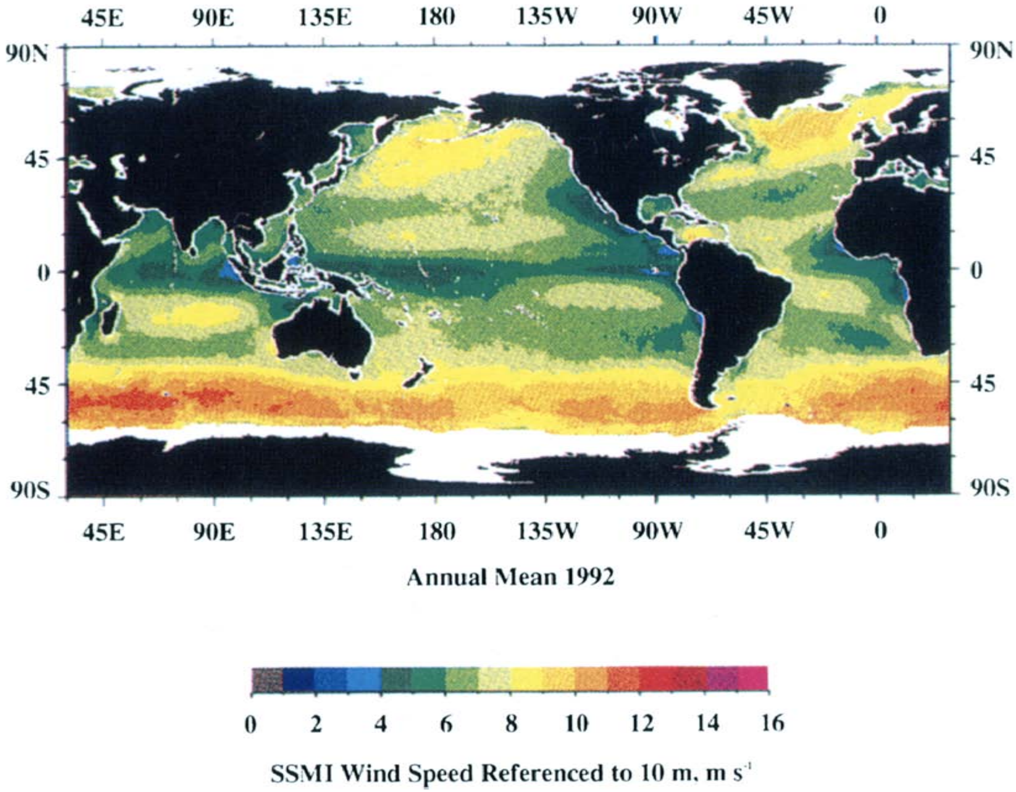

Figure 1.9.2. Global annual mean of the SSMI (Special Sensor Microwave Imager) surface wind speed for 1991. Courtesy of David Halpern (from Halpern et al., July 1993). JPL Publication 93-10.

within the accuracies specified for the SSM/I. Biases (buoy-SSM/I) were generally less than 1 m/s and RMS differences were less than 2 m/s. However, in the western equatorial Pacific, biases were generally greater than 1–3 m/s and RMS differences closer to 2–3 m/s. According to Waliser and Gautier, "... there are still some difficulties to overcome in understanding the influences that local synoptic conditions (e.g. clouds/rainfall), and even background atmospheric and oceanic climatology effects, have on the retrieval of ocean-surface wind speeds from spaceborne sensors."

The most comprehensive space-borne measurement of the wind field is made using a microwave scatterometer which measures the radar scattering cross-section of the sea surface at different incidence and azimuthal angles. The SEASAT scatterometer demonstrated the applicability of this instrument for the measurement of open-ocean wind speed and direction. Using a combination of fan-beam antennas, the scatterometer is able to compute both the wind speed and direction. As with many other satellite borne systems, the scatterometer uses the Doppler shift of the received signal to compute the speed component while multiple fan-beam antennas (called sticks) are required to unambiguously resolve the wind direction. Since scattering cross-section at radar frequencies is mostly related to the small wavelets that form when the wind acts on the sea surface, the scatterometer signal is actually related to the wind stress rather than to the wind speed. Unlike anemometers and other like instruments, no additional conversion from wind speed to wind stress is needed. The problem is that all historical calibration information is based on wind speed and direction, rather than wind stress. As a consequence, all present algorithms still convert the scatterometer measurements to wind speed and direction. Studies of SEASAT scatterometer data (Pierson, 1981; Guymer *et al.*, 1981) have demonstrated the ability of the satellite scatterometer to reliably measure wind speed and direction relative to ship and buoy observations. New scatterometers are flying on the European ERS-1 satellite and on the NASA–Japan ADEOS missions and other ERS satellites.

Trenworth and Olson (1988) consider the surface wind field computed by the European Centre for Medium-range Weather Forecasting (ECMWF) to be the best winds for general operational global analyses. ECMWF forecast-analyses of surface wind components at 10 m height are issued twice a day at 00 and 12 UTC. Numerical modelers examining large-scale circulation in the Pacific Ocean typically make use of the monthly mean and annual wind stress climatology provided by the Hellerman and Rosenstein (1983) wind fields. These data have problems near the equator where they tend to underestimate wind strength.

1.10 PRECIPITATION

Precipitation is one of the most difficult and challenging measurements to make over the ocean. Simple rain gauges installed on ships are invariably affected by salt spray and wind flow over the ship's hull and superstructure, and the short space and time scales of precipitation make it difficult to interpret point measurements. Rain gauges have two conflicting requirements that make use on shipboard difficult. First the gauge needs to be installed away from the ship influences, such as salt spray, which calls for positioning as high as possible on a mast. However, this conflicts directly with the second requirement, which calls for the regular maintenance of the gauge by ship's personnel. Few systematic studies have been made of precipitation measurements taken from ships, and little effort is made today to instrument ships to routinely observe rainfall over the ocean. A 25-year time-series from Ocean Station P (Figure 1.10.1) in the northeast Pacific is one of a few in the open ocean (most others were taken at Ocean Weather Stations similar to Station P). Unless some entirely new sampling procedure is developed, this situation is unlikely to change for the foreseeable future.

One new technique is to infer rainfall from variations in the upper-ocean acoustic noise. While it may seem a bit confusing to interpret ocean upper-layer acoustic noise both in terms of rainfall and wind, the frequency signatures of the two noise-generating mechanisms are sufficiently different to be distinguishable. Research is needed to define the accuracy of such a procedure and make at-sea precipitation measurements possible from moorings. These will still only provide point measurements and will not yield an improved spatial picture of the rainfall distribution. There are indications that future microwave satellite sensors, both active and passive, might be used to infer spatial variations in precipitation activity. SEASAT results were again encouraging in this regard but the validity of such measurements was not yet established. At any rate, it is presently impossible to attach any accuracy limits to what few ocean rain data are available. These data are so lacking that their relatively large uncertainty is not important. Any improvement in the analysis of precipitation measurements awaits the technical progress required to produce reliable at-sea rain data.

The 1987 launch of the Special Sensor Microwave Imager (SSM/I) on one of the Defense Meteorological Satellite Program satellites provided a new opportunity to infer precipitation from microwave satellite measurements. While a precipitation algorithm was developed prior to the launch (Hollinger, 1989) later studies have improved upon this algorithm to formulate better retrievals of precipitation over both

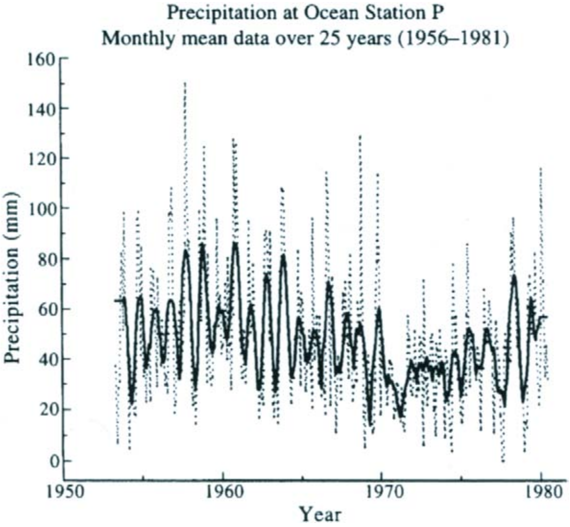

Figure 1.10.1. A 25-year time-series (1956–1981) of precipitation collected from Canadian Weather Ships at Ocean Station PAPA (50°N, 145°W) in the northeast Pacific. Solid line is from use of a Savitsky-Golay smoother (order = 13 months). (Data courtesy, Sus Tabata.)

land and ocean. In the list of "environmental products" for the SSM/I the "precipitation over water" field shows a 25 km resolution, a range of 0–80 mm/h, an absolute accuracy of 5 mm/h for quantization levels of 0, 5, 10, 15, 20, and $\geq$25 mm/h. This algorithm utilized both the 85.5 and 37 GHz SSM/I channels, thus limiting the spatial resolution to the 25 km spot sizes of the 37 GHz channel.

A study by Spencer *et al.* (1989) employed only the two different polarizations of the 85.5 GHz channel, thus allowing the resolution to improve to the 12.5 km per spot size of this channel. This algorithm was compared with 15-min rain gauge data from a squall system in the southeast United States (Spencer *et al.*, 1989). The 0.01 inch (0.039 mm) rain gauge data were found to correlate well ($r^2 = 0.7$) with the SSM/I polarization corrected 85.5 GHz brightness temperatures. This correlation is surprisingly high considering the difference in the sampling characteristics of the SSM/I versus the rain gauge data. Portions of a rain system adjacent to the squall line were found to have little or no scattering signature in either the 85.5 or the 37 GHz SSM/I data due likely to the lack of an ice phase presence in the target area. This appears to be a limitation of the passive microwave methods to discern warm rain over land.

1.11 CHEMICAL TRACERS

Oceanographers use a variety of chemical substances to track diffusive and advective processes in the ocean. These chemical tracers can be divided into two primary categories: *conservative* tracers such as salt and helium whose concentrations are affected only by mixing and diffusion processes in the marine environment; and *nonconservative* tracers such as dissolved oxygen, silicate, iron, and manganese whose concentrations are modified by chemical and biological processes, as well as by mixing and diffusion. The *conventional* tracers, temperature, salinity, dissolved oxygen and nutrients (nitrate, phosphate and silicate), have been used since the days of Wüst (1935) and Defant (1936) to study ocean circulation. More recently, *radioactive* tracers such as radiocarbon (^{14}C) and tritium (^{3}H) are being used to study oceanic motions. The observed concentrations of those substances which enter from the atmosphere must first be corrected for natural radioactive decay and estimates made of these substance's atmospheric distribution prior to their entering the ocean. If these radioactive materials decay to a stable daughter isotope, the ratio of the radioactive element to the stable product can be used to determine the time that the tracer was last exposed to the atmosphere. *Transient tracers*, which we will consider separately, are chemicals added to the ocean by anthropogenic sources in a short time span over a limited spatial region. Most transient tracers presently in use are radioactive. What is important to the physical oceanographer is that chemical substances that enter the ocean from the atmosphere or through the seafloor provide valuable information on a wide spectrum of oceanographic processes ranging from the ventilation of the bottom water masses, to the rate of isopycnal and diapycnal (cross-isopycnal) mixing and diffusion, to the downstream evolution of effluent plumes emanating from hydrothermal vent sites.

Until recently, many of these parameters required the collection and post-cast analysis of water bottle samples using some which are then subsampled and analyzed by various types of chemical procedures. There are excellent reference books presently available that describe in detail these methods and their associated problems (e.g. Grasshoff *et al.*, 1983; Parsons *et al.*, 1984). The book by Grasshof *et al.* (1983) also contains an excellent section on water samples and their application to chemical analyses. There are important concerns for the reliability of the chemical measurements regarding contamination of the sampling bottle or the subsampling procedure. Also, the volumes required for different chemical analyses vary greatly. A list of sample volumes for chemical observations as part of the World Ocean Circulation Experiment (WOCE) can be found in Volume I of the WOCE Implementation Plan (WOCE, 1988). It is certain that the collection of these volumes will include both presently available "off-the-shelf" samplers, sampling systems newly developed by private companies and sampling units designed and built by scientists. In any case, the precision and accuracy of these measurements depends, in part, on the sampling technique used.

Modern chemical "sniffers" (or chemical pumps) are being developed that allow for *in situ* analysis of samples (Lupton *et al.*, 1993). The requirement for *in situ* chemical sampling of hydrothermal vents lead to the development of the submersible chemical analyzer (SCANNER) for analyses of Mn and Fe, the SUAVE (submersible system used to assess vented emissions) for Mn, Fe, Si, H_2S, and one of PO_4 or Cl, and the ZAPS (zero angle photon spectrophotometer) for detecting dissolved Mn to ambient seawater concentrations (≤ 1 nmol l^{-1}) (Lilley *et al.*, 1995). The SCANNER and SUAVE systems comprise online colorimetric chemical detectors while ZAPS is a fiber-optic spectrometer which combines solid-state chemistry with PMT detection to make flow-through *in situ* chemical measurements.

For many chemical measurements, no single set of procedures applies so that groups, or individual scientists, must be responsible for their own data quality. It is impossible to evaluate after-the-fact the influences of sampling technique, sample history (storage, etc.) and analysis technique. It is therefore more difficult to attach levels of accuracy to these diverse methods. In this text, we will make some general comments regarding potential problems for each of the important parameters. For a more extensive discussion of chemical tracers, the reader is referred to Broecker and Peng (1982) and Charnock *et al.* (1988).

1.11.1 Conventional tracers

1.11.1.1 Temperature and salinity

If it were not for large-scale geographical differences in heat and buoyancy fluxes through the ocean surface from the overlying atmosphere, ocean temperatures and salinity would be nearly homogeneous, disrupted only by input from geothermal heating through the seafloor (Warren, 1970; Jenkins *et al.*, 1978; Reid, 1982). In fact, below 1500 m depth the salinity range throughout the world ocean is only about 0.5 psu despite the regular deep-water formation at high latitudes (Warren, 1983). Temperature, salinity, and density distributions enable us to identify different water masses and track the movement of these water masses in the world oceans.

Atlases of temperature and salinity for the Atlantic Ocean were produced by Wüst (1935) and Defant (1936) using data from the 1925–1927 *Meteor Expedition*. These maps help define the depths of vertical mixing and upwelling in the upper ocean and reveal the extent of ventilation of deep and intermediate waters by sinking of cold, high salinity, high density water from the Southern Ocean and the Labrador Sea.

Updated atlases for the Atlantic were presented in Fuglister (1960) and Worthington (1976). Similar maps for the Pacific Ocean were produced by Reid (1965) and Barkley (1968). Reid's atlas included distributions of dissolved oxygen and inorganic phosphate/phosphorous. An atlas of water properties for the North Pacific was presented by Dodimead *et al.* (1963) and Favorite *et al.* (1976). Wyrtki (1971) provided conventional tracer data for the Indian Ocean obtained from the International Indian Ocean Expedition. An atlas of the Bering Sea is provided by Sayles *et al.* (1979). A summary of the global water mass distribution can be found in Emery and Meincke (1985). Surveys conducted during the World Ocean Circulation Experiment (1991–1997) will provide updated maps of conventional tracer distributions in the global ocean.

1.11.1.2 Dissolved oxygen

Along with temperature and salinity, dissolved oxygen concentration is considered one of the primary scalar properties needed to characterize the physical attributes of marine and freshwater environments. Although it is not usually a conservative quantity, dissolved oxygen serves as a valuable tracer for mixing and ventilation throughout the water column and is a key index of water quality in regions of strong biological oxygen demand (BOD). This demand may arise from animal respiration, bacteria-driven decay, or nonorganic chemical processes (the discharge of pulp-mill effluent into the marine environment places a heavy burden on oxygen levels). Dissolved oxygen is widely used by physical oceanographers to delineate water-mass distributions, to estimate the timing and intensity of coastal upwelling processes and to establish the occurrence of deep water renewal events in coastal fjords. In a study of the North Pacific, Reid and Mantyla (1978) found that dissolved oxygen gives the clearest signal of the subarctic cyclonic gyre in the deep ocean.

The apparent oxygen utilization (AOU) is the difference between the possible saturated oxygen content at a given pressure and temperature, and the actually observed oxygen content (Figure 1.11.1). Below the euphotic zone, this parameter provides an approximate measure of biological demand due to respiration and decay. It also is commonly used to trace water-mass movement and to determine the "age" (defined as the time away from exposure to the surface source) of oceanic water masses. Use of AOU suggests that the intermediate waters of the northeast Pacific have an age of several thousand years and are among the oldest (last to be ventilated) waters of the world ocean. Mantyla and Reid (1983) arrived at similar conclusions based on global distributions of potential temperature, salinity, oxygen and silicate. A more complete discussion of this parameter can found in Chapter 3 of Broecker and Peng (1982).

The "core-layer" method introduced by Wüst (1935) identified water masses, and their boundaries, on the basis of maxima or minima in temperature, salinity and dissolved oxygen content. In the ocean, dissolved oxygen levels are high near the surface where they contact the atmosphere but rapidly diminish to a minimum near 500–1000 m due to the decay of upper-ocean detritus. Oxygen values again increase with depth toward the bottom. Wyrtki (1962) discusses the relationship between the observed subsurface oxygen minimum in the North Pacific and the general circulation of the ocean, suggesting that it is to be a balance between upward advection, downward diffusion and *in situ* biological/chemical consumption. Miyake and Saruhashi (1967) argued that the effect of horizontal advection has a much greater effect on

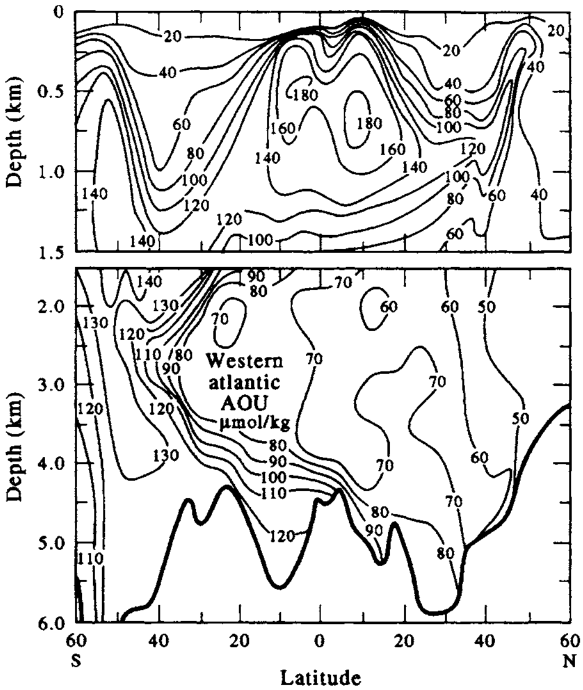

Figure 1.11.1. Vertical section of Apparent Oxygen Utilization (AOU) in mol/kg for the western basin of the Atlantic Ocean. (Figure 3.9 from GEOSECS program, Broecker and Peng, 1982.) The section is broken at 1500 m depth.

dissolved oxygen distributions than horizontal diffusion and biological consumption. In certain deep regions of the ocean, such as the Weddell Enderby Basin off Antarctica, the consumption of oxygen is below the detectable limit of the data so that oxygen may serve as a conservative chemical tracer (Edmond *et al.*, 1979).

When water bottle sampling was the only method for oceanographic profiling, the measurement of dissolved oxygen was only slightly more cumbersome and time-consuming than the measurement of temperature and salinity. The advent of the modern CTD with its rapid temperature and conductivity responses has left oxygen sampling behind. Thus, despite the importance of dissolved oxygen distributions to our understanding of chemical processes and biological consumption in the ocean, dissolved oxygen is far less widely observed than temperature or salinity. At present, there are two principal methods for measurement of dissolved oxygen: (1) water bottle sampling followed by chemical "pickling" and endpoint titration using the Winkler method (Strickland and Parsons, 1968; Hichman, 1978); and (2) electronic sampling using a membrane covered polarographic "Clark" cell (Langdon, 1984). The primary problems with standard water-bottle sampling of dissolved oxygen are the potential for sample contamination by the ambient air when the subsampling is carried out on deck, poor sampling procedure (such as inadequate rinsing of the sample bottles), and the oxidization effects caused by sunlight on the sample. Thus, laboratory procedures call for the immediate fixing of the solution after it is drawn from the water bottle by the addition of manganese chloride and alkaline iodide. During the pickling stage of the Winkler method, the dissolved oxygen in the sample oxidizes Mn(II) to Mn(III) in alkaline solution to form a precipitate MnO_2. This is followed by oxidation of added I^- by the Mn(III) in acidic solution. The resultant I_2 is titrated with thiosulfate solution using starch as an endpoint indicator. After the sample is chemically "fixed", the precipitate that forms can be allowed to settle for 10–20 min. At this stage, samples may be stored in a dark environment for up to 12 h before they need to be titrated. Parsons *et al.* (1984) give the precision of their recommended spectrophotometric method as $\pm 0.064/N$ (mg/l), where N is the number of replicate subsamples processed. The Winkler method is accurate to 1% provided the chemical analysis methods are rigorously applied. Another measure is the percentage saturation, which is the ratio of dissolved oxygen in the water to the amount of oxygen the water could hold at that temperature, salinity and pressure. Saturation curves closely follow those for dissolved oxygen.

In situ electronic dissolved oxygen sensors have been developed for use with profiling systems such as the CTD. All existing sensors use a version of the Clark cell which operates on the basis of electro-reduction of molecular oxygen at a cathode. When used in a polarographic mode, the electric current supplied by the cathode is proportional to the oxygen concentration in the surrounding fluid. To lessen the sensitivity of the device to turbulent fluctuations in the fluid, the electrode is covered with an electrolyte and membrane. Oxygen must diffuse down-gradient through the membrane into the electrolyte before it can be reduced at the surface of the cathode. There are a number of drawbacks with the present systems. First of all, the diffusion of oxygen through the boundary layer near the surface of the probe is slow, limiting the response time of the cell to several minutes. Also, the electrochemical reaction within the cell consumes oxygen and stirring may be required to maintain the correct external oxygen concentration. Changes in the structure of the cell—due to alterations in the diffusion characteristics of the membrane as a result of temperature, mechanical stress and biofouling and to deterioration of the electrolyte and surfaces—require that the cell be recalibrated every several hours. The need for frequent recalibration limits the use of the polarographic technique for profiling and mooring applications. Langdon (1984) uses a pulse technique to reduce the calibration drift. This improves long-term stability but time constants are still the order of minutes.

The YSI (Yellow Springs Instruments) and Beckman (Beckman part No. 147737) polaragraphic dissolved oxygen sensors (Brown and Morrison, 1978) sense the oxygen content by the current in an electrode membrane combined with a thermistor for membrane temperature correction. The current through this membrane depends on the dissolved oxygen in the water and the temperature of the membrane. Samples of both membrane current and temperature are averaged every 1.024s giving a resolution of 0.5 μA (microamps) with an accuracy of ± 2 μA over a range of 0–25 μA. These *in situ* sensors have yet to be critically evaluated with reference to well tested and approved methods. There are concerns with changes in the membrane over the period of operations and problems with calibration. Nevertheless, as measurement technology improves, an *in situ* oxygen sensor will be a high priority in that it saves considerable processing time and avoids errors possible with shipboard processing.

Fluorescence quenching is a promising technique that may make it possible to couple the modern CTD with a rapid and stable dissolved oxygen sensor. Although the use of fluorescence quenching for oxygen determination has been known since the 1930s (Kautsky, 1939) and widely used for *in vivo* measurement of the partial pressure of oxygen in blood (Peterson *et al.*, 1984), the first application in oceanography was not reported until 1988 (Thomson *et al.*, 1988). This fluorescence-based dissolved oxygen sensor operates on the principle that the fluorescence intensity of an externally light-excited fluorophore will be attenuated or "quenched" in direct relation to the concentration of dissolved oxygen in an ambient fluid (Figure 1.11.2a). Optimum results are obtained using high-intensity blue-light source (wavelength of 450–500 nm) since this is the wavelength that most readily excites the known fluorophores. Results from a six-day time-series record of dissolved oxygen concentration from a moored instrument in Saanich Inlet in 1987 suggests that the technique can be used to

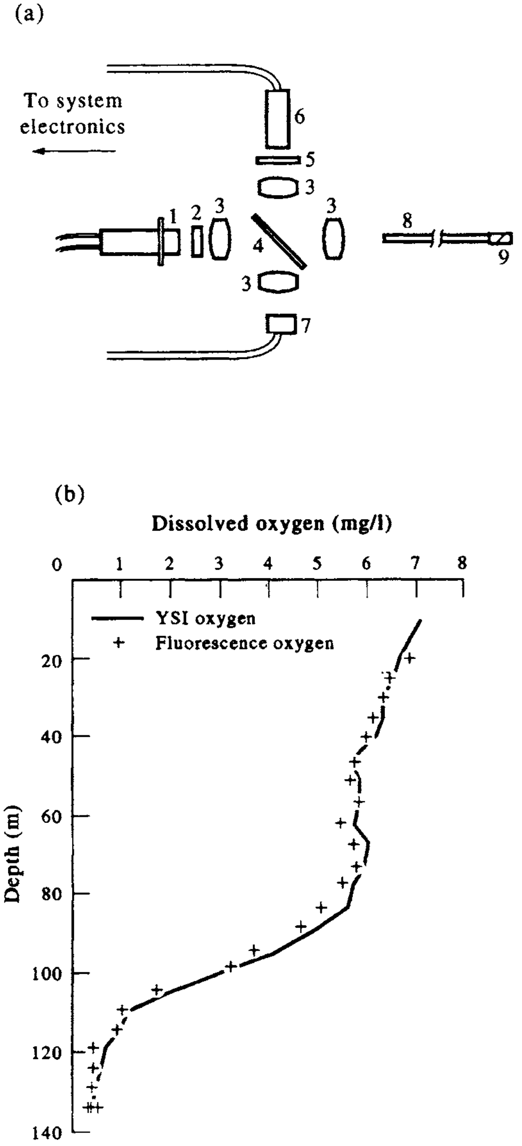

Figure 1.11.2. (a) Schematic of the first solid-state dissolved oxygen sensor. System uses blue-light from (1) to excite a fluorophore in the sensor tip (9). The concentration of dissolved oxygen in the ambient fluid sensed by (6) is proportional to the degree of quenching of blue light fluoresed by the chemical-dopped sensor. (b) Simultaneous profiles of oxygen in Saanich Inlet. YSI = YSI dissolved oxygen sensor. (From Thomson et al., 1988.)

build a rapid (<1 s) response profiling sensor (Figure 1.11.2b) with long-term stability and high (<0.1 ml/l) sensitivity. The fact that the oxygen spectra closely resemble the temperature spectra for the entire frequency band up to a period of 2 h suggests that the oxygen data are at least as stable as the thermistor on the Aanderaa RCM4 current meter that was used in the moored study. Since no blue-light source was available, the prototype device relied on a high-power white-light source and a car battery to drive the system. The present technological problem is to fabricate a blue-light source and a chemically-stable, fiber-optic, fluorescence-quenching probe capable of withstanding the rigors of shipboard operations and high hydrostatic pressures. Until now, lack of a commercial blue-light source with sufficient power (≈1 mW) to produce a strong fluorescence response appears to be the main impediment the development of the new dissolved oxygen sensor. The recent fabrication of blue-light light-emitting diodes (LED) and lasers will make it possible to rapidly sample dissolved oxygen as well as other dissolved gases such as carbon dioxide.

1.11.1.3 Nutrients

Nutrients such as nitrate, nitrite, phosphate and silicate are among the "old guard" of oceanic properties obtained on standard oceanographic cruises. One need only examine the early technical reports published by oceanographic institutions to appreciate the considerable effort that went into collection of these data on a routine basis. Oceanographers are again beginning to use these data on a routine basis to understand the distribution and evolution of water masses. However, there are a number of problems with nutrient collection that need to be heeded. To begin with, the data must be collected in duplicate (preferably triplicate) in small 10 mm vials and frozen immediately after the samples are drawn using a "quick freeze" device or alcohol bath. This is to prevent chemical and biological transformations of the sample while it is waiting to be processed. Careful rinsing of the nutrient vials is required as the samples are being drawn. Silicate must be collected using plastic rather than glass vials to prevent contamination by the glass silicate. Plastic caps must not be placed on too tightly and some space must be left in the vials for expansion of the fluid during freezing. Nutrient sample analysis is labour-intensive, time-consuming work. Although storage time can be extended to several weeks, we strongly recommend that nutrients be processed as soon as possible after collection, preferably on board the research ship using an autoanalyzer. With individual parameter techniques this is less likely to be possible than with more recent automated methods which have been developed to handle most nutrients (Grasshof *et al.*, 1983). These automated systems, which use colorimetric detection for the final measurement, need to be carefully standardized and maintained. Under these conditions, they are capable of providing high quality nutrient measurements on a rapid throughput basis.

Profiles of nutrients and dissolved oxygen for the North Pacific are presented in Figure 1.11.3. As first reported by Redfield (1958), the concentrations of nitrate, phosphate, and oxygen are closely linked except near source or sink regions of the water column. A weaker relationship exists between these variables and silicate. Nitrite only occurs in significant amounts near the sea surface where it is associated with phytoplankton activity in the photic zone and in the detritus layer just below the seasonal depth of the mixed layer. Although the linear relationships between these parameters varies from region to region, the reason for the strong correlations is readily explained. Within the photic zone, phytoplankton fix nitrogen, carbon and

(a) Marathon station 11 (24°48.3'N, 154°37.8'W)

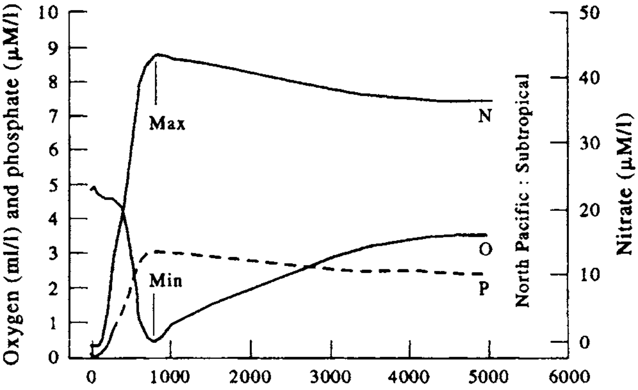

(b) Marathon station 50 (38°30.3'N, 152°0.3'W)

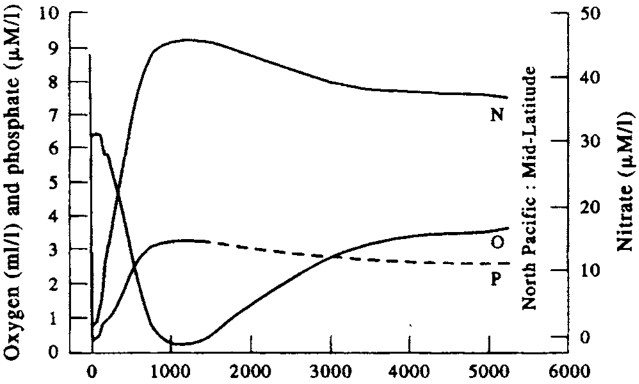

(c) Marathon station 86 (53°41.1'N, 151°58.9'W)

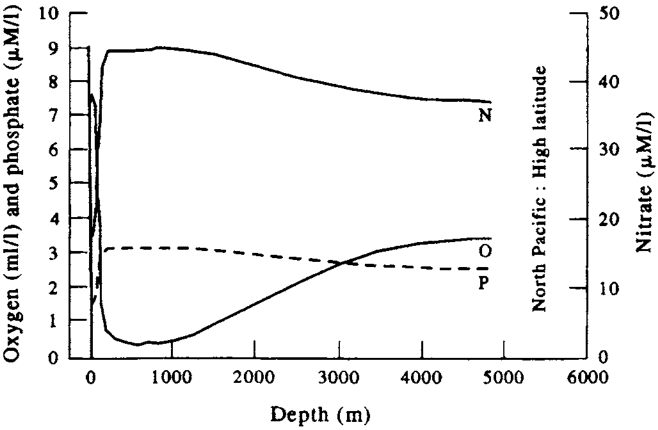

Figure 1.11.3. Plots of nitrate (N), phosphate (P) and dissolved oxygen (O) for the North Pacific. (a) Station 11 at 24°48.3'N; 154°37.8'W; (b) Station 50 at 38°30.3'N; 152°00.3'W; (c) Station 86 at 53°41.1'N; 151°58.9'W. (Data from Martin et al., 1987.)

other materials using sunlight as an energy source and chlorophyll as a catalyst. In regions of high phytoplankton activity such as mid-latitudes in summer, the upper layers of the ocean are supersaturated in oxygen and depleted in nutrients. That is, there are sources and sinks for oxygen and nutrients. However, below the photic zone, bacterial decay and dissolution of detritus raining downward from the upper ocean leads to chemical transformations of oxidized products. This, in turn, leads to a reduction of oxygen compounds and corresponding one-to-one release of nitrate, phosphate and silicate. This linear relation would prevail throughout the ocean below the photic zone if weren't for other sources and sinks for these chemicals. For example, we now know that silicate enters the ocean through resuspension of bottom sediments and from hydrothermal fluids vents from mid-ocean ridge systems (Talley and Joyce, 1992). Chemosynthetic production by bacteria in hydrothermal plumes is also a source/sink region as the analog to photosynthetic processes in the upper ocean.

It is generally thought that limitations in upper ocean nutrients, especially nitrates, combined with zooplankton predation (grazing) and turbulent mixing processes control primary (phytoplankton) productivity in the ocean. More recently, it has been proposed that other nutrients such as the aeolian supply of iron compounds might ultimately control productivity in areas such as the equatorial and subarctic Pacific and the Southern Ocean where nitrate concentrations are high year-round but spring and fall blooms do not occur (Chisholm and Morel, 1991). These high nutrient, low chlorophyll (HNLP) regions have become the focus of increasing numbers of multidisciplinary studies.

In a classic paper, Redfield (1958) suggested that organisms both respond to and modify their external environments. His premise was that the nitrate of the ocean and the oxygen of the atmosphere are determined by the biochemical cycle and not conditions imposed on the organisms through factors beyond their control. Support for his thesis was derived from the fact that the well-defined nitrogen, phosphorous, carbon, and oxygen compositions of plankton in the upper ocean were almost identical to the concentrations of these elements regenerated from chemical processes in the 95% of the ocean that lies below the autotrophic zone. As pointed out by Redfield, the synthesis of organic material by phytoplankton leads to oceanic changes in concentration of phosphorous, nitrogen, and carbon in the ratio 1:15:106. During heterotrophic oxidation and remineralization of this biogenic material (i.e. decomposition of these organisms), the observed ratios are 1:15:105. Thus, for every phosphorous atom that is used by phytoplankton during photosynthesis in the euphotic zone, exactly 15 nitrogen atoms and 106 carbon atoms are used up. Alternatively, for every phosphorous atom that is liberated during decomposition in the deep ocean, exactly 15 nitrogen and 105 carbon atoms are liberated. The oxidation of these atoms during photosynthesis requires about 276 oxygen atoms while during decomposition 235 oxygen atoms are withdrawn from the water column for each atom of phosphorous that is added. If this process were simply one way, the primary nutrients would soon be completely depleted from the upper ocean. That is why life supporting replenishment of depleted nutrients to the upper ocean through upwelling and vertical diffusion of deeper nutrient rich waters is such an important process to the planet. [Bruland *et al.* (1991) give a modern version of the Redfield ratios based on phytoplankton collected under bloom conditions as: C:N:P:Fe:Zn:Cu,Mn,Ni,Cd = 106:16:1:0.005:0.002:0.0004 (see also Martin and Knauer, 1973).]

According to the above ratios, the formation of organic matter by phytoplankton in the surface autotrophic zone leads to the withdrawal of carbonate, nitrate, and phosphate from the water column. Oxygen is released as part of photosynthesis and the upper few meters of the ocean can be supersaturated in oxygen at highly productive times of the year. When the plants die and sink into the deeper ocean, decomposition by oxidation returns these compounds back to the seawater. Thus, increases in carbonate, nitrate, and phosphate concentrations below the euphotic zone are accompanied by a corresponding decrease in oxygen levels. This process leads to a rapid increase in nitrate and phosphate and a corresponding rapid decrease in oxygen within the upper kilometer or so of the ocean (Figure 1.11.3). Nitrate and phosphate reach subsurface maximums at intermediate depths and then begin to decrease slowly with depth to the seafloor. Oxygen, on the other hand, falls to a mid-depth minimum (the oxygen minimum layer) before starting to increase slowly with depth toward the seafloor. In the upper zone, the balance of chemicals is altered considerably by biological activity while near the coast, the balance is altered by runoff which provides a different ratio of nutrients. However, below the surface layer, the changes occur in the manner suggested by the Redfield ratios (Redfield *et al.*, 1963). Note that the concentration of silicate is almost like that of the other nutrients, except that it doesn't reach a maximum at mid depth and becomes more decoupled from the accompanying oxygen curve. This suggests a source function for silicate in the deep ocean. Indeed, there are two sources; resuspension and dissolution of siliceous material from rocks and other inorganic material on the seafloor and the injection of silicates into the ocean from hydrothermal venting along mid-ocean ridges and other magmatic source regions in the deep ocean.

The fact that carbon and oxygen concentrations greatly exceed the levels required by plankton while those of phosphorous and nitrogen were identical to those observed on average in the ocean (carbon is at least 10 times that needed for photosynthesis), prompted Redfield to suggest that phosphate and nitrate are limiting factors to oceanic primary productivity. It is thought that nitrate (NO_3) is the primary limiting factor although phosphorous limitation is still important in certain coastal areas. Airborne iron is also thought to be a limiting nutrient for primary productivity in the open ocean. Evidence for this is based on the year-round absence of phytoplankton blooms in the subarctic Pacific, equatorial Pacific and Southern Ocean despite the high near-surface concentrations of nitrate and phosphate. In these areas, autotrophic processes fail to exploit NO_3 and PO_4. The idea is that iron, or some other mineral, limits growth, which is not the case in areas served by aeolion transport from the land. Unfortunately, it not yet possible to sort out the effects of iron limitations from grazing by herbivorous zooplankton or from physical mixing in the surface layer which prevents stratification from confining the animals to a thin upper layer. A recent experiment conducted over an 8 km square area of the equatorial Pacific 500 km south of the Galápagos Islands showed that iron enrichment can dramatically increase surface productivity. Using sulfur hexafluoride to track the 480 kg of iron sulfate solution added to the ocean, scientists found that the rate of growth and total mass of phytoplankton doubled over a period of three days. However, the iron soon precipitated out of solution as ultra-fine particles and sank, causing a sharp decrease in productivity levels. The question of iron enrichment and ocean productivity remains unresolved.

1.11.1.4 Silicate

The oceanic distribution of many elements is determined by their involvement in the biochemical cycle. Nitrate and phosphate are associated with the labile tissue and protoplasm of surface plankton whereas silicate and alkalinity are linked to the refractory hard parts of the organisms. The term "silicate" applies to dissolved reactive silicate [monosilicic acid, $Si(OH)_4$; Iler, 1979] measured from water samples. Since most of the silicate undergoes dissolution in the water column rather than the seafloor (Edmond *et al.*, 1979), its distribution serves as tracer for water-mass mixing and advection. The advantage of silica over carbonates or other compounds is that siliceous sediments are found only in well-defined areas associated with surface upwelling and their distribution is not particularly dependent on depth. According to Edmond *et al.* (1979) the average flux of dissolved silica from the sediments to the deep ocean is about 3 μmol/cm^2/year which is sufficient to make it a useful tracer of deep sea flow. Large fluxes are observed in the Weddell-Enderby Basin off Antarctica and in the northern Indian Ocean.

In the extreme northeast Pacific (northeast of 45°N, 160°W), silicate concentration increases with depth to the bottom while in the equatorial Pacific no anomalies are observed despite the presence of opaline deposits. The increased silicate with depth in the northeast Pacific appears to be associated, in part, with westward advection of dissolved siliceous sediments deposited over the continental margin of the wind-induced upwelling domain that extends from British Columbia to Baja California along the west coast of North America. As noted by Edmond *et al.* (1979), the existence of silica sources at the seafloor makes it impossible to use global correlations with the extensive silicate distribution data to determine the distribution of other variables such as trace metals. Historical data, together with transect data collected along 47°N (Talley *et al.*, 1988), further suggest that both the intermediate silica maximum in the depth range 2000–2400 m and the near-bottom silica maximum in Cascadia Basin to the east of the Juan de Fuca Ridge (Figure 1.11.4) may be due, in part, to hydrothermal venting of high silicate waters (Talley and Joyce, 1992). The silica in the hydrothermal plumes emanating from the vents originates as silicates stripped from the crustal rocks by the high-temperature hydrothermal fluids. Other factors include vertical flux divergence of settling silicate particles, dissolution from opaline bottom sediments, and up-slope injection from the bottom boundary layer.

Macdonald *et al.* (1986) point out that improper thawing of frozen silicate samples can result in a significant and variable negative bias in seawater determination of silicate. The problem arises from conversion of reactive silicate to a nonreative, polymetric form in the frozen sample. This polymerization need not affect accuracy for frozen samples provided that sufficient thawing time is allowed for depolymerization to the reactive form. To control bias, the analyst must adjust the length of time between thawing and analysis. The appropriate "waiting time" varies according to the salinity of the sample, the silicate concentration and the length of time the sample was frozen. Waiting time increases with the time that the samples were frozen and with silicate/salinity ratio. For example, deep silicate samples collected from the northeast Pacific (salinity ≈ 35 psu; silicate ≈ 180 μmol/l) and stored for one to two months must be thawed for about 8 h before processing. This increases to 24 h for samples stored for more than five to six months. Macdonald *et al.* conclude that "If the objectives of sampling can accept a 5% negative bias and a slight loss of precision,

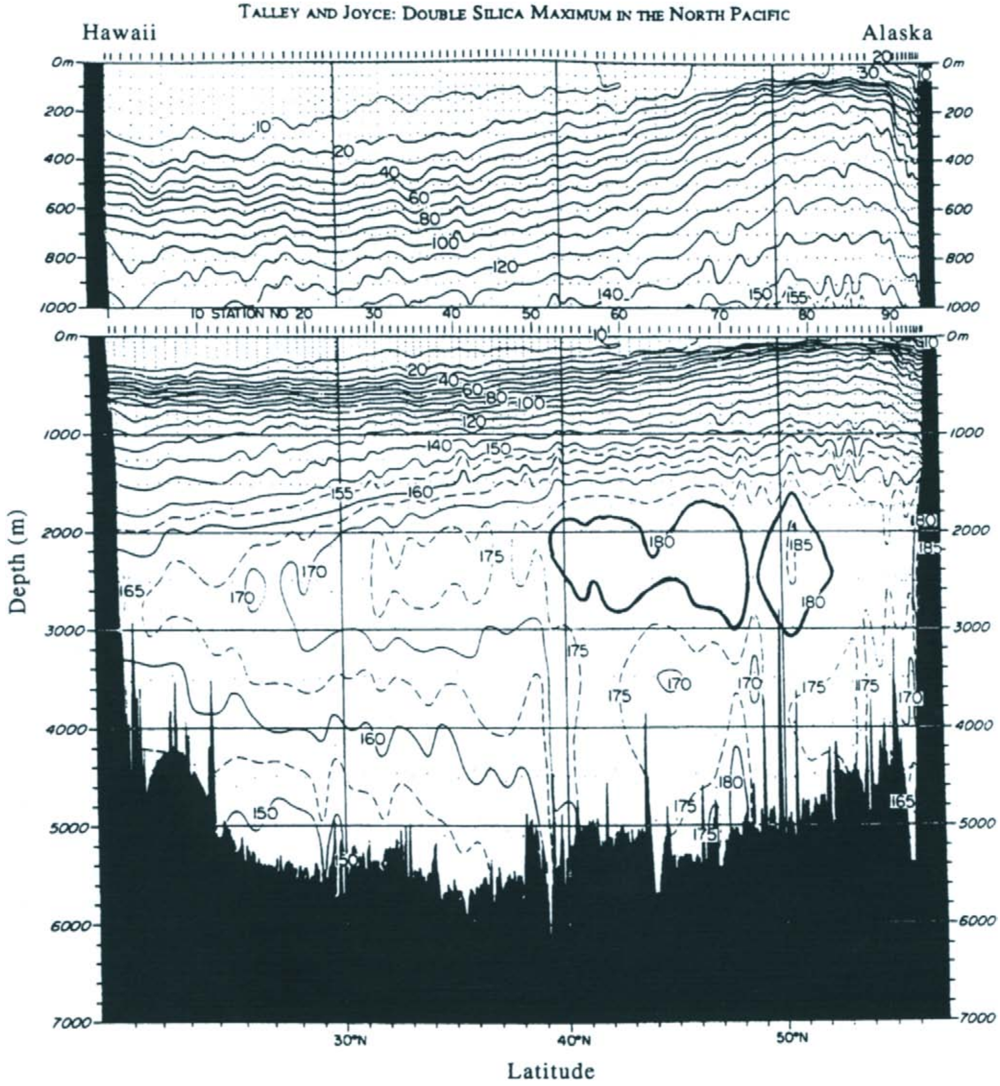

Figure 1.11.4. The meridional distribution of silica (micromoles per liter) in the North Pacific along approximately 152°W (Hawaiian region to Kodiak Island, Alaska). Mid-depth maximum values in excess of 180 μmol/l are emphasized. (From Talley et al., 1991; Talley and Joyce, 1992.)

then freezing is a simple method for storing a wide range of samples. However, samples should be analyzed as soon as practicable".

1.11.2 Light attenuation and scattering

The light energy in a fluid is attenuated by the combined effects of absorption and scattering. In the ocean, absorption involves a conversion of light into other forms of energy such as heat; scattering involves the redirection of light by water molecules, dissolved solids and suspended material without the loss of total energy. Transmissometers are optical instruments that measure the clarity of water by measuring the fraction of light energy lost from a collimated light beam as it passes along a known pathlength (Figure 1.11.5). Attenuation results from the combined effects of absorption and shallow-angle Rayleigh (forward) scattering of the light beam by impurities and fine particles in the water. Water that is completely free of impurities is optically pure. Nephelometers (or turbidity meters) measure scattered light and respond primarily to the first-order effects of particle concentrations and size. Depending on manufacturer, commercially available nephelometers examine scattered light in the range from 90° to 165° to the axis of the light beam. Most instruments use infrared light with a wavelength of 660 nm. Because light at this wavelength is rapidly absorbed in water (63% attenuation every 5 cm), there is little contamination of the source beam due to sunlight except within the top meter or so of the water column.

The intensity $I(r)$ of a light beam of wavelength λ traveling a distance r through a fluid suspension attenuates as

$$I(r) = I_o \exp(-cr) \tag{1.11.1}$$

where I_o is the initial intensity at $r = 0$ and $c = c(\lambda)$ is the rate of attenuation per unit distance. Attenuation of the light source occurs through removal or redirection of light beam energy by scattering and absorption. In the ocean, visible long-wave radiation (red) is absorbed more than visible short-wave radiation (blue and green) and what energy is left at long wavelengths undergoes less scattering than at short wavelengths. As a consequence, the ocean appears blue to blue-green when viewed from above. The exact color response depends on the scattering and absorption characteristics of the materials in the water including the dissolved versus the suspended phase—factors that are used to advantage in remote sensing techniques. For a fixed monochromatic light source, the clarity of the water, measured relative to distilled uncontaminated water, provides a quantitative estimate of the mass or volume concentration of suspended particles. Such material can originate from a variety of sources including terrigenous sediment carried into the coastal ocean by runoff, from current-induced resuspension of material in the benthic layer, or from detectable concentrations of plankton.

The "Secchi disk" is one of the simplest and earliest methods for measuring light attenuation in the upper layer of the ocean. A typical Secchi disk consists of a flat, 30-

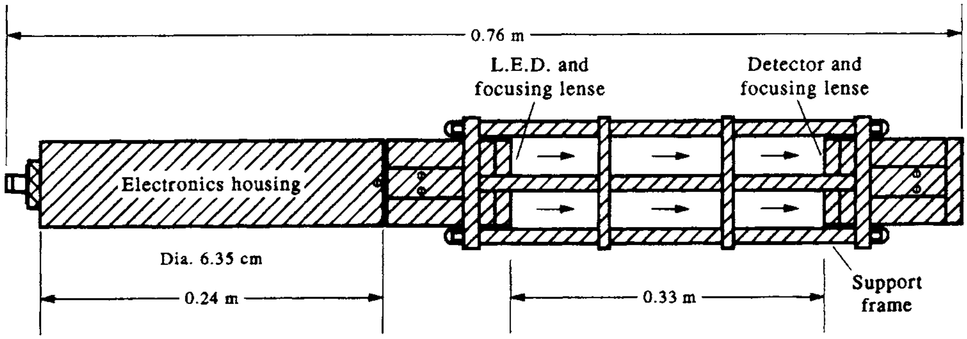

Figure 1.11.5. Exploded view of a Sea-Tech transmissometer. Red light of wavelength 690 nm passes from the light-emitting diode (LED) to the sensor over a fixed path length of 0.25 m.

cm diameter white plate that is lowered on a marked line (suspended from the disk center) over the side of the ship. The depth at which the disk can no longer be seen from the ship is a measure of the amount of surface light that reaches a given depth and can be used to obtain a single integrated estimate of the extinction coefficient, $c(\lambda)$. The disk is still in use today. For example, Dodson (1990) used Secchi disk data from a series of lakes in Europe and the U.S.A. that suggest a direct relationship between the depth of day–night (diel) migration of zooplankton and the amount of light penetrating the epihelion. In this case, the zooplankton minimize mortality from visually feeding fish and maximize grazing rate. Despite its simplicity, there are a number of problems with this technique, notwithstanding the fact that it fails to give a measure of the water clarity as a function of depth and is limited to near-surface waters. In addition, the visibility of the disk will depend on the amount of light at the ocean surface (and type of light through cloud cover), on the roughness of the ocean surface, and the eyesight of the observer. Today, oceanographers rely on transmissometers and nephelometers to determine the clarity of the water as a function of depth.

A typical transmissometer consists of a constant intensity, single frequency light source and receiving lens separated by a fixed pathlength, r_o. The attenuation coefficient in units of m^{-1} is then found from the relation

$$c = -(1/r_o)\ln(I/I_o) \qquad (1.11.2)$$

in which r_o is measured in meters, and I/I_o is the ratio of the light intensity at the receiver versus that transmitted by the red (660 nm) LED. This choice of light wavelength is useful because it eliminates attenuation from dissolved organic substances consisting mainly of humic acids or "yellow matter" (also called "gelbstoff"; Jerlov, 1976). The Sea Tech transmissometer (Bartz *et al.*, 1978) has an accuracy of $\pm 0.5\%$ and a small ($<1.03^\circ$ or 0.018 radians) receiver acceptance angle that minimizes the complication of the collector receiving specious forward-scattering light. To obtain absolute values, the source and lens must be calibrated in distilled water and air since scatter can effect the results. As an example, a 0.25 m pathlength transmissometer which has a calibration value of $I_o = 94.6\%$ in clean water and reading of 89.1% in the ocean corresponds to a light attenuation coefficient

$$c = -4\ln(I/I_o) = -4\ln(0.891/0.946) = 0.240\,\mathrm{m}^{-1} \qquad (1.11.3)$$

Values of c in the ocean range from around 0.15 m^{-1} for relatively clear offshore water for concentrations of particles as low as 100 μg/l to around 21 m^{-1} for turbid coastal water with particle concentrations of 140 mg/l (Sea Tech user's manual). In studies of hydrothermal venting, measurement of water clarity is often one of the best methods to determine the location and intensity of the plume (Baker and Massoth, 1987; Thomson *et al.*, 1992; Figure 1.11.6).

Problems with the transmissometer technique are: (1) drift in the intensity of the light source with time; (2) clouding of the lens by organic and inorganic material which affect the *in situ* calibration of the instrument; and (3) scattering, rather than absorption, of the light. If we ignore the influence of dissolved substances, the attenuation coefficient, c, depends on the concentration of the suspended material but also on the size, shape, and index of refraction of the material (Baker and Lavelle, 1984). Thus, a linear relationship between c and particle concentration C such that

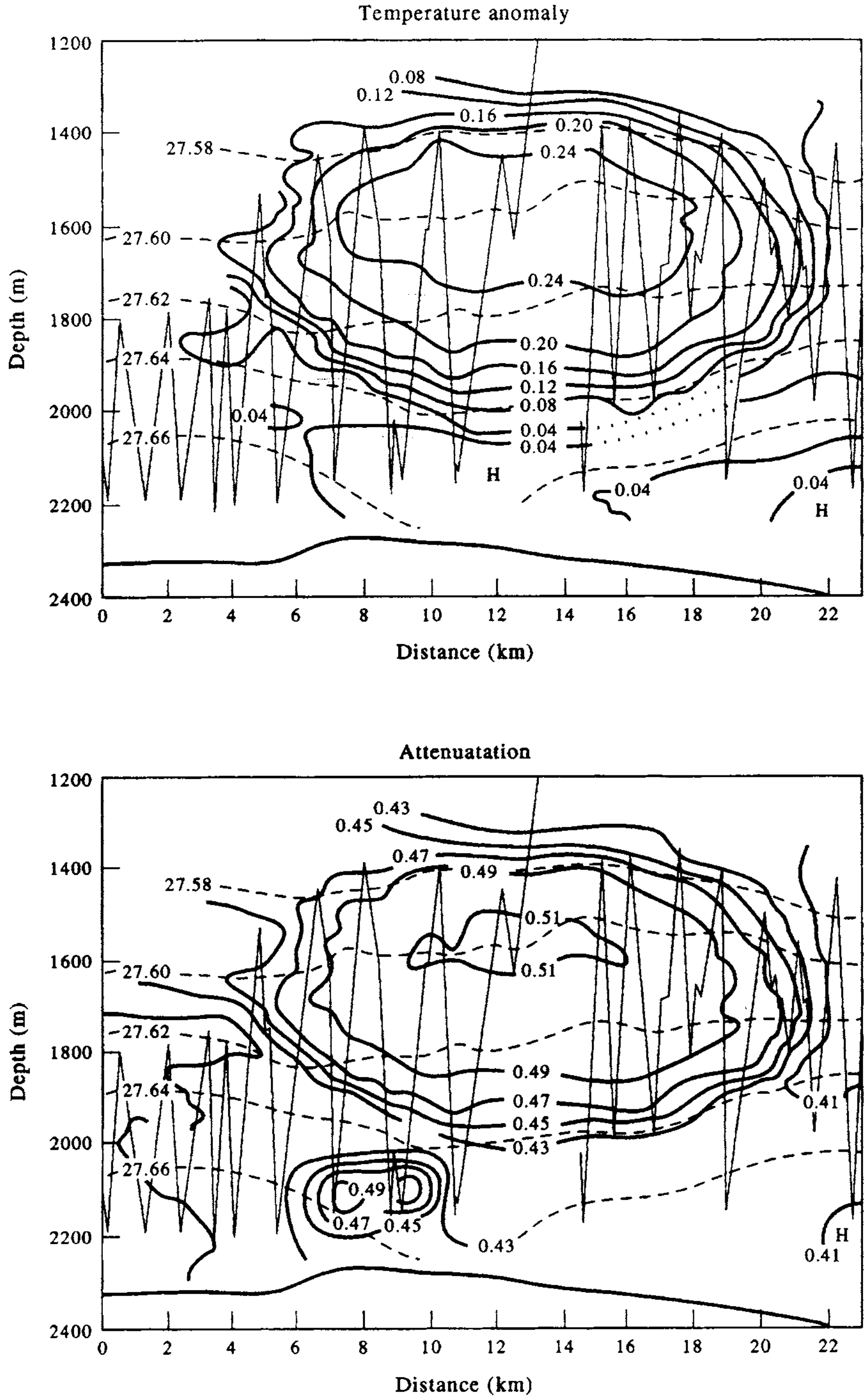

Figure 1.11.6. Cross-sections of temperature anomaly (°C) and light attenuation coefficient (m^{-1}) for the "megaplume" observed near the hydrothermal main site on the Cleft Segment of Juan de Fuca Ridge in the northeast Pacific in September 1986. Temperature anomaly gives temperature over the plume depth relative to the observed background temperature. Dotted line shows σ_θ surfaces and solid line the saw-tooth track of the towed CTD path. (From Baker et al., 1989.)

$$c = \alpha C + \alpha_o \tag{1.11.4}$$

only occurs when the effects of size, shape and index of refraction are negligible or mutually compensating. After concentration, particle size is the next most important variable effecting clarity. Accurate estimates of concentration therefore require calibration in terms of the distribution of particle sizes and shapes in suspension as for example in Baker and Lavelle (1984). Laboratory results demonstrate that calibrations of beam transmissometer data in terms of particle mass or volume concentration are acutely sensitive to the size distribution of the particle population under study. There is also a trend of decreasing calibration slopes from environments where large particles are rare (deep ocean) to those where they are common (shallow estuaries and coastal waters). Theoretical attenuation curves agree more with observation when the natural particles are treated as disks rather than as spheres as in Mie scattering theory. The need for field calibration is stressed.

The results of Baker and Lavelle (1984) can be summarized as follows: (1) calibration of beam transmissometers is acutely sensitive to the size distribution of the particle population under study; (2) theoretical calculations based on Mie scattering theory and size distributions measured by a Coulter counter-agree when attenuation for glass spheres is observed but underestimate the attenuation of natural particles when these particles are assigned an effective optical diameter equal to their equivalent spherical diameter deduced from particle volume measurements; (3) treating particles as disks expands their effective optical diameter and increases the theoretical attenuation slope close to the observed values; (4) there is a need to collect samples along with the transmissometer measurements, especially where the particle environment is nonhomogeneous.

Transmissometers are best used for measuring the optical clarity of relatively clear water whereas nephelometers are most suitable for measuring suspended particles in highly turbid waters. In murky waters, nephelometers have superior linearity over transmissometers while transmissometers are more sensitive at low concentrations. "Turbidity" or cloudiness of the water is a relative, not an absolute term. It is an apparent optical property depending on characteristics of the scattering particles, external lighting conditions and the instrument used. Turbidity is measured in nephelometer units (NTUs) referenced to a turbidity standard or in Formazin Turbidity Units (FTUs) derived from diluted concentrations of 4000-FTU formazin, a murky white suspension that can be purchased commercially. Since turbidity is a relative measure, manufacturers recommend that calibration involve the use of suspended matter from the waters to be monitored. This is not an easy task if one is working in a deep or highly variable regime.

1.11.3 Oxygen isotope: $\delta^{18}O$

The ratio of oxygen isotope 18 to oxygen isotope 16 in water is fractionated by differences in weight. The lighter element ^{16}O is more easily evaporated than ^{18}O and is therefore a measure of temperature; the higher the temperature the greater the $H_2{}^{18}O/H_2{}^{16}O$ ratio. In contrast to the variability in the surface ocean, average $H_2{}^{18}O/H_2{}^{16}O$ ratios for the deep ocean (>500 m depth) vary by less than 1%. This ratio (in percent) is expressed in conventional delta "δ" notation as

$$\delta^{18}O(\%) = (R_{\text{std}}/R_{\text{sample}} - 1) \times 10^{10}$$

where $R = H_2{}^{18}O/H_2{}^{16}O$ is the ratio of the two main isotopes of oxygen and the subscript "std" refers to Standard Mean Ocean Water (SMOW). The low variability in $\delta^{18}O$ values in waters in the deep sea has led to widespread use of oxygen isotopes as a paleothermometric indicator. These methods assume relatively little variation (about 1%) in the $\delta^{18}O$ values of deep-ocean water over geological time. The $\delta^{18}O$ values of carbonate, silica, and phosphate precipitated by both living and fossil marine organisms, such as foramininferans, radiolarians, coccolithophorids, diatoms, and barnacles, have been used to estimate temperatures of the water in which the organism lived based on temperature-dependent equilibria between the oxygen in the water and the biomineralized phase of interest. The $\delta^{18}O$ values vary in space and time in different regions of the ocean. For example, shallow continental shelves are influenced by freshwater input, particularly at high latitudes. Thus, oxygen removed from seawater by organisms should reflect oceanic conditions at the time. Salinity and ^{18}O content are related in most ocean waters with similar processes influencing both in tandem.

According to Kipphut (1990), the $H_2{}^{18}O/H_2{}^{16}O$ ratio in seawater in the Gulf of Alaska shows only slight variation except near those coastal margins where there is significant input of freshwater from melting of large glaciers ($\delta^{18}O \approx -23\%$) and runoff from coastal precipitation ($\delta^{18}O \approx -10\%$). Precipitation is generally depleted in the heavier isotopes of oxygen because of isotopic fractionation processes which occur during evaporation and condensation. Since the fractionation processes are temperature dependent, precipitation at higher latitudes and elevations shows progressively lower $H_2{}^{18}O/H_2{}^{16}O$ ratios. The ratio is a conservative property of water and when combined with salinity may be useful in determining distinct components of water masses. The isotope data south of Alaska suggest that the coastal waters in southwestern Alaska are derived from a combination of glacier melt and runoff from as far east as south-central Alaska. If we add the freshwater added by runoff from the large rivers of northern British Columbia, the Alaska Coastal Current (Royer, 1981; Schumacher and Reed, 1986) is continuous feature flowing more than 1500 km from the southern Alaska Panhandle to Unimak Pass at the beginning of the Aleutian Island chain.

1.11.4 Helium-3; helium/heat ratio

Helium-3 (^3He) is an inert and stable isotope of helium whose residence time of about 4000 years in the ocean makes it a useful tracer for oceanic mixing times and deepsea circulation. There are two main sources in the ocean. In the upper mixed layer and thermocline, ^3He is produced by the β-decay of anthropogenic tritium; in the deep ocean, ^3He originates with mantle degassing of primordial helium from mid-ocean ridge hydrothermal vents. Anderson (1993) also argues that ^3He and neon from hotspot magmas and gases may reflect an extraterrestrial origin; specifically, subduction of ancient pelagic sediments rich in solar ^3He and neon originate with interplanetary dust particles now being recycled at oceanic hotspots. [For counterarguments see Hiyagon (1994) and Craig (1994)]. The distinct isotopic ratio of mantle helium ($^3He/^4He = 10^{-5}$) versus a ratio of 10^{-6} for atmospheric helium makes $^3He/^4He$ a useful tracer in the ocean. In a classic paper, Lupton and Craig (1981) showed that the $^3He/^4He$ ratio in the 2500 m deep core of the hydrothermal plume emanating from the East Pacific Rise at 15°S in the Pacific Ocean was 50 higher than the ratio of atmospheric helium. The helium plume could be traced more than 2000 km westward from the venting region on the crest of the mid-ocean ridge (Figure 1.11.7). To quote the authors, "In magnitude, scale, and striking asymmetry, this plume is one of the most remarkable features of the deep ocean, resembling a volcanic cloud injected into a steady east wind". Helium-3 is now used extensively as tracer for hydrothermal plumes in active spreading regions such as the Juan de Fuca Ridge in the northeast Pacific and the East Pacific Rise in the South Pacific.

Data collected during GEOSECS indicates that the deep Pacific is the oceanic region most enriched in ^{3}He with a mean ratio concentration δ^3He value of 17% compared with 10% in the Indian Ocean, 7% in the Southern Ocean and 2% in the Atlantic (Jamous *et al.*, 1992). The core of the plume at the East Pacific Rise has a value of 50%. [Here, $\delta^3\text{He}(\%) = (R/R_a - 1)\times 100$, where $R = {}^3\text{He}/{}^2\text{He}$ is the isotopic ratio of the sample and R_a is the atmospheric ratio.] The differences in concentration relate directly to the differences in hydrothermal input and inversely to the degree of deep-water ventilation. For example, there is a considerably greater hydrothermal activity in the Pacific than in the Atlantic while the Atlantic deep water is highly ventilated compared with the Pacific. Similarly, the values of δ^3He ($\approx$ 28) at the bottom of the Black Sea reflect the presence of a strong source at the seafloor. In contrast, the strong correlation between dissolved oxygen concentration and ^{3}He in the Southern Ocean (Figure 1.11.8) indicates that the distributions of these tracers in this region of the world ocean are mainly determined by ventilation processes.

Early vent-fluid samples taken from hydrothermal systems on the Galapagos Rift and at 21°N on the East Pacific Rise were found to have nearly equal ratios of ^{3}He to heat despite the considerable geographical separation of the sites and widely different fluid exit temperatures ($\approx$20 and 350°C, respectively). Here, "heat" is the excess

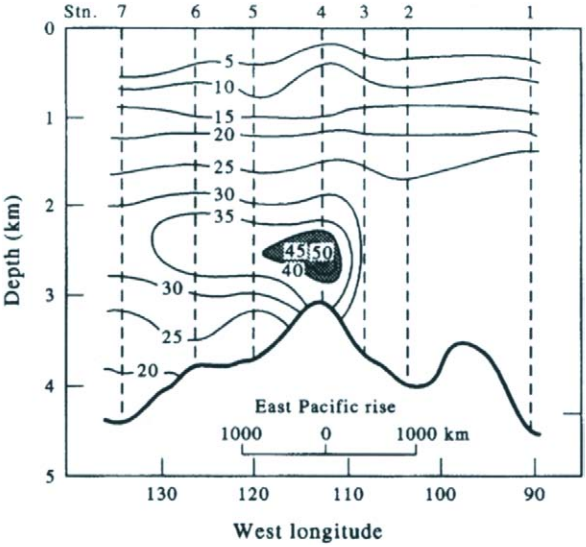

Figure 1.11.7. Cross-section of δ(^{3}He) over the East Pacific Rise at 15°S. The level of neutral plume bouyancy, as determined by the core depth of the ^{3}He plume, is about 400 m above the ridge crest. The ratio is defined as $\delta(^3\text{He}) = (R/R_{ATM} - 1)\times 100$ where $R = {}^3\text{He}/{}^4\text{He}$ and $R_{ATM} = 1.40\times 10^{-6}$. (From Lupton and Craig, 1981.)

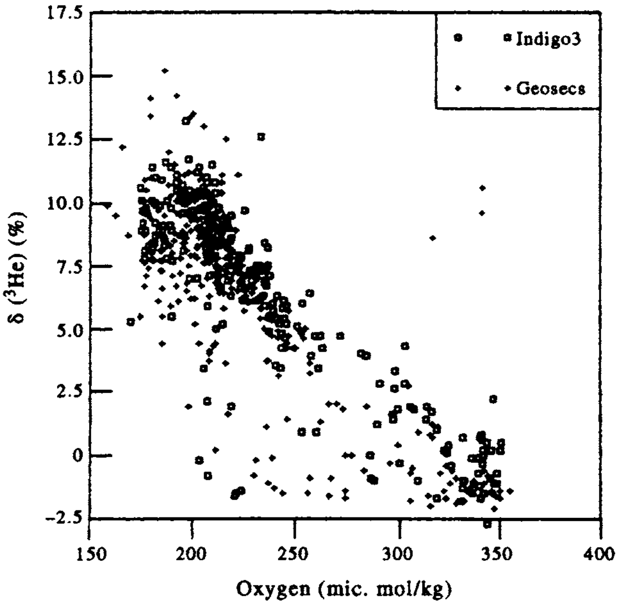

Figure 1.11.8. Correlation between dissolved oxygen concentration O_2 and ^{3}He in the Southern Ocean indicates that the distributions of these tracers in the region of the world ocean are mainly determined by ventilation processes. Combination of GEOSECS and INDIGO-3 data. (From Jamous et al., 1992.)

amount of heat (in calories or joules) added to the ambient water by geothermal processes. By combining independent estimates of the mantle flux of ^{3}He within the ocean with the observed ratio ^{3}He/Heat $\approx 0.5 \times 10^{-12}$ cm^3 STP cal^{-1}, Jenkins *et al.* (1978) calculated a global oceanic hydrothermal heat flux of 4.9×10^{19} cal/year. An examination of the ^{3}He/Heat ratios in the 20-km wide megaplume observed in August 1986 on Juan de Fuca Ridge (Lupton *et al.*, 1989) has shown that the ratios can vary by as much as an order of magnitude and that heat fluxes based on ^{3}He measurements must be taken with caution. Specifically, the ratio ^{3}He/Heat was found to vary with height within the megaplume formed during the hydrothermal event. The megaplume had lower helium values and five times the temperature anomaly as the near-bottom chronic venting regime. Since helium is extracted from the magma by the circulating fluids in the hydrothermal system, the relatively low ratios of ^{3}He/Heat in the megaplume presumably resulted from relatively high water-to-rock ratios and the youth of the hydrothermal fluid prior to its injection into the overlying ocean. Lupton *et al.* (1989) suggest that a value of $\approx 2 \times 10^{-12}$ cm^3 STP He cal^{-1} may be a reasonable estimate for the average ^{3}He/Heat signature of fluids vented into the oceans by mid-ocean ridge hydrothermal systems.

1.12 TRANSIENT CHEMICAL TRACERS

"Transient tracers" are anthropogenic compounds that are injected into the ocean over spatially limited regions within well-defined periods of time. The time "window" makes these compounds especially well suited to studies of upper-ocean mixing and deep-sea ventilation. Transient tracers are commonly used to constrain solutions of global "box" models used to investigate climate-scale carbon dioxide fluxes within coupled atmosphere–ocean systems (Broecker and Peng, 1982; Sarmiento *et al.*, 1988), and in generalized inverse models incorporating both data and ocean dynamics to determine oceanic flow structure (see Bennett, 1992). The timed release into the ocean may take place over a few hours, as in the case of rhodamine dye, or last longer than a century, as in the case of chlorofluorocarbons (CFCs). Injection of certain tracers, such as radiocarbon (^{14}C) greatly augments the natural distributions of these chemicals while for others, such as CFCs and tritium (^{3}H), the tracer is superimposed on an almost nonexistent background concentration. Because of the slow advection and mixing processes in the ocean, as well as the extensive research needed to measure the tracer distributions, most tracers are used in the study of seasonal to decadal scale oceanic variability. For all transient tracers, studies are limited by imperfect knowledge of the surface boundary conditions during water-mass formation. This is especially true of tracers entering from the atmosphere. Tritium and radiocarbon are radioactive isotopes whose observed concentrations must first be corrected for natural radioactive decay. Both tracers have widespread use in descriptive studies and large-scale numerical modeling of ventilation of the deep ocean and the transformation of water masses over periods of decades. Our main purpose in this section is to provide a brief outline of the types of studies possible with transient tracers. Only results for the main tracers will be presented; secondary tracers such as krypton-85 and argon-39 are not discussed.

1.12.1 Tritium

During the late 1950s and early 1960s, large amounts of bomb-produced radiocarbon (^{14}C), strontium (^{90}Sr) and tritium (^{3}H) were released into the stratosphere during above-ground testing of thermonuclear weapons (Figure 1.12.1a, b). Of these, "bomb" tritium (the heaviest isotope of hydrogen) has an extensive database and is measurable to high precision and sensitivity. Tritium is incorporated directly in water molecules as HTO so that it is a true water-mass tracer. Most of the tritium was produced by tests conducted in the northern hemisphere and was eventually deposited onto the earth's surface north of 15°N (Weiss and Roether, 1980; Broecker *et al.*, 1986). Deposition into the oceans is through vapor diffusion and rainfall at a ratio of roughly 2:1 according to observational data. A study by Lipps and Hemler (1992) suggests that the ratio varies according to the type of rainfall. The large fronts across the Pacific and Atlantic oceans at subtropical latitudes impede lateral mixing and the southward transport of tritium. As a result, tritium with a half-life of 12.43 years serves as a useful tracer for water motions on time-scales of decades. It is most useful when combined with measurements of its stable, inert daughter product ^{3}He. This combination helps determine the age of tritium entering the ocean and provides additional information on the distribution of tritium in the atmosphere before it entered the ocean (Jenkins, 1988). Most large-scale studies are based on the extensive tritium data collected in the North Pacific during the Geochemical Ocean Sections Study (GEOSECS: 1972–1974) and Long Lines (1983–1985). Roughly 0.3 litres of seawater are required for the measurement of tritium by beta-decay counting.

Tritium in natural waters is expressed in "tritium units" (TU), which is the abundance ratio $^{3}H/^{1}H \times 10^{18}$. The ratio abundance corresponds to 7.09 disintegrations per min per kg of water. To remove the effect of normal radioactive decay from a data series, the tritium concentrations are corrected to a common

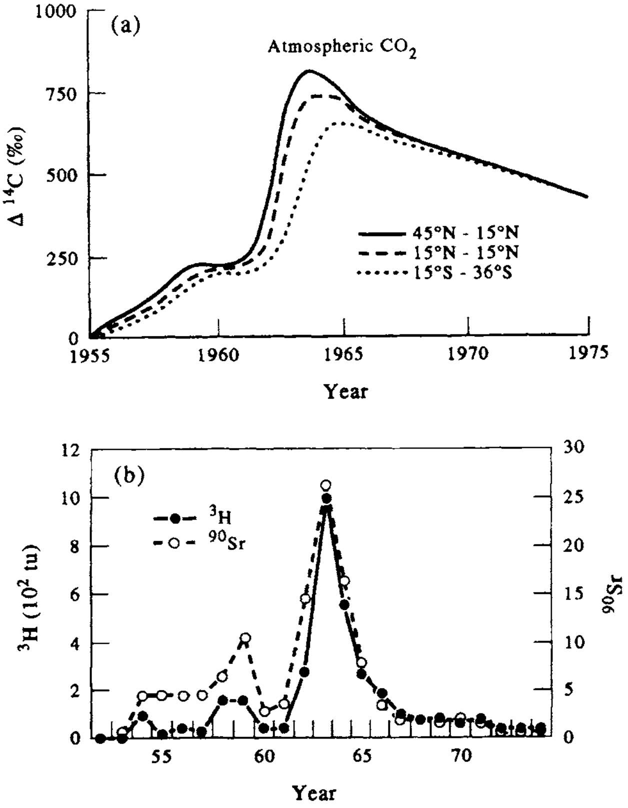

Figure 1.12.1. Time-series of bomb-produced elements released into the stratosphere during above-ground testing of thermonuclear weapons during the late 1950s and early 1960s: (a). radiocarbon (^{14}C) and (b). strontium (^{90}Sr) from measurements of atmospheric carbon dioxide and tritium (^{3}H) based on rain at Valencia Ireland. (Adapted from Quay et al., 1983; Broecker and Peng, 1982.)

reference of January 1, 1981. Thus, TU81N is the ratio of ^{3}H/^{1}H a sample would have as of 1981/01/01. The measurement error for "decay-corrected". data is 0.05TU or 3.5%, whichever is greater (Van Scoy *et al.,* 1991). Water having values less than 0.2TU81 are considered to reflect cosmogenic background levels or arise from dilution by mixing of bomb tritium. The fact that decay-corrected tritium is a conservative quantity that was added to a selected area of the world ocean in a relatively short period of time (Figure 1.12.2) makes it attractive as an oceanic tracer. Changes in the spatial distribution of tritium with time provide a measure of horizontal advection while depth penetration on isopycnals that do not outcrop to the atmosphere are indicative of cross-isopycnal (diapycnal) mixing. Fine (1985) uses upper ocean tritium data from the GEOSECS program to show that there is a net transport of 5×10^6 m^3/s in the upper 300 m from the Pacific to the Indian Ocean through the Indonesian Archipelago. This contrasts with values of 1.7×10^6 m^3/s obtained using hydrographic data (Wyrtki, 1961) and 5–14 $\times 10^6$ m^3/s from salt and mass balances (Godfrey and Golding, 1981; Piola and Gordon, 1984; Gordon, 1986). Gargett *et al.* (1986) have examined the nine-year record of tritium from Ocean Station P (50°N, 145°W) in the northeast Pacific. Results suggest that the observed vertical distribution of tritium in this region is determined mainly through advection along isopycnals rather than by

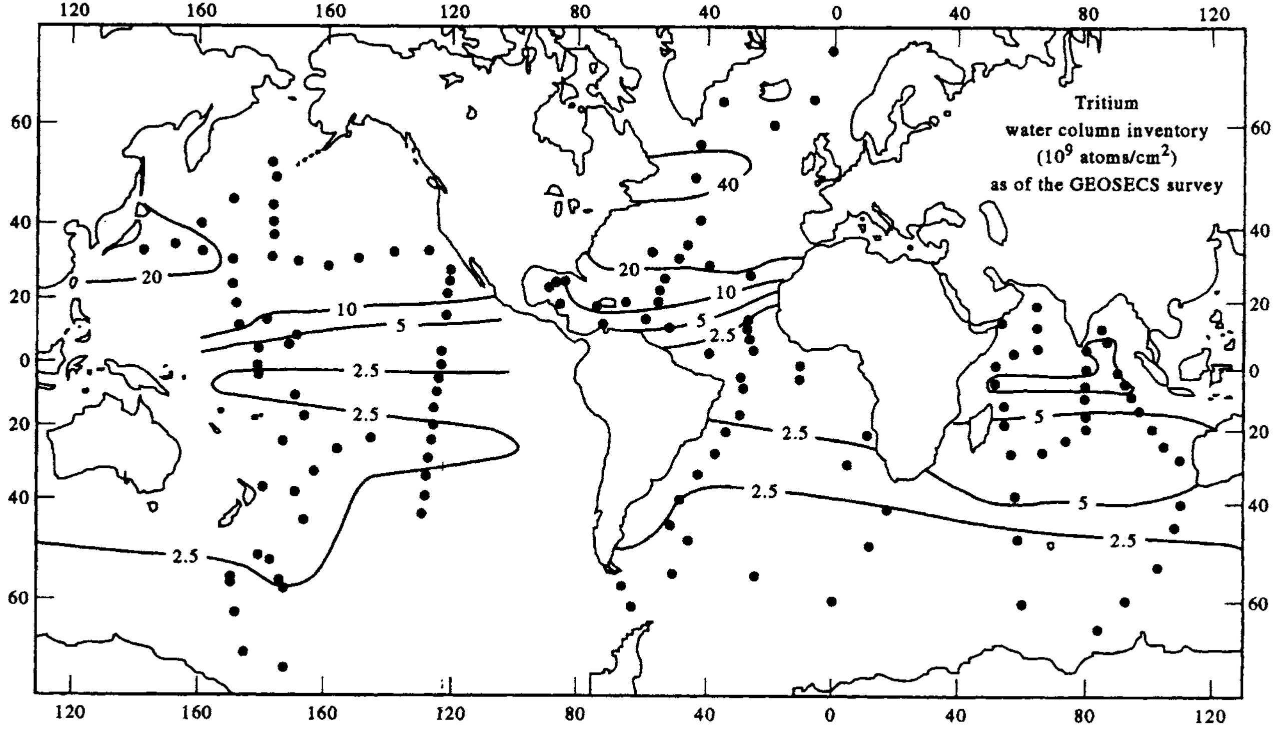

Figure 1.12.2. Decay-corrected tritium (TU81) water column inventories over the world oceans based on results obtained as part of the GEOSECS program and NAGS expedition. (Adapted from Broecker et al., 1986.)

isopycnal or diapycnal diffusion in the density range of maximum vertical tritium gradient. Tritium data studied by Van Scoy *et al.* (1991) show evidence for wind-driven circulation to the depth of the dissolved oxygen minimum near 1000 m depth (σ_t = 27.40) in subpolar regions of the North Pacific. The authors conclude that, after two decades of mixing, advection along isopycnal surfaces appears to be the dominant process influencing the distribution of tritium in the North Pacific and that cross-isopycnal mixing in the subpolar region is important for ventilating the nonoutcropping isopycnals. According to Van Scoy *et al.* (1991), tritium has penetrated on average 100 m deeper into the ocean during the 10 years between the GEOSECS and Long Lines surveys. Depletions of tritium in the upper ocean are seen in the tropics and at high southern latitudes. Moreover, the above-background tritium levels observed on nonoutcropping isopycnals surfaces in the North Pacific indicate that ventilation is still taking place despite the absence of deep convective mixing in this region. In the Atlantic Ocean, deep convection is the dominant mechanism for the invasion of surface waters into the deep ocean (Figure 1.12.3).

Tritium data are used to constrain circulation models for the world ocean. For example, tritium records combined with a three-box model of the Japan Sea—a comparatively isolated oceanic region with a mean depth of 1350 m—have yielded overturn times for the deep water of 100 years and overall residence times of 1000 years (Watanabe *et al.*, 1991). Similar estimates for this region based on the same box-model constrained by ^{226}Ra and ^{14}C data yielded a turnover time of 300–500 years for deep water and 600–1300 years for the residence time (Harada and Tsunogai, 1986). Applications to larger oceanic basins are generally less successful. Memery and Wunsch (1990) found that the tritium data did not strongly constrain their circulation model for the North Atlantic and that large errors ($\approx$20%) in the input of tritium at the surface can be accommodated by relatively minor changes in the model circulation. According to Wunsch (1988), "Any uncertainty in the transient tracer boundary conditions and sparse interior ocean temporal coverage greatly weakens the ability of such tracers to constrain the ocean circulation". Although the authors still believe in the usefulness of tritium records, they suggest that chlorofluorocarbons will improve modeling capability since the atmospheric concentration of these compounds remains relatively high despite the 1988 Montreal Accord and are better known than for tritium.

Jenkins (1988) describes the use of the tritium–^{3}He age, which takes advantage of the radioactive clock of ^{3}He and the long time-scale of tritium to measure the elapsed time since the Helium gas was in equilibrium with the atmosphere. Time scales for which this combined tracer is useful are 0.1–10 years.

1.12.2 Radiocarbon

Carbon-14 (^{14}C) dating requires prior knowledge of long-term variations in the ^{14}C/^{12}C ratio in the atmosphere. Because of the difficulties in separating radiocarbon produced from thermonuclear devices and cosmic rays, bomb-generated radiocarbon is a less useful tracer of upper ocean processes than is tritium. The problem of using radiocarbon data collected prior to 1958 together with tritium measurements to establish the prenuclear levels of radiocarbon is discussed by Broecker and Peng (1982). Once the prenuclear surface-water cosmic radiocarbon concentration is known for each locality, water column inventories for bomb-radiocarbon can be obtained from the depth profiles of ^{14}C/C, ^{3}H, and $\sum CO_2$ concentration obtained as part of

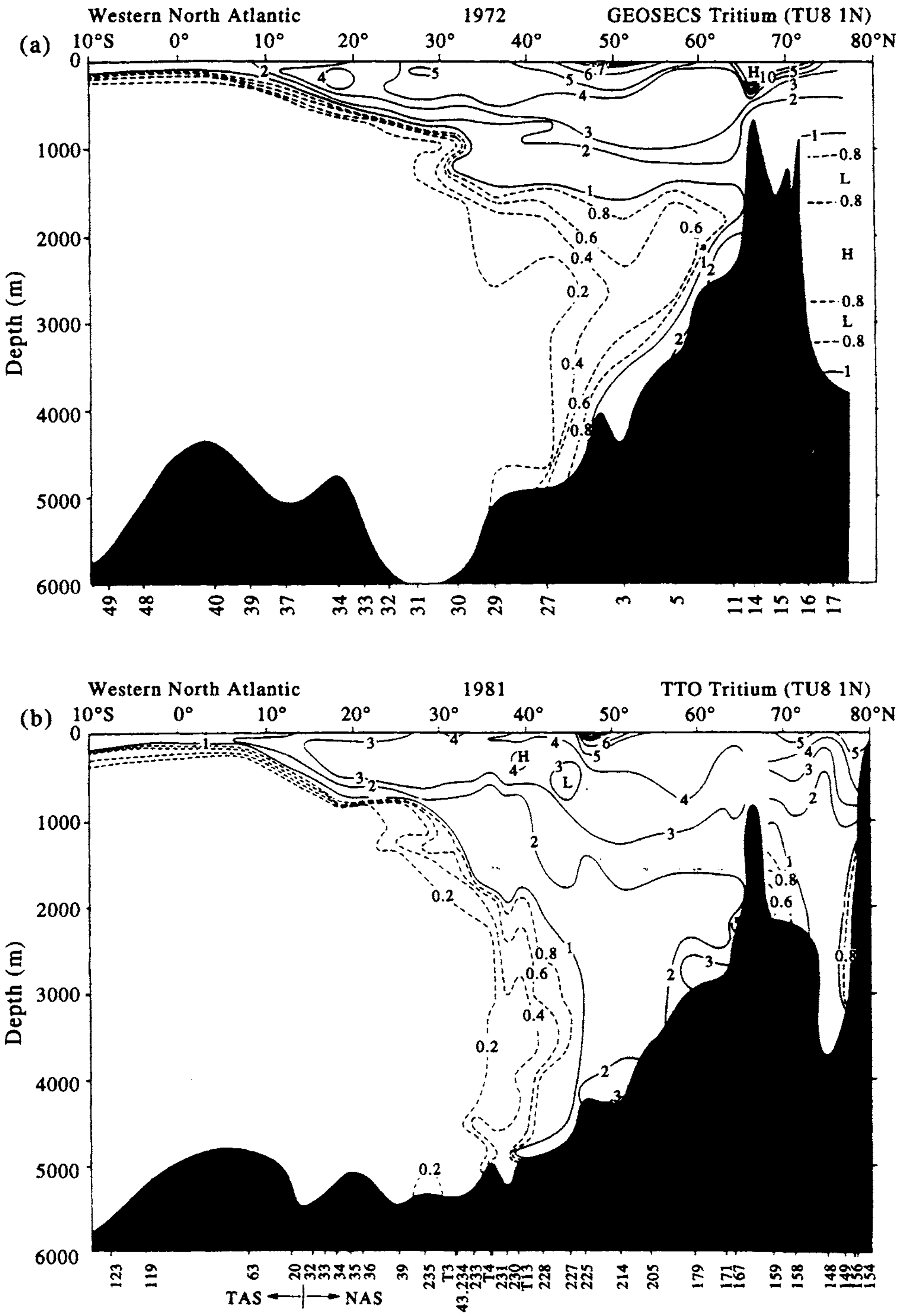

Figure 1.12.3. Cross-section of tritium (TU81N) concentrations in the western Atlantic Ocean (a) GEOSECS 1972; (b) TTO 1981. (From Östlund and Rooth, 1990.) Results suggest that the observed vertical distribution of tritium in this region is determined mainly through advection along isopycals rather than by isopycnal or diapyncal diffusion in the density range of maximum vertical tritium gradient.

the GEOSECS, NORPAX and TTO programs (Broecker *et al.*, 1985). Bomb-produced radiocarbon is delivered through a nearly irreversible process from the atmosphere to the ocean so that it is possible to estimate the amount of this isotope that has entered any given region of the ocean. As a result of this production, levels of $^{14}CO_2$ increased by about a factor of two in the northern hemisphere during the late 1950s and early 1960s. Measurement of radiocarbon by beta decay requires 200–250 litres of seawater to give the desired accuracy of 3–4 ppt. Age resolution is 25–30 years for abyssal oceanic conditions for which the introduction of bomb-radiocarbon effects remain negligible. Radiocarbon has a half-life of 5680 years and decays at a fixed rate of 1% every 83 years. A rapid onboard technique for measuring radiocarbon using an accelerator mass spectrometer is described by Bard *et al.* (1988). This technique decreases the sample size by 2000 compared with that using the standard β-counting method.

By convention, radiocarbon assays are expressed as $\Delta^{14}C$, which is the deviation in parts per thousand (ppt) of the $^{14}C/^{12}C$ ratio from that of a hypothetical wood standard with $\delta^{13}C$ = $^{13}C/^{12}C$ = −25 ppt and corrected from the actual $\delta^{13}C$ values (around 0 ppt for seawater to exactly −25 ppt to compare with the wood standard). The standard is a way to compare the observed ratio of carbon isotopes to the atmospheric value prior to the industrial revolution of about 1850. The quantity of ^{14}C in a sample of seawater is proportional to the actual uncorrected $^{14}C/^{12}C$ ratio $(1 + 0.001\delta^{14}C)$. More precisely

$$\Delta^{14}C = \delta^{14}C - 2(\delta^{13} + 25)(1 + \delta^{14}C/1000) \qquad (1.12.1)$$

where

$$\begin{aligned}\delta^{14}C = 1000[(^{14}C/C)\,\text{sample} \\ - (^{14}C/C)\ \text{standard}]/(^{14}C/C)\,\text{standard}]\end{aligned} \qquad (1.12.2)$$

Pre-bomb $\Delta^{14}C$ values from corals collected in the early 1950s average around −50 (±5) ppt (Druffel, 1989). Thus, any $\Delta^{14}C$ value above −50 ppt will indicate the presence of anthropogenic radiocarbon, mainly produced by the atmospheric nuclear testing in the early 1960s. The determination of inventories for bomb-produced radiocarbon in the ocean is much more complex than for bomb tritium. The reason is that the amount of natural tritium in the sea is negligible compared with the amount of bomb-produced tritium. In the case of radiocarbon, the delivery of isotopes to the ocean requires a better knowledge of wind speeds over the ocean and of the wind speed dependence of the CO_2 exchange rate.

The concentration of ^{14}C in the ocean is influenced by several processes. For example, bottom water formation in the Weddell Sea and the North Atlantic provides a direct input of surface water ^{14}C (Figure 1.12.4). Additional input of ^{14}C to the deep sea can occur by transport along isopycnals, by vertical mixing in the main oceanic thermocline, by lateral mixing of water masses and by upwelling in coastal and equatorial regions. Addition of CO_2 and ^{14}C comes from the dissolution of carbonate skeletons and the oxidation of organic materials from sinking particles. Stuiver *et al.* (1982) use radiocarbon data from GEOSECS to estimate abyssal (>1500 m) waters replacement times for the Pacific, Atlantic and Indian Oceans of 510, 275, and 250 years, respectively. The deep waters of the entire world ocean are replaced on average

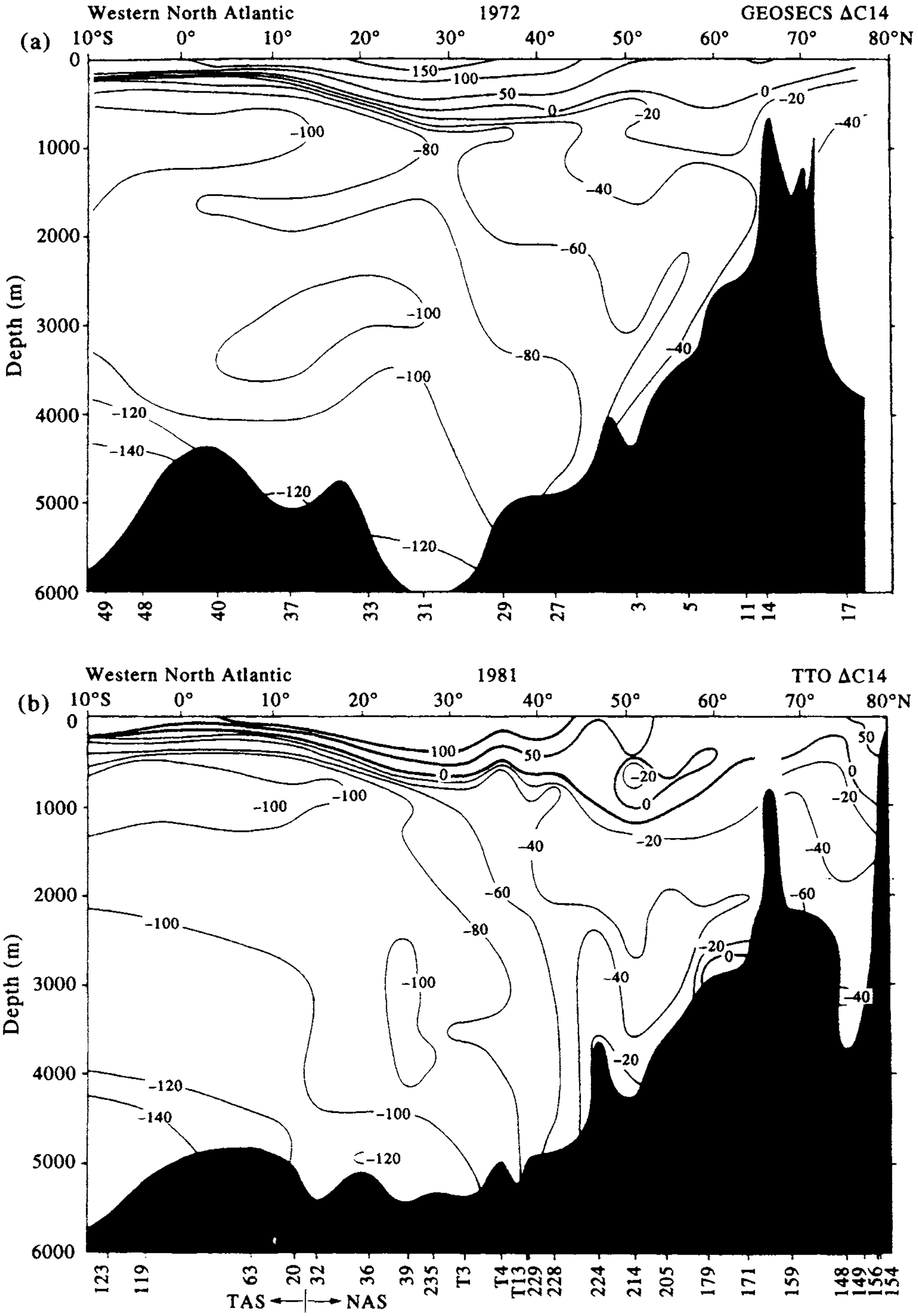

Figure 1.12.4. Cross-section of radiocarbon concentrations in the western Atlantic Ocean (a) GEOSECS 1972; (b) TTO 1981 (cf. Figure 1.12.3). Note that significant changes occur mainly in the deep waters north of 40°N. (From Östlund and Rooth, 1990.)

every 500 years. Östlund and Rooth (1990) found a relative decrease in the difference in $\Delta^{14}C$ between the surface and the northerly abyssal layers of the North Atlantic of 25–30%. If this were due to vertical diffusivity a high value of 10 cm^2/s would be required based on a scale depth of 1 km and 10 years between surveys. This is a factor of 10 too large so that high latitude injection processes must be responsible for the observed evolution below 1000 m depth. Measurements of $\Delta^{14}C$ from seawater and organisms from the Pacific coast of Baja California (Druffel and Williams, 1991) revealed the effects of coastal upwelling and bottom-feeding habits. Dilution of nearshore waters by upwelling accounts for reduced radioactive carbon levels observed near the coast while feeding on sediment-derived carbon explains the reduced levels of ^{14}C in sampled organisms relative to dissolved inorganic carbon in the water column. Broecker *et al.* (1991) have addressed the concerns about the accuracy of ventilation flux estimates for the deep Atlantic due temporal changes in the $^{14}C/C$ ratio for atmospheric CO_2. Despite the fact that $\Delta^{14}C$ values have declined from about 10 to −20 ppt over the past 300 years due to changes in the solar wind and the addition of $\Delta^{14}C$-free CO_2 to the atmosphere from fossil fuel burning, temporal effects have been considerably buffered in the ocean and errors in radiocarbon ages are too low by only 10–15%. The reason is that the northern and southern source waters for the Atlantic deep water have $\Delta^{14}C$ ratios, and hence relative time variabilities, considerably lower than the atmospheric ratio.

1.12.3 Chlorofluorocarbons

Chlorofluorocarbons (CFCs) are a group of volatile anthropogenic compounds that until the 1988 Montreal Protocol found increasingly widespread use in aerosol propellants, plastic foam blowing agents, refrigerants and solvents. Also known as chlorofluoromethanes (CFMs) and “Freons” (a Dupont tradename), most of these chemicals eventually find their way into the atmosphere where they play a primary role in the destruction of stratospheric ozone. The two primary compounds CFC-12 or F-12 (CF_2Cl_2) and CFC-11 or F-11 ($CFCl_3$) have respective lifetimes in the troposphere of 111 and 74 years. Although more than 90% of production and release of F-11 and F-12 takes place in the northern hemisphere, the meridional distributions of these compounds in the global troposphere are relatively uniform due to the high stability of the compounds and the rapid mixing that occurs in the lower atmosphere. The source function at the ocean surface differs by only about 7% from the northern hemisphere to the southern hemisphere (Bullister, 1989). During the period 1930–1975 the ratio F-11/F-12 in the atmosphere and ocean surface increased with increasing uses of these chemicals (Figure 1.12.5). The regulation of CFC use in spray cans in the U.S.A. during the late 1970s decreased the rate of CFC-11 increase so that the ratio F-11/F-12 ratio in the atmosphere has remained nearly constant. As a consequence, measurements of the ratio provide information on when a particular water mass was last in contact with the atmosphere. In shelf waters the CFCs concentration is determined by rates of mixed layer entrainment, gas exchange and mixing with source water. At a removal rate of about 1% per year from the atmosphere by stratospheric photolysis, CFCs will serve as ocean tracers well into the next century.

Since they are chemically inert in seawater, chlorofluorocarbons are used to examine gas exchange between the atmosphere and ocean, ocean ventilation and mixing on decadal scales. The limit of detection of F-11 and F-12 in seawater volumes

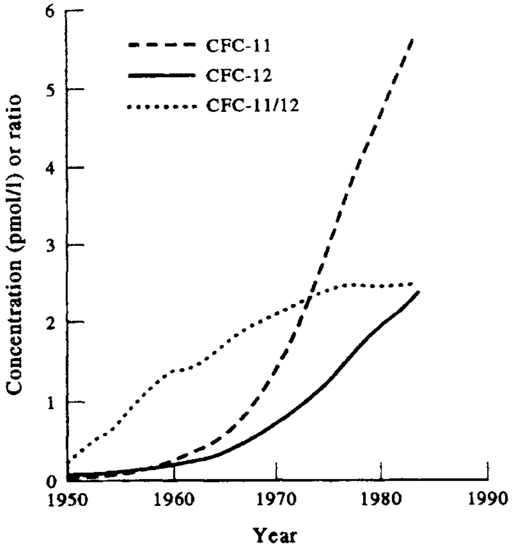

Figure 1.12.5. CFC-12 and CFC-11 concentrations in the upper ocean for T = −1°C and S = 34.3 psu as function of time. (From Trumbore et al., 1991.)

as small as 30 ml is better than 5×10^{-15} mole/kg seawater (Bullister and Weiss, 1988), or roughly three orders of magnitude higher than near-surface concentrations in the ocean. Modern techniques allow for processing of CFCs at sea with processing times of the order of hours. Gammon *et al.* (1982) examined the vertical distribution of CFCs at two offshore sites in the northeast Pacific. Using a one-dimensional vertical diffusion/advection model driven by an exponential surface source term, they obtained a characteristic depth penetration of 120–140 m. For the Gulf of Alaska station at 50°N, 140°W, vertical profiles of F-11 and F-12 gave consistent vertical diffusivities of order 1 cm^2/s and an upwelling velocity of 12–14 m/year. Woods (1985) used CFCs to estimate the transit time and mixing of Labrador seawater from its northern source region to the equator along the western Atlantic Ocean boundary. In a related study, Wallace and Lazier (1988) used CFCs and a simple convection model to examine recently renewed Labrador seawater formed by deep convection to depths greater than 1500 m following a severe winter in the North Atlantic. Their observed CFC levels of 60% saturation with respect to contemporary atmospheric concentrations suggest that deep convection took place too rapidly for air–sea gas exchange to bring CFC levels to equilibrium. Trumbore *et al.* (1991) have used CFCs collected in 1984 to examine recent deep water ventilation and bottom water formation near the continental shelf in the Ross Sea in the Antarctic Ocean. Using CFC data combined with conventional (temperature, salinity, dissolved oxygen and nutrient) tracer data in a time-dependent convection model they estimate shelf-water resident times of about three years for the Ross Sea. At the other end of the globe, Schlosser *et al.* (1991) use hydrographic and CFC data to suggest that formation of Greenland Sea Deep Water decreased in the 1980s. The dissolved F-12 concentration in Figure 1.12.6 illustrates several aspects of the circulation in the North Atlantic. In particular, we note the core of the Labrador Seawater mentioned earlier in this section, the presence of a lense of Mediterranean outflow water ("Meddy") at 22°N and the core of high CFC over the equator which is

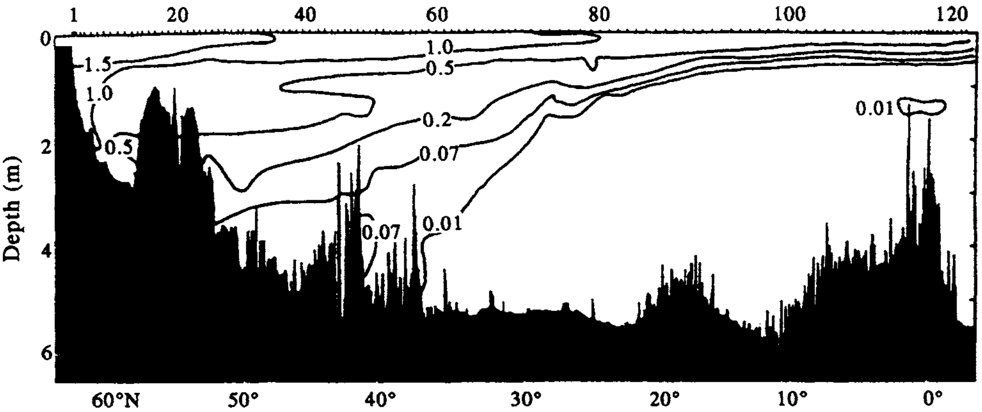

Figure 1.12.6. Dissolved CFC-12 concentrations ($\times 10^{-12}$ mole/kg) along a North Atlantic section. (From Bullister, 1989.)

thought to be a longitudinal extension of flow from the western boundary near Brazil (Bullister, 1989).

1.12.4 Radon-222

Radon (^{222}Rn) is a chemically inert gas with a radioactive half-life of 3.825 days. It occurs naturally as a radionuclide of the ^{238}U series and is injected into the atmosphere by volcanic eruptions. The gas has proven particularly useful at time-scales of a few days to weeks for examining the rate of gas transfer between the atmosphere and the ocean surface (Peng *et al.*, 1979), in studies of water column mixing rates (Sarmiento *et al.*, 1976), and for estimating the heat and chemical fluxes from hydrothermal venting at mid-ocean ridges (Rosenberg *et al.*, 1988; Kadko *et al.*, 1990).

The new application of ^{222}Rn studies to hydrothermal venting regions has been especially successful (Rosenberg *et al.*, 1988). In this case, it is assumed that there is a constant flux of radon into the effluent plume that typically rises several hundred meters above the venting region at depths of 2–3 km on the ridge axis. Typical venting regions have scales of 100 m and are spaced at several kilometers along the ridge axis. Waters exiting from black smokers can be up to 400°C. At steady state, the amount of radon lost to radioactive decay at some point in the laterally spreading nonbuoyant plume is balanced by a supply of radon from the venting region. To obtain the total heat (or chemical species) issuing from the venting region, the observer first uses a submersible or towed sensor package to measure the ratio of radon to heat (or species) anomaly, $^{222}\mathrm{Rn}/\Delta\mathrm{T}$, in the plume near the vent orifice—before the radon in the plume has a chance to disperse or age. The observer then uses a towed sensor package to map the total inventory of radon in the spreading plume (Figure 1.12.7). Taking into account the effect of cold water entrainment on the rising plume at Endeavour Ridge in the northeast Pacific (47°47′N, 129°06′W), Rosenberg *et al.* (1988) found an initial radon/ΔT value of 0.03 dpm (disintegrations per minute—the standard unit of measurement for radioactive materials) or 55 atoms per joule. They then used hydocast bottle data to estimate the standing crop of radon above 2100 m depth as $^{222}\mathrm{Rn}(\mathrm{Total}) = 8\times10^{12}$ dpm. At steady-state, hydrothermal venting must be adding this much radon to the system so that the total heat emanating from the vents is

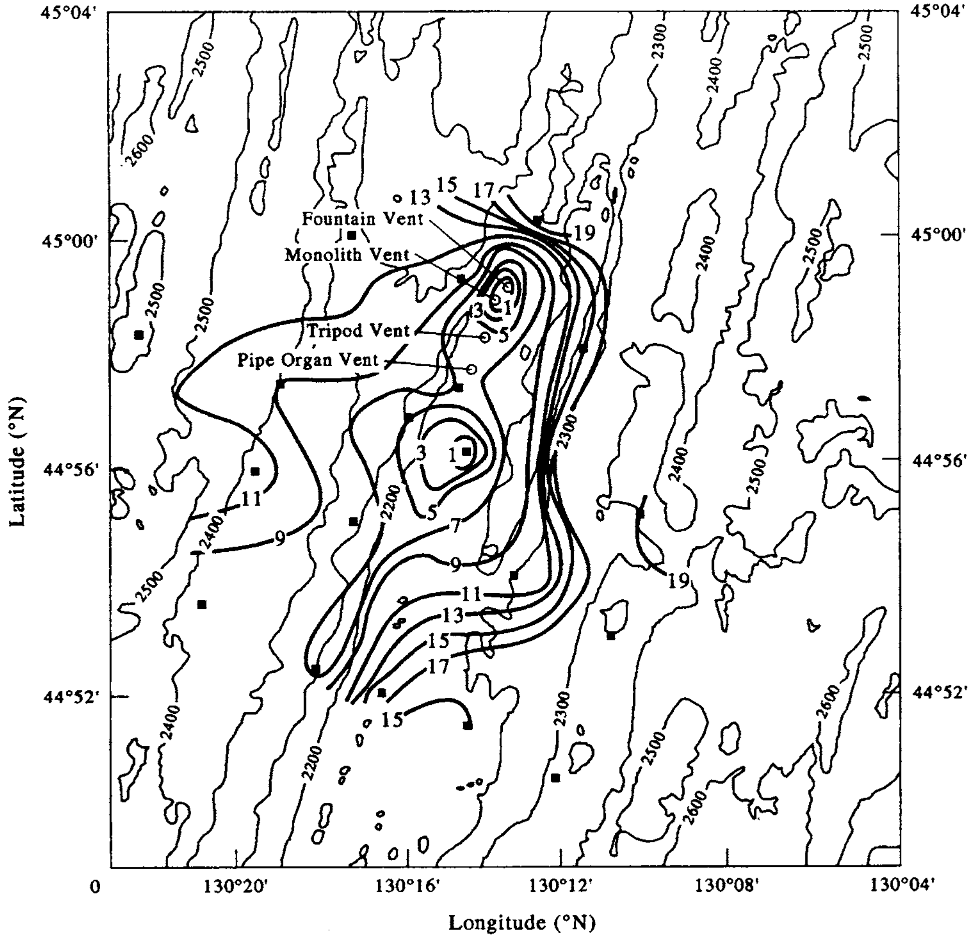

Figure 1.12.7. Apparent age of the neutrally-buoyant plume on the isopycnal surface $\sigma_\theta = 27.68$ *(roughly 2100 m depth) at the Cleft Segment of Juan de Fuca Ridge in the northeast Pacific. Distribution based on Radon-222 data for September 1990. Depths in meters. Plume rises from the hydrothermal vent depth of 2280 m to approximately 2100 m. (From Gendron et al., 1993.)*

$$^{222}\text{Rn}\,(\text{Total})/(^{222}\text{Rn}/\Delta T) = 3(\pm 2) \times 10^9\,\text{watts} \qquad (1.12.3)$$

which compares with estimates based on direct measurements of the total heat content anomaly of the plume in combination with local currents (Baker and Massoth, 1986, 1987; Baker *et al.*, 1995). Gendron *et al.* (1993) have used ^{222}Rn to examine time variability in hydrothermal venting on the Cleft Segment of Juan de Fuca Ridge and to estimate the age of the plume as a function of location relative to the known vent sites. They found that the hydrothermal flux decreased from 2.2±0.3 GW in 1990 to 1.2±0.2 GW in 1991 (1 GW = 10^9 watts).

The estimates using radon-222 in the ocean are complicated by the fact that radon concentration is a function of both radioactive decay and dilution with ambient seawater. Similar estimates can be made using ^{3}He to heat ratios combined with the total inventory of ^{3}He in the ocean. The result (Jenkins, 1978) is a global hydrothermal heat flux of 4.9×10^{19} cal/year. Baker and Lupton (1990) have used the ^{3}He/heat ratio as a possible indicator of magmatic/tectonic activity at ridge segments. The change from a ratio of 4.4×10^{-12} cm^3 STP cal^{-1} immediately following the megaplume eruption at Cleft segment to 1.3×10^{-12} cm^3 STP cal^{-1} two years later suggests that high ratios may be indicative of venting created or profoundly perturbed by a magmatic–tectonic event, while lower values may typify systems at equilibrium.

1.12.5 Sulfur hexafluoride

In certain instances, there is a distinct advantage to a controlled and localized release of a chemical into the environment. Prefluorinated tracers such as sulfur hexachloride (SF_6) and perfluorodeclin (PFD) are among the new generation of deliberately released tracers used to measure mixing and diffusion rates in the ocean. These substances are particularly good at examining vertical mixing. Their appeal is that they are a readily detectable conservative tracers that have no significant effect on the environment and no toxicity. A thorough description of the use of these tracers as well as rhodamine dyes can be found in Watson and Ledwell (1988). In the case of rhodamine dyes, the detection limit by fluorometers is set by the background fluorescence of natural substances in water which is about 1 part in 10^{12} in the deep ocean. For SF_6 the background limit is set by dissolution from the atmosphere where the compound is present at 1–2 parts in 10^{12} by volume. Surface values in the ocean are roughly 5×10^{-17} and diminish to zero in deep water. The instrumental detection for SF_6 is limited to about 1/10 of the near-surface value (Watson and Liddicoat, 1985). PFD has no measurable background level in the ocean and is limited by instrumental detection to about 1 part in 10^{16}. For a release of 1 metric ton (≡ 1 tonne) at a given density level in an experiment, these detection limits translate to maximum horizontal scales of 100 km for rhodamine dye, 1000 km for PFDs and basin scales for SF_6. Lifetimes for the tracers range from months to about a year. Despite their usefulness, the long-term prognosis for SF_6 and PFDs is limited as industrial injection of SF_6 into the atmosphere and medical use of PFDs will eventually increase background levels and take away from their ability to serve as tracers.

Rhodamine dye is used mainly in coastal studies. SF_6 has been used successfully in WOCE. The North Atlantic Tracer Release Experiment (NATRE) was a large-scale WOCE-related study using SF_6 to examine the stirring and diapycnal mixing in the pycnocline of the North Atlantic. In May 1992, 139 kg of sulfur hexafluoride was released on the isopycnal surface 26.75 kg/m^3 (310 dbar) along with eight SOFAR floats and six pop-up drifters in the eastern subtropical Atlantic near 25.7°N, 28.3°W. To sample the tracer, investigators towed a vertical array of 20 integrating sample at 0.5 m/s through the patch. A prototype 18-chamber sampler at the center of the array obtained a lateral resolution of about 360 m. The average profile increased from a RMS thickness of 6.8 m after 14 days to a RMS thickness of about 45 m by April 1993, yielding a diapycnal eddy diffusivity of 0.1–0.2 cm^2 s^{-1}. To be successful, experiments like NATRE require the tracer to be injected on a constant density surface rather than a constant depth. Internal wave oscillations and other vertical motions would broaden the tracer concentration more than necessary if it were released at a constant depth. Care must be taken during injection to ensure the tracer's buoyancy is correct and that the turbulent wake of the injection apparatus is not excessive.

1.12.6 Strontium-90

The distribution of bomb-produced ^{90}Sr in the ocean is quite similar to that of tritium. However as pointed out by Toggweiler and Trumbore (1985), ^{90}Sr has the virtue that the ratio ^{90}Sr/Ca incorporated into coral skeletons has the same value as this ratio in seawater. Corals average out seasonal variations in the ^{90}Sr content of seawater so that annual bands provide a time-averaged measure of the amount of strontium in the water. The results of Toggweiler and Trumbore (1985) suggest that waters move into the Indian Ocean via passages through the Indonesian Archipelago. In addition, the data suggest that there is a large-scale transport of water between the temperate and tropical North Pacific.